

24p

REPORT NO. GDCA-BGJ72-017
CONTRACT F04701-72-C-0054

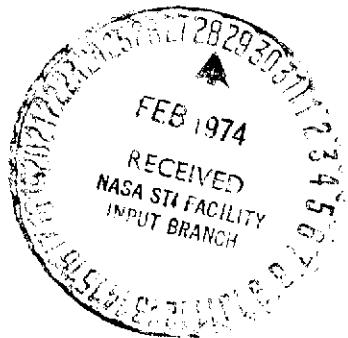
(NASA-CR-132409) ATLAS F ENTRY
AEROTHERMIC STUDY Final Report (General
Dynamics Corp.) 167 p HC \$11.50 CSDL 22B
160

N74-17566

Unclas
G3/31 30140

ATLAS F ENTRY AEROTHERMIC STUDY

FINAL REPORT



GENERAL DYNAMICS
Convair Aerospace Division

REPORT NO. GDCA-BGJ72-017

**ATLAS F ENTRY
AEROTHERMIC STUDY**

FINAL REPORT

December 1972

Prepared Under
TCP 2491 to
Contract F04701-72-C-0054

Prepared by
CONVAIR AEROSPACE DIVISION OF GENERAL DYNAMICS
San Diego, California

FOREWORD

This study was initiated at the request of NASA Langley Research Center (LRC) and accomplished under TCP 2491 to Contract F04701-72-C-0054 by arrangement between SAMSO and NASA-LRC. The study was conducted under the direction of J. Dunavant, the NASA-LRC Technical Monitor, and R. Romero of the Atlas E/F Project Office. Listed below are the personnel who participated in the study and their areas of cognizance:

R.S. Wentink	Study Manager
A. Arcidiacono	} Aeroballistics
R. Norell	
D.R. Lukens	} Control Dynamics
R. L. Watson	
W. McDonald	Electrical Systems
G.B. Wood	Instrumentation
R.R. Henry	R F System
E.W. Schwartz	Space Thermodynamics
J.E. Dyer	Structural Analysis
R. J. Conway	Thermodynamics-Launch Vehicle

PROCEEDING PAGE SEVENTEEN NOT FILMED

TABLE OF CONTENTS

Section	Page
1	INTRODUCTION 1-1
2	STUDY RESULTS AND DISCUSSION 2-1
2.1	Mission and Trajectory Evaluation 2-1
2.1.1	Mission Evaluation. 2-1
2.1.2	Aerodynamics Coefficients 2-2
2.1.3	Reference Trajectory and Dispersion Analysis . 2-5
2.2	Entry Attitude Predictability 2-13
2.2.1	Entry Attitude History Simulation. 2-13
2.2.2	Attitude Following HIRS and Pitch Tumbling Rocket Firings 2-23
2.3	Vehicle Structural Integrity. 2-29
2.3.1	Thermodynamic Analysis 2-29
2.3.2	Structural Modifications 2-35
2.3.3	Loads and Structural Analysis 2-40
2.4	Heating Rate Sensors 2-56
2.4.1	Introduction 2-56
2.4.2	Analytic Model 2-56
2.4.3	Results 2-59
2.4.4	Gage Location 2-63
2.5	Vehicle Attitude Measurement 2-132
2.6	Data Transmission 2-135
2.6.1	S-Band RF Transmission 2-135
2.6.2	Alternate Approaches to the Problem 2-136
2.6.3	Alternate Concept — X-Band 2-138
2.6.4	Special S-Band RF Transmission Test 2-140
2.6.5	Modifications to the S-Band Telemeter 2-142
2.7	Summary of Modifications and Special Equip- ment Required 2-145
3	PROGRAM CONSIDERATIONS 3-1
3.1	Schedule Considerations 3-1
3.2	Cost Considerations 3-1
3.3	Range Data Availability/Arrangement 3-1

TABLE OF CONTENTS (Continued)

Section		Page
4	CONCLUSIONS AND RECOMMENDATIONS	4-1
4.1	Mission and Trajectory.	4-1
4.2	Entry Attitude Predictability	4-1
4.3	Vehicle Structural Integrity	4-1
4.4	Heating Rate Sensors	4-2
4.5	Vehicle Attitude Sensor.	4-2
4.6	Data Transmission	4-3
4.7	Program Considerations	4-3
5	REFERENCES	5-1

LIST OF FIGURES

Figure		Page
1-1	Study logic flow	1-3
2-1	Typical ABRES F/HIRS tank configuration	2-3
2-2	Aerodynamic force and moment axis system	2-4
2-3	Lateral Force Coefficients	2-6
2-4	Lateral Force Coefficient Derivatives	2-6
2-5	Axial Force Coefficient	2-7
2-6	Pitching and Yawing Moment Coefficients	2-7
2-7	Pitching and Yawing Moment Coefficient Derivatives	2-8
2-8	Center of Pressure Location	2-8
2-9	Dynamic Pressure versus Altitude	2-9
2-10	Relative Velocity and Mach Number versus Altitude	2-9
2-11	Altitude versus Time.	2-10
2-12	Slant Range and Elevation Angle versus Time for Ennylabegan Telemetry Station	2-10
2-13	Slant Range and Elevation Angle versus Time for Roi Namur Radar Tracking Station	2-11
2-14	Tank Entry Impact Dispersions	2-11
2-15	Analog flow diagram - pitch plane simulation	2-14
2-16	Axis system	2-15
2-17	Nose position history (IYY = 200,000 ft, $\dot{\theta} = 0^\circ/\text{sec}$, $\theta = 0^\circ$)	2-17
2-18	Nose position history (IYY = 200,000 ft, $\dot{\theta} = -10^\circ/\text{sec}$, $\theta = 0^\circ$)	2-18
2-19	Nose position history (IYY = 200,000 ft, $\dot{\theta} = 45^\circ/\text{sec}$, $\theta = 0^\circ$)	2-18
2-20	Nose position history (IYY = 200,000 ft, $\dot{\theta} = -90^\circ/\text{sec}$, $\theta = 0^\circ$)	2-19
2-21	Nose position history (IYY = 155,000 ft, $\dot{\theta} = -120^\circ/\text{sec}$, $\theta = -90^\circ$)	2-19
2-22	Nose position history (IYY = 185,000 ft, $\dot{\theta} = -120^\circ/\text{sec}$, $\theta = -90^\circ$)	2-20
2-23	Nose position history (IYY = 155,000 ft, $\dot{\theta} = -150^\circ/\text{sec}$, $\theta = -90^\circ$)	2-20
2-24	Nose position history (IYY = 185,000 ft, $\dot{\theta} = -150^\circ/\text{sec}$, $\theta = -90^\circ$)	2-21
2-25	Nose position history (IYY = 80,000 ft, $\dot{\theta} = -180^\circ/\text{sec}$, $\theta = -90^\circ$)	2-21

LIST OF FIGURES (Continued)

Figure		Page
2-26	Nose position history (IYY = 155,000 ft, $\theta = -180^\circ/\text{sec}$, $\theta = -90^\circ$)	2-22
2-27	Nose position history (IYY = 200,000 ft, $\theta = -180^\circ/\text{sec}$, $\theta = 0^\circ$)	2-22
2-28A	Atlas tank oscillations during reentry, 80,000 ft	2-24
2-28B	Atlas tank oscillations during reentry, 155,000 ft	2-25
2-28C	Atlas tank oscillations during reentry, 200,000 ft	2-26
2-29	Typical post-VECO sequence	2-27
2-30	LO ₂ tank pressure rise rate resulting from heat transfer while tumbling.	2-31
2-31	150F propellant tank pressure	2-31
2-32	151F propellant tank pressure	2-32
2-33	LO ₂ vent system (side view)	2-37
2-34	LO ₂ vent system (looking forward).	2-37
2-35	Pitch rotation rocket location.	2-38
2-36	Axial acceleration profile 180°/sec pitch maneuver	2-43
2-37	Atlas F skin gage/skin temperature summary	2-45
2-38	Atlas F propellant tank limit allowable bending moments at max temperature	2-47
2-39	Aerodynamic bending moment on tumbling Atlas F (tumbling in pitch plane)	2-48
2-40	Lateral acceleration on tumbling Atlas (tumbling in pitch plane).	2-49
2-41	Atlas F mass distribution - Total wt = 7684 lb, cg = Sta. 942.1	2-51
2-42	Inertia bending moment on tumbling Atlas F (tumbling in pitch plane)	2-52
2-43	Net bending moment on tumbling Atlas F tank	2-52
2-44	Axial force distribution tumbling Atlas F.	2-53
2-45	Atlas F tumbling reentry bending moment distribution	2-53
2-46	Atlas F tumbling reentry variation of maximum lateral acceleration with altitude	2-55
2-47	Comparison of computer model and experimental data representation	2-75
2-48	Atlas ABRES F/HIRS trajectory	2-76
2-49	Atlas reentry heating for 180 deg/sec pitch rate computer program tabulation of cold wall heat flux	2-77
2-50	Schematic of generalized computer model for heating rate sensors	2-77
2-51	Atlas reentry heating for 180 deg/sec pitch rate model 01, 15 mil gage, 16 mil skin, no gap radiation	2-78

LIST OF FIGURES (Continued)

Figure		Page
2-52	Atlas reentry heating for 180 deg/sec pitch rate model 02, 10 mil gage, 16 mil skin, no gap radiation	2-79
2-53	Atlas reentry heating for 180 deg/sec pitch rate model 03, 8 mil gage, 16 mil skin, no gap radiation	2-80
2-54	Atlas reentry heating for 180 deg/sec pitch rate model 04, 6 mil gage, 16 mil skin, low gap radiation	2-81
2-55	Atlas reentry heating for 180 deg/sec pitch rate model 05, 5 mil gage, 16 mil skin, low gap radiation	2-82
2-56	Atlas reentry heating for 180 deg/sec pitch rate model 06, 4 mil gage, 16 mil skin, low gap radiation	2-83
2-57	Atlas reentry heating for 180 deg/sec pitch rate model 07, 3 mil gage, 16 mil skin, low gap radiation	2-84
2-58	Atlas reentry heating for 180 deg/sec pitch rate model 08, 2 mil gage, 16 mil skin, low gap radiation	2-85
2-59	Atlas reentry heating for 180 deg/sec pitch rate model 09, 1 mil gage, 16 mil skin, low gap radiation	2-86
2-60	Atlas reentry heating for 180 deg/sec pitch rate model 10, 8 mil gage, 16 mil skin, max gap radiation. . . .	2-87
2-61	Atlas reentry heating for 180 deg/sec pitch rate model 11, 6 mil gage, 16 mil skin, max gap radiation. . . .	2-88
2-62	Atlas reentry heating for 180 deg/sec pitch rate model 12, 4 mil gage, 16 mil skin, max gap radiation. . . .	2-89
2-63	Atlas reentry heating for 180 deg/sec pitch rate model 13, 2 mil gage, 16 mil skin, max gap radiation. . . .	2-90
2-64	Atlas reentry heating for 180 deg/sec pitch rate model 14, 8 mil gage, 16 mil skin, gap radiates, $h_i=10$	2-91
2-65	Atlas reentry heating for 180 deg/sec pitch rate model 15, 6 mil gage, 16 mil skin, gap radiates, $h_i=10$	2-92
2-66	Atlas reentry heating for 180 deg/sec pitch rate model 16, 4 mil gage, 16 mil skin, gap radiates, $h_i=10$	2-93
2-67	Atlas reentry heating for 180 deg/sec pitch rate model 17, 2 mil gage, 16 mil skin, gap radiates, $h_i=10$	2-94
2-68	Atlas reentry heating for 180 deg/sec pitch rate model 18, 8 mil gage, 16 mil skin, heat leak, $\rho=485$	2-95
2-69	Atlas reentry heating for 180 deg/sec pitch rate model 19, 6 mil gage, 16 mil skin, heat leak, $\rho=485$	2-96
2-70	Atlas reentry heating for 180 deg/sec pitch rate model 20, 4 mil gage, 16 skin, heat leak, $\rho=485$	2-97
2-71	Atlas reentry heating for 180 deg/sec pitch rate model 21, 8 mil gage, 16 mil skin, heat leak, $\rho=48.5$	2-98
2-72	Atlas reentry heating for 180 deg/sec pitch rate model 22, 6 mil gage, 16 mil skin, heat leak, $\rho=48.5$	2-99

LIST OF FIGURES (Continued)

Figure		Page
2-73	Atlas reentry heating for 180 deg/sec pitch rate model 23, 4 mil gage, 16 mil skin, heat leak, rho=48.5 . . .	2-100
2-74	Atlas reentry heating for 180 deg/sec pitch rate model 24, 8 mil gage, 16 mil skin, heat leak, rho=4.85 . . .	2-101
2-75	Atlas reentry heating for 180 deg/sec pitch rate model 25, 6 mil gage, 16 mil skin, heat leak, rho=4.85 . . .	2-102
2-76	Atlas reentry heating for 180 deg/sec pitch rate model 26, 4 mil gage, 16 mil skin, heat leak, rho=4.85 . . .	2-103
2-77	Atlas reentry heating for 180 deg/sec pitch rate model 27, 4 mil gage, 16 mil skin, heat leak, rho=4.85 . . .	2-104
2-78	Atlas reentry heating for 180 deg/sec pitch rate model 28, 2 mil gage, 16 mil skin, heat leak, rho=4.85 . . .	2-105
2-79	Atlas reentry heating for 180 deg/sec pitch rate model 29, 16 mil skin only, epsilon= .15 (in-out), hi=4 . . .	2-106
2-80	Atlas reentry heating for 180 deg/sec pitch rate model 30, 8 mil gage, 8 mil skin, gap radiates, hi=10 . . .	2-107
2-81	Atlas reentry heating for 180 deg/sec pitch rate model 31, 8 mil gage, 8 mil skin, 20 mil spacer/48.5 . . .	2-108
2-82	Atlas reentry heating for 180 deg/sec pitch rate model 32, 8 mil gage, 8 mil skin, 20 mil spacer/24.2 . . .	2-109
2-83	Atlas reentry heating for 180 deg/sec pitch rate model 33, 8 mil gage, 16 mil skin, 20 mil spacer/97.0 . . .	2-110
2-84	Atlas reentry heating for 180 deg/sec pitch rate model 34, 8 mil gage, 16 mil skin, 20 mil spacer/48.5 . . .	2-111
2-85	Atlas reentry heating for 180 deg/sec pitch rate model 35, 8 mil gage, 16 mil skin, 20 mil spacer/24.2 . . .	2-112
2-86	Atlas reentry heating for 180 deg/sec pitch rate model 36, 8 mil gage, 24 mil skin, 20 mil spacer/97.0 . . .	2-113
2-87	Atlas reentry heating for 180 deg/sec pitch rate model 37, 8 mil gage, 24 mil skin, 20 mil spacer/48.5 . . .	2-114
2-88	Atlas reentry heating for 180 deg/sec pitch rate model 38, 8 mil gage, 24 mil skin, 20 mil spacer/24.2 . . .	2-115
2-89	Atlas reentry heating for 180 deg/sec pitch rate model 39, 6 mil gage, 8 mil skin, 20 mil spacer/97.0 . . .	2-116
2-90	Atlas reentry heating for 180 deg/sec pitch rate model 40, 6 mil gage, 8 mil skin, 20 mil spacer/48.5 . . .	2-117
2-91	Atlas reentry heating for 180 deg/sec pitch rate model 41, 6 mil gage, 8 mil skin, 20 mil spacer/24.2 . . .	2-118
2-92	Atlas reentry heating for 180 deg/sec pitch rate model 42, 10 mil gage, 8 mil skin, 20 mil spacer/97.0 . . .	2-119
2-93	Atlas reentry heating for 180 deg/sec pitch rate model 43, 10 mil gage, 8 mil skin, 20 mil spacer/48.5 . . .	2-120

LIST OF FIGURES (Continued)

Figure		Page
2-94	Atlas reentry heating for 180 deg/sec pitch rate model 44, 10 mil gage, 8 mil skin, 20 mil spacer/24.2	2-121
2-95	Model 21 heating rate sensor ΔT and cold wall heat flux input versus entry heating time	2-122
2-96	Model 23 heating rate sensor ΔT and cold wall heat flux input versus entry heating time	2-122
2-97	Model 28 heating rate sensor ΔT and cold wall heat flux input versus entry heating time	2-123
2-98	Model 34 heating rate sensor ΔT and cold wall heat flux input versus entry heating time	2-123
2-99	Computer output results: (a) maximum sensor temper- ature versus gage thickness; (b) heat sensor maximum ΔT versus skin thickness	2-124
2-100	Response of 5% density spacer sensor models	2-125
2-101	Response of 10% density spacer sensor models.	2-126
2-102	Response of 20% density spacer sensor models.	2-127
2-103	Model 39 sensor output performance comparison with heat flux input	2-128
2-104	Cross-section through high performance heating rate sensor.	2-128
2-105	Model 34 sensor output performance comparison with heat input flux	2-129
2-106	Cross-section through recommended heating rate sensor	2-129
2-107	Sketch of heating rate sensor on Atlas tank skin with cutaway section of sensor gage	2-130
2-108	An electrical analog of heat rate sensor	2-130
2-109	Recommended heat sensor locations on Atlas F	2-131
2-110	Blackout boundaries.	2-137
2-111	Proposed X-Band TLM configuration	2-140
2-112	Alternate S-Band telemetry configurations	2-143
3-1	NASA aerothermic experiments implementation plan	3-2

LIST OF TABLES

Table		Page
2-1	Entry parameter variations	2-1
2-2	ABRES tank altitude crossing times and impact coordinates	2-12
2-3	Assumed mass properties (moment of inertia)	2-13
2-4	Atlas displacement, rate and angular momentum	2-28
2-5	Pitch rocket performance data	2-39
2-6	Allowable tank pressure at temperature	2-46
2-7	Heating rate ratio curve points for computer model	2-64
2-8	Cold wall heat flux history	2-65
2-9	Model characteristics	2-66
2-10	Material heat conduction properties.	2-74
2-11	Alternate data recovery systems.	2-138
2-12	S-Band telemetry system alternatives	2-144

SUMMARY

The Convair Aerospace Division of General Dynamics Corporation performed a \$35,000 study for the NASA Langley Research Center (via arrangements with SAMSO) to establish the feasibility of obtaining heat transfer data on an expended Atlas F booster launch vehicle, as a secondary experiment. It is desired to obtain data in the altitude range of 300,000 to 200,000 feet during entry conditions, with a velocity in the range of 20,000 to 25,000 feet per second, and through a range of vehicle attitudes of ± 90 degrees. These data are desired for correlation with turbulent heat transfer and boundary layer transition data obtained from wind tunnel test facilities. The data would also be valuable in assessing rarified gas and surface catalicity effects in a "real gas" environment.

The objectives of the study were:

- a. Identify what vehicle modifications and special equipment are required
- b. Devise conceptual solutions for the required vehicle modifications and special equipment
- c. Prepare a schedule and cost estimate to accomplish the program.

Evaluation of the concept requires a study of the following issues:

- a. What is the most suitable primary mission on which to plan the secondary experiment?
- b. Is the entry pitch attitude history predictable (and satisfactory)?
- c. Can the vehicle structural integrity be maintained down to 200,000 feet altitude?
- d. Are suitable heat sensors available or readily devised?
- e. Can vehicle pitch, yaw, and roll attitudes be determined during entry?
- f. Can the data be acquired at the ground station?

The study indicated that:

- a. The program concept is feasible but probably more costly than initially expected.
- b. A time span of 18 months from go-ahead to flight will be required.
- c. Modifications to the baseline Atlas F configuration are required to the following items:

- (1) High impulse retrorocket system (HIRS) pitch rocket mounting and alignment procedure.
 - (2) HIRS adapter access door.
 - (3) Sustainer engine LO₂ suction line.
 - (4) S-band telemetry system.
 - (5) Discrete timer.
 - (6) Miscellaneous equipment mountings.
- d. Special equipment of the following type will be required:
- (1) Heating sensors employing a thin gage (0.008 inch) with a controlled heat leak to a heat sink.
 - (2) Northrop NIS-200 type inertial platform system for attitude sensing.
 - (3) An additional HIRS retromotor and mounts to provide the high pitch rotation rate required.
 - (4) LO₂ tank venting system (new design)

The following additional conclusions and recommendations are offered:

- a. The most favorable launch vehicle is an ABRES vehicle without a HIRS pitch (tumble) maneuver.
- b. The time interval between reaching 300,000 and 200,000 feet will be 8.9 seconds.
- c. The velocity in this interval will be essentially constant at about 22,200 feet per second.
- d. An initial pitch rotation rate (prior to entry) of 180 degrees per second is required to insure a satisfactory and predictable entry mode.
- e. The thrusts of the various rockets must be carefully aligned through the vehicle roll axis to keep yaw components of rotation to an acceptable level.
- f. The vehicle roll rate during the data gathering can be maintained at less than 30 degrees per second, which is desirable.
- g. Venting of the LO₂ tank must start shortly after the HIRS retrorocket firing, to prevent overpressurization.
- h. Modifications to improve the aerodynamic cleanliness of the front end do not appear to be attainable for an acceptable cost.
- i. The vehicle tanks are capable of sustaining entry loads down to 200,000 feet altitude.

- j. Some components, mounted by welds and brackets to the tank, will be loaded beyond their original design criteria. An "engineering judgement" type review indicated they will probably not cause a tank failure, but additional analysis is required and recommended for assurance.
- k. Simple propellant tank skin-mounted thermocouples will not be satisfactory as heat sensors.
- l. Existing vehicle equipment is not adequate for measuring the vehicle attitude during entry.
- m. The existing S-band telemetry system will probably be subjected to RF "blackout" at altitudes of 250,000 to 110,000 feet. A simple S-band telemetry evaluation test is suggested and recommended for further definition of this potential problem.
- n. An X-band data transmission system, of the type used on the NASA-LRC conducted RAM program is the most favored solution if the S-band is found to be unacceptable.
- o. Radar tracking data and sounding rocket (to 225,000 feet) are available from the Kwajalein Test Range.

1

INTRODUCTION

The prediction of aerodynamic heating (during entry conditions) of a large hypersonic vehicle, such as the space shuttle orbiter, is a complex problem involving the acceptance of assumptions of major significance to the accuracy of that prediction. One basic assumption of paramount significance is the methodology used to extrapolate aerothermodynamic data obtained using a wind tunnel model, whose length is generally about a foot, to make the data applicable to a full scale vehicle about two orders of magnitude larger. To further compound the difficulty of extrapolation, wind tunnel test conditions of density (or static pressure) and gas stream enthalpy can differ from the actual entry conditions by several orders of magnitude, also. The Langley Research Center (LRC) of NASA has sponsored a study to explore the feasibility of obtaining aerodynamic heating data using the expended Atlas F booster vehicle as a test model after completion of its primary role of launching a space payload. The scheme would provide test data during entry from 300,000 to 200,000 feet altitude using a model of the same magnitude as the space shuttle orbiter, and under conditions of density and stream enthalpy which are essentially identical. These data could then be used to assess the validity of the currently used assumptions.

A \$35,000 study contract was awarded to the Convair Aerospace Division of General Dynamics Corporation to identify the modifications to the baseline Atlas F booster vehicle, determine the additional special hardware required, and to provide necessary design concepts. The basic approach suggested by LRC is relatively straightforward:

- a. Provide pitch plane rotation of 180 deg/sec to achieve four to five complete turns of the vehicle to achieve data over an angle of attack range of 0 to 90 degrees through the range of altitude.
- b. Provide approximately 50 heating sensors distributed circumferentially and longitudinally in the aerodynamically clean areas of the propellant tank skin areas, to assess axial and circumferential heating rate variation and boundary layer transition distances.
- c. Provide measurement of vehicle attitude (pitch, yaw, and roll) to correlate with the measured heating data.
- d. Acquire vehicle altitude-time tracking data from the Kwajalein Test Range (KTR) radars, and altitude-density data from a sounding rocket launched from KTR.

This approach generated five basic requirements to be satisfied by the Atlas F booster vehicle:

- a. Pitch attitude history must be predictable; i. e., that the desired pitch rate be maintained approximately constant throughout the altitude range without being driven to a quasi-stable tail-first mode by aerodynamic forces.
- b. Vehicle structural integrity must be maintained down to 200,000 feet.
- c. Vehicle-mounted heat sensors must be devised which are sensitive enough at the lower heating rates encountered in the 300,000 foot altitude region, and are capable of withstanding the high heating rates in the 200,000 foot region.
- d. Vehicle pitch, yaw, and roll attitude histories must be determined, through the use of existing on-board inertial components, or by new means to be conceptually devised.
- e. A data transmission link (or method) must be established to transfer the heating and attitude data to a ground station.

The basic approach followed to satisfy these requirements was to first assess the capability of the baseline "as is" vehicle. Then, if changes were required, the satisfaction of the requirements through modifications to the existing hardware was investigated before new hardware concepts were explored. In the case of heating sensors (which obviously were not provided in the baseline vehicle), thermocouples mounted on the propellant tank skin were considered first.

The Air Force/Space and Missile System Organization (AF/SAMSO), which has cognizance for Atlas F launch program, supplied the following guidelines for use in the study tradeoffs and program development considerations:

- a. The modification of hardware and procedures required to perform the reentry data gathering must be compatible with the primary payload mission and requirements.
- b. The reentry data gathering shall be considered as a secondary experiment.
- c. NASA will fund all costs arising from special hardware, vehicle modifications, and installation of equipment.
- d. Provision for the receipt of telemetry at or during reentry is a NAS responsibility in the event the frequency is different from the S band, currently used.
- e. The accomplishment of this secondary experiment is subject to the launch schedule and requirements of the primary mission.

The overall study logic flow is presented schematically in Figure 1-1.

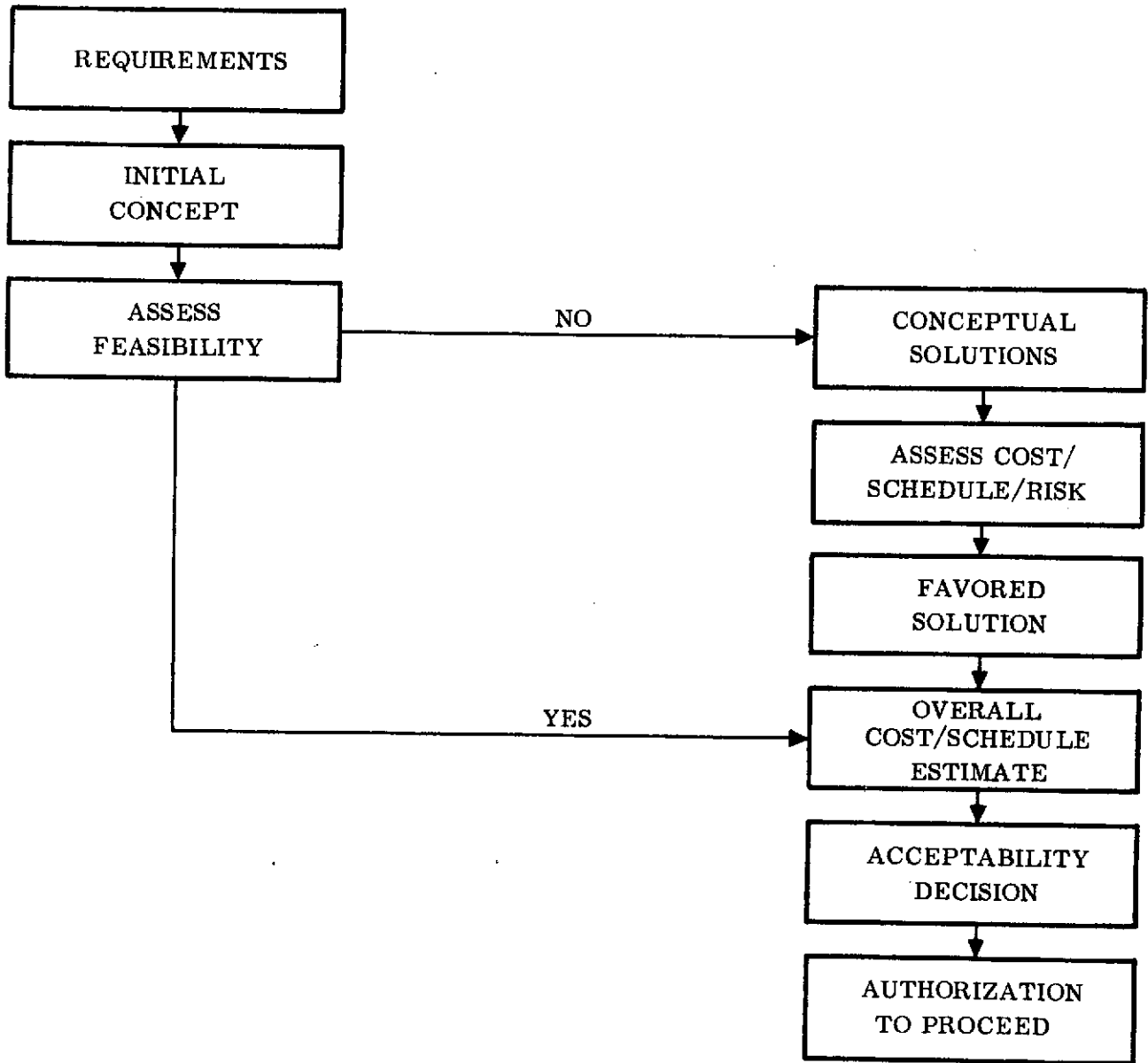


Figure 1-1. Study logic flow.

2

STUDY RESULTS AND DISCUSSION

2.1 MISSION AND TRAJECTORY EVALUATION

2.1.1 MISSION EVALUATION. The initial step in the study was to survey the various missions being planned, to select the one most suitable for the data gathering experiment. The Atlas SLV-3 launches from ETR were considered and discarded because:

- a. Atlas/Centaur booster achieves a velocity of only 8,000 feet per second (approximately) in the altitude range of interest.
- b. SLV-3 have numerous restrictions because of their classified payloads, and generally have low payload margins available for a secondary experiment.

The Atlas F missions to be launched from WTR are more amenable. Three basic families of launches are available for consideration:

- a. Polar-Orbital
- b. Navy sub-orbital to KTR
- c. Air Force/ABRES sub-orbital to KTR.

The variation of significant trajectory parameters for these families is shown in Table 2-1.

Table 2-1. Entry parameter variations.

Mission	T 300K → 200K (sec.)	V _R (ft/sec.)	γ _R (deg.)
Polar-Orbital	17	23,400	-14.5
Navy sub-orbital	11.5	23,100	-22.2
ABRES	8.9	22,400	-30.0

All three types of missions have earth relative velocities (V_R) approximately 23,000 per second, which is similar to the velocity of a typical earth-orbiting vehicle at entry (approximately 25,000 feet per second). The Polar-Orbital launches have the lowest earth relative flight path angle (γ_R) (-14.5 degrees) and therefore the longest time interval from 300K to 200K feet altitude (T) (17 sec) in which to acquire data. However,

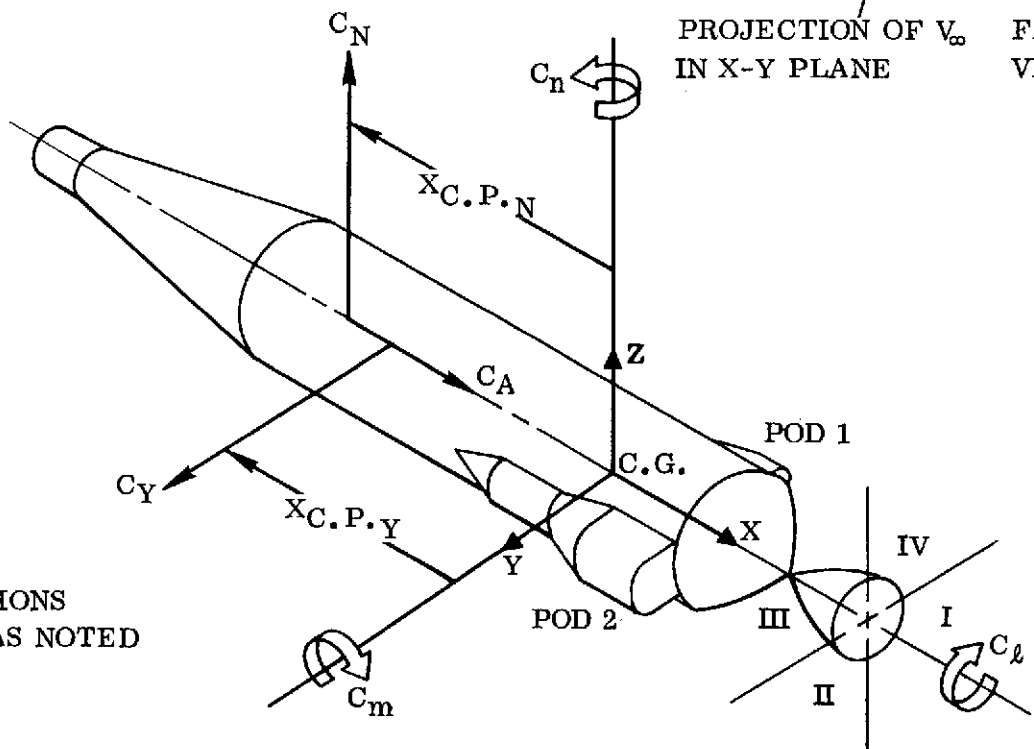
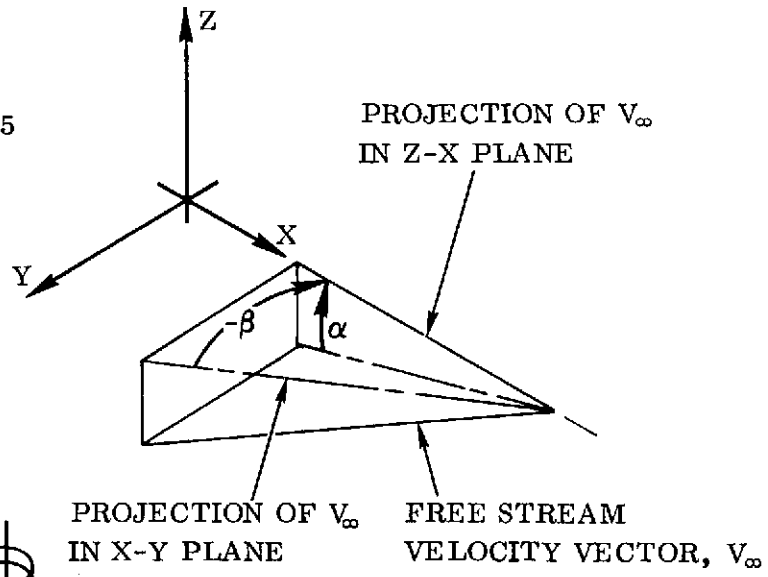
the impact point is in the South Atlantic in the vicinity of Antarctica, and it would present a very difficult problem to supply a mobile telemetry station. This, coupled with the facts that there are only two available launches in the desired time period and both will probably have low payload margins, led to abandonment of further consideration of the Polar-Orbital missions. The Navy missions use a yaw rotation to aid in gaining separation from the payload. The difficulties present in neutralizing this yaw rotation prior to providing the pitch rotation required for this mission led to dropping them from further consideration, also. The remaining family (the ABRES missions) is compatible, and in addition offers the advantage of a greater number flights available from which to choose. This is significant, since the design of the pitch tumbling rocket modification is unique to the family of missions selected, and if it is not possible to conduct the experiment on the specific launch vehicle originally selected (for whatever reason) long delays can be more easily avoided awaiting a subsequent launch of the next vehicle in the ABRES family.

Within the ABRES family, there are some vehicles which do not require a HIRS pitch (tumble) maneuver prior to retrorocket firing. The use of one of these would result in a much higher confidence level in that the motion of the vehicle at entry initiation is principally in the pitch plane. This is because it eliminates the source of roll position uncertainty at time of pitch tumbling rocket firing associated with the HIRS pitch rotation rocket, which amounts to at least $\pm 20^\circ$ (refer to Section 2.2 for details). For this reason, one of these is recommended as the first choice for the launch vehicle for this experiment, if possible. At this time, the launch vehicle definition and the missions to be flown in 1974 are not firmly defined; thus, it is not possible to state firmly if one can be used. If not, another vehicle of the ABRES family would be the second choice.

The second step was to perform an aerodynamic coefficients and trajectory analysis study to provide the reference information required to conduct the dynamic entry simulation, heating and structural loads analysis, and telemetry RF transmission evaluation.

2.1.2 AERODYNAMICS COEFFICIENTS. The aerodynamics coefficients computations were performed for the typical ABRES F/HIRS tank configuration shown in Figure 2-1, for an averaged tank reentry velocity of 22,200 ft/sec and for angle of attack increments of ten degrees (0 to 180-deg). The standard Atlas F aerodynamic axes system shown in Figure 2-2 was used for the coefficients, except for the reference length and the location of the axes origin. The latter was located at the sustainer center of gravity, Atlas Station 935, while the value of the former was assumed to be ten feet. The coefficients were generated using the Hypersonic Aerodynamic Parameter Program (Reference 1) for the configuration shown in Figure 2-1. The coefficients (used in dynamic entry simulation and trajectory analysis) and the figures pertaining to them are given in the following list.

- NOTES: 1. AXIS ORIGIN LOCATED AT ATLAS STATION 935
 2. REFERENCE AREA = 78.5 SQ. FT.
 3. REFERENCE LENGTH = 10 FT.



POSITIVE DIRECTIONS SHOWN EXCEPT AS NOTED

Figure 2-2. Aerodynamic force and moment axis system.

- a. Lateral Force Coefficients, C_N and C_Y vs Angle of Attack: Figure 2-3
- b. Lateral Force Coefficient Derivatives with Respect to Angle of Attack, $C_{N\alpha}$, $C_{Y\beta}$ vs Angle of Attack: Figure 2-4
- c. Axial Force Coefficient, C_A vs Angle of Attack: Figure 2-5
- d. Pitching and Yawing Moment Coefficients, C_m and C_n vs Angle of Attack: Figure 2-6
- e. Pitching and Yawing Moment Coefficient Derivative with Respect to Angle of Attack, $C_{n\beta}$ and $C_{m\alpha}$ vs Angle of Attack: Figure 2-7
- f. Center of Pressure Location, X_{CP} vs Angle of Attack: Figure 2-8

2.1.3 REFERENCE TRAJECTORY AND DISPERSION ANALYSIS. Nominal and dispersed trajectories were simulated from entry at 300,000 feet to impact. The nominal trajectory used a typical set of ABRES mass properties data and configuration (Figure 2-1), a C_{DA} value corresponding to a tumbling tank, and nominal Kwajalein winds and atmospheric data (Reference 2). In addition, trajectories for the cases of constant zero and 90 degrees angle of attack were simulated for comparison.

Owing to a lack of data for Kwajalein atmosphere dispersions, an auxiliary trajectory simulation was made using identical inputs to the previously described case except a nominal Patrick atmosphere (Reference 3) was used to evaluate the effect of the different atmospheres on the entry trajectory. As expected, the difference was slight in the altitude range of 300K to 200K feet. This permitted the use of density dispersions for the Patrick atmosphere (which is available in Reference 3) together with wind dispersion data for the Kwajalein area (Reference 4) to simulate 3-sigma (dispersed atmospheric conditions) trajectories. The slant range and elevation angles to Ennylabegan and Roi Namur, the Kwajalein Test Range telemetry and radar tracking station sites, respectively, were also calculated to assist the data transmission studies contained in Section 2.6. The entry trajectory parameters are shown in Figures 2-9 through 2-14 and Table 2-2, as follows:

- a. Dynamic Pressure vs Altitude: Figure 2-9
- b. Relative Velocity and Mach Number vs Altitude: Figure 2-10
- c. Altitude vs Time: Figure 2-11
- d. Tank Slant Range and Elevation Angle vs Time for Ennylabegan (Telemetry) Station: Figure 2-12
- e. Tank Slant Range and Elevation Angle vs Time for Roi Namur (Radar Tracking) Station: Figure 2-13
- f. Tank Reentry Impact Dispersions: Figure 2-14
- g. Tank Altitude Crossing Times and Impact Coordinates vs Trajectory Simulations: Table 2-2

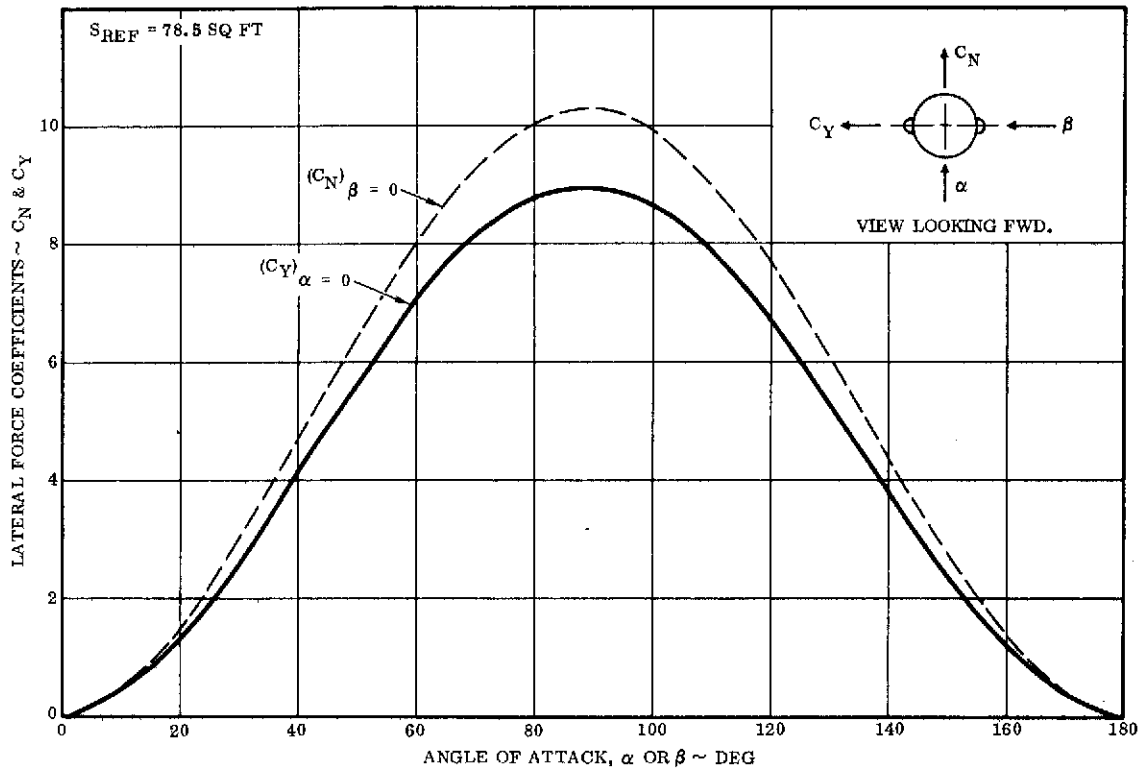


Figure 2-3. Lateral force coefficients.

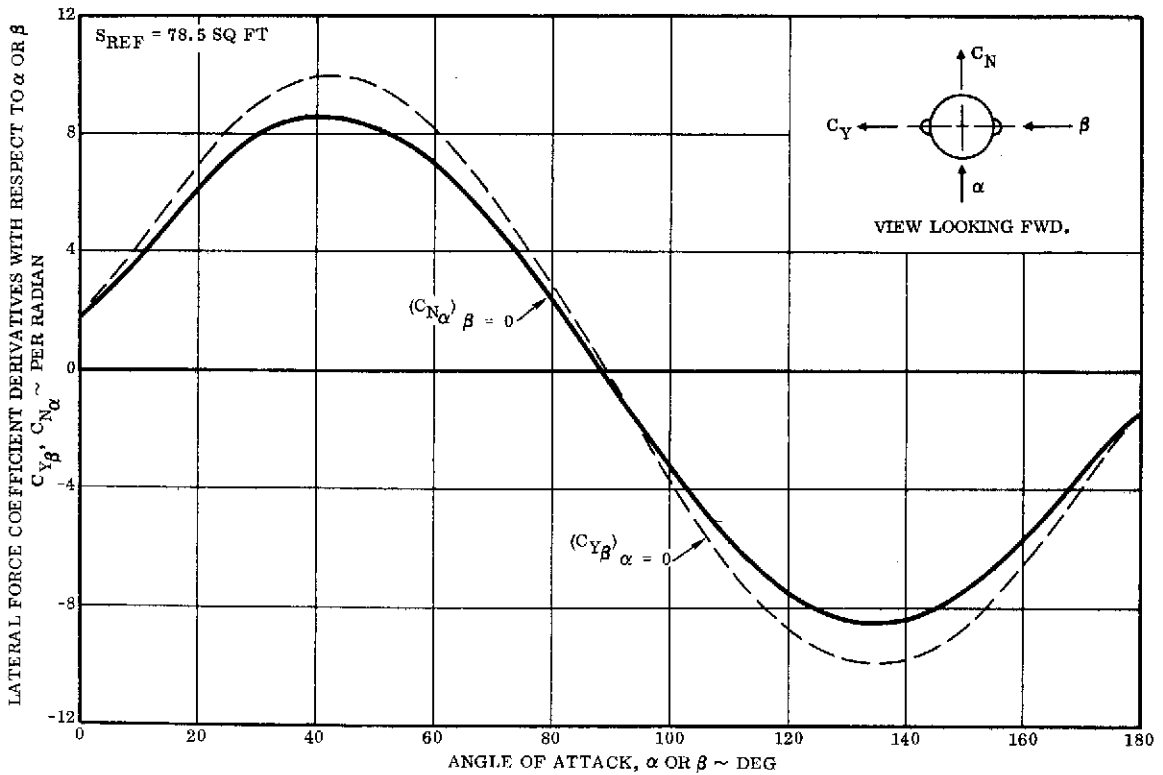


Figure 2-4. Lateral force coefficient derivatives.

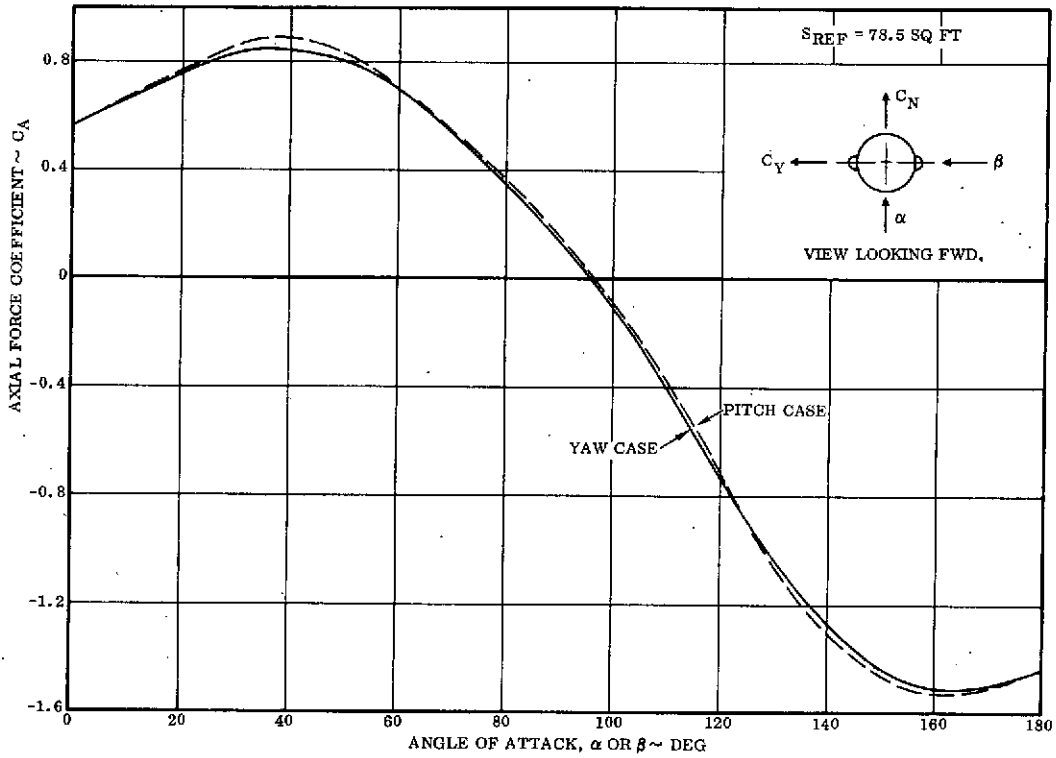


Figure 2-5. Axial force coefficient.

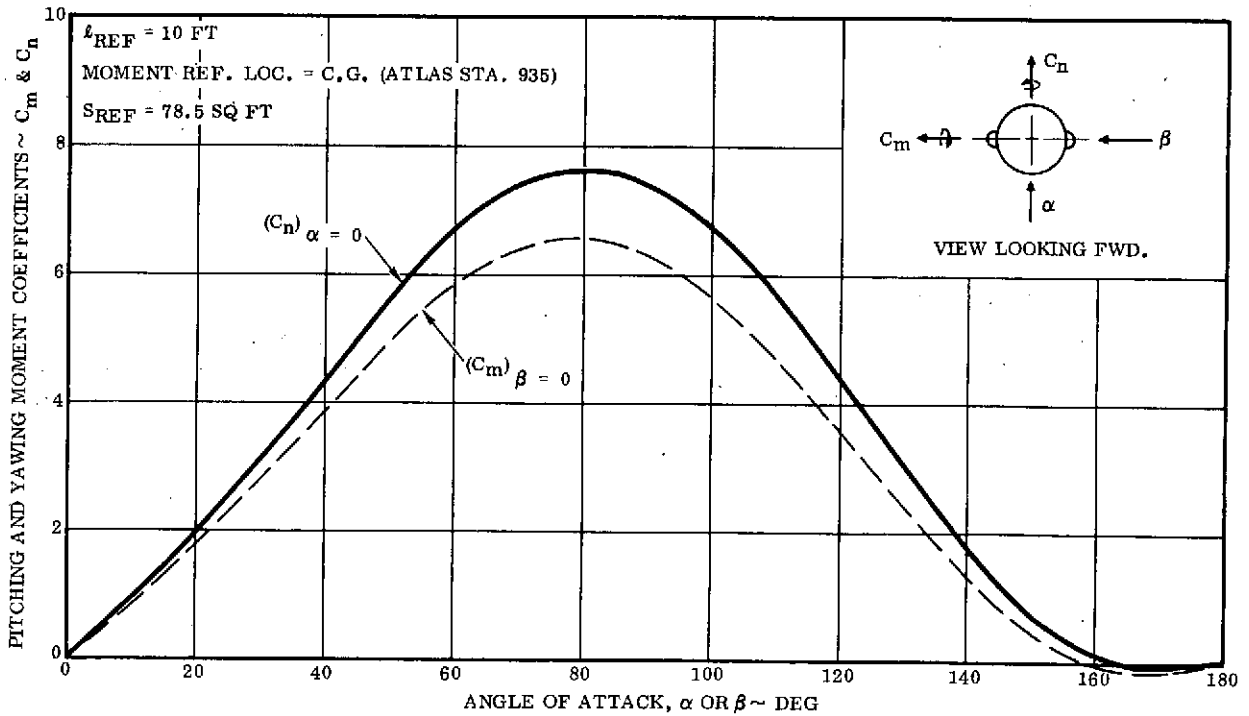


Figure 2-6. Pitching and yawing moment coefficients.

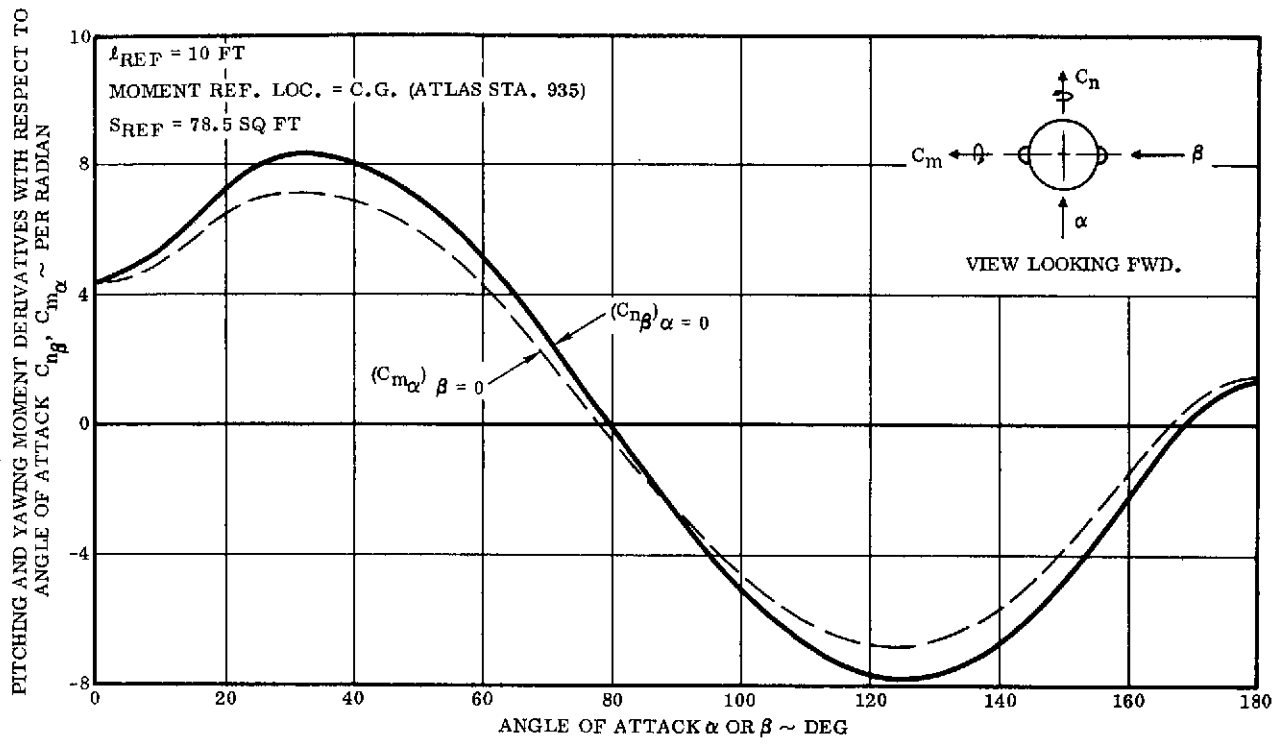


Figure 2-7. Pitching and yawing moment coefficient derivatives.

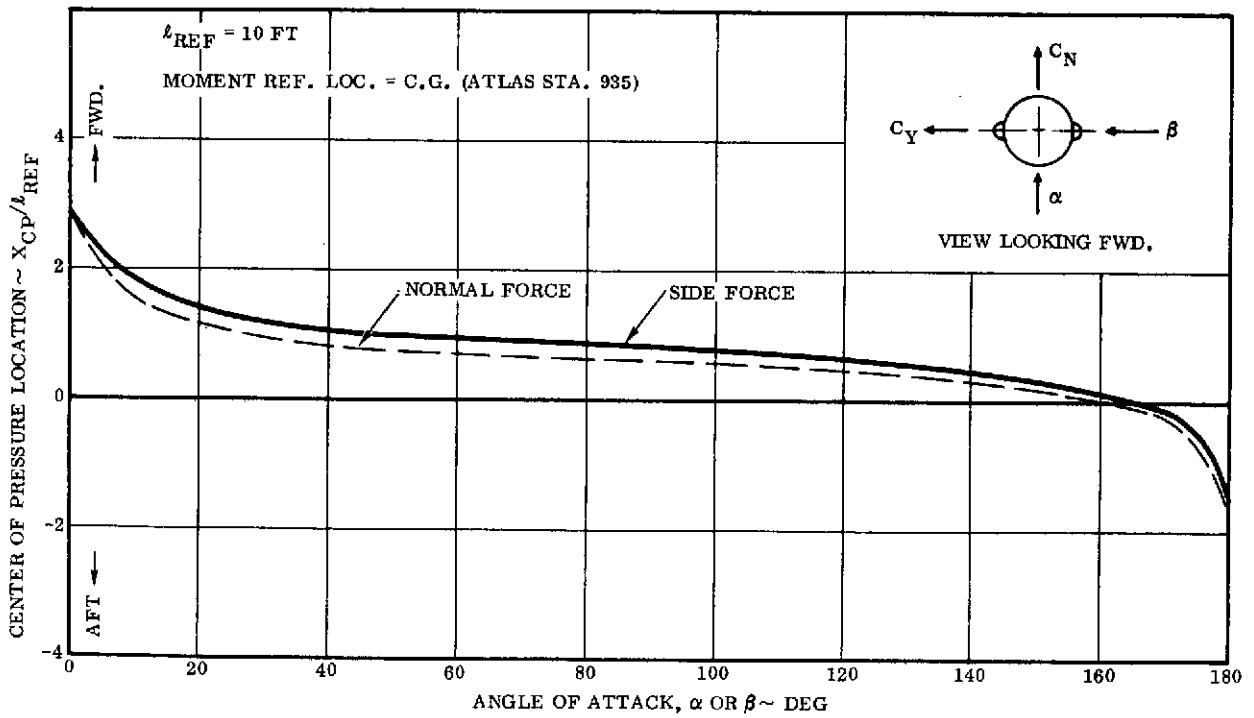


Figure 2-8. Center of pressure location.

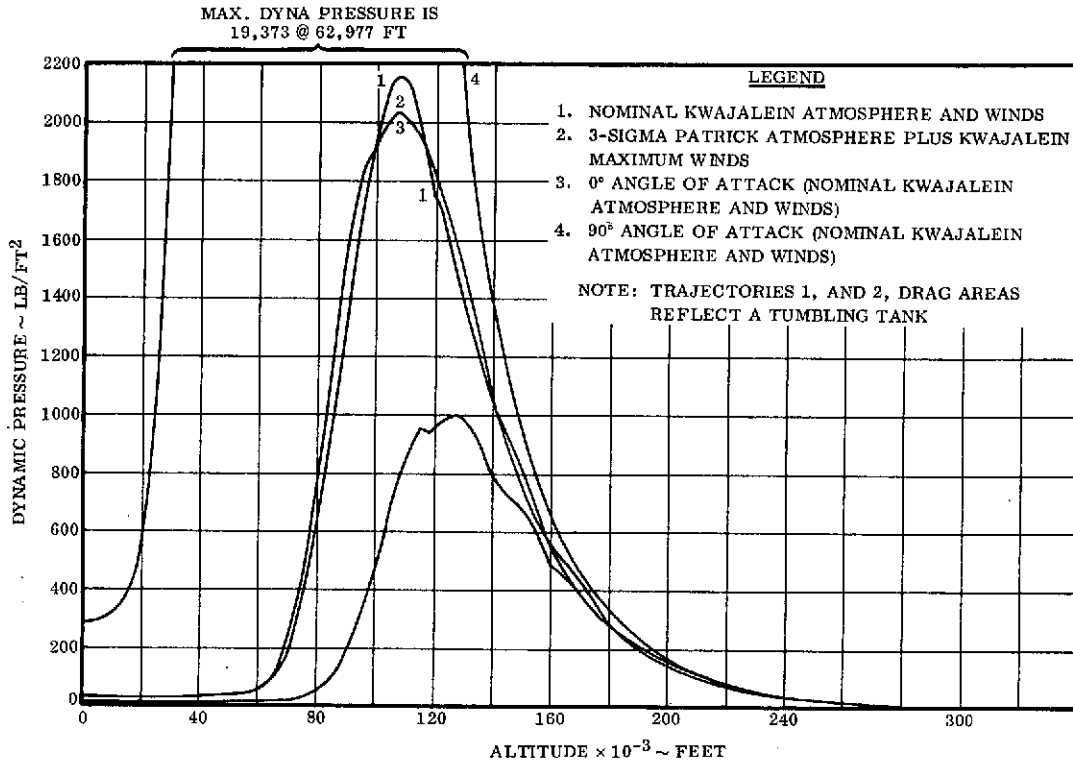


Figure 2-9. Dynamic pressure versus altitude.

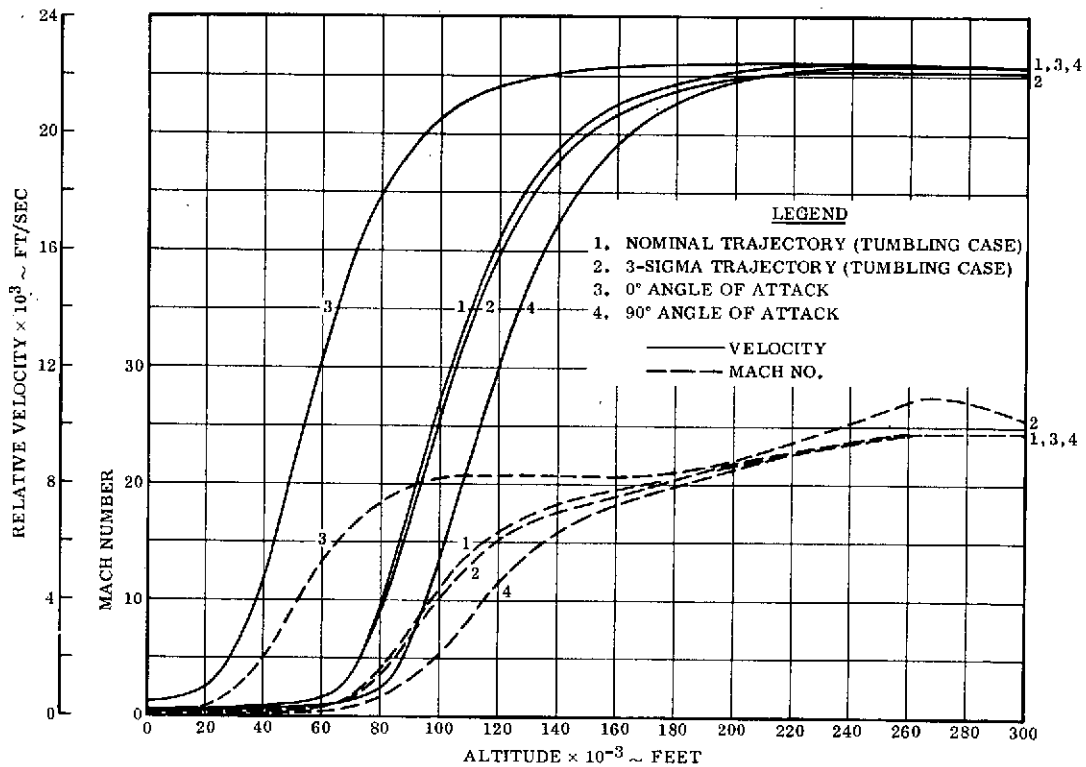


Figure 2-10. Relative velocity and Mach number versus altitude.

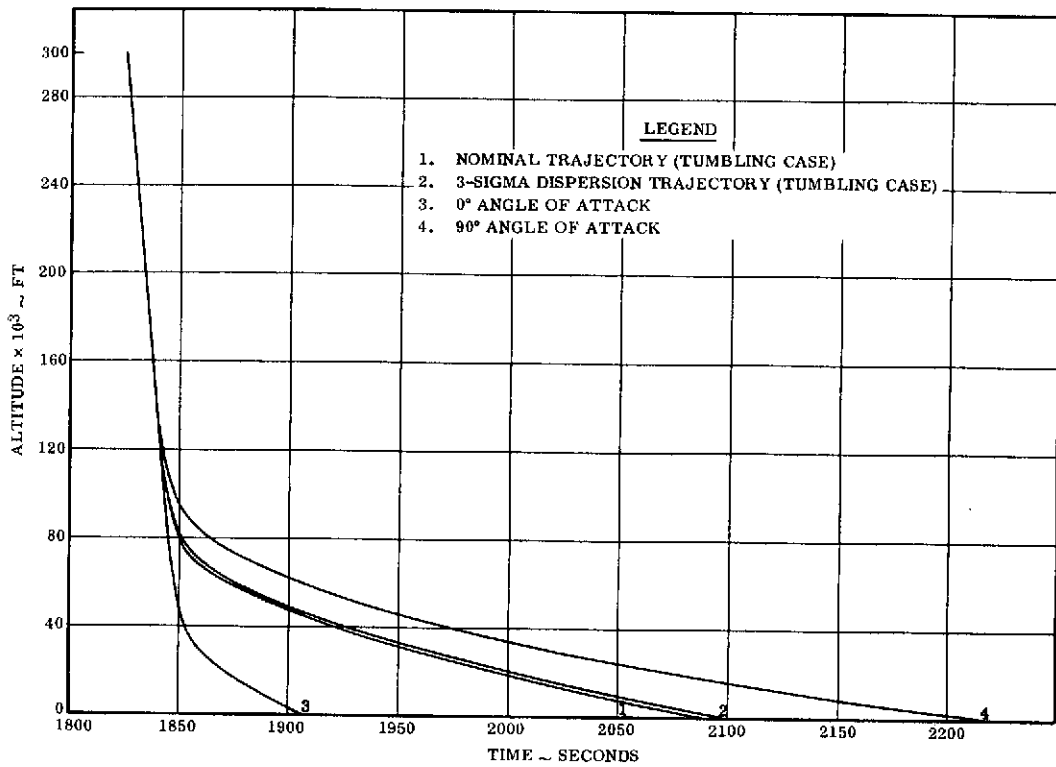


Figure 2-11. Altitude versus time.

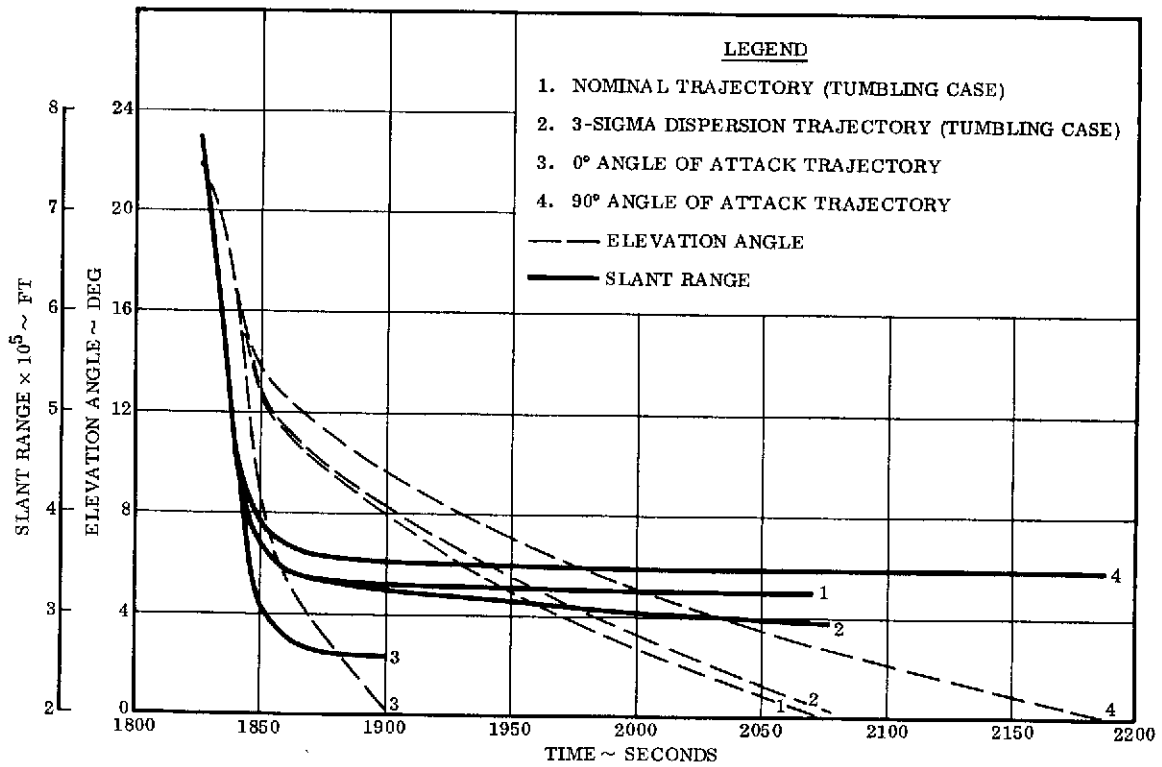


Figure 2-12. Slant range and elevation angle versus time for Ennylabegan telemetry station.

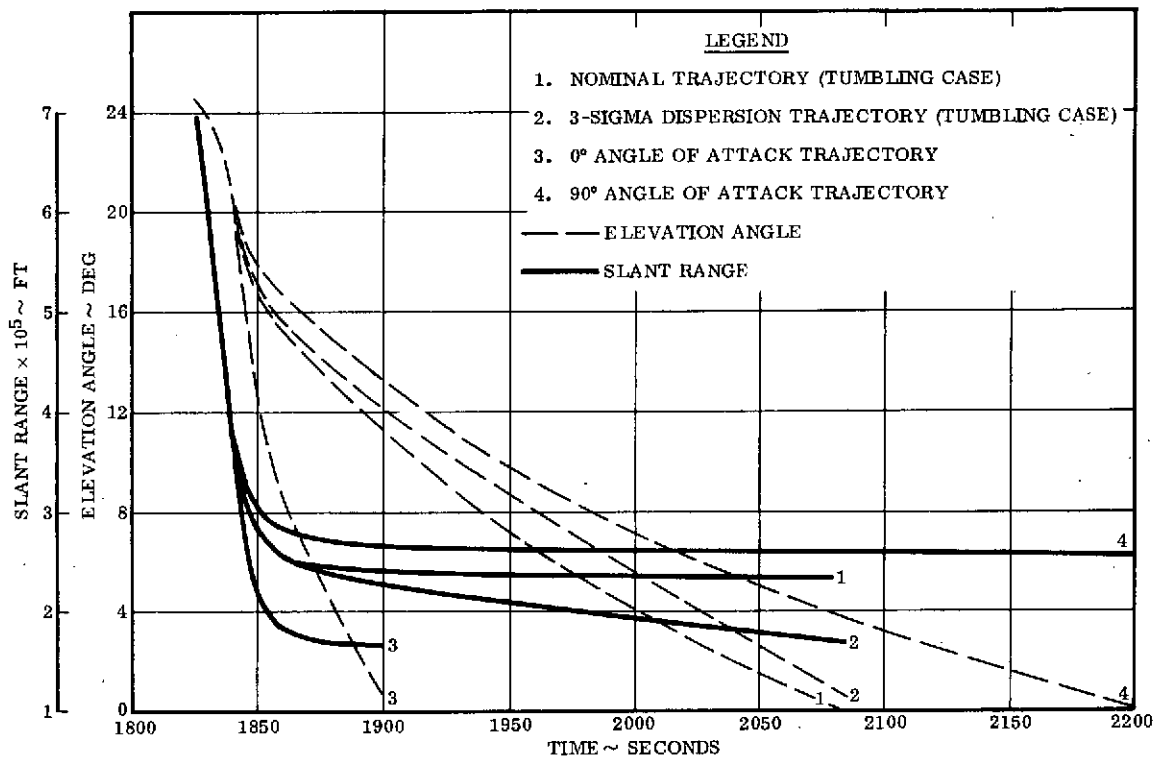


Figure 2-13. Slant range and elevation angle versus time for Roi namur radar tracking station.

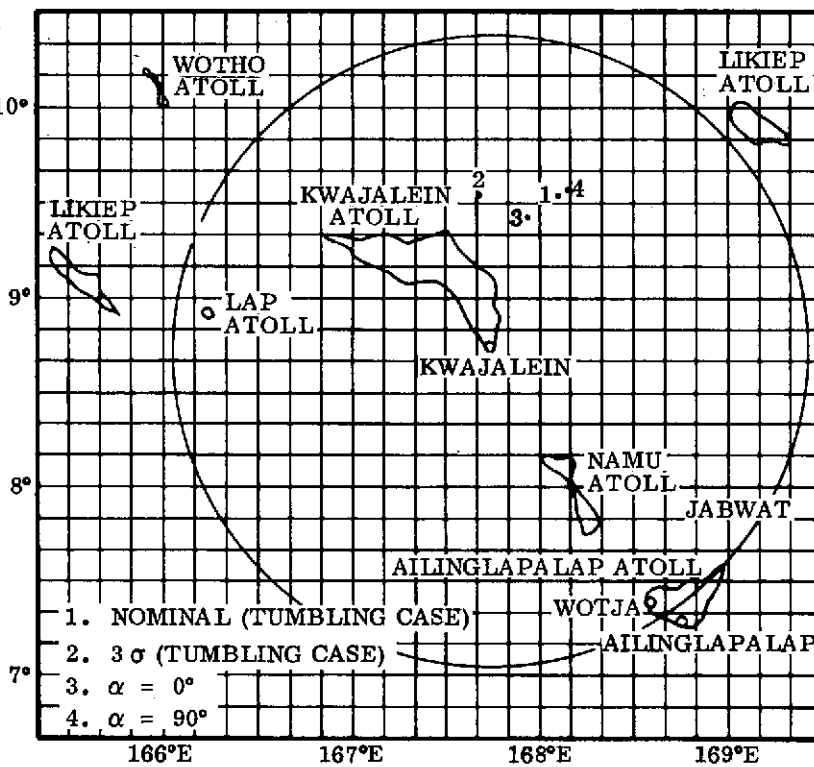


Figure 2-14. Tank entry impact dispersions.

Table 2-2. ABRES tank altitude crossing times and impact coordinates.

	Nominal (Tumbling Case)	3- σ ** (Tumbling Case)	Angle of Attack $\alpha = 0^\circ$	Angle of Attack $\alpha = 90^\circ$
300,000 to 200,000 ft Δt (sec)	8.8535	8.8535	8.8535	8.9160
Impact Time (sec) from Liftoff	2089.7368	2096.2506	1904.6541	2215.0472
*Impact Δt from nominal (sec)	0	+6.5138	-185.0827	+125.3104
Impact Latitude	9° 32' 15.2"	9° 32' 22.3"	9° 25' 39.5"	9° 34' 25.3"
Impact Longitude	168° 6' 39.9"	167° 40' 57.9"	167° 56' 19.8"	168° 9' 50.6"
* Later impact (+), Earlier Impact (-)				
** Patrick hot atmosphere dispersion data and maximum Kwajalein winds				

An examination of the data given in Figures 2-9 through 2-13 discloses the relative insensitivity of trajectory parameters to atmospheric density and wind variations (and the vehicle attitude whether tumbling or at a constant angle of attack of zero or 90 degrees) for altitudes of 200K or above. The Hot Day density results in a velocity (Figure 2-10) only about 300 feet per second lower than for a Standard Day. This is presumably caused by the greater number of air molecules present above 300K feet which results in more drag at the higher altitudes and slows the vehicle slightly. The effects on altitude vs time (Figure 2-11) and slant range and elevation angle (Figures 2-12 and 2-13) are negligible.

2.2 ENTRY ATTITUDE PREDICTABILITY

A dynamic analysis was performed to assess the effects of the entry aerodynamic forces on the pitch plane rotation rate history. The objective was to assure that the vehicle, initially given a specified pitch rate, would not be driven by aerodynamic forces into the quasi-stable tail first attitude prior to reaching 200,000 feet altitude, and thereby preclude obtaining the desired heating data. In addition, the pitch, yaw, and roll rates induced by the firing of the HIRS rockets at the end of the primary mission were evaluated, since these become the initial conditions for the secondary mission of gathering heating data.

2.2.1 ENTRY ATTITUDE HISTORY SIMULATION

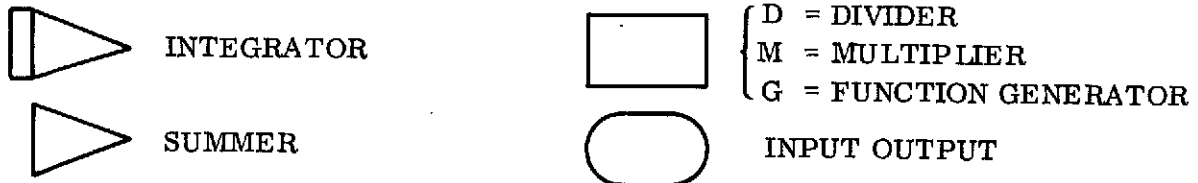
2.2.1.1 Introduction. A MIDAS-generated* digital computer program was used in this investigation. This was a single plane simulation of the Atlas F missile during re-entry. The only forces acting on the vehicle were aerodynamic forces and gravity. The program would accept as inputs arbitrary vehicle properties; mass, inertia plus initial rate, attitude, velocity vector, and altitude.

The aerodynamic properties, such as overturning moment, were taken from Figures 2-3 through 2-6. The vehicle mass properties were chosen to be representative of those required for a typical ABRES mission in the 1974 time period. These are listed in Table 2-3 below.

Table 2-3. Assumed mass properties (moment of inertia).

Item	I_{yy} (slug-ft ²)
Minimum (Fwd. Adapters Jettisoned)	80,000
Nominal Vehicle and Residuals	155,000
Maximum Residual Propellants	200,000

2.2.1.2 Discussion of Simulation. The CDC 6400 simulation solves for the vehicle state, velocity, altitude, attitude, and rate as a function of time. The program, being MIDAS generated, was first charted as an analog flow diagram, shown in Figure 2-15. The following nomenclature is used:



* Modified Integration Digital Analog Simulation (MIDAS) is designed to solve the system of differential equations associated with an analog description of the vehicle/flight control system (e.g., integrators, summers, relays, etc.). MIDAS interprets data taken directly from an analog schematic diagram, generates a FORTRAN IV source deck, and solves the resulting differential equations.

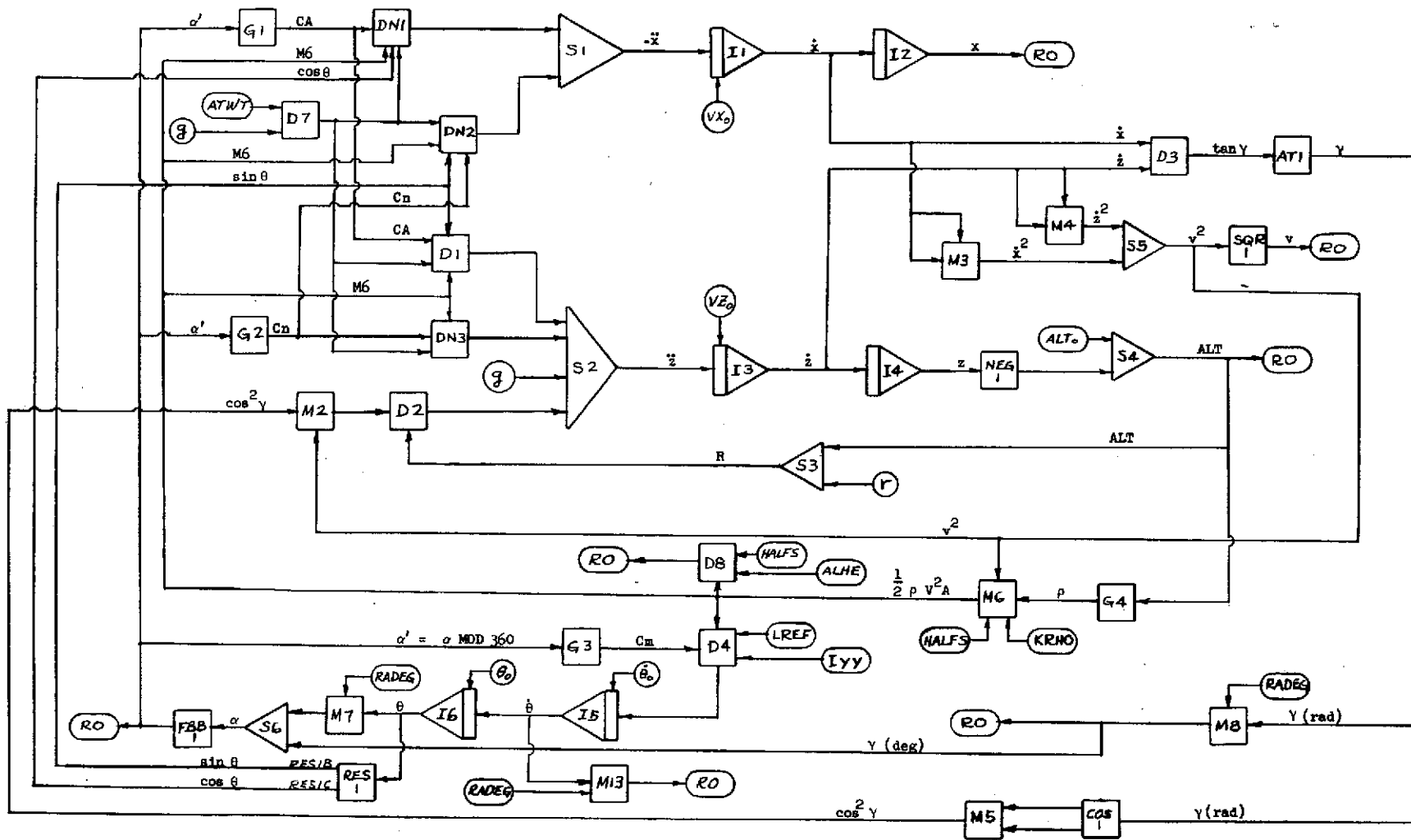


Figure 2-15. Analog flow diagram - pitch plane simulation.

The equations of motions are common for a stability axis system approach to this type of a problem. The axis system is shown in Figure 2-16, with the following nomenclature

θ = Attitude (deg)

α = Angle of Attack (deg)

δ = Flight Path Angle (deg)

Z = Local Vertical

X = Local Horizontal

V = Velocity Vector

F_n = Normal Force (lb)

F_d = Drag Force (lb)

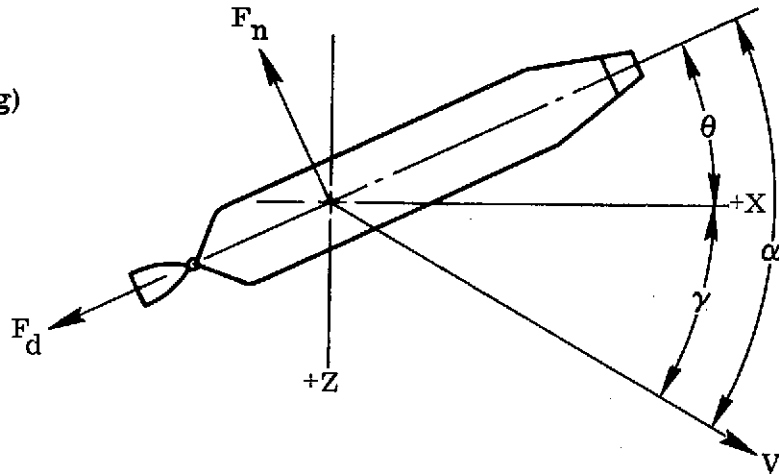


Figure 2-16. Axis system.

The remaining relations are listed below, for completeness.

$$M_p = C_m \frac{1}{2} \rho V^2 S l_{REF}$$

$$F_d = C_d \frac{1}{2} \rho V^2 S l_{REF}$$

$$F_n = C_n \frac{1}{2} \rho V^2 S l_{REF}$$

$$\rho = f(\text{alt})$$

$$\text{alt} = Z_0 \int VZ dt$$

$$V = (VX^2 + VZ^2)^{1/2}$$

$$VX = VX_0 - \frac{1}{M} \int [F_d \cos \theta + F_n \sin \theta] dt$$

$$VZ = VZ_0 - \frac{1}{M} \int [F_n \cos \theta - g + M V^2 \cos^2 \alpha / R - F_d \sin \theta] dt$$

$$d^2\theta/dt^2 = M_p / I_{yy}$$

$$\gamma = \tan^{-1} VZ/VX$$

$$\alpha = \gamma + \theta$$

$$R = r + \text{alt} - Z$$

$$C_m = f(\alpha)$$

$$C_n = f(\alpha)$$

$$C_d = f(\alpha)$$

where:

$$M_p = \text{Pitching Moment (lb)}$$

$$C_m = \text{Aerodynamic Moment Coefficient}$$

$$\rho = \text{Density (slug/ft}^3\text{)}$$

$$C_d = \text{Drag Coefficient}$$

$$C_n = \text{Normal Force Coefficient}$$

$$S = \text{Reference Areas (ft}^2\text{)}$$

$$l_{\text{REF}} = \text{Reference Length (ft)}$$

$$\text{alt} = \text{Altitude (ft)}$$

$$V_X = \text{Velocity Component in X Direction (ft/sec)}$$

$$V_Z = \text{Velocity Component in Z Direction (ft/sec)}$$

$$M = \text{Vehicle Mass (slugs)}$$

$$R = \text{Distance to Center of Earth (ft)}$$

$$r = \text{Radius of Earth (ft)}$$

$$I_{yy} = \text{Pitch Moment of Inertia about cg (slug ft}^2\text{)}$$

$$f() = \text{Function of Variable in } ()$$

2.2.1.3 Results. The vehicle pitch attitude behavior is shown in Figures 2-17 through 2-27. A simplified plotting scheme has been utilized in an attempt to present the significant results of the computer runs without requiring reference to the computer printouts. These contain so much auxiliary data that the primary results are obscured. Figure 2-17 is taken as an example, and is discussed in depth to explain the method of presenting the data.

Figure 2-17 represents a view of the vehicle which an observer moving along with the vehicle cg would be seeing from the right side. The solid outline of the vehicle represents its attitude at 300,000 ft. A moving coordinate system with Z being down

and X being local horizontal is shown for reference purposes. The circular line (with arrows impressed to indicate direction of travel) indicates the trajectory or position of the nose.

In Figure 2-17, the vehicle is horizontal with zero rate at entry initiation. The vehicle starts to rotate in a counterclockwise direction in response to aerodynamic forces, and continues through the aerodynamically stable tail-first position (owing to inertia), to about 60 degrees beyond. At this point it stops and reverses direction of rotation as a result of aerodynamic forces. The altitude at instant of stopping is labeled and, in this instance, was 230,000 ft. The altitude at the end of the run was slightly below 200,000 ft: usually 190,000 ft. As a second change of rotation was not indicated, the vehicle was rotating in a clockwise direction at the end point of the simulation.

2.2.1.4 Discussion of Results. The initial conditions and vehicle inertia parameters were varied. The effect of various vehicle and aerodynamic parameters was approximated by varying mass moment of inertia. A larger mass moment of inertia was felt to be more critical at low initial rates, and a low mass moment of inertia at the high spin rates. For very low initial rates — 0 to 45 deg/sec (Figures 2-17 through 2-19), the vehicle did not complete one revolution.

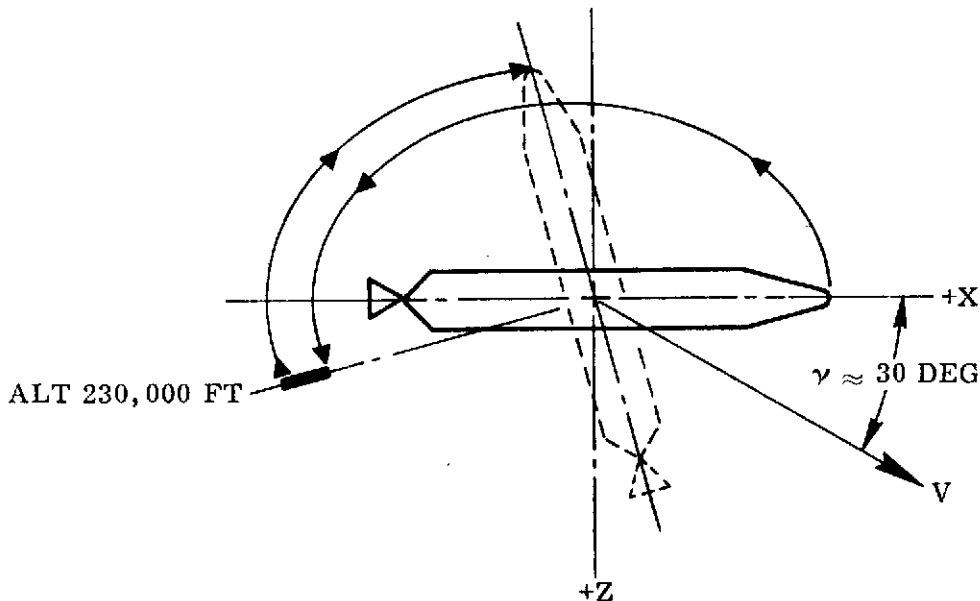


Figure 2-17. Nose position history ($I_{YY} = 200,000 \text{ ft}^2$, $\dot{\theta} = 0^\circ/\text{sec}$, $\theta = 0^\circ$).

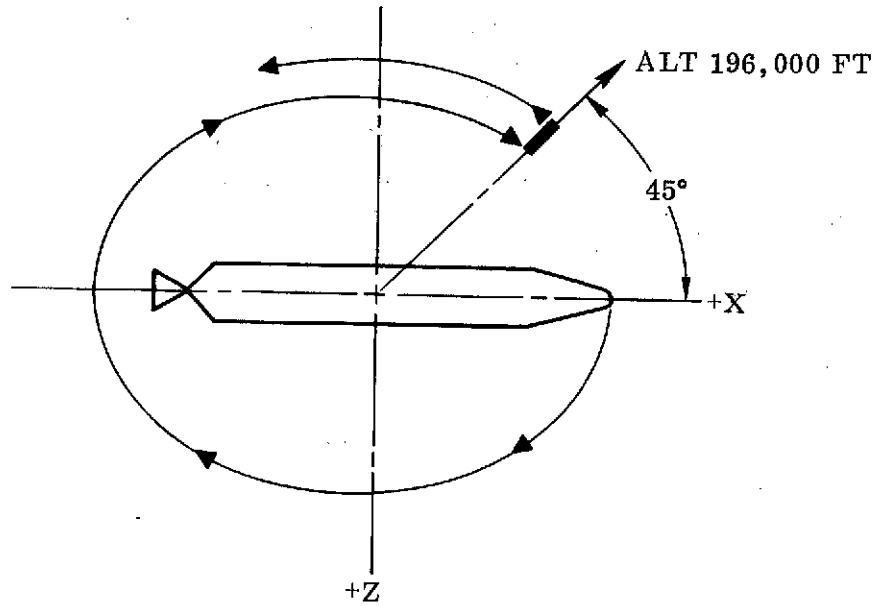


Figure 2-18. Nose position history ($I_{YY} = 200,000$ ft, $\dot{\theta} = -10^\circ/\text{sec}$, $\theta = 0^\circ$).

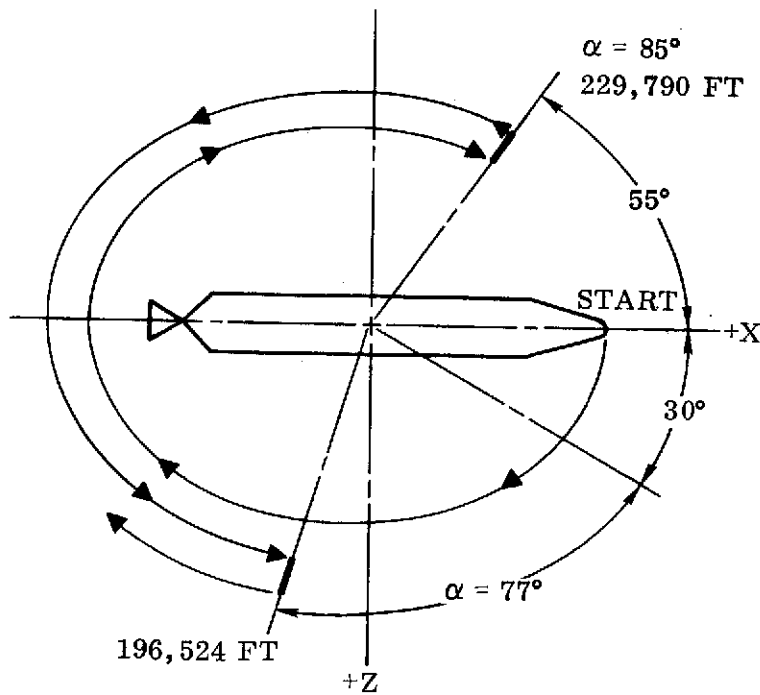


Figure 2-19. Nose position history ($I_{YY} = 200,000$ ft, $\dot{\theta} = 45^\circ/\text{sec}$, $\theta = 0^\circ$).

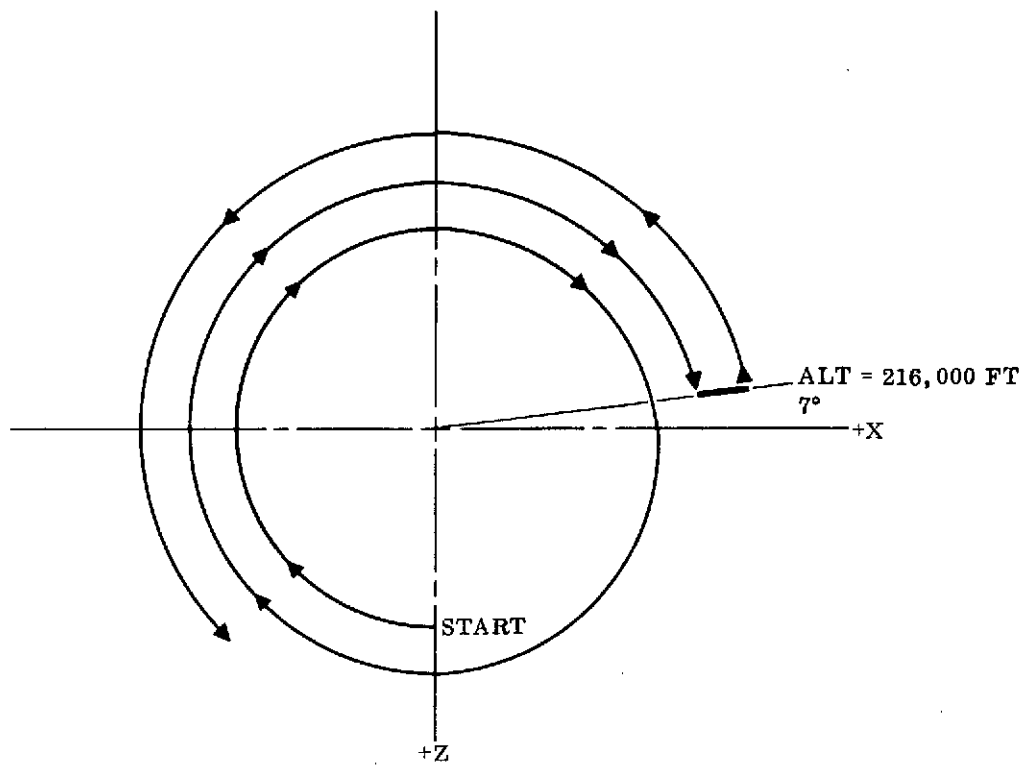


Figure 2-20. Nose position history ($Y = 200,000$ ft, $\dot{\theta} = -90^\circ/\text{sec}$, $\theta = 0^\circ$).

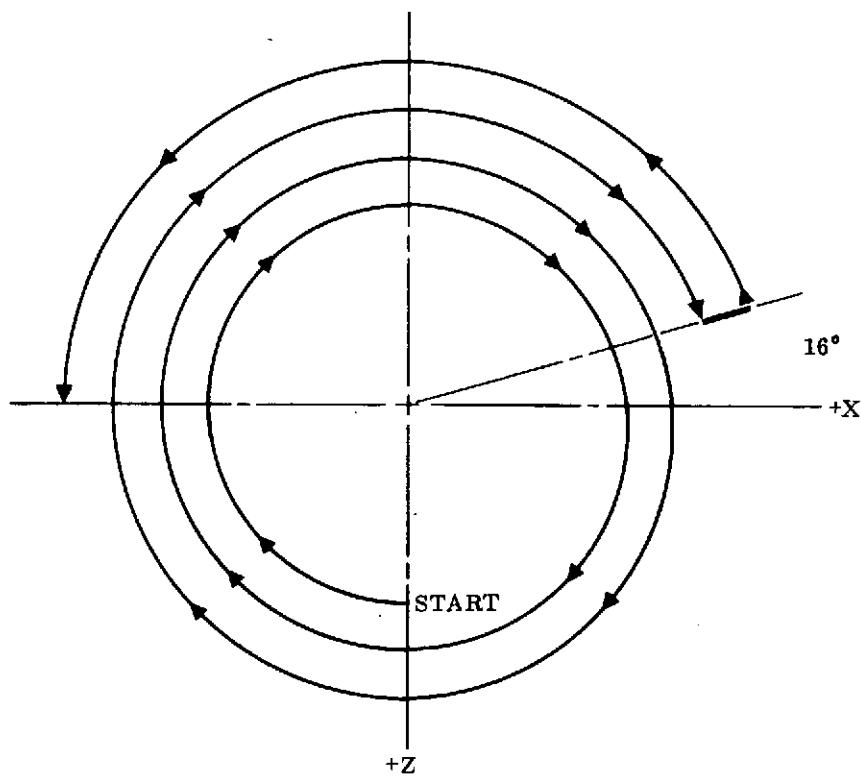


Figure 2-21. Nose position history ($Y = 155,000$ ft, $\dot{\theta} = -120^\circ/\text{sec}$, $\theta = -90^\circ$).

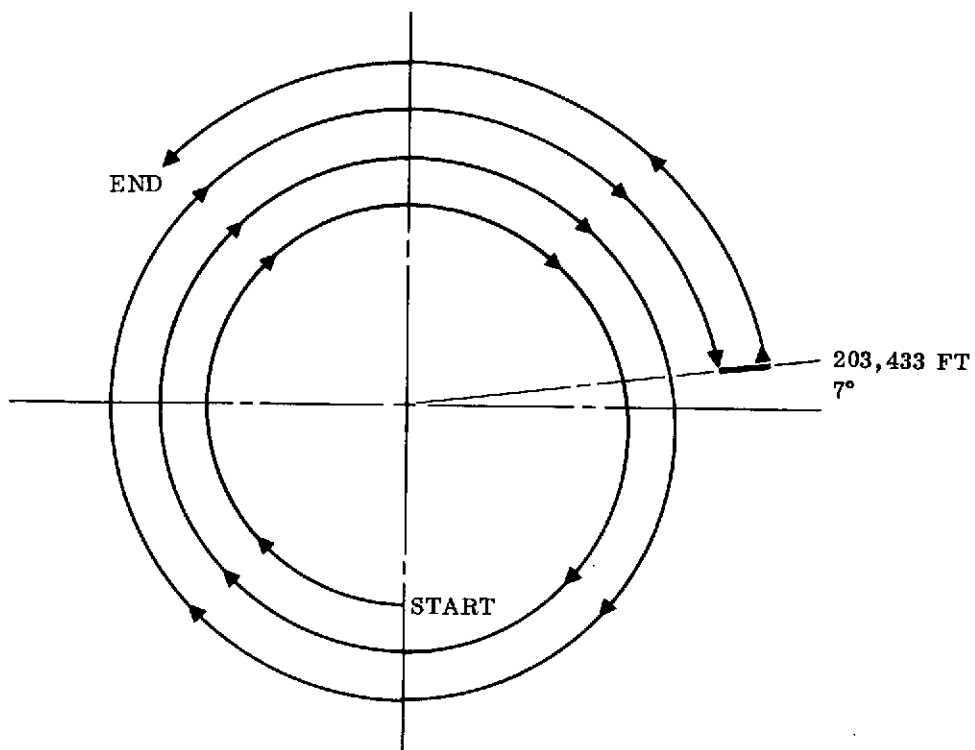


Figure 2-22. Nose position history ($IYY = 185,000 \text{ ft}$, $\dot{\theta} = -120^\circ/\text{sec}$, $\theta = -90^\circ$).

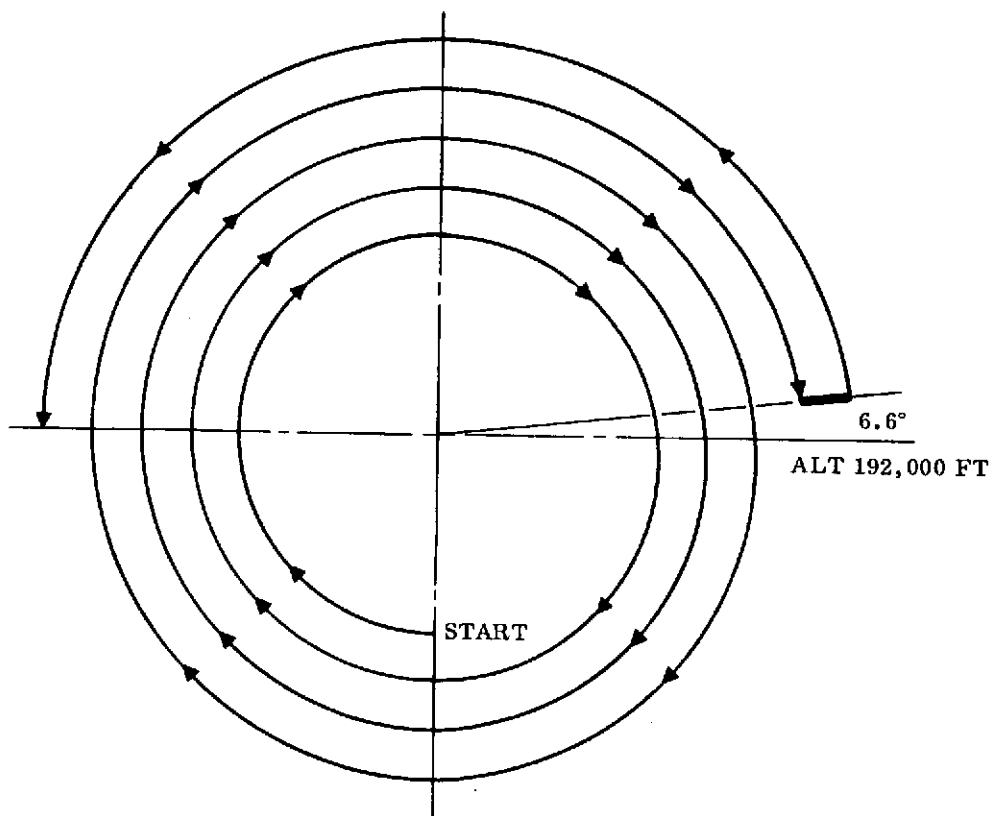


Figure 2-23. Nose position history ($IYY = 155,000 \text{ ft}$, $\dot{\theta} = -150^\circ/\text{sec}$, $\theta = -90^\circ$).

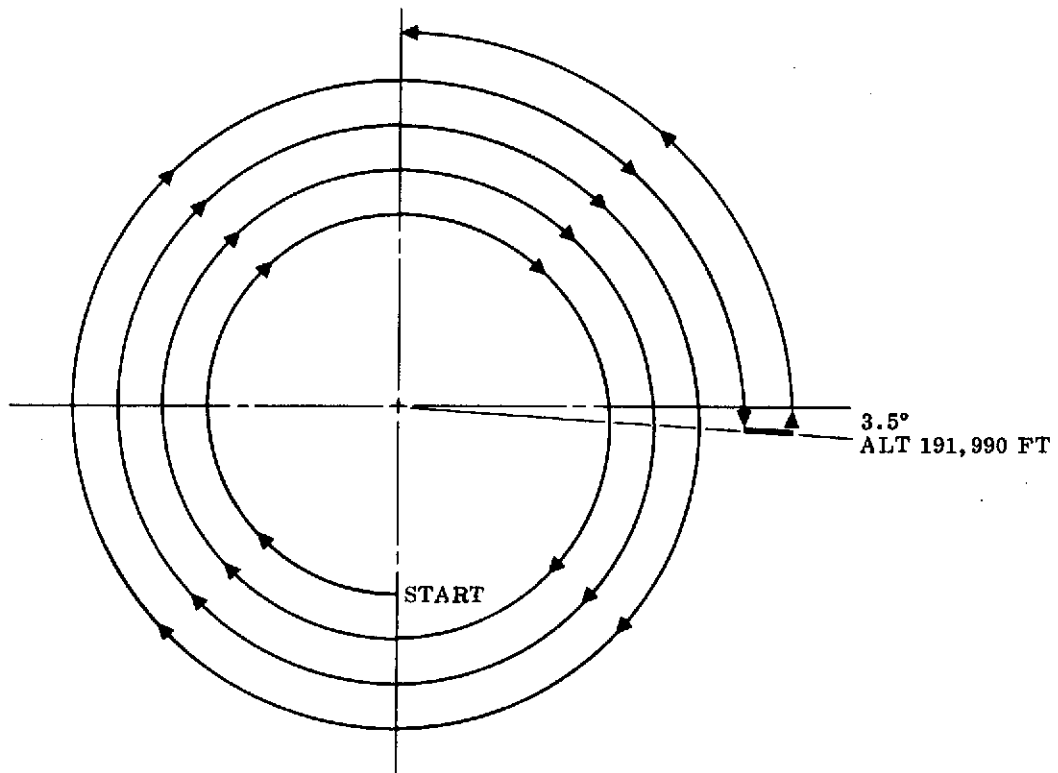


Figure 2-24. Nose position history ($IYY = 185,000$ ft, $\dot{\theta} = -150^\circ/\text{sec}$, $\theta = -90^\circ$).

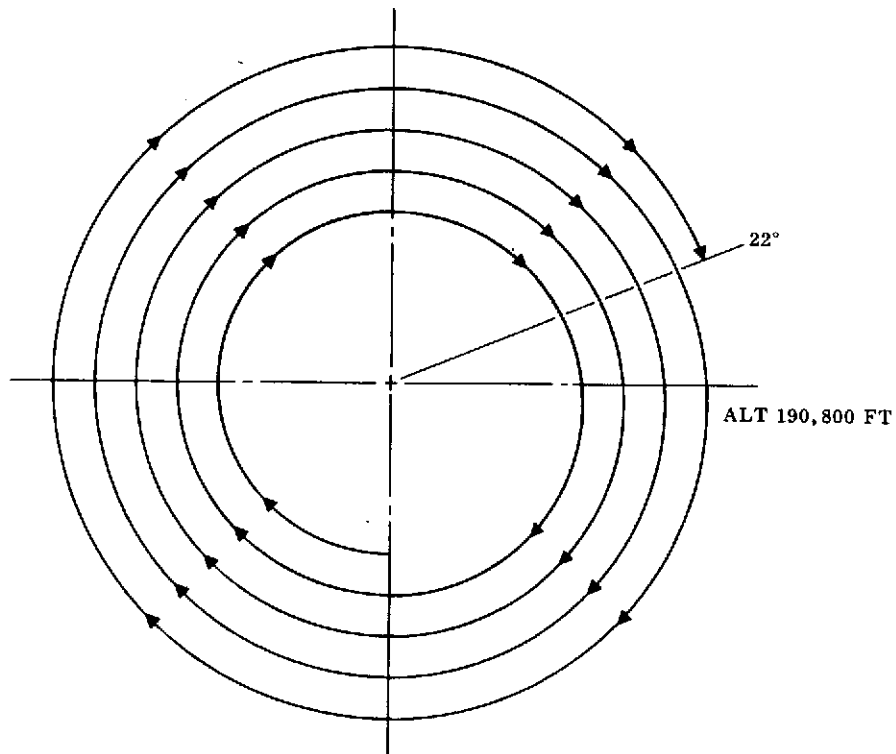


Figure 2-25. Nose position history ($IYY = 80,000$ ft, $\dot{\theta} = -180^\circ/\text{sec}$, $\theta = -90^\circ$).

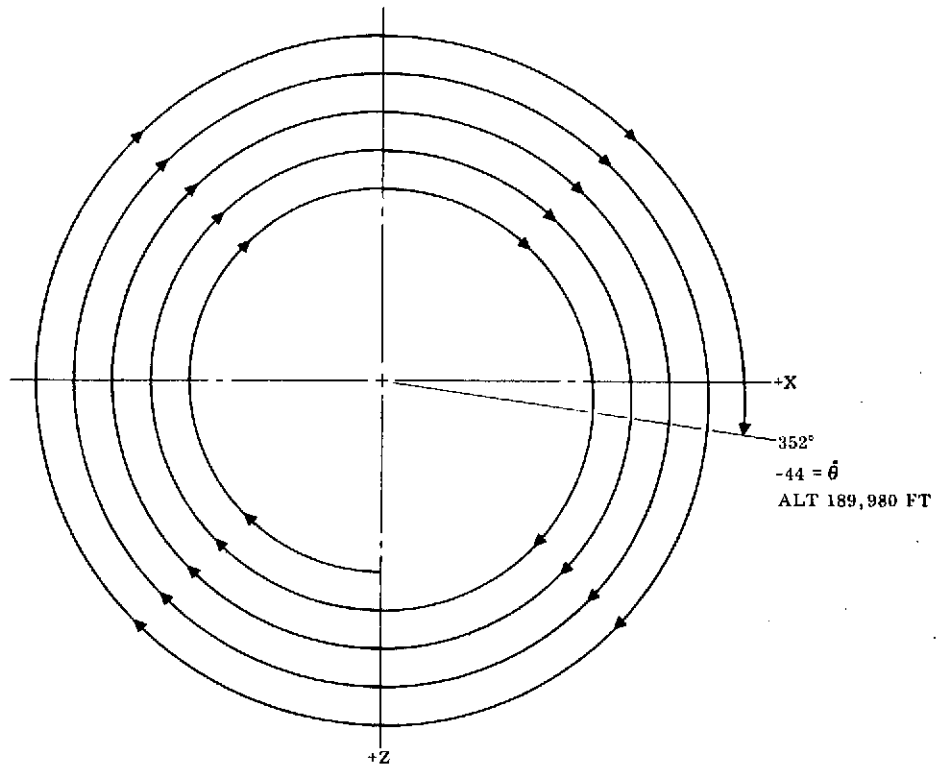


Figure 2-26. Nose position history (IYY = 155,000 ft, $\dot{\theta} = -180^\circ/\text{sec}$, $\theta = -90^\circ$).

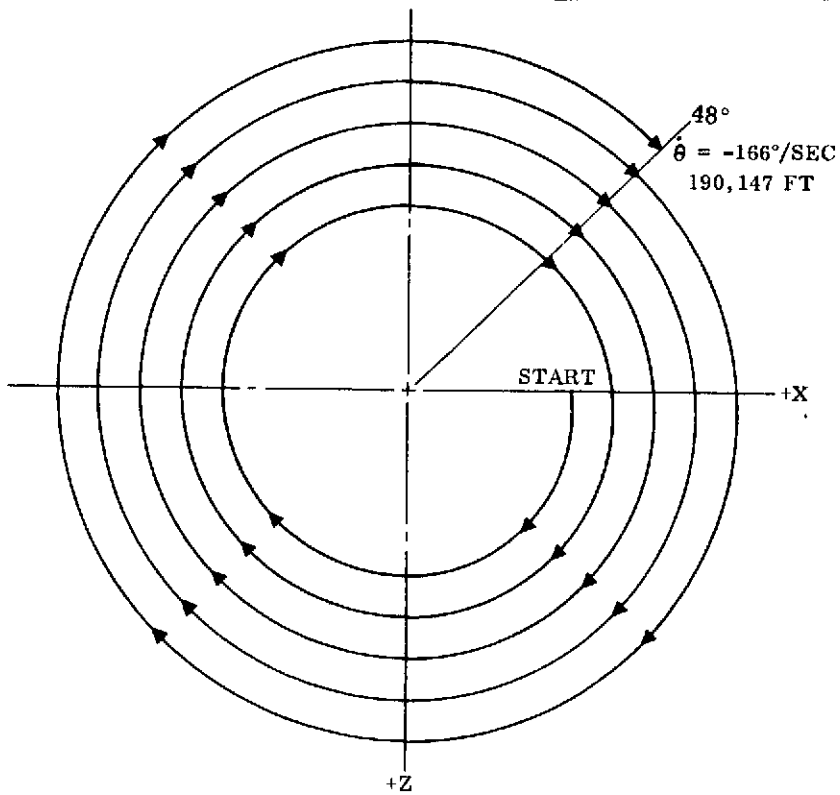


Figure 2-27. Nose position history (IYY = 200,000 ft, $\dot{\theta} = -180^\circ/\text{sec}$, $\theta = 0^\circ$).

At initial rates of 90 and 120 degrees per second, one and two complete turns were obtained, respectively. However, the vehicle reverted to a tail-first attitude before reaching 200,000 ft altitude, as shown in Figures 2-20 through 2-22.

At 150 degrees per second, three complete turns were obtained, and the vehicle did not revert to a tail-first attitude before reaching 200,000 ft, as inferred from Figures 2-23 and 2-24. This case is marginal, however, and if rates of this magnitude are considered they will need to be considered on a mission peculiar basis.

All runs with initial rates of 180 degrees per second, shown in Figures 2-25 through 2-27, were still tumbling upon reaching 200,000 ft, and completed about four and three-quarter turns. Additional data, consisting of vehicle attitude, pitch rate, and altitude are shown in Figure 2-28 for these runs.

2.2.1.5 Conclusions. From these runs, it is concluded that an initial pitch tumbling rate of at least 150 degrees per second is required to assure that the vehicle will continue to rotate as desired, down to an altitude of 200,000 feet. The 180 degrees per second rate (desirable from the standpoint of increasing the amount of heating data obtained at a given angle of attack) should result in a predictable and satisfactory pitch plane entry mode.

2.2.2 ATTITUDE FOLLOWING HIRS AND PITCH TUMBLING ROCKET FIRINGS

2.2.2.1 Discussion. To determine the Atlas attitude and plane of rotation at the end of the pitch tumble rocket firing, the following assumptions were made.

- a. Mass properties were typical of an Atlas having the HIRS adapter and an additional payload spacer.
- b. A normal HIRS sequence to provide 110 degrees of tank pitch rotation prior to firing of HIRS retrorockets is used (see Figure 2-29).
- c. One second after HIRS retro termination, fire the pitch tumble rocket to increase the tumble rate to approximately 180 degrees per second.
- d. Both HIRS pitch and final tumble (pitch rotation) rocket thrust vector aligned to pass through vehicle centerline.

The rotation rates, displacements, and angular momentum components were calculated in local body coordinates then resolved into the body axis system which existed at vernier engine cutoff (VECO). The direction and sense of the total angular momentum vector determine the tank tumbling plane and direction of rotation. The total momentum vector direction relative to the body axis system at VECO is at an angle of -34.39 degrees in the pitch plane and a yaw angle of +16.02 degrees, and the sense is negative. The tumble rate about the axis of maximum inertia is -175.02 deg/sec. This results in a vehicle motion which is essentially a yaw rotation (flat spin) in a plane with an

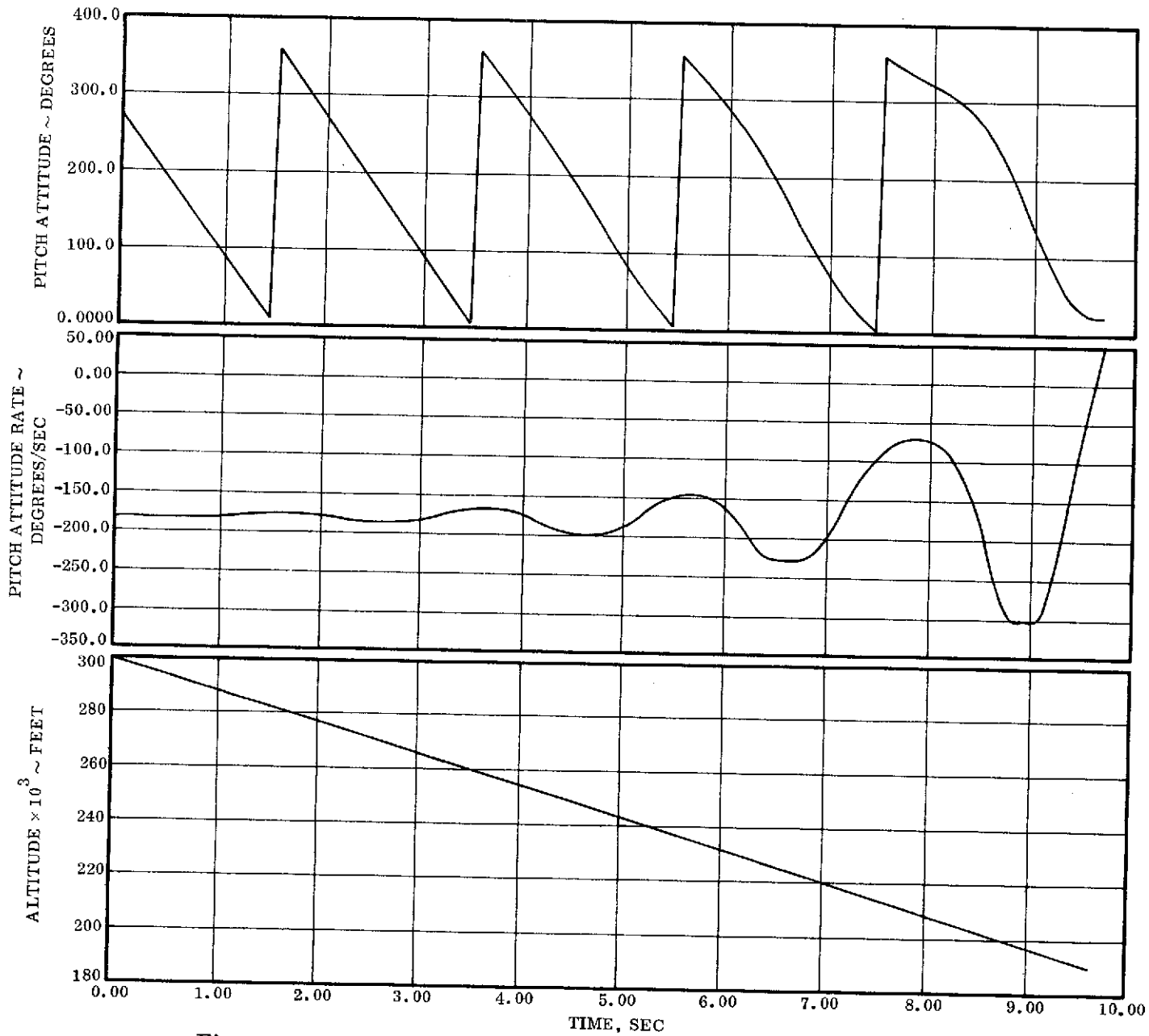


Figure 2-28A. Atlas tank oscillations during reentry, 80,000 ft.

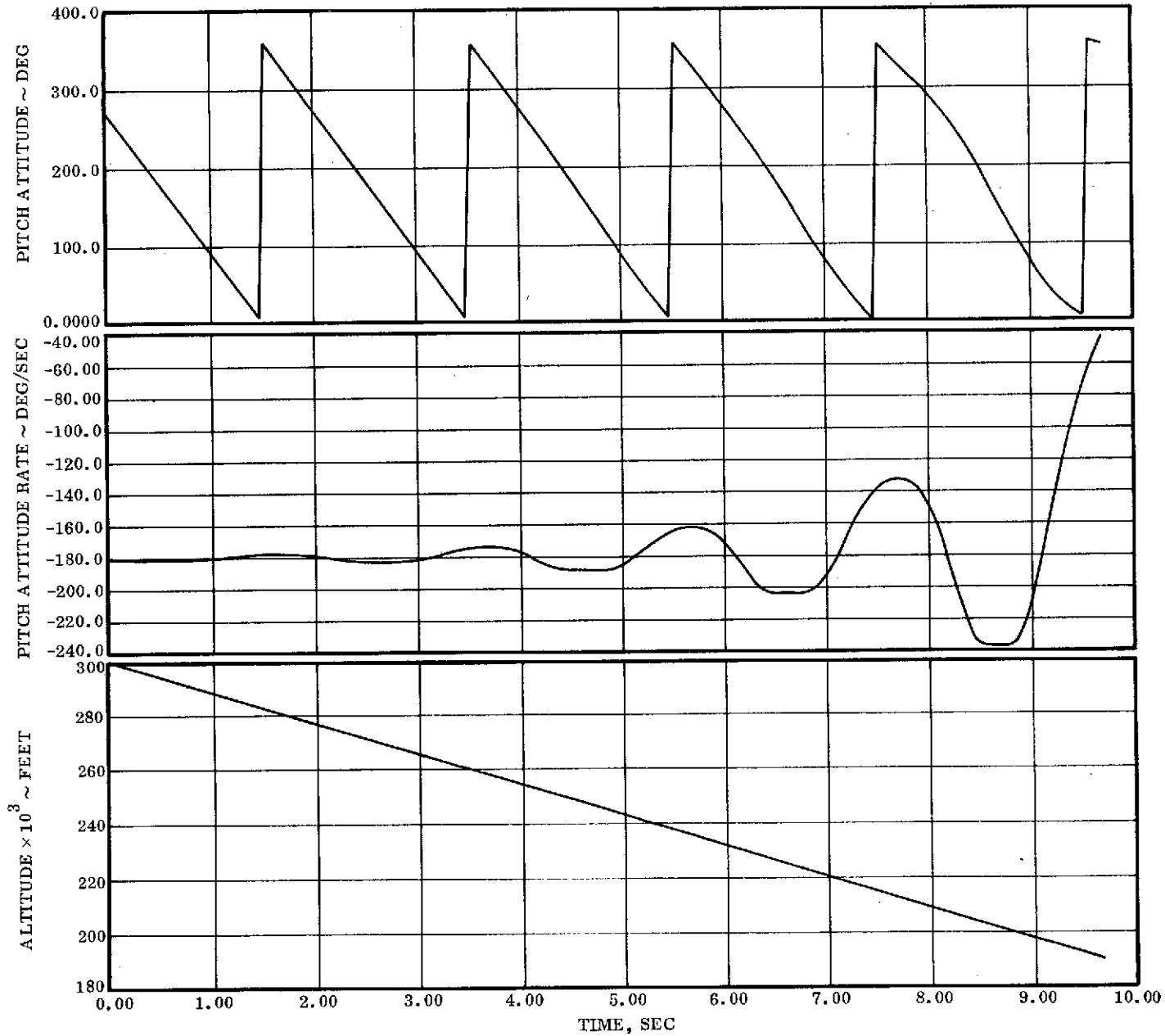


Figure 2-28B. Atlas tank oscillations during reentry, 155,000 ft.

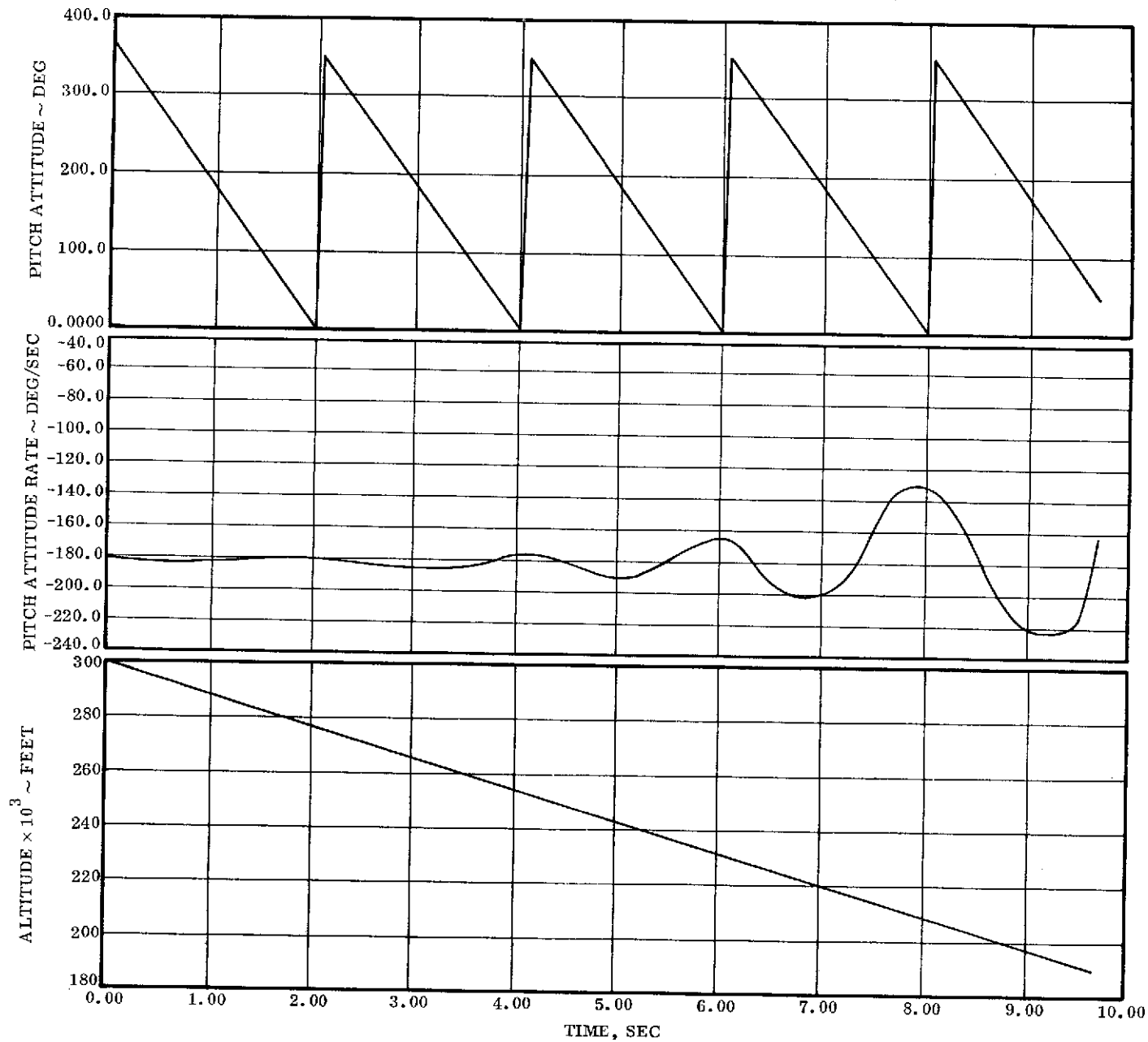


Figure 2-28C. Atlas tank oscillations during reentry, 200,000 ft.

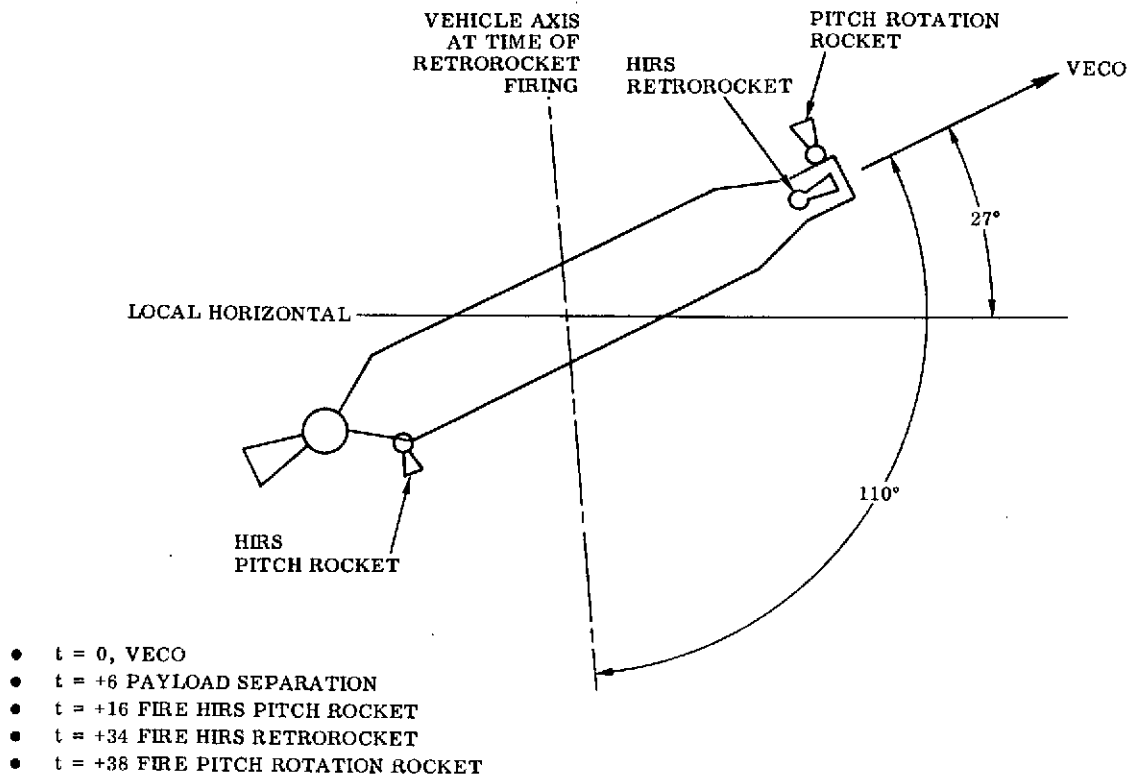


Figure 2-29. Typical post-VECO sequence.

approximate angle of attack of 10° at the start of entry. This would not be acceptable for this mission. The results are shown in Table 2-4.

The final tumble motion of the tank shown in Table 2-4 departs from a pure pitch plane spin due to the roll rate developed during the normal HIRS pitch rocket firing and the relatively long coast until final tumble rocket firing. The roll rate is caused by the center of gravity offset from the tank centerline and the fact that the HIRS pitch rocket thrust is directed to intersect the tank centerline. (The roll rates in Table 2-4 were nominals; the three sigma dispersions are approximately $\pm 60\%$ of nominal.)

The roll rates can be significantly reduced by directing the HIRS pitch and tumble rocket thrust axes to intersect the expected roll axis of the tank. Dispersions due to uncertainties in dry tank cg location and SECO propellant residual cannot be eliminated. For this condition, the nominal roll rate at the end of HIRS pitch rocket firing is zero, with a dispersion of ± 1.92 degrees per second. After the completion of the tumble rocket firing, the vehicle rotation is nominally in the pitch plane, but has a dispersion of about ± 30 degrees (3σ) about this plane. An almost pure pitch plane spin can be achieved by aligning the tumble rocket thrust vector through the vehicle roll axis, and utilizing a launch vehicle which does not employ a HIRS maneuver. The use of this type of vehicle is recommended.

Table 2-4. Atlas displacement, rate and angular momentum.

Event	Atlas Attitude Rel. to VECO, deg	Atlas Rate deg/sec	Angular Momentum Rel. to VECO, lb-ft-sec
VECO	$\phi = 0$ $\theta = 0$ $\psi = 0$	P = 0.04 Q = 0.04 R = 0.05	HX = 3.1 HY = 108.6 HZ = 136.9
End of HIRS Pitch Firing	$\phi = -2.26$ $\theta = -4.06$ $\psi = 0.5$	P = -3.24 Q = -5.81 R = 0.013	HX = -250.9 HY = -15770.5 HZ = 991.7
End of HIRS Retro- Firing	$\phi = -77.5$ $\theta = -135.86$ $\psi = 3.9$	P = -5.46 Q = -7.88 R = 2.10	HX = -4596.9 HY = -11742.7 HZ = -3840.7
End of Tumble Firing	$\phi = -28.9$ $\theta = -405.5$ $\psi = -78.86$	P = 39.45 Q = -172.5 R = 50.6	HX = -384649.5 HY = -110458.2 HZ = -263330.0

where:

- ϕ , P roll measurements, positive CW viewed from rear
- θ , Q pitch measurements, positive Nose up
- ψ , R yaw measurements, positive Nose right viewed from rear
- x positive forward
- y positive right viewed from rear
- z positive down

The roll rate existing at the completion of the tumble rocket firing is expected to be the maximum rate during the remainder of the flight. The viscous action between the residual propellants and the tank walls will tend to reduce the roll rate during coast. Also, the aerodynamically induced rolling moments developed during entry are expected to be oscillatory rather than unidirectional, because the vehicle is rotating end-over-end. The combination of viscous and aerodynamic moments during entry is also expected to reduce the magnitude of the average roll rate.

2.2.2.2 Conclusions. The alignment of the HIRS pitch and tumble (pitch rotation) rocket thrust vectors is critical. These should be directed through the vehicle roll axis (instead of the vehicle centerline, as is currently done) to minimize their consequent undesired contributions to yaw plane motion. This mission should be flown on a launch vehicle not employing a HIRS pitch maneuver, if available.

2.3 VEHICLE STRUCTURAL INTEGRITY

The overall category of vehicle structural integrity studies contains three different subtasks:

- a. Pressure histories of the LO₂ and fuel tanks, and whether venting or jettisoning of the residual propellants is required.
- b. Basic modifications to the vehicle which have a structural impact; e.g., pitch rotation rocket mounting scheme, and the loads induced.
- c. Pitch plane spinup and entry loads/structural integrity analysis.

2.3.1 THERMODYNAMIC ANALYSIS

2.3.1.1 LO₂ Tank. The purpose of this study was to determine whether it is required to jettison residual LO₂ in order to insure propellant tank structural integrity to a re-entry altitude of 200,000 ft. The concern was primarily directed towards the potential for rapid pressure rise in the LO₂ tank resulting from vaporization of oxygen. However, the high acceleration forces resulting from a pitch rate of 70 to 180°/sec will restrict residual LO₂, other than that which is trapped in the feed lines, to the forward bulkhead. Here, up to 2030 pounds of residual liquid is well shielded from reentry and solar heating and is not expected to significantly affect pressure rise rate during the 8.9 seconds of reentry heating. The liquid which is trapped in the feed lines, however, will be exposed to significant aerodynamic heat flux. This effect should be included in future analyses to determine the potential for vapor addition to the LO₂ tank during reentry.

Except for feed line boiloff, the presence of LO₂ residual may be less of a threat to propellant tank structural integrity than ullage gas heating during the pre-entry coast. Ullage heating from the tank wall is given by:

$$Q = h A (T_W - T_g)$$

where

Q = heat transfer from tank wall, Btu/hr

h = heat transfer coefficient, Btu/hr ft² °F

A = wall area, 1123 ft²

T_W = wall temperature, °R

T_g = ullage gas temperature, °R

The heat transfer coefficient, as given in Reference 4, is:

$$h = (0.22 + .093X) \left| T_W - T_g \right|^{1/3} \left(\frac{T_W + T_g}{1120} \right)^{-(.63 + .159X)} \left(\frac{P}{14.7} \right)^{2/3} \left(\frac{a}{g_0} \right)^{1/2}$$

where

X = ratio of helium mass to total ullage mass

P = ullage pressure, psia

a = local acceleration, ft/sec²

g₀ = 32.2 ft/sec²

For a perfect gas of constant mixture ratio, constant volume, and zero mass transfer, the pressure rise rate for a given heat transfer rate is given by:

$$\dot{P} = \frac{QR}{V C_V}$$

where

\dot{P} = pressure rise rate, psf/hr

R = specific gas constant of the ullage mixture, ft lbf/lbm °F

V = ullage volume, 2525 ft³

C_V = specific heat of the ullage mixture at constant volume, Btu/lbm °F

Pressure rise rates are plotted in Figure 2-30 versus average wall-to-gas temperature difference. Curves are shown for average gravity fields which result from vehicle pitch rates of 180°/sec. and 70°/sec., the range of the proposed reentry study vehicle rates, and 8°/sec., which corresponds to the pitch rates induced by the HIRS on Atlas 150F and 151F, to be discussed.

The best indication of the potential pressure rise after payload separation is given by the test data of Atlas 150F and 151F. LO₂ and fuel pressure data of these vehicles are shown in Figures 2-31 and 2-32. Both vehicles utilized the HIRS but differ from current F vehicles in that the LO₂ tank skins at the conical section were thicker, and therefore cooler. The hotter current Atlas F skins should generate higher pressure rates. The characteristics of 150F and 151F pressure histories are similar. At pitch rocket firing, shortly after VECO, a slight drop in LO₂ tank pressure

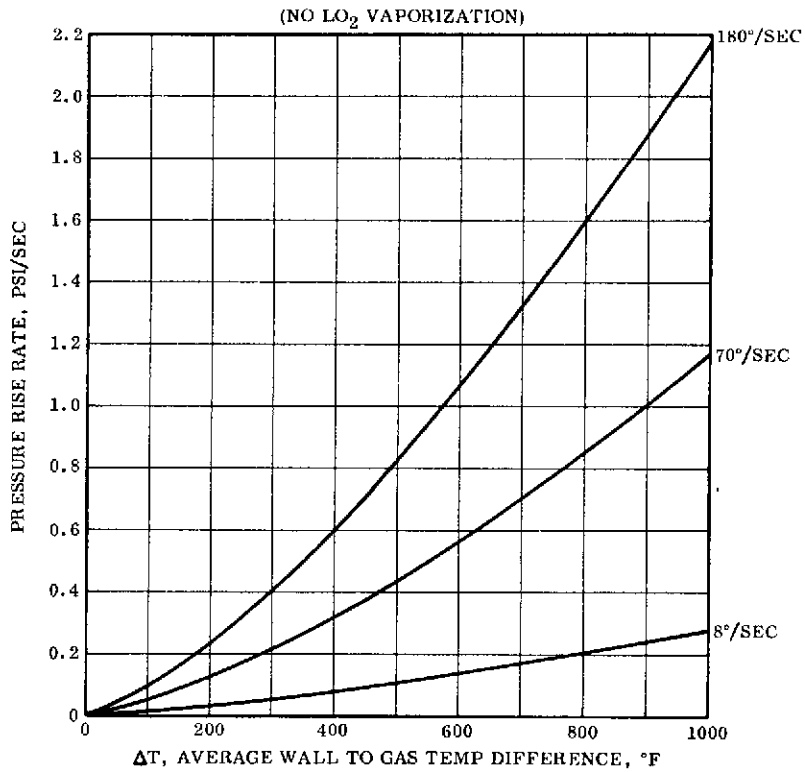


Figure 2-30. LO₂ tank pressure rise rate resulting from heat transfer while tumbling.

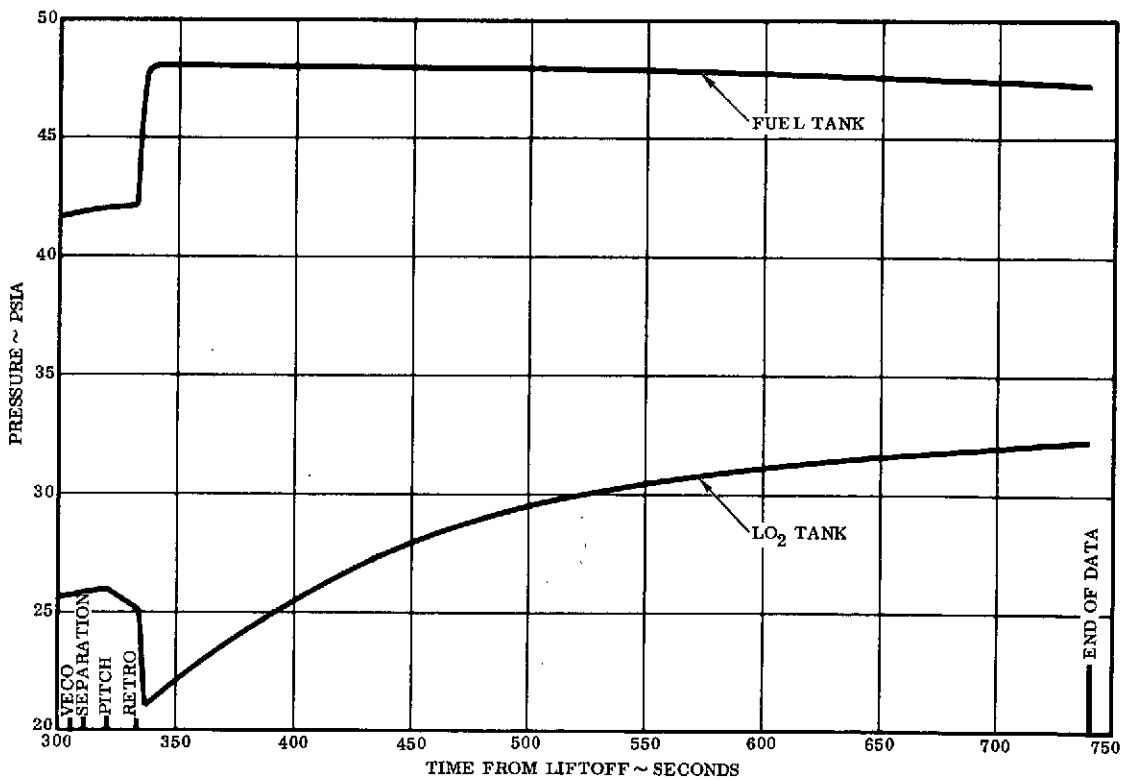


Figure 2-31. 150F propellant tank pressure.

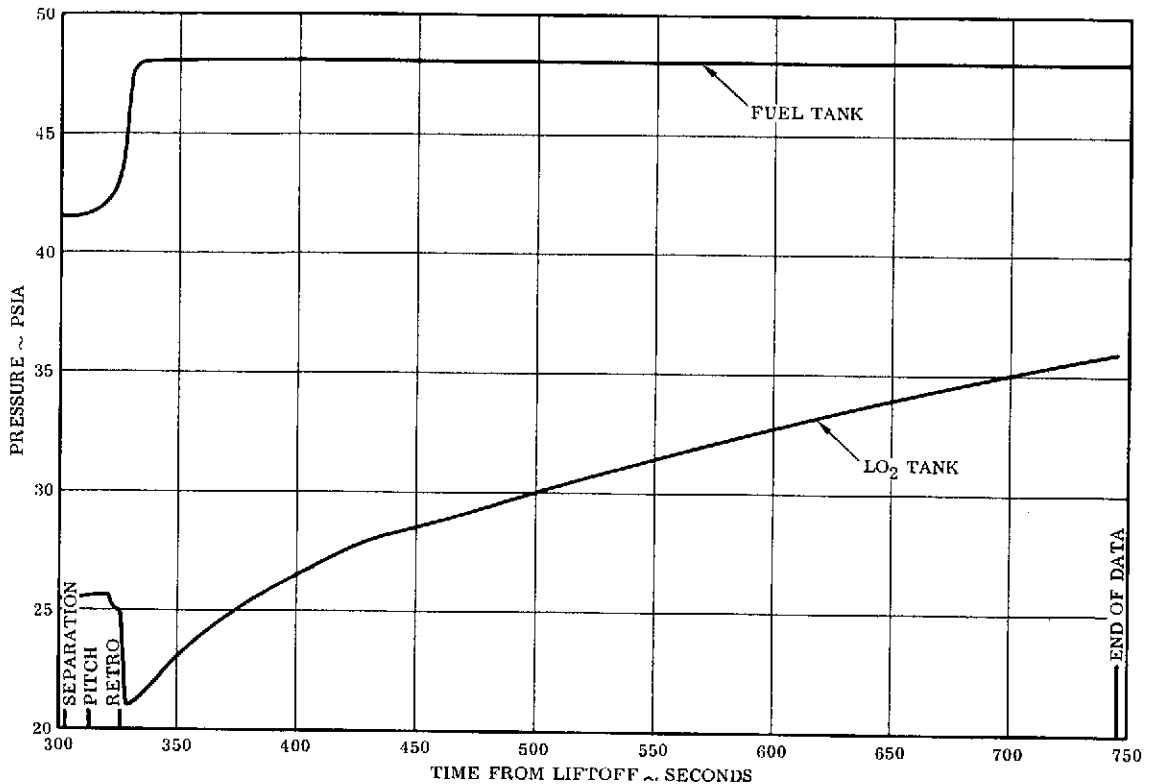


Figure 2-32. 151 F propellant tank pressure.

was noted. At retrorocket firing, a 4 to 5 psia LO₂ tank pressure drop was accompanied by an increase in fuel tank pressure.

These rapid changes in pressure result from liquid-gas heat transfer, as propellants pass to the forward ends of the tanks during retrorocket firing. The reversal in pressure rate in the LO₂ tank shortly after retro-fire indicates that LO₂ quickly becomes settled under the 8°/sec pitch rate. The subsequent pressure rise rate, as high as 0.1 psi/sec, can theoretically occur for a wall-to-gas temperature difference of 500°F (Figure 2-30). Figure 2-30 shows that a pitch rate of 180°/sec would result in a significantly higher pressure rise rate. The pressure rise rate decreases with time as the gas temperature warms, such that a given equilibrium pressure will eventually occur, whatever the initial pressure rise rate.

Assuming the LO₂ tank ullage gas was chilled to 200°R during retro fire, causing the pressure to drop to 21 psia on 150F and 151F, a pressure of 70 psia can be reached before the solar radiation equilibrium temperature occurs. The solar radiation equilibrium temperature for a cylinder with axis normal to the sun vector is 685°R for a solar absorptivity of 0.48 and emissivity of 0.175. Since reentry to 300,000 ft does not occur until 1825 seconds after liftoff, it would appear feasible that intermediate bulkhead reversal and propellant tank failure might occur prior to reentry.

For this analysis, it was assumed that the mass flow through the LO₂ tank pressurization system relief valve is negligible. This valve is located in the helium supply line at the staging disconnect, which is well aft of the center of gravity. The point where the pressurization line opens to the LO₂ tank is near the top of the forward bulkhead. Under a pitch rotation of 180°/sec, an LO₂ tank pressure of over 100 psia would be required to drive a head of liquid to the center of gravity station where it would then be thrown to the relief valve. Below this pressure, only the gas vaporized in the line can escape. For saturated vapor conditions, the initial flow rate is approximately 1.0 pound per second and drops off as the liquid is chilled by flashing vapor. The lower pitch of 150F and 151F would allow liquid to reach the valve, where one would expect a higher mass flow rate. However, it is conceivable that liquid flashing as it passes to the zero pressure side of the valve restriction might result in frozen oxygen stopping relief flow completely.

Based on this preliminary analysis, some method of pressure relief in the LO₂ tank is required.

2.3.1.2 Fuel Tank. A preliminary analysis was performed to estimate the fuel tank pressure history through atmospheric reentry to 200,000 feet. Flight test data from Atlas F vehicles utilizing the HIRS shows a characteristic pressure rise from 41 to 48 psia when the retrorockets are fired. This pressure rise results from ullage gas heating to about 520°R by the residual fuel, unsettled by the HIRS pitch and retrorockets. After the HIRS maneuver, fuel tank pressure remains relatively constant or drops slightly as solar heating is compensated for by intermediate bulkhead heat loss.

Reentry pressure rise calculations were made, assuming initial ullage conditions of 48 psia and 520°R. The wall temperatures provided in Figure 2-71 in subsection 2.4 were used for boundary conditions. The temperature history used was calculated for a laminate of 8 mils and 16 mils of stainless steel separated by 20 mils of material having one-tenth the density of stainless steel. The inner and outer layer temperatures are shown in Figure 2-71.

The temperature gradient across the laminate is small and the thermal mass is equivalent to 27 mils of stainless steel, approximately the thickness of the Atlas F fuel tank. The outer surface emissivity used for this model was also that of the Atlas fuel tank. These similarities are sufficient to justify using the average of the curves shown in Figure 2-71 for wall temperature during reentry.

Wall to gas heat transfer was calculated assuming a turbulent free convection heat transfer coefficient given by:

$$h = 0.313 \Delta T^{1/3} F_T (P/14.7)^{2/3} (a/g_0)^{1/3} \text{ Btu/hr ft}^2 \text{ }^\circ\text{F, Reference 5}$$

where

ΔT = wall to gas temperature difference, °F

F_T = temperature correction factor

P = ullage pressure, psia

a/g_0 = acceleration, 4 g resulting from tumbling.

and;

$$F_T = (T_{avg}/520)^{-0.789}$$

where T_{avg} = average temperature of wall and gas, °R

The effect of heat transfer on pressure rise for a constant volume process is given by:

$$\dot{P} = \frac{RQ}{VC_V}$$

where

\dot{P} = pressure rise rate, psf/hr

R = specific gas constant, 386 ft-lb/lb °F

C_V = specific heat at constant volume, 0.74 Btu/lb °F

V = ullage volume, 1500 ft³

Q = heat transfer, Btu/hr

$$Q = hA \Delta T$$

where A = Fuel tank wall area, 520 ft²

The corresponding temperature rise rate is:

$$\dot{T} = \frac{V}{mR} \dot{P} \text{ °F/hr}$$

where:

m = ullage mass, 52 lb

The intermediate bulkhead heat transfer was neglected.

The above equations were combined and integrated numerically over a 10-second period starting at 300,000 ft altitude and 48 psi. This integration resulted in a tank pressure of 52 psi at 187,000 ft altitude.

The pressure rise rates obtained in this study compare well with the pressure rise rates observed during the tumbling reentry of Atlas 113F (Reference 4) when wall temperature and acceleration corrections are applied, thereby lending credence to this preliminary procedure.

2.3.2 STRUCTURAL MODIFICATIONS. A preliminary study was performed to define Atlas structural modifications required to accomplish the tumbling reentry maneuver. Three tasks were identified:

- a. Vent system for the Atlas LO₂ tank.
- b. Pitch rocket sizing and placement.
- c. Aerodynamic clean-up of the HIRS adapter.

2.3.2.1 LO₂ Tank Vent System. The LO₂ tank pressure rise during apogee coast and reentry to 200,000 ft will require tank venting to maintain structural integrity. Based on the allowable hoop stress on the 301 CRES tank skins at elevated temperature, the maximum allowable LO₂ tank pressure is 21.1 psi, which is well below the expected maximum pressure of approximately 70 psi without venting.

Three venting concepts were investigated:

- a. Open main LO₂ valve on sustainer engine, and blowdown through the LO₂ injector.
- b. Add pyrotechnic valve, pressure relief valve, and associated non-propulsive overboard dump lines on forward LO₂ bulkhead, and vent residual fluid forward.
- c. Add valves and lines similar to above concept to the sustainer engine LO₂ line, and vent residual fluids aft.

The first concept requires the development of a hydraulic power source to actuate the main LO₂ valve (and to keep the engine gimbal actuators nulled to prevent undesired yaw moments). Currently, hydraulic power is provided by a pump driven by the sustainer engine turbopump, and the power ceases at engine cutoff. Also required is the development of an LO₂ tank pressure sensor/main LO₂ valve control logic network to provide modulation of this valve to maintain the tank pressure at approximately 21 psia. The development time for this concept was determined to be unacceptably long.

The second concept was assessed to be unacceptable because of the risk of the vented oxygen being entrained in the airflow over the heating sensors and invalidating the heat transfer data. Usable data can only be obtained when the vehicle is oriented in the range of ± 90 degrees in pitch attitude, because of the flow field disturbances caused by the protuberances and equipment exposed when the vehicle attitude is tail first. This consideration led to the adoption of the ground rule that the fluids must be dumped at the aft end of the vehicle.

The third concept was selected for further investigation on the basis that the development time would be appreciably shorter than that required for the first concept.

The proposed LO₂ tank vent system is shown in Figures 2-33 and 2-34. The venting system consists of a shearable butterfly type pyrotechnic valve in series with a poppet type pressure relief valve capable of maintaining LO₂ tank pressure of approximately 20 psi. The vent system would be led off one of the 4-inch diameter sustainer engine oxidizer supply ducts and connected to a balanced overboard dump manifold, which would minimize unbalanced disturbing forces on the vehicle when the tank is being vented.

The results of the formal cost estimating exercise conducted at the end of the study suggest that other alternate venting concepts should be investigated. The costs for the qualification testing to assure no increase in risk to the primary mission were significantly higher than originally anticipated. Specifically, concepts requiring little or no qualification testing of assemblies (such as the relief valve/pyrotechnic valve/engine suction lines in this concept) should be sought.

2.3.2.2 Pitch Rocket Sizing and Placement. To evaluate pitch rocket sizing and placement, the baseline Atlas F inertias were used together with total pitch rocket impulse requirements based on an initial pitch rate of 30 rpm (180°/sec). Several configurations and locations were considered for the pitch rocket system, including:

- a. Mounting the pitch rockets on the Atlas thrust cone, similar to the present pitch rockets used with the HIRS. This concept was not feasible due to space and clearance limitations which prevented the rather large pitch rockets required for the high (180°/sec) pitch rate from being mounted on the thrust cone.
- b. Mounting fore/aft facing rockets in the sides of the Atlas tank. Relative inefficiency of the short moment arm about the cg for the fore/aft facing rockets together with the complexity of added tank weldments and mounting brackets made this concept unattractive.
- c. Mounting pitch rockets in the forward payload transition adapter. This concept minimizes changes to the overall vehicle and was selected as being most feasible, although it requires adapter modifications. It provides the most efficient placement of the pitch rockets. The selected pitch rocket configuration (shown in Figure 2-35) consists of a single HIRS retrorocket mounted normal to the vehicle centerline at the payload transition adapter/HIRS adapter interface (Station 415) and a Thor pitch rocket (currently used with the HIRS) mounted at its present location (Station 1198) on the aft thrust cone.

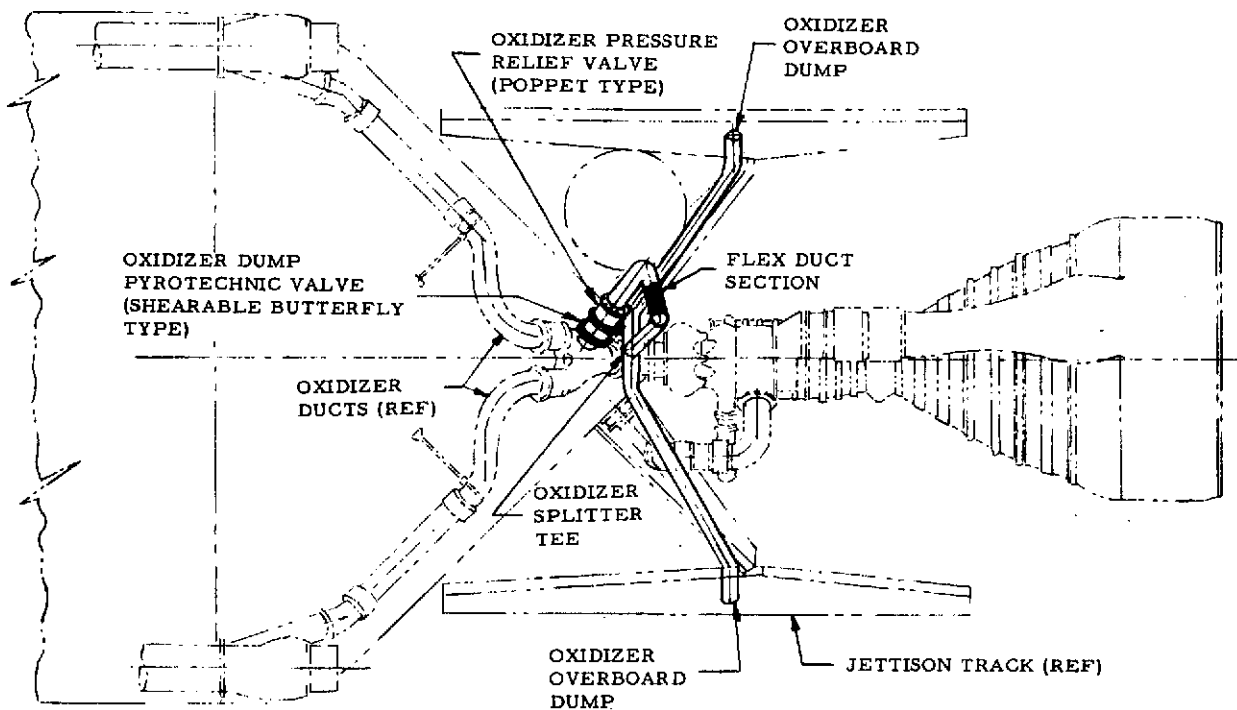


Figure 2-33. LO₂ vent system (side view).

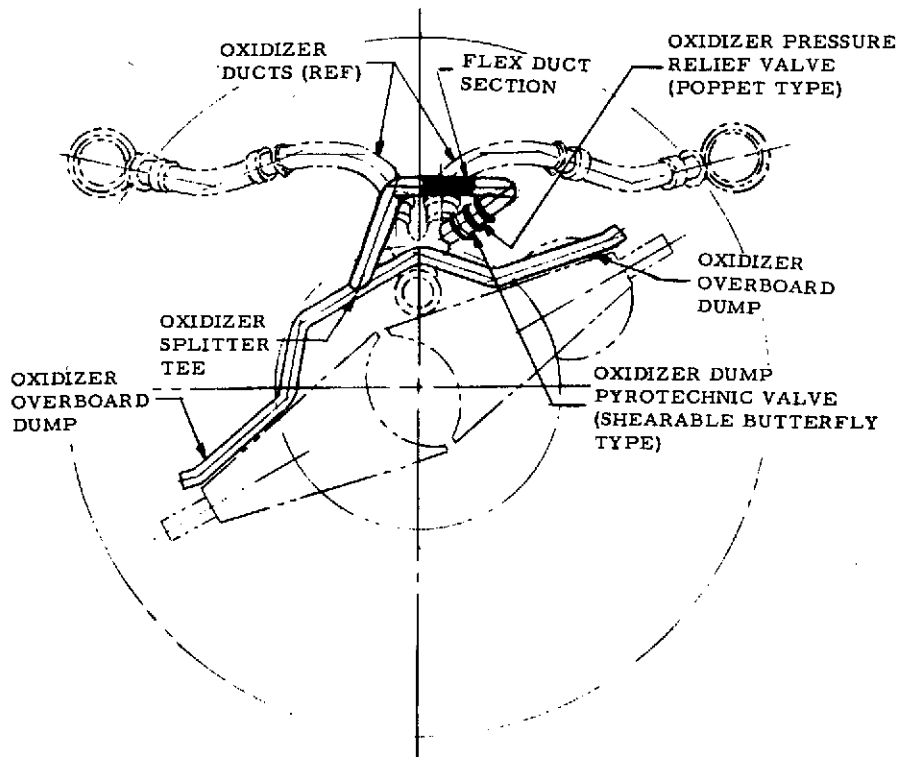


Figure 2-34. LO₂ vent system (looking forward).

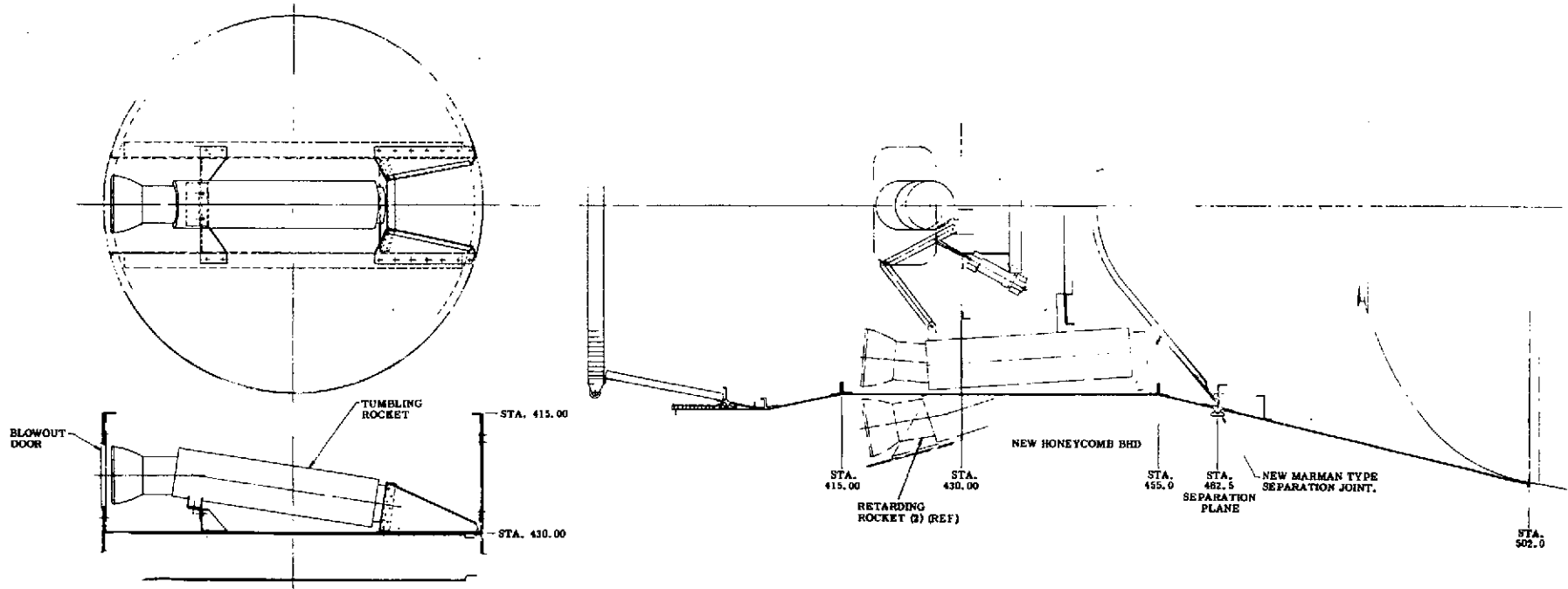


Figure 2-35. Pitch rotation rocket location.

Performance characteristics of the selected pitch rockets are shown in Table 2-5.

Table 2-5. Pitch rocket performance data.

HIRS Retro Rocket	Thor Pitch Rocket
Total impulse = 8610 lb-sec	Total impulse = 1185 lb-sec
Burn time = 3.18 sec	Burn time = 1.385 sec
Average thrust = 2708 lb	Average thrust = 855 lb
Maximum thrust = 4060 lb	

Final angular velocity of the vehicle was calculated using the rocket motor performance data of Table 2-5.

$$\omega = \frac{I_t X_t}{I_{xx}}$$

where

ω = angular velocity, rad/sec

I_t = total impulse of rocket, lb-sec

X_t = moment arm about cg, ft

I_{xx} = total vehicle pitch moment of inertia, slug-ft²

$$\omega = \frac{(8610)(\frac{942-415}{12}) + (1185)(\frac{1198-942}{12})}{130380}$$

$$= 3.09 \text{ rad/sec}$$

$$= 177^\circ/\text{sec}$$

(If a slightly higher impulse is required to account for increased moment of inertia or aerodynamic drag, an additional Thor retrorocket could be installed at Station 1198. Using the baseline vehicle mass properties, this would result in an angular velocity of 3.28 rad/sec (188°/sec). This system would require modification to the present HIRS pitch rocket installation to incorporate provisions for two motors on the Atlas thrust cone.)

Structural modifications required to incorporate the pitch rocket at Station 415 include:

- a. A new frame at Station 415 incorporating provisions for mounting a HIRS retrorocket normal to the vehicle roll axis.

- b. Modifying one of the HIRS adapter access doors below Station 415 to incorporate a cutout and blow-out port cover for the pitch rocket.

2.3.2.3 Aerodynamic Clean-Up of the HIRS Adapter. For the baseline configuration, the payload deployment mechanism and protruding HIRS retrorockets result in a relatively dirty aerodynamic configuration. Since an aerodynamically clean nose section is desirable for the reentry heating experiment, several methods for cleaning up the HIRS adapter area were considered, including reclosing the HIRS retrorocket doors and separating the HIRS/fwd adapters from the Atlas.

2.3.2.3.1 Reclosing HIRS Retrorocket Doors. The mechanism used to extend the HIRS retrorockets into their firing position is presently an irreversible mechanical system. Once the two doors, with the retrorockets attached, are rotated outward into the open position they cannot be reclosed without extensive modification to the present flight-proven system. Due to the requirement for these modifications, separation of the adapters from the Atlas was selected as the most feasible method of providing an aerodynamically clean shape with minimum modifications to existing systems.

2.3.2.3.2 Separating the HIRS/Fwd. Adapters. With this concept, as shown in Figure 2-35, the forward adapters are separated from the Atlas at a new separation joint at Station 462.5. A new fiberglass honeycomb bulkhead is installed on the aft HIRS adapter at that station to provide an aerodynamic fairing for reentry. Primary modifications to the existing HIRS adapter include:

- a. Removal of the thermal bulkhead at Station 455.0.
- b. Addition of a separation joint (Marmon type or shaped charge) at Station 462.5.
- c. Addition of a new fiberglass honeycomb bulkhead at Station 462.5.

Further consideration of modifications for aerodynamic cleanup were dropped, as it became apparent that the cost of such a modification would not be acceptable. Any modification of this area would necessarily involve primary load carrying structure, vital to the primary mission. Extensive (costly) testing would be required to reduce the risk to the primary mission to an acceptable level.

2.3.3 LOADS AND STRUCTURAL ANALYSIS. A preliminary loads and structural analysis of the Atlas F vehicle was performed to assess feasibility of the tumbling reentry maneuver. Loads and vehicle structural capability were evaluated: for the spinup maneuver which accelerates the vehicle to an angular velocity of 180°/sec about the pitch axis shortly after HIRS retrorocket firing; and for tumbling reentry of the Atlas tank to 200,000 ft altitude. Normal structural safety factors were used in the analysis. Where negative margins were indicated, the effects of reduced safety factors were considered.

2.3.3.1 Spinup Maneuver Loads Analysis. This analysis was divided into four parts:

- a. Determination of acceleration limits used for design of the Atlas F booster.
- b. Establishment of axial and lateral accelerations on the vehicle due to the spinup maneuver.
- c. Comparison of the allowable design accelerations with the accelerations produced by the tumble maneuver.
- d. Separate evaluation of major components for which the tumble maneuver accelerations exceed the original design limits.

2.3.3.1.1 Vehicle Design Acceleration Limits. The design limit load factors for the E/F missile are:

<u>Condition</u>	<u>Longitudinal</u>	<u>Lateral</u>
Max Aero Disturbance	+ 2.5 g	± 2.5 g
BECO	+ 10.0 g	± 1.0 g

In addition, light equipment (under 25 lb) is designed to the following vibration criteria:

<u>Area</u>	<u>Acceleration</u>
Nose Adapter	6 g
Tank Section	8 g
Propulsion Section	16 g

These accelerations are applied in any direction.

2.3.3.1.2 Spinup Maneuver Accelerations. The axial acceleration at a point on the vehicle due to a constant angular velocity is:

$$N_{\text{axial}} = \frac{r \omega^2}{g}$$

N_{axial} = axial load factor, g

r = distance from cg, ft

ω = angular velocity, rad/sec

g = 32.2 ft/sec²

for an angular velocity of π rad/sec (180°/sec)

$$N_{\text{axial}} = \frac{\pi^2 r}{g}$$

The lateral acceleration at a point on the vehicle due to the pitch rocket thrust load is:

$$\begin{aligned} N_{\text{lat}} &= N_{\ell \text{ cg}} + N_{\ell \alpha} \\ &= \frac{T}{W} + \frac{T dr}{I_{\text{xx}} g} \end{aligned}$$

where

N_{lat} = lateral load factor, g

T = pitch rocket thrust, lb

W = weight of vehicle, lb

d = pitch rocket moment arm about cg, ft

r = distance from cg, ft

I_{xx} = vehicle moment of inertia about the cg, slug ft²

g = 32.2 ft/sec²

Using the pitch rocket data defined in Table 2-5:

$$\begin{aligned} N_{\text{lat}} &= \frac{4060}{7684} + \frac{(4060)(527) r}{(130380)(12)(32.2)} \\ &= .528 + .0425 r \end{aligned}$$

$$(N_{\text{lat}})_{\text{MAX}} < 2.5$$

2.3.3.1.3 Compare Design and Applied Accelerations. Maximum lateral acceleration occurs at the forward end of the vehicle. At Station 415 the lateral acceleration is 2.4 g, which is less than the maximum design value. Design and applied axial accelerations are compared in Figure 2-36. The axial acceleration due to 180°/sec angular velocity exceeds the design limits only in the forward nose area. The major equipment of concern in this region are the HIRS adapter and the boiloff valve installation.

2.3.3.1.4 Specific Component Evaluation.

a. HIRS Adapter

The HIRS adapter stress analysis (GDA-AQE-64-011) was reviewed for margins of safety which might be critical for the tumble maneuver loads.

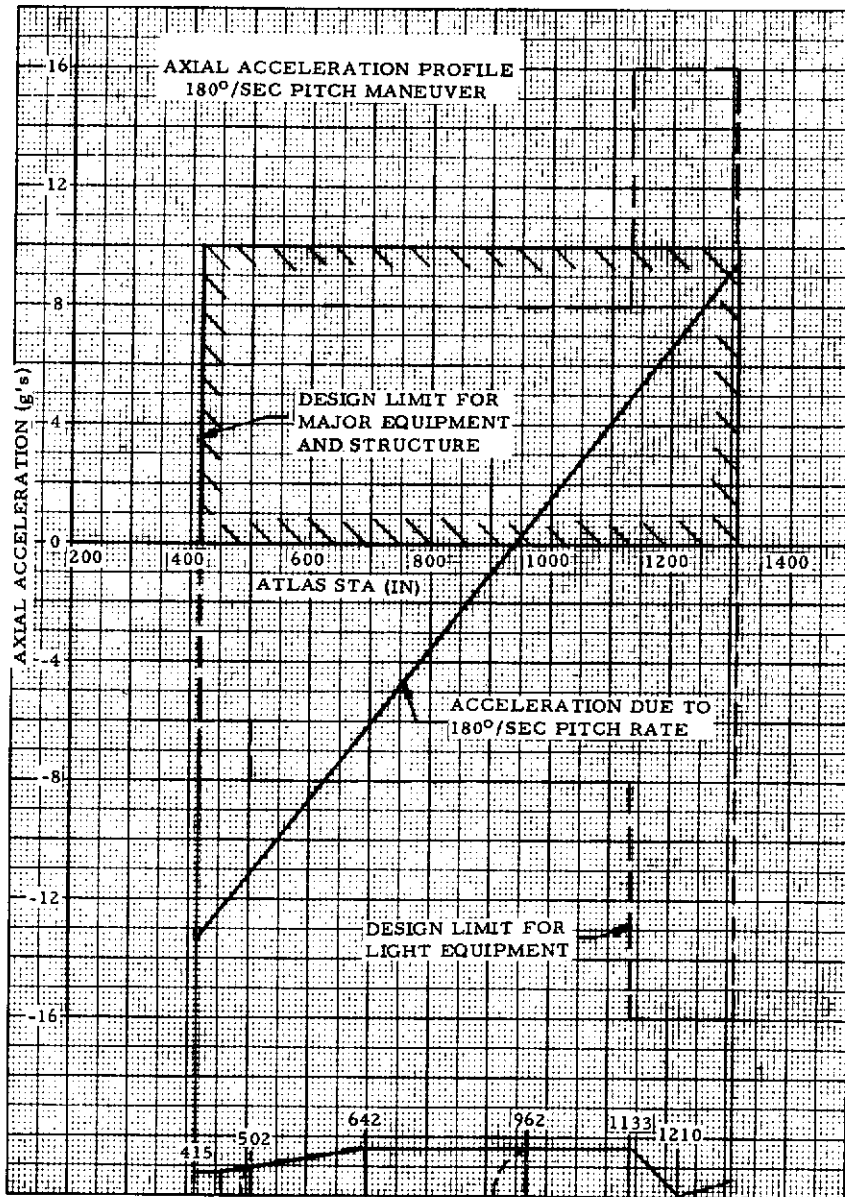


Figure 2-36. Axial acceleration profile 180°/sec pitch maneuver.

The following items, identified as being potentially critical, were evaluated separately and found to have positive margins for the pitch maneuver loads:

- (1) 27-75287-9, Ring Attach Rivets (Station 455)
- (2) 27-75284-53, Channel (Station 430)
- (3) Forward Adapter Access Door Attachments
- (4) 27-75811-7, Aft Adapter Ring Attachments (Station 455)
- (5) Aft Ring to Adapter Attach Rivets (Station 502)

b. Boiloff Valve Installation

A formal stress analysis does not exist for the Atlas F boiloff valve installation. An evaluation of the boiloff valve for the pitch maneuver loads would require a new stress analysis, beyond the scope of this study. An analysis of the boiloff valve installation should therefore be included in any additional studies of the feasibility of this concept.

2.3.3.2 Reentry Loads Analysis. A preliminary loads analysis was performed on the tumbling Atlas vehicle during reentry to 200,000 ft altitude. The analysis consisted of:

- a. Defining LO₂ and fuel tank pressure limits based on estimated maximum skin temperatures.
- b. Determining vehicle overall bending capability.
- c. Establishing maximum aerodynamic and inertia loads on the vehicle during reentry to 200,000 ft.
- d. Comparing overall tank allowable and applied bending loads.
- e. Evaluating local aerodynamic and inertia loads on components.

2.3.3.2.1 LO₂ and Fuel Tank Pressure Limits. Estimated maximum skin temperatures from entry to 200,000 ft are shown in Figure 2-37. These temperatures are maximum stagnation line temperatures, neglecting the effects of vehicle roll. Maximum allowable tank pressures corresponding to these temperatures are shown in Table 2-6. Using a 1.25 ultimate factor of safety, the LO₂ tank pressure is limited to 16.9 psig and the fuel tank pressure to 61.7 psig. The corresponding ultimate (burst) pressure at maximum temperature is 21.1 psig and 77.2 psig for the LO₂ tank and fuel tank respectively.

Since maximum temperature occurs at 200,000 ft, it can be considered an ultimate loading condition. Allowable overall vehicle bending capability was therefore evaluated at a maximum LO₂ relief valve setting corresponding to the ultimate allowable pressure of 21 psig. Assuming a relief valve reseal pressure tolerance of 1.0 psi, the minimum LO₂ tank pressure used for determining overall tank bending capability is 20 psig. Fuel tank bending capability is based on a pressure of 50 psig.

Table 2-6. Allowable tank pressure at temperature.

Tank	Station	Radius	Skin t	Temp	Heat Factor	Weld Factor	Allow Ult Hoop Stress	Allow Pressure
LO ₂ Tank	522.0	39.0	.011	1040	.385	.979	75,383	16.9
	542.0	42.5	.012	980	.485	.977	94,769	21.4
	562.0	46.1	.012	980	.485	.977	94,769	19.7
	582.0	49.7	.013	920	.585	.976	114,192	24.2
	602.0	53.2	.014	870	.675	.974	131,490	27.7
	622.0	56.8	.014	870	.675	.974	131,490	25.9
	642.2F	60.4	.015	820	.750	.972	145,800	28.9
	642.2A	60.4	.022*	600	.875	1.000	131,250	38.2
	667.0	60.0	.014	870	.675	.974	131,490	24.5
	696.1	60.0	.014	870	.675	.974	131,490	24.5
	725.2	60.0	.015	820	.750	.972	145,800	29.1
	754.3	60.0	.015	820	.750	.972	145,800	29.1
	783.4	60.0	.016	800	.770	.970	149,380	31.8
	812.5	60.0	.017	760	.800	.968	154,880	35.0
	841.6	60.0	.018	720	.820	.966	158,424	37.9
	870.7	60.0	.018	720	.820	.966	158,424	37.9
	899.8	60.0	.019	700	.830	.964	160,024	40.4
	928.9	60.0	.020	660	.850	.962	163,540	43.5
960.0	60.0	.023	580	.880	.957	168,432	51.5	
Fuel Tank	992.5	60.0	.027	500	.905	.949	171,769	61.7
	1025.0	60.0	.027	500	.905	.949	171,769	61.7
	1057.5	60.0	.028	480	.910	.947	172,354	64.3
	1090.0	60.0	.029	460	.915	.945	172,935	66.8
	1122.5	60.0	.030	450	.920	.943	173,512	69.4
	1133.0F	60.0	.035	400	.935	.934	176,341	81.4
	1133.0A	60.0	.028**	480	.910	1.000	153,790	114.8
	1160.5F	49.5	.028**	480	.910	1.000	153,790	98.3
	1160.5A	49.5	.038	380	.940	.929	174,652	92.4
	1175.7A	32.7	.025	540	.895	.953	170,587	73.5

*Denotes 1/2 H 301 CRES

**Denotes 3/4 H 301 CRES

NOTE: Allowable pressure is based on a 1.25 ult factor of safety.

2.3.3.2.2 Overall Vehicle Bending Capability. Overall bending capability of the Atlas F propellant tanks at maximum temperature is shown in Figure 2-38. In addition to LO₂ and fuel tank allowables based on standard Atlas post-buckling criteria and an ultimate factor of safety of 1.25, LO₂ tank allowables were calculated based on allowing post-buckling of all skins at limit applied load. These latter allowables are compatible with the "ultimate" type loading experienced by the vehicle during reentry to 200,000 ft.

2.3.3.2.3 Aerodynamic and Inertia Loads. Two configurations were considered when evaluating aerodynamic and inertia loads during reentry: the baseline configuration, with HIRS and payload adapters attached; and the alternate configuration, with payload and forward HIRS adapters separated from the vehicle. Mass properties are summarized below:

<u>Configuration</u>	<u>Weight</u> (lb)	<u>cg</u> (in.)	<u>I_{xx}</u> (slug ft ²)
Baseline	7684	942.1	130,380
W/O Adapters	6712	1000.3	77,380

A preliminary evaluation of angle of attack effects indicated maximum vehicle loads occur at a relative angle of attack near 90°.

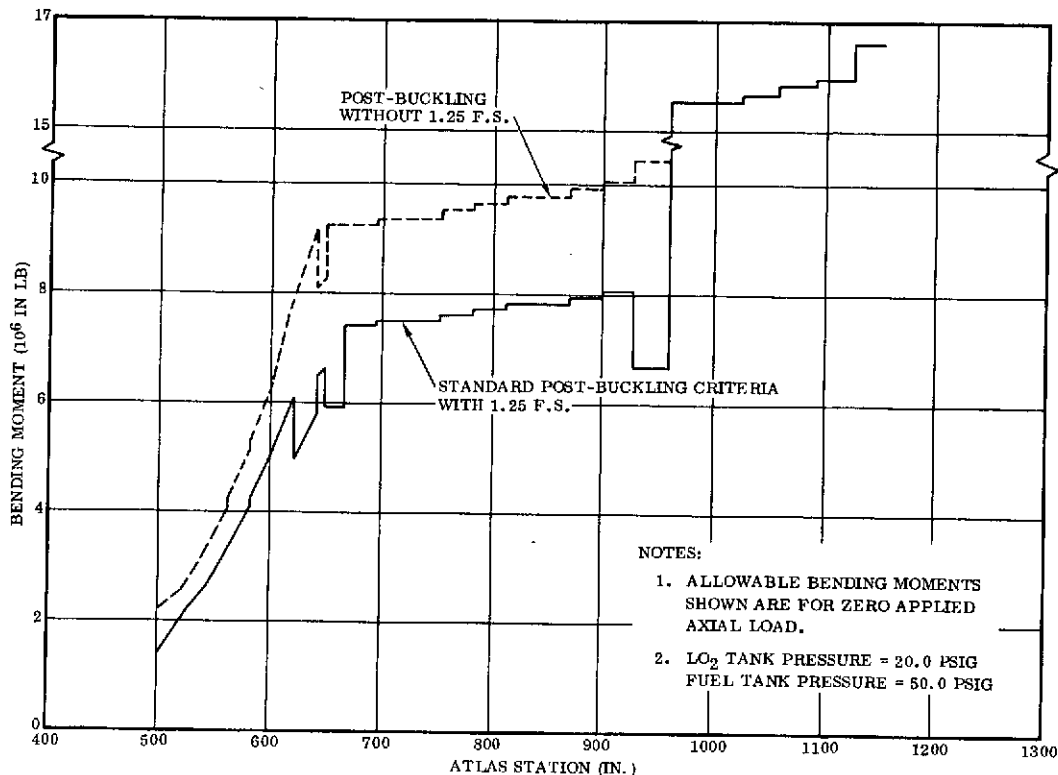


Figure 2-38. Atlas F propellant tank limit allowable bending moments at max temperature.

Aerodynamic data shown in Figure 2-3 were used to calculate total normal aerodynamic loads in the pitch plane at 200,000 ft altitude and $\alpha = 90^\circ$.

C. P. at Station 860

CN = 10.3

$q = 160 \text{ lb/ft}^2$

Normal aero force

$$\begin{aligned} N &= CN q A_{REF} \quad (A_{REF} 78.5 \text{ ft}^2) \\ &= (10.3)(160)(78.5) \\ &= 129368 \text{ lb} \end{aligned}$$

Aero moment about the cg.

$$\begin{aligned} M_{942.1} &= (129368)(942.1 - 860) = 10.621 \times 10^6 \text{ in. lb (baseline)} \\ M_{1000.3} &= (129368)(1000.3 - 860) = 18.150 \times 10^6 \text{ in. lb (W/O adapters)} \end{aligned}$$

Using these total aerodynamic loads and assuming the normal aero coefficient distribution at high angle of attack is proportional to the projected area of the vehicle, an approximate normal force distribution was developed and integrated along the vehicle to obtain the aerodynamic bending moment distribution shown in Figure 2-39.

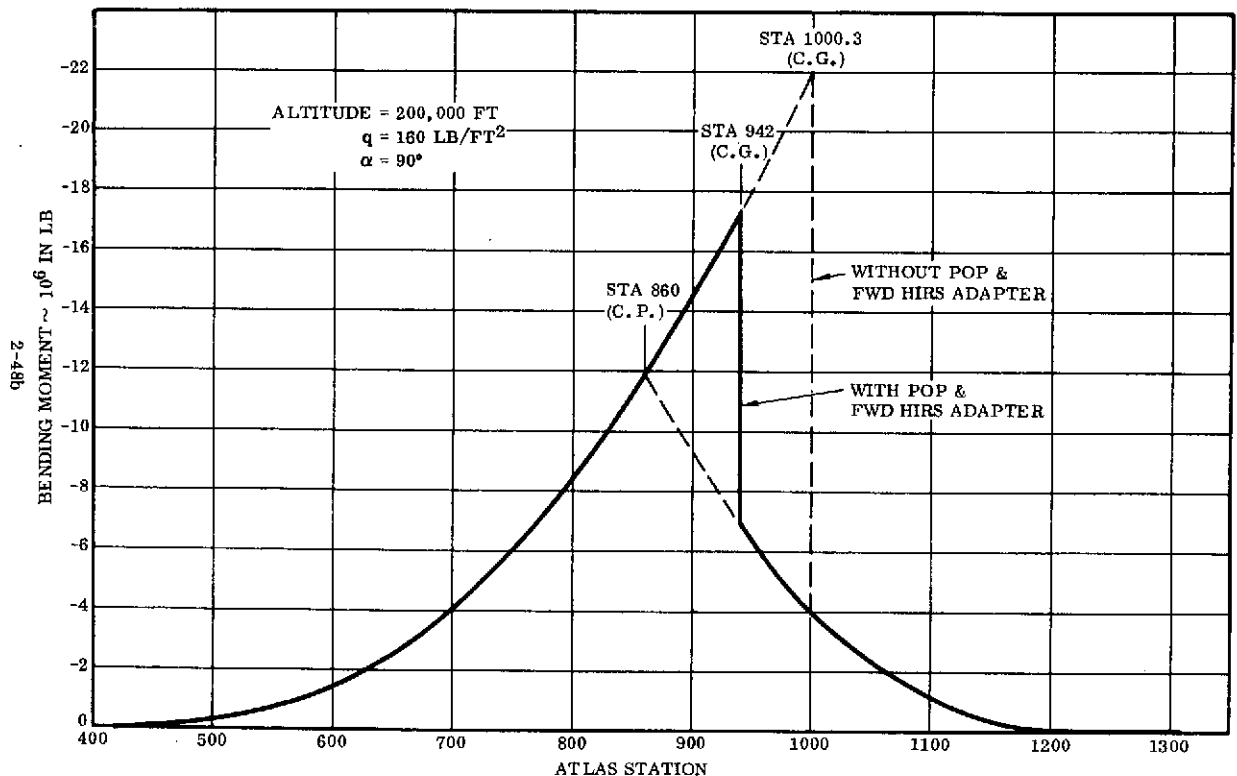


Figure 2-39. Aerodynamic bending moment on tumbling Atlas F (tumbling in pitch plane).

2.3.3.2.3.1 Aerodynamic Axial Force. The axial force coefficient, C_A , varies sharply with α near 90° , and since C_A is a minimum at $\alpha = 90^\circ$, C_A for $\alpha = 80^\circ$ was conservatively used to calculate the total aerodynamic axial force on the vehicle.

At 200,000 ft altitude:

$$A = C_A q A_{REF}$$

$$= (.40)(160)(78.5) = 5020 \text{ lb}$$

2.3.3.2.3.2 Inertia Loads. The applied aerodynamic loads are balanced by the vehicle inertias and accelerations listed below:

Configuration	Mass Properties		Aero Loads			Acceleration (at cg)		
	Wt (lb)	I_{xx} (slug-ft ²)	Lateral (lb)	Axial (lb)	Moment (in. lb)	Lateral (g)	Axial (g)	Pitch (rad/sec ²)
Baseline	7684	130380	129368	5020	10.621×10^6	16.8	.65	6.79
W/O Adapters	6712	77380	129368	5020	18.150×10^6	19.2	.75	19.54

Total lateral acceleration along the vehicle including effects of the pitch acceleration is plotted in Figure 2-40.

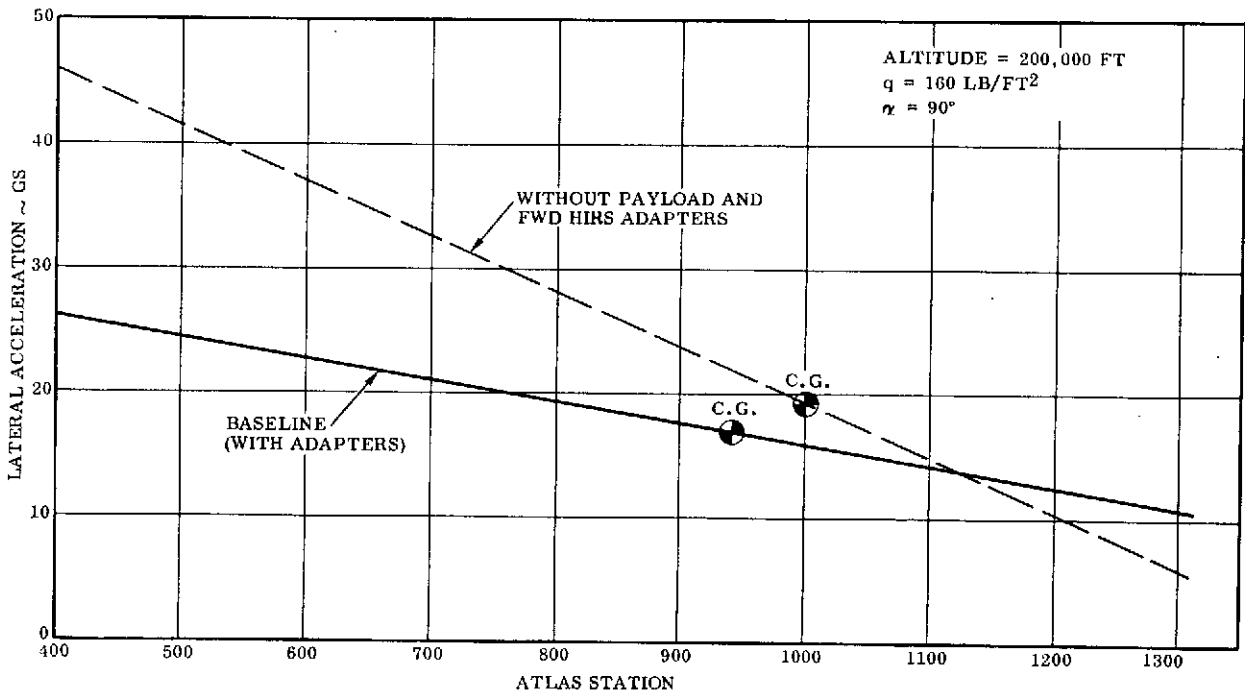


Figure 2-40. Lateral acceleration on tumbling Atlas (tumbling in pitch plane).

Mass distribution for the baseline vehicle is shown in Figure 2-41. The inertia bending moment distribution for the baseline vehicle, shown in Figure 2-42, was obtained by integrating this mass distribution with the lateral acceleration profile of Figure 2-40 along the vehicle. For the configuration without adapters, a total of 738 pounds was removed forward of Station 455.

The total net bending moment in the tank structure is the sum of the applied aerodynamic loading and the balancing inertia forces. These total net bending moments are shown in Figure 2-43. It is interesting to note that removal of the forward HIRS and payload adapter mass significantly reduces total vehicle bending. The heavy mass items are concentrated at the ends of the vehicle whereas the distributed aerodynamic forces are a maximum near the vehicle cg. The resulting inertia bending forces predominate and tend to be relieved by the aero loading. Removal of the 738-lb adapter mass at the nose of the vehicle tends to balance the inertia and aero distributions more closely, thus reducing total net bending moment.

2.3.3.2.3.3 Inertia Axial Loading. Vehicle axial accelerations are produced by aerodynamic axial forces acting on the vehicle and the high (180°/sec) pitch rates experienced during the tumble maneuver.

Total combined aerodynamic and inertia axial force distribution for the baseline vehicle is plotted in Figure 2-44.

2.3.3.2.4 Applied and Allowable Load Comparison. Applied and allowable bending moments are compared in Figure 2-45. The allowable bending moments conservatively neglect the effects of the applied axial tension loading shown in Figure 2-44. This conservatism increases the allowable bending moments 5 to 15% over the values shown in Figure 2-45. With post-buckling of the forward LO₂ tank skins, the Atlas F structure will support the maximum bending moments calculated during tumbling reentry to 200,000 ft. If the payload and forward HIRS adapters are removed to provide a clean reentry shape, the overall bending of the Atlas tank is reduced by approximately one half.

2.3.3.2.5 Component Loading Analysis. Local component loads result from the high axial and lateral accelerations and from the aerodynamic loads on fairing surfaces during reentry. Maximum axial accelerations are plotted in Figure 2-36 and maximum lateral accelerations are plotted in Figure 2-40. Transient lateral accelerations approaching 20 g at the vehicle cg and in excess of 40 g at the nose can be experienced during reentry at 200,000 ft and an angle-of-attack near 90°. Maximum axial acceleration at the nose exceeds 11 g. Design limit load factors at maximum aerodynamic disturbance are +2.5g for longitudinal and ±1.0g for lateral. The corresponding values at BECO are +10.0g and ±1.0g respectively. Vibration criteria for lightweight equipment (under 25 pounds) is acceleration in any direction of 6g in the nose adapter area, 8g in the tank section, and 16g in the propulsion section.

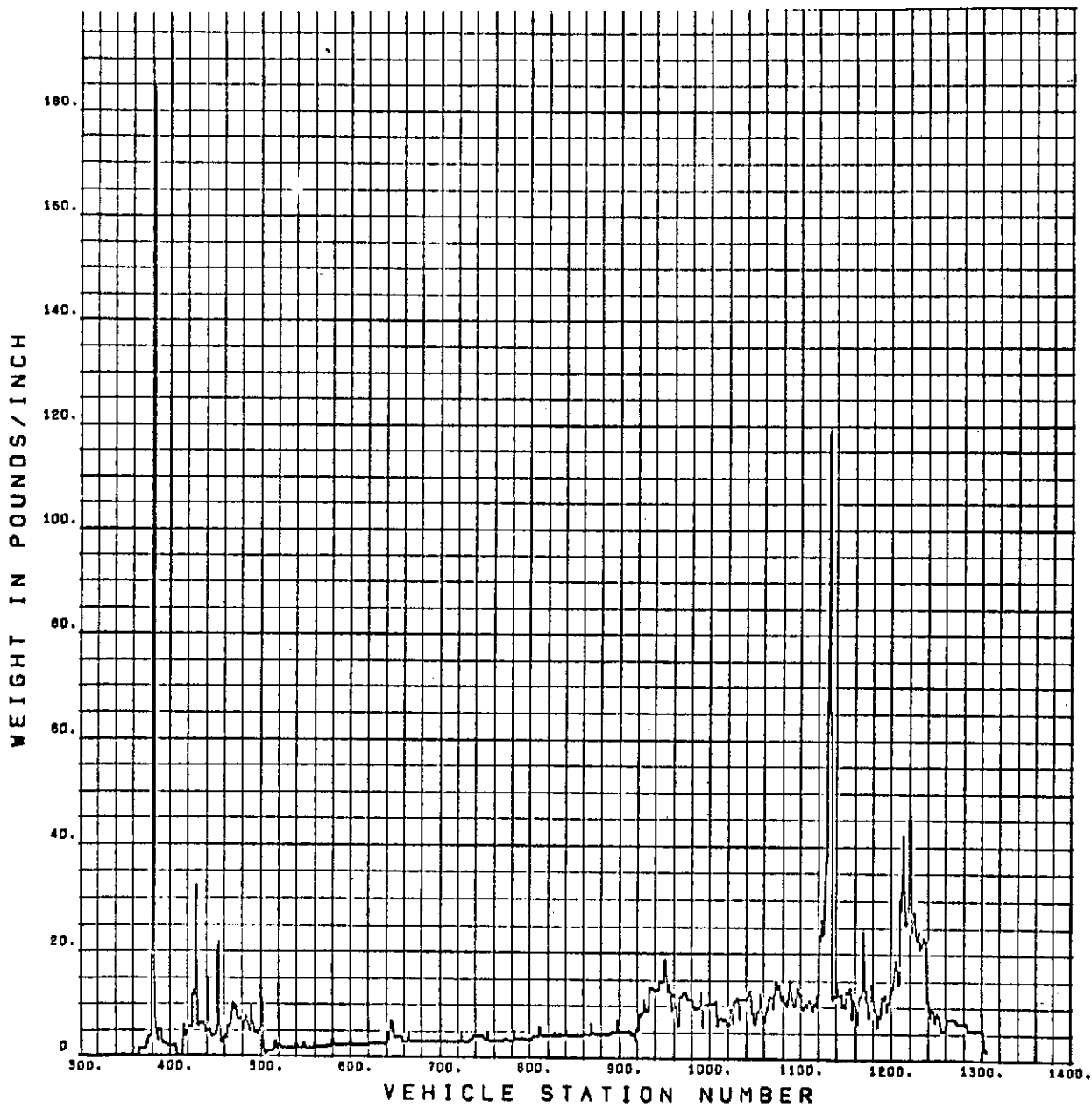


Figure 2-41. Atlas F mass distribution - Total wt = 7684 lb, cg = Sta. 942.1.

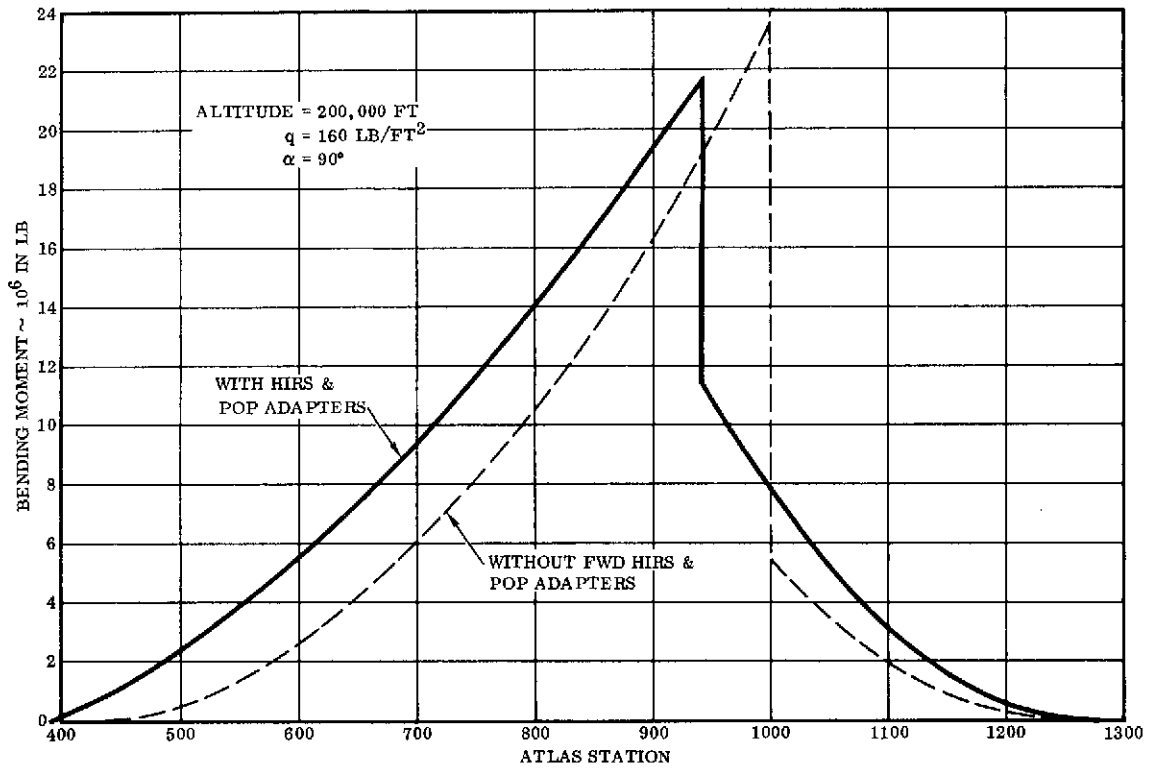


Figure 2-42. Inertia bending moment on tumbling Atlas F (tumbling in pitch plane).

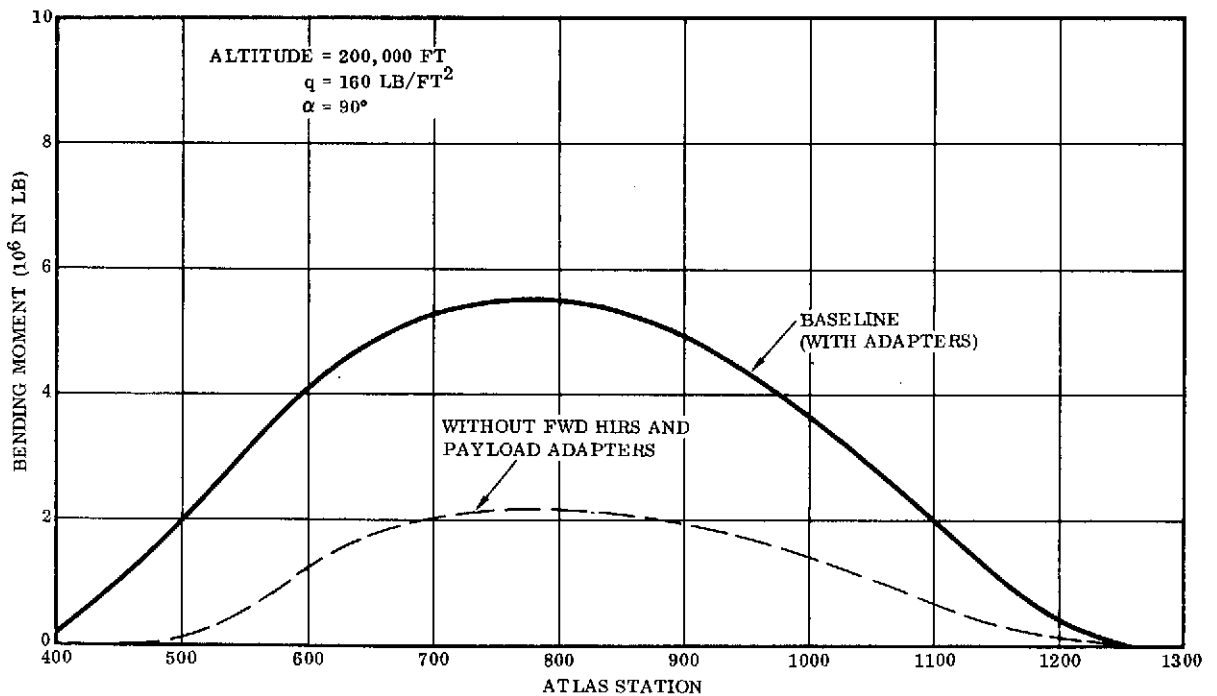


Figure 2-43. Net bending moment on tumbling Atlas F tank.

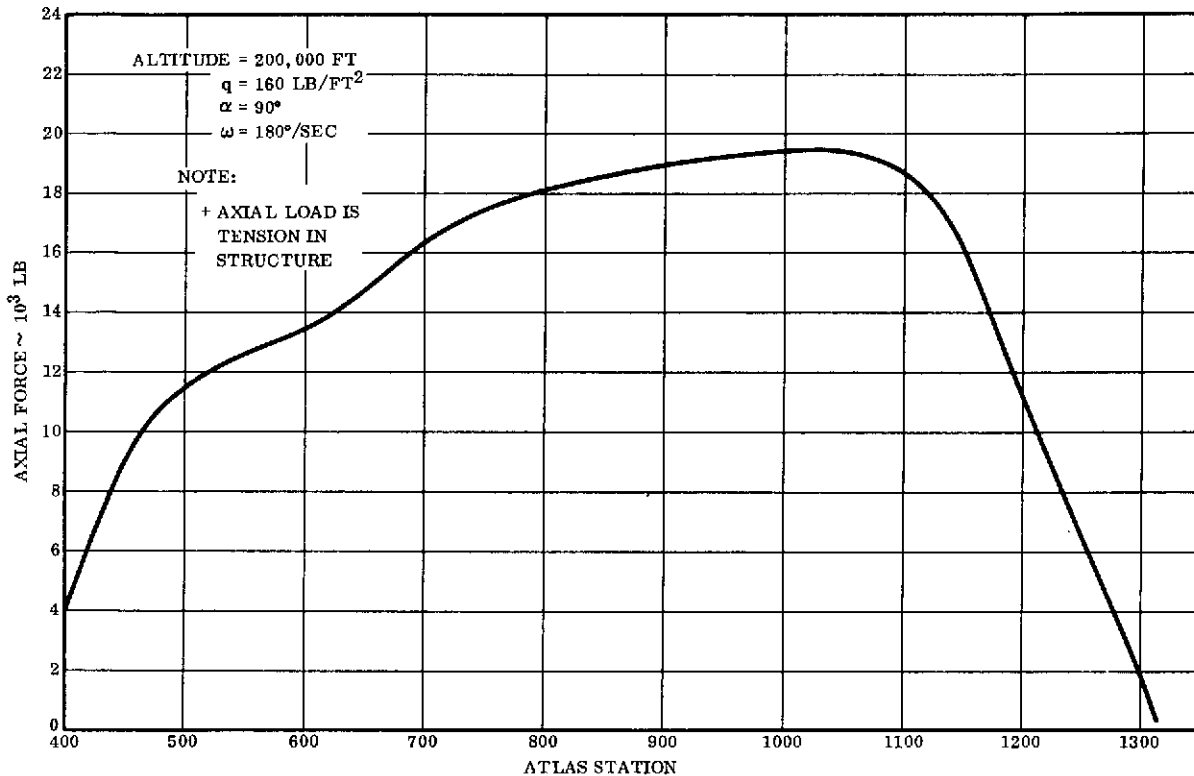


Figure 2-44. Axial force distribution tumbling Atlas F.

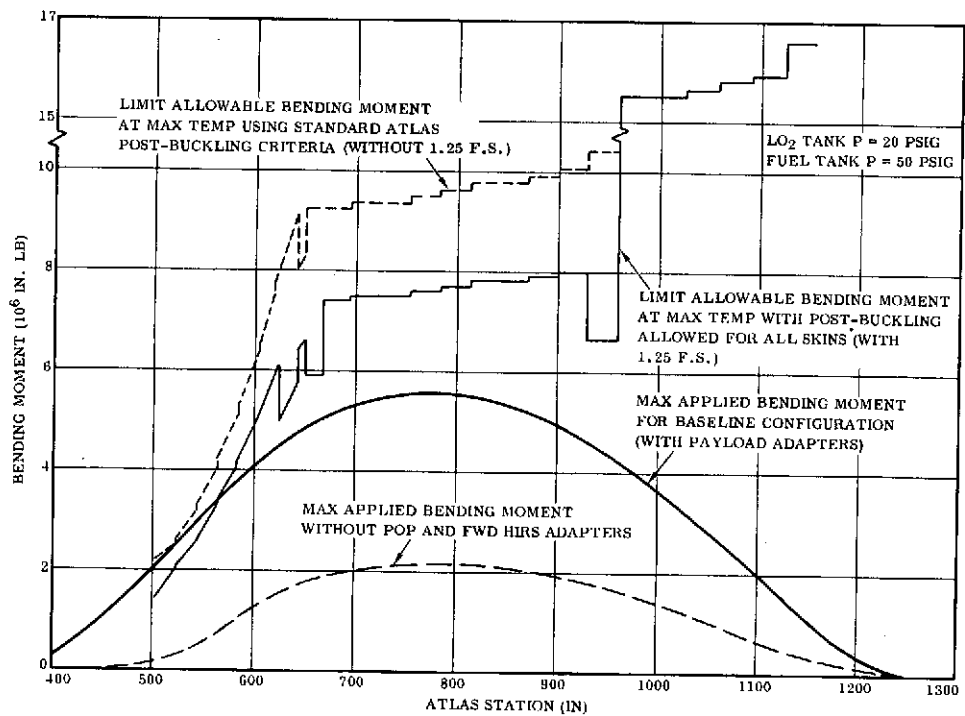


Figure 2-45. Atlas F tumbling reentry bending moment distribution.

The applied accelerations exceed the design limits for essentially all components and their attachments by a large factor. Some type of an ultimate analysis would thus have to be performed on each component and attachment to insure its structural integrity for these high load factors. A study of this type was beyond the scope of this study. Two alternative approaches were therefore considered:

- a. Identify major components and their attachments, whose structural failure could destroy the LO₂ or fuel tank structural integrity. Using engineering judgement based on experience with the Atlas, provide an "educated guess" as to whether the components would survive the reentry environment. Critical components identified include:
 - (1) Boiloff valve installation
 - (2) LO₂ feed ducts
 - (3) LO₂ tank baffles
 - (4) Vernier engine installation
 - (5) Helium bottle installation
 - (6) Sustainer engine installation
 - (7) LO₂ start bottle installation
 - (8) Fuel start bottle installation

Preliminary estimates of the survivability of these components and attachments are that, although yielding and large deformations may occur in the support structure, there is a good probability that the components or mounts would not fail in a manner which would destroy the vehicle at an altitude higher than 200,000 feet. A new analysis would be required to verify the structural integrity of these components because the existing formal design criteria (e.g., 2.5 g lateral) and structural analysis is based on the normal launch ascent model (mission). For this, most of the above components are filled with propellants or fluids, pressurized to powered flight levels, or are otherwise being operated under different conditions than exist during the coast and entry mode of significance here. As a result, the allowable load factors for the entry mode are appreciably higher than would be inferred from the existing design criteria.

- b. The second approach is to make the conservative assumption that the component and/or attachment will fail at the ultimate load factor contained in the existing criteria, and determine at what altitude this condition is encountered.

Considering that most of the components (except the boiloff valve) are mounted aft of Station 942, and applying this reasoning:

$$\text{Ultimate load factor} = 1.25 \times 2.5 = 3.1 \text{ g}$$

Lateral acceleration = 3.1 (shown in Figure 2-46)

Altitude = 240,000 feet (Station 942)

Using a similar approach, and considering lightweight components (less than 25 pounds) mounted on the tank, the onset of ultimate loading would occur at approximately 215,000 feet. This approach tends to confirm the "educated guess" that the vehicle will maintain structural integrity during reentry through most, if not all, of the 300,000 to 200,000 foot altitude range of interest in the experiment.

A detailed analysis of aerodynamic loads on the pods and fairings at the high angles of attack experienced during reentry also was beyond the scope of this study. However, it is felt that, due to the low q (approximately 160 lb/ft^2) experienced during reentry to 200,000 ft, maximum local aerodynamic loads should not exceed those during boost when maximum q is approximately $1,000 \text{ lb/ft}^2$.

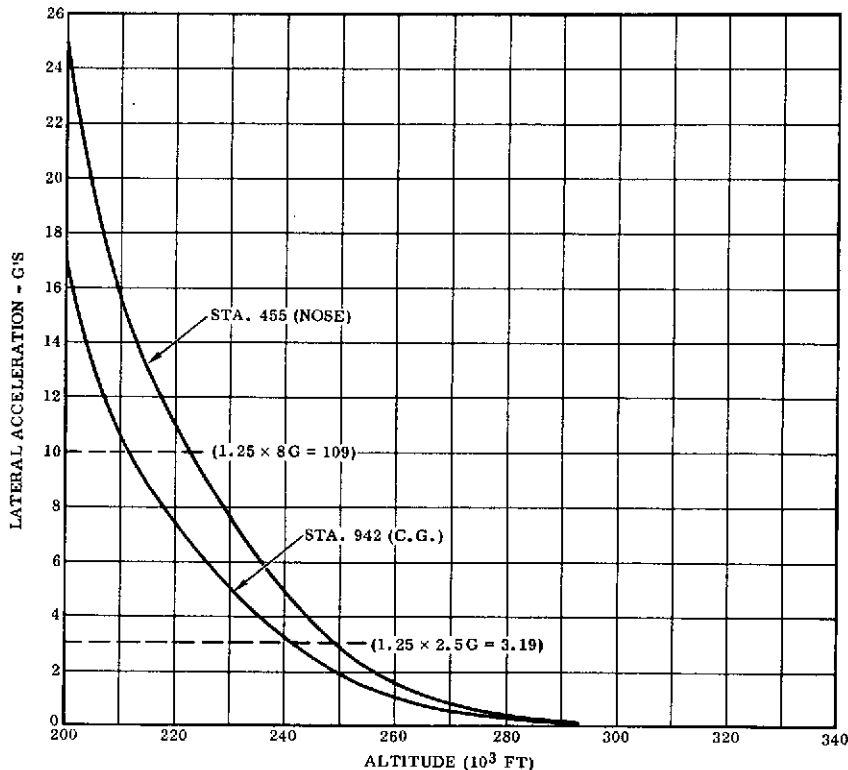


Figure 2-46. Atlas F tumbling reentry variation of maximum lateral acceleration with altitude.

2.4 HEATING RATE SENSORS

2.4.1 INTRODUCTION. One of the more difficult problems in obtaining useful heat transfer data from a tumbling Atlas sustainer tank during reentry is the definition of heating rate sensors suitable for this application. This part of the study was undertaken to define the heating rate sensor physical characteristics, and to present heating rate sensor response to an anticipated typical reentry heating environment between the altitudes of 300,000 to about 200,000 feet. The assumption that the Atlas is tumbling in pitch only, without roll or yaw, presents the most severe conditions with respect to rate of change of a local surface heating rate. Hence, a heating rate sensor that can meet the more difficult requirements of pitch-only tumbling will also meet entry conditions where pitch, roll, and yaw are simultaneously present. The figures and tables pertaining to this discussion are presented in a group following the text at the end of this subsection (2.4).

2.4.2 ANALYTIC MODEL. Typical reentry trajectory parameters for an ABRES tank are presented in Figures 2-10 and 2-11. The altitude range of maximum interest, 300,000 to 200,000 feet is traversed in only 8.9 seconds. To obtain a maximum of heat transfer data, the Atlas is assumed to be tumbling at 180° per second. About 4.5 revolutions are completed in this time period.

Heating rates vary widely during each revolution. To permit estimation of anticipated heating rates during entry, the Atlas was assumed to be a long cylinder. A point was selected midway on the bottom centerline on the cylinder for positive angles of attack to 90°, for yaw = 0°, and roll = 0°. A representative heating rate ratio was evolved for pitch angles of 0° through 360°, using the experimental data of Beckwith and Gallaher, Reference 6, as a basis. Heating rate values to stagnation heating rate (90° pitch, $\alpha = 90^\circ$) employed for this study appear in Figure 2-47. Heating rate ratios are symmetrical about $\alpha = 90^\circ$ for $\pm 90^\circ$, and about $\alpha = 270^\circ$ for $\pm 90^\circ$. This appears reasonable as the point selected, midway along the cylinder, results in the same boundary layer run distance from a leading edge.

Also shown in Figure 2-47 is a computer model representation of the heating rate ratio curve. During computer runs, linear interpolation is used between designated points. The designated points for the computer model appear in Table 2-7 for 360 degrees of positive pitch.

As the pitch condition without yaw or roll changes represents the widest excursions of heating rates expected during an Atlas entry, reference heating rates were determined for a mid-station location for an ABRES tank trajectory. Aerodynamic/Structural Heating Computer Program P5613, Reference 7, was used to generate the basic heating rates between 0° and 80° angle of attack. The 90° angle of attack heating rate was extrapolated using the experimental data representation in Figure 2-47.

The calculation results appear in Figure 2-48, in which cold wall heat flux, \dot{q}_0 , is shown as a function of entry altitude for three angles of attack.

To ascertain the response of selected heating rate sensors to the entry environment, cold wall heat flux was determined for subsequent computer usage as a function of entry time. Entry time was assumed to start at 300,000-ft altitude. The resulting heat flux values appear in Table 2-8.

A plot of the computer model cold wall heat flux as a function of entry time appears in Figure 2-49. The most extreme heating rate gradients are about 100 Btu/ft²-sec per second for increasing heat flux, and about 105 Btu/ft²-sec per second for decreasing heat flux.

Various sensors were considered within the constraints of installation limitation on an Atlas tank. Such limitations include a prohibition on installation in the tanks of instrumentation units that have not been thoroughly flight qualified through extensive ground testing. Fully qualified hardware would minimize risk to the primary mission payload. Since no heating rate sensor hardware has been qualified for Atlas tank interior installation, all sensors and instrumentation leads must be externally mounted on the tanks.

Another limitation on externally mounted sensors is that their attachment use the same spot welding techniques employed to assemble the tanks. The attachment plate (sensor skin) thickness must be no greater than equal to and preferably be less than the parent skin thickness of the Atlas tank. The attachment plate material is to be the same as the tank material, 301 type stainless steel. The attachment method should permit the attainment of the full tensile strength of the basic tank material to which it is mounted. This provides assurance that potential failures due to stress would occur in the sensors and not in the Atlas tank. Instrumentation lines are stainless steel sheathed leads whose outside diameter is 0.062 inch or less. These leads are attached to the tank by thin 0.003-inch 301 stainless steel clips that are microspot-welded to the tank exterior. The instrumentation lines are in the sheathed leads and are electrically insulated by a packed ceramic powder. Ends of the sheathed leads are sealed by a silicon compound to provide a moisture barrier.

Extensive experience has been gained during Atlas flights in which tank skin temperatures were measured by Chromel-Constantan grounded junction thermocouples. Each of the 0.010-inch diameter thermocouples wires is microspot-welded to the tank about 0.050 inch apart. The wires then enter a common stainless steel sheathed lead. The route of the sheathed lead immediately after the thermocouple junction on the tank is aft, to minimize aerothermodynamic disturbance. The low level dc voltage from the thermocouple is amplified, and signals from several thermocouples (or other units) are commutated to give a sampling rate of 5 to 30 per second before transmission by the telemetry system to ground or ship stations.

Considering the known limitations and also the extensive flight experience with thermocouple systems, a suitable heat transfer rate sensing device that would utilize thermocouples was sought. The selected sensor devices were then modeled as a

transient heat conduction problem with variable boundary conditions for running in computer program P5121. Program P5121 consists of a standard Convair computer program P2162 (Reference 8) modified to accept an arbitrary heat flux input table containing up to 40 entries. A schematic of the generalized computer model appears in Figure 2-50.

In Figure 2-50, the element shown as "gage" is the outermost surface of the sensor. The cold wall heat flux, q_0 , is applied to the outermost surface of the gage. The 1.25-inch dimension is used to minimize lateral heat conduction edge effects during the 9-second entry period. The sensor skin is the inner surface of the heat sensor. The recess shown at the bottom of the sensor skin provides thermal isolation (air gap) from the Atlas skin when the sensor is welded as a unit to the Atlas tank. A spacer between the gage and the skin completes the generalized model. In the computer model, node elements denoted as A through F, were used. Contact resistances between nodes was assumed to be zero. Heat transfer by radiation to environment, to the tank interior, and between gage and skin were defined by surface emissivity ϵ , as noted, and by temperature levels. A heat transfer coefficient to the inner surface of the sensor skin was employed in some cases where the appropriate fluid temperature was 500°R. These cases provided computer simulation where the sensor skin is also the Atlas tank skin.

A total of 44 different heating rate sensors that would employ thermocouples to determine transient temperatures of selected regions of the sensor were run, using computer program P5121. The specific items included in each sensor model are detailed in Table 2-9. Listing of a given node as zero thickness denotes that this node is not employed in the computer program except for its infinite thermal conductivity. No gap is assumed or implied. However, a gap, when used between nodes, has dimensions as tabulated and also an effective thermal conductivity of zero. Heat transfer may occur only by radiation across an internodal gap.

Properties for transient heat conduction are listed in Table 2-10 for each material specified by number in Table 2-9. The 0.020-inch thick spacer material (see Figure 2-50 and Table 2-9) may be any of the following: a honeycomb; vertically oriented and uniformly spaced thin wafers; small diameter, uniformly spaced wires as columns; or a porous matrix, to give the appropriate density noted in Table 2-10. Thus, a 10% density spacer means that 10% of the volume of the spacer is solid material and that the spacer has a thermal conductivity between sensor gage and skin that is 10% of a solid spacer. The basic material of the spacer was always 301 stainless steel in the computer model.

In the computer runs, an initial temperature of 500°R (40°F) was assumed for all elements of the sensor at the start of entry. This value represents an average temperature that may be expected following the fairly long suborbital flight. Temperatures of the computer nodes are those corresponding to a one-dimensional analysis through the thickness of the heating rate sensor. The maximum calculation interval was 0.05 second. When the temperature rise of a node exceeded 5°F during a calculation interval,

the interval was automatically shortened and the calculation repeated in the computer program. The minimum calculation interval required was 0.000118 second. Computed temperatures to 0.01°F were printed out for each 0.10 second of the entry time period. Results of the P5121 computer analysis for model listed in Table 2-9 for 180 degrees per second pitch rate appear in Figures 2-51 through 2-94.

2.4.3 RESULTS. Figures 2-51 through 2-94 present plots of computer nodes A and F temperatures as a function of entry time. Figure 2-51 (Model 1) through Figure 2-67 (Model 17) results are for a thermally isolated outer plate (gage), a gap, and an inner sensor skin. Various gage thickness, various radiation exchanges to the environment, and radiation exchange between nodes were employed. No thermal conductivity path was provided between the A node and the F node (see Figure 2-50). The result showed that radiation exchange between nodes had no significance over the entry period of 10 seconds (extended beyond the required range by 1.1 seconds). Therefore, special high emissivity coatings on the interior of such a sensor have no value for this short duration application.

Radiation to the environment from node A becomes important only when node A temperature exceeds about 1000°F. But to attain temperatures above 1000°F where environmental radiation can be useful for cooling requires a gage thickness of about one mil (0.001 inch) for this entry trajectory. As seen in Figure 2-59 (Model 9), however, environmental radiation will not cool a one mil gage rapidly enough to follow the steep descent in heat flux rate curves. Thus, sensors cooled by radiation are inadequate because: (a) very high operating temperatures are required to sense rapid decreases in heat flux rate; and (b) the physical thickness of the gage precludes a practical installation from the standpoint of temperature measurement and general handling on the vehicle.

Thicker gages offer advantages, in that outer surface temperatures can be held to more reasonable levels (about 1000°F maximum). Such sensors are practical to instrument and for general handling. Where radiation heat loss is not significant, as in Figure 2-51 (Model 1), the gage temperature represents a cumulation of heat input. Since the density and heat capacity of the gage are known, slope of the temperature time curve can theoretically give the heating rate as a function of time. Unfortunately, this method tends to break down when sudden excursions to low rates of heat flux occur, as the basic telemetered data is not sufficiently accurate. This arises because the basic telemetry system has a specification accuracy, end to end, of $\pm 5\%$ (node temperature, to thermocouple, to reference junction temperature, to amplifier, to radio frequency link, to receiver, to recording, to decoding, to readout). Where adequate preflight calibrations can be made, accuracies to $\pm 2\%$ have been observed. Scattering of temperature data points as received would severely hamper the single element calorimeter type gage for this Atlas entry heat sensor application, as slope measurement errors will exceed temperature readout errors.

Since the basic problem in making suitable sensors was associated with the ability to cool the gage element rapidly, another sensor construction was investigated. In this alternate sensor type, a conduction heat path between the gage and the sensor skin (called a spacer) was provided. The 0.020-inch-thick spacer (except for Model 28 which was 0.004 inch thick), provided a controlled heat leak through variation in installed configuration spacer density of 301 stainless steel material. Figure 2-68 (Model 18) through Figure 2-78 (Model 28) present the computer results for gage-spacer-skin configurations with external radiation from Node A to the environment (surface emissivity, ϵ , = 0.90). The designation, RHO = 485 on the curve heading signifies 100% density 301 stainless steel (485 lbm/ft³) spacer. In the same manner RHO = 48.5 is a 10% density spacer and RHO = 4.8 is 1% density spacer. The figures give temperatures versus entry time for computer Node A and F.

Examination of the basic curve plots does not, at first glance, show the admirable characteristics of this type sensor. However, a differential temperature plot, Node A minus Node F temperature, is immediately significant. Figure 2-95 presents the heating rate sensor ΔT and cold wall heat flux input versus entry heating time for Model 21 (see Figure 2-71 also). It is immediately apparent that heating rate sensor ΔT provides a fairly good representation of heat flux input. Lagging phase shift from the input is noted, ranging from about 0.05 second in the valleys just prior to increased heat flux levels to about 0.20 second at peak values of heat flux. The time constant for the gage-heat leak spacer causes additional time shift on descending heating rate to valley levels.

Figure 2-96 shows the computer output for Model 23, which differed from Model 21 only in the sensor gage thickness. In Model 23, the gage was 4 mils thick and in Model 21 the gage was 8 mils thick. The obvious effect in decreasing gage thickness is to reduce the time phase shifts in direct proportion.

Figure 2-97 presents Model 28 performance, in which the thickness of the spacer was greatly reduced from 20 mils to 4 mils. The spacer material was 1% density 301 stainless steel. The results show that the time phase shift is primarily dependent upon the magnitude of the heat leak rather than upon the total mass of the spacer element. Excellent agreement between input heat flux and heat sensor ΔT output is apparent, thus presenting evidence that only a minimum processing of flight data will be required when using this type sensor.

Models 18 through 28 used radiation interchange between nodes and also radiation to the environment. As it was suspected that radiation introduced added complexities without real merit as a minor cooling method, a new series of computer runs was made without radiation cooling. Figure 2-98 presents heating rate sensor ΔT without radiation cooling, and cold wall heat flux input versus entry time for Model 34. (The basic temperature plots for Nodes A and F appear in Figure 2-84 for Model 34.) Figure 2-98, for no radiation, may be compared with Figure 2-95, with radiation. Dropping the radiation factors does not upset the heat balance relationship significantly. Radiation

may be ignored when the maximum heating rate sensor temperature is below 1000°F and emissivity of the sensor elements is below about 0.25. The 301 stainless steel skin on the Atlas has an emissivity of about 0.15.

Another conclusion was also reached through analysis of the computer runs. A complex computer model is not required. Three computer nodes are fully adequate to represent the gage, spacer, and sensor skin. The advantage of the simpler model is the greatly reduced computer run time required to reduce flight data taken with this type heating rate sensor.

To permit a closer selection of sensor element size and characteristics, a composite result of all the computer runs was prepared for the 180-degree pitch rate entry. Figure 2-99(a) presents the maximum sensor temperature attained during entry versus gage thickness. As expected, the single thickness element sensor (isolated gage) forms a single line curve. The multiple element sensors form multiple curves depending upon the internal configuration. All multiple element sensors fall within an acceptable range of maximum temperatures. Figure 2-99(b) shows plots of heat sensor maximum ΔT versus sensor skin thickness for various configurations. The lower density spacer gives the greatest ΔT between computer Nodes A and F. Also, increasing sensor skin thickness increased the maximum ΔT . Increased ΔT is advantageous to the telemetry system, as a higher thermocouple voltage is available. However, increased sensor skin thickness adds to the protuberance from the Atlas tank skin, tending to mask the basic data sought.

A more detailed examination of the heating rate sensor response to the maximum heat input rate decrease expected for Atlas entry will aid in selection of the more optimum sensor characteristics. This particular entry condition is the most difficult condition to be sensed accurately by a heating rate sensor. Figure 2-100 presents the heating rate sensor ΔT and heat input rate versus a narrow band of entry time. Models 32, 35, 38, 41 and 44 all employ the 5% density 0.020-inch-thick stainless steel spacer. Figure 2-101 presents the results for Models 31, 34, 37, 40 and 43 which use 10% density spacers. Figure 2-102 shows results for Models 30, 33, 36, 39 and 42 which employed 20% density spacers. In Figures 2-100, 2-101 and 2-102, Models 39, 40 and 41 use 6 mil and Models 42, 43 and 44 use 10 mil gage thickness. All other models use 8 mil gage and vary the sensor skin thickness. The greatest overall influence on results is due to the density of spacers. The greater the density, the lower the heat resistance, and the sensor ΔT output more nearly approximates the heat input curve. There is a slight advantage in using a lower gage thickness.

Model 39 represents the best overall configuration with respect to performance for an externally mounted heat rate sensor on the Atlas tank. Model 39 sensor output performance comparison with heat flux input on a ratio basis appears in Figure 2-103. Figure 2-104 shows a cross-sectional view of a 0.024-inch-thick configuration that would give Model 39 performance. To sense low temperature differences between gage and sensor skin accurately a thermopile arrangement would be necessary.

Grounding of the thermopile system to avoid extraneous inputs to the telemetry amplifier would be accomplished at one point on the skin. The remainder of the thermopile system would be electrically, but not thermally, isolated. The thermopile system would be installed in a central location of the heat sensor and serve as a spacer. The spacer outside the thermopile region would consist of more conventional stainless steel webs spaced to give the required spacer density. Model 39 spacer density is 10% solid for a 0.010-inch thickness (equals 20% solid for a 0.020-inch thickness). While this heating rate sensor can show excellent performance, its complexity would undoubtedly be reflected in high procurement costs. These were not evaluated during this study.

Model 34 was selected as the best overall configuration, considering the many conflicting requirements, including cost, for an entry heating rate sensor to be installed on an Atlas tank. The output performance of Model 34 sensor compared with heat flux input appears in Figure 2-105. Other Model 34 sensor performance appears in Figures 2-98 and 2-101. A cross-sectional view through this recommended heat rate sensor appears in Figure 2-106. Since both gage and skin thermocouple junctions may be grounded, two thermocouples should be used to obtain the required ΔT reading. As this would degrade accuracy to about $\pm 6\%$, an alternate system is recommended in which the sensor skin thermocouple junction is electrically isolated from the skin. This would permit the sensor ΔT to be read directly, as both hot and cold junctions of the thermocouple would be in the heat sensor. Convair Aerospace telemetry tests have shown that such directly obtained differential temperatures can be accurate to about $\pm 2\%$. This system would also permit the gage thermocouple junction to serve as a separate hot junction for independent gage temperature measurement if required.

The 0.10 second print-out of the computer runs is very evident in the sensor output curves in Figures 2-100 through 2-105. This result suggests that flight sensors be sampled at a rate not less than 10 per second and preferably at 20 per second. A lower rate of sampling of about one per second is satisfactory for an independent determination of surface (gage) temperature to be used as a reference wall temperature.

The physical construction of Model 34 would be essentially as illustrated in Figure 2-50. The spacer would consist of milled or chem-milled grooves 0.020-inch deep, 0.072-inch wide and spaced 0.080-inch apart as shown in cross section in Figure 2-106. Chromel wire, 2 mils diameter, is micro spot welded to the gage. A Constantan wire, 2 mils diameter, is microspot welded near or on each chromel wire. The Constantan wires, one from the gage and one from the skin can be placed in a single stainless steel sheath in which the wires are insulated by a packed insulating powder. As a practical size for the wires in the sheathed lead is about 10 mils, the required 2 mil diameter near the weld junction is obtained by chemical etching. The small diameter wire at and near the weld junctions is necessary to avoid having the wires act as a heat sink, and as an undefined heat leak. A sketch showing the installation on the Atlas tank skin appears in Figure 2-107.

The sensor, as illustrated in Figures 2-104 and 2-107, may be assembled together with its sheathed lead, sealed, and tested individually before being installed on the Atlas tank. End to end calibration is also practical after installation on the Atlas tank. A known variable heating rate source can be provided by a small heat lamp, or by a hot air jet. Sudden initiation or interruption of heating can be accomplished with a rotating shutter device. The response of the heating rate sensor to such heat pulses can be ascertained prior to flight.

An electrical analog of the heat rate sensor appears in Figure 2-108. The analog model can be of value in the eventual reduction of flight data. R3 and R4 have large values and serve only equalized voltages at all points over a relatively long period, and thus establish uniform initial conditions. Capacitor C1 and resistor R2 are equivalent to the heat capacitance of the gage and the heat flow resistance of the spacer. Capacitor C2 is equivalent to the heat capacitance of the sensor skin. R1 and the input voltage, together, are equivalent to the heat flux input. The output voltage corresponds to the sensor ΔT output. Since all elements of the heating rate sensor are known, necessary corrections may be applied to the output readings to arrive at the heat input rate as a function of time. The reverse problem solution employing sensor output to obtain heating rate input was not attempted during this brief study. However, the solution should not be difficult using either analog or digital computer methods.

2.4.4 GAGE LOCATION. Figure 2-109 shows the recommended location for 50 heating rate sensors on an Atlas F. Twenty sensors are located on Quad I - Quad IV intersection beginning at Station 514 and then aft at 24-inch spacings. Five sensors are located in each of Quad II, Quad III, and Quad IV beginning at Station 538, and then aft at 96-inch spacings. In Quad I seven sensors are used beginning at Station 538 and then aft at 96-inch spacings. Three additional sensors are located at Station 730 in Quad I and Quad II to obtain circumferential heating rates at approximately equal radial angles from the Atlas centerline.

The overall placement selection offers adequate circumferential sampling of heating rates at five Atlas F stations. More detailed circumferential sampling is provided at Station 730 over about one-half of the body. Station 730 was selected as it is removed as far as practicable from possible disturbing influences of the nose adapter, side mounted equipment pods, and sustainer engine hardware at the base. A high sensor density longitudinal line on the most open Atlas F side is provided to permit an easier assessment of transitional effects as influenced by length. Since circumferentially mounted sensors are also in line between successive stations, additional, less detailed, longitudinal information is available at other angular locations. Sensors located at the aft end of the vehicle between the fuel pressurization line and equipment pod serve to provide heating data where known disturbing influences exist.

2.4.5 CONCLUSIONS AND RECOMMENDATIONS. A heating rate sensor can be constructed whose direct output is in excellent agreement with expected aerodynamic entry heating rate input to an Atlas vehicle that is tumbling in pitch up to 180 degrees per

second. As the elements of the sensor are simple, the output signal can be further conditioned by relatively simple analog or digital computer methods to give a nearly exact agreement between input heating rates and processed output indications. A recommended sensor is a 301 stainless steel unit about three inches overall diameter and 0.044-inch thick. It consists of an outer 0.008-inch thick plate (gage), a 0.020-inch thick spacer that is 10% solid, and an inner 0.016-inch thick plate (skin). Differential temperature between gage and skin, measured by conventional thermocouples, is the heating rate sensor output. The skin is spot welded to the outer surface of the Atlas tank.

Surface temperature thermocouple and heating rate sensor outputs do not require a continuous telemetry channel during a tumbling Atlas entry. Rather, a commutated output of a brief reading of each of several thermocouples and heating rate sensors in succession is recommended. A sampling rate of one per second is recommended for surface temperature level indications and 20 per second for heating rate sensor outputs.

A recommended distribution on an Atlas F expended tank, to obtain entry heating rate data, was prepared.

Table 2-7. Heating rate ratio curve points for computer model.

<u>Pitch Angle</u>	<u>Heating Rate Ratio</u> <u>$\dot{q}_0/\dot{q}_{(90^\circ \text{ stagnation})}$</u>
10°	.15
55°	.90
90°	1.00
125°	.90
170°	.15
190°	.10
350°	.10
370°	.15

Table 2-8. Cold wall heat flux history.

<u>Entry Time</u> <u>Seconds</u>	<u>Coldwall Heat Flux</u> <u>q_0, Btu/Ft² - Sec</u>	<u>Reference</u> <u>Altitude, Ft.</u>
.000	.05	300,000
.056	.57	
.306	3.76	
.500	4.40	
.694	4.23	
.944	.76	
1.056	.52	288,140
1.944	.70	
2.056	1.08	
2.306	7.02	
2.500	8.30	
2.694	7.92	
2.944	1.33	
3.056	.97	265,670
3.944	1.22	
4.056	1.90	
4.306	12.10	
4.500	14.10	
4.694	13.25	
4.944	2.36	
5.056	1.62	243,200
5.944	2.00	
6.056	3.08	
6.306	19.45	
6.500	22.30	
6.694	21.25	
6.944	3.72	
7.056	2.55	220,720
7.944	3.08	
8.056	4.72	
8.306	29.70	
8.500	34.30	
8.694	31.85	
8.944	5.55	
9.056	3.78	198,250
9.944	4.40	
10.056	6.70	187,020

Table 2-9. Model characteristics.

Model Number	Computer Node	Thickness Inches	Emissivity, ϵ	Material Number	h , Btu/Ft ² - Hr - °F
1	A	.002	.90	1	4.0
	B	.013	.90	1	
	C	.005		0	
	D	.005		0	
	E	0	.15	00	
	F	.016	.15	1	
2	A	.002	.90	1	4.0
	B	.008	.90	1	
	C	.005		0	
	D	.005		0	
	E	0	.15	00	
	F	.016	.15	1	
3	A	.002	.90	1	4.0
	B	.006	.90	1	
	C	.005		0	
	D	.005		0	
	E	0	.15	00	
	F	.016	.15	1	
4	A	.002	.90	1	4.0
	B	.004	.90	1	
	C	.005		0	
	D	.005		0	
	E	0	.15	00	
	F	.016	.15	1	
5	A	.002	.90	1	4.0
	B	.003	.90	1	
	C	.005		0	
	D	.005		0	
	E	0	.15	00	
	F	.016	.15	1	
6	A	.002	.90	1	4.0
	B	.002	.90	1	
	C	.005		0	
	D	.005		0	
	E	0	.15	00	
	F	.016	.15	1	

Table 2-9. Model characteristics. (Continued)

Model Number	Computer Node	Thickness Inches	Emissivity, ϵ	Material Number	h , Btu/Ft ² -Hr-°F
7	A	.002	.90	1	4.0
	B	.001	.90	1	
	C	.005		0	
	D	.005		0	
	E	0	.15	00	
	F	.016	.15	1	
8	A	.002	.90	1	4.0
	B	0	.90	00	
	C	.005		0	
	D	.005		0	
	E	0	.15	00	
	F	.016	.15	1	
9	A	.001	.90	1	4.0
	B	0	.90	00	
	C	.005		0	
	D	.005		0	
	E	0	.15	00	
	F	.016	.15	1	
10	A	.002	.90	1	4.0
	B	.006	.90	1	
	C	.005		0	
	D	.005		0	
	E	0	.90	00	
	F	.016	.15	1	
11	A	.002	.90	1	4.0
	B	.004	.90	1	
	C	.005		0	
	D	.005		0	
	E	0	.90	00	
	F	.016	.15	1	
12	A	.002	.90	1	4.0
	B	.002	.90	1	
	C	.005		0	
	D	.005		0	
	E	0	.90	00	
	F	.016	.15	1	

Table 2-9. Model characteristics. (Continued)

Model Number	Computer Node	Thickness Inches	Emissivity, ϵ	Material Number	h , Btu/Ft ² -Hr-°F
13	A	.002	.90	1	4.0
	B	0	.90	00	
	C	.005		0	
	D	.005		0	
	E	0	.90	00	
	F	.016	.15	1	
14	A	.002	.90	1	10.0
	B	.006	.90	1	
	C	.005		0	
	D	.005		0	
	E	0	.90	00	
	F	.016	.15	1	
15	A	.002	.90	1	10.0
	B	.004	.90	1	
	C	.005		0	
	D	.005		0	
	E	0	.90	00	
	F	.016	.15	1	
16	A	.002	.90	1	10.0
	B	.002	.90	1	
	C	.005		0	
	D	.005		0	
	E	0	.90	00	
	F	.016	.15	1	
17	A	.002	.90	1	10.0
	B	0	.90	00	
	C	.005		0	
	D	.005		0	
	E	0	.90	00	
	F	.016	.15	1	
18	A	.002	.90	1	10.0
	B	.006	.90	1	
	C	.010		1	
	D	.010		1	
	E	0	.90	0	
	F	.016	.15	1	

Table 2-9. Model characteristics. (Continued)

Model Number	Computer Node	Thickness Inches	Emissivity, ϵ	Material Number	h , Btu/Ft ² - Hr - °F
19	A	.002	.90	1	10.0
	B	.004	.90	1	
	C	.010		1	
	D	.010		1	
	E	0	.90	00	
	F	.016	.15	1	
20	A	.002	.90	1	10.0
	B	.002	.90	1	
	C	.010		1	
	D	.010		1	
	E	0	.90	00	
	F	.016	.15	1	
21	A	.002	.90	1	10.0
	B	.006	.90	1	
	C	.010		3	
	D	.010		3	
	E	0	.90	00	
	F	.016	.15	1	
22	A	.002	.90	1	10.0
	B	.004	.90	1	
	C	.010		3	
	D	.010		3	
	E	0	.90	00	
	F	.016	.15	1	
23	A	.002	.90	1	10.0
	B	.002	.90	1	
	C	.010		3	
	D	.010		3	
	E	0	.90	00	
	F	.016	.15	1	
24	A	.002	.90	1	10.0
	B	.006	.90	1	
	C	.010		5	
	D	.010		5	
	E	0	.90	00	
	F	.016	.15	1	

Table 2-9. Model characteristics. (Continued)

Model Number	Computer Node	Thickness Inches	Emissivity, ϵ	Material Number	h , Btu/Ft ² - Hr - °F
25	A	.002	.90	1	
	B	.004	.90	1	
	C	.010		5	
	D	.010		5	
	E	0	.90	00	
	F	.016	.15	1	10.0
26	A	.002	.90	1	
	B	.002	.90	1	
	C	.010		5	
	D	.010		5	
	E	0	.90	00	
	F	.016	.15	1	10.0
27	A	.004	.90	1	
	B	0	.90	00	
	C	.020		5	
	D	0		00	
	E	0	.90	00	
	F	.016	.15	1	10.0
28	A	.002	.90	1	
	B	0	.90	00	
	C	.004		5	
	D	0		00	
	E	0	.90	00	
	F	.016	.15	1	10.0
29	A	0	.15	00	
	B	0		00	
	C	0		00	
	D	0		00	
	E	0		00	
	F	.016	.15	1	4.0
30	A	.008	0	1	
	B	0	0	00	
	C	.020		2	
	D	0		00	
	E	0	0	00	
	F	.008	0	1	0.0

Table 2-9. Model characteristics. (Continued)

Model Number	Computer Node	Thickness Inches	Emissivity, ϵ	Material Number	h , Btu/Ft ² - Hr - °F
31	A	.008	0	1	0.0
	B	0	0	00	
	C	.020		3	
	D	0		00	
	E	0	0	00	
	F	.008	0	1	
32	A	.008	0	1	0.0
	B	0	0	00	
	C	.020		4	
	D	0		00	
	E	0	0	00	
	F	.008	0	1	
33	A	.008	0	1	0.0
	B	0	0	00	
	C	.020		2	
	D	0		00	
	E	0	0	00	
	F	.016	0	1	
34	A	.008	0	1	0.0
	B	0	0	00	
	C	.020		3	
	D	0		00	
	E	0	0	00	
	F	.016	0	1	
35	A	.008	0	1	0.0
	B	0	0	00	
	C	.020		4	
	D	0		00	
	E	0	0	00	
	F	.016	0	1	
36	A	.008	0	1	0.0
	B	0	0	00	
	C	.020		2	
	D	0		00	
	E	0	0	00	
	F	.024	0	1	

Table 2-9. Model characteristics. (Continued)

Model Number	Computer Node	Thickness Inches	Emissivity, ϵ	Material Number	h , Btu/Ft ² -Hr-°F
37	A	.008	0	1	
	B	0	0	00	
	C	.020		3	
	D	0		00	
	E	0	0	00	
	F	.024	0	1	0.0
38	A	.008	0	1	
	B	0	0	00	
	C	.020		3	
	D	0		00	
	E	0	0	00	
	F	.024	0	1	0.0
39	A	.006	0	1	
	B	0	0	00	
	C	.020		2	
	D	0		00	
	E	0	0	00	
	F	.008	0	1	0.0
40	A	.006	0	1	
	B	0	0	00	
	C	.020		3	
	D	0		00	
	E	0	0	00	
	F	.008	0	1	0.0
41	A	.006	0	1	
	B	0	0	00	
	C	.020		4	
	D	0		00	
	E	0	0	00	
	F	.008	0	1	0.0
42	A	.010	0	1	
	B	0	0	00	
	C	.020		2	
	D	0		00	
	E	0	0	00	
	F	.008	0	1	0.0

Table 2-9. Model characteristics. (Concluded)

Model Number	Computer Node	Thickness Inches	Emissivity, ϵ	Material Number	h , Btu/Ft ² - Hr - °F
43	A	.010	0	1	
	B	0	0	00	
	C	.020		3	
	D	0		00	
	E	0	0	00	
	F	.008	0	1	0.0
44	A	.010	0	1	
	B	0	0	00	
	C	.020		4	
	D	0		00	
	E	0	0	00	
	F	.008	0	1	0.0

Table 2-10. Material heat conduction properties.

Material No.	Temperature, °R	Density lbm/ft ³	Specific Heat Btu/lbm - °F	Conductivity, Btu/Ft ² - Hr - °F/Ft	Remarks
00	All	0	0		Node absent conductivity is infinite
0	All	0	0	0	No conductivity, Radiation exchange
1	450	485	.107	8.892	Solid 301 Stainless Steel
	650	485	.118		
	850	485	.125		
	1450	485		13.50	
2	450	97	.107	1.778	20% Solid 301 Stainless Steel
	650	97	.118		
	850	97	.125		
	1450	97		2.700	
3	450	48.5	.107	.8892	10% Solid 301 Stainless Steel
	650	48.5	.118		
	850	48.5	.125		
	1450	48.5		1.350	
4	450	24.25	.107	.4446	5% Solid 301 Stainless Steel
	650	24.25	.118		
	850	24.25	.125		
	1450	24.25		.6750	
5	450	4.85	.107	.0889	1% Solid 301 Stainless Steel
	650	4.85	.118		
	850	4.85	.125		
	1450	4.85		.1350	

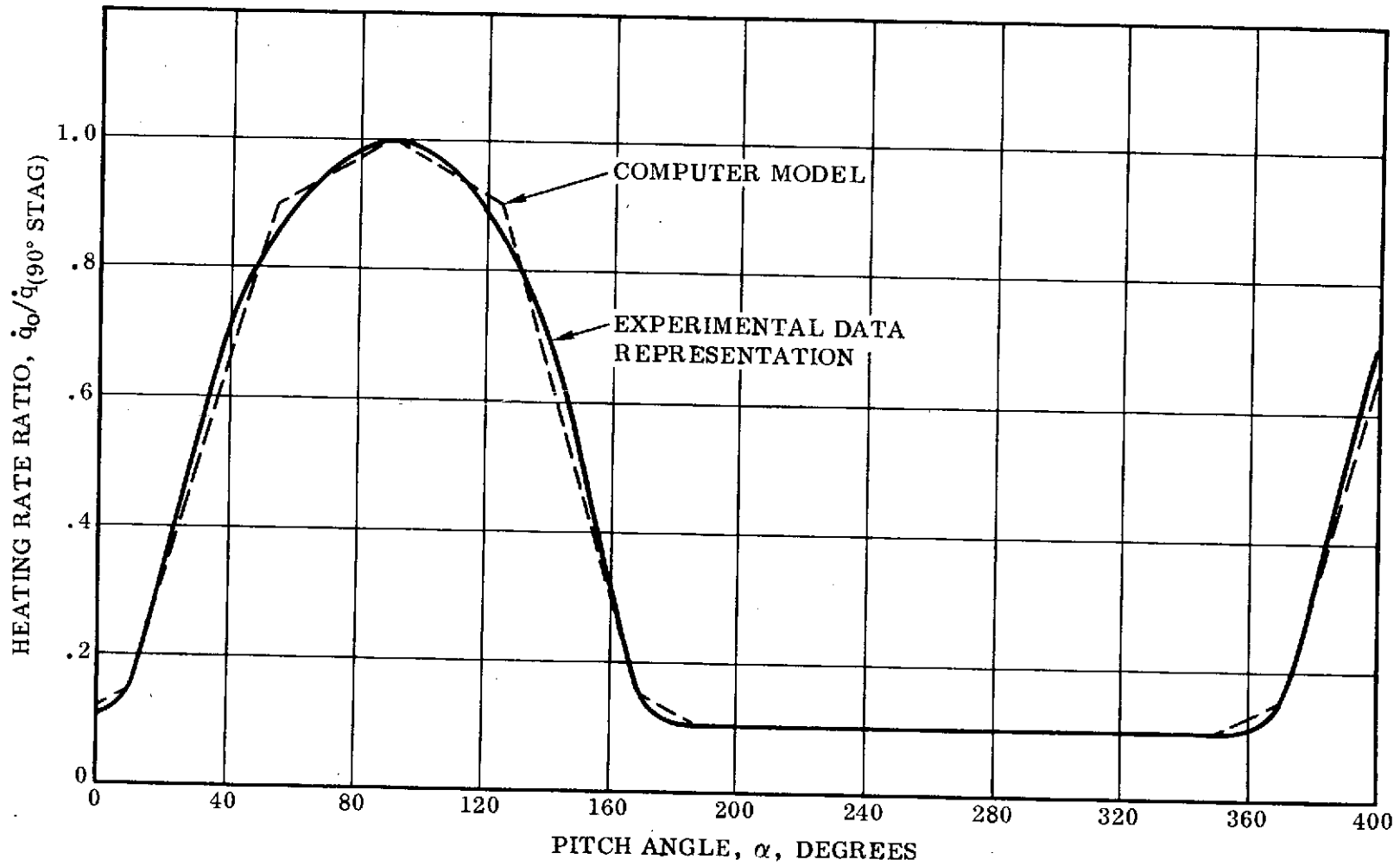


Figure 2-47. Comparison of computer model and experimental data representation.

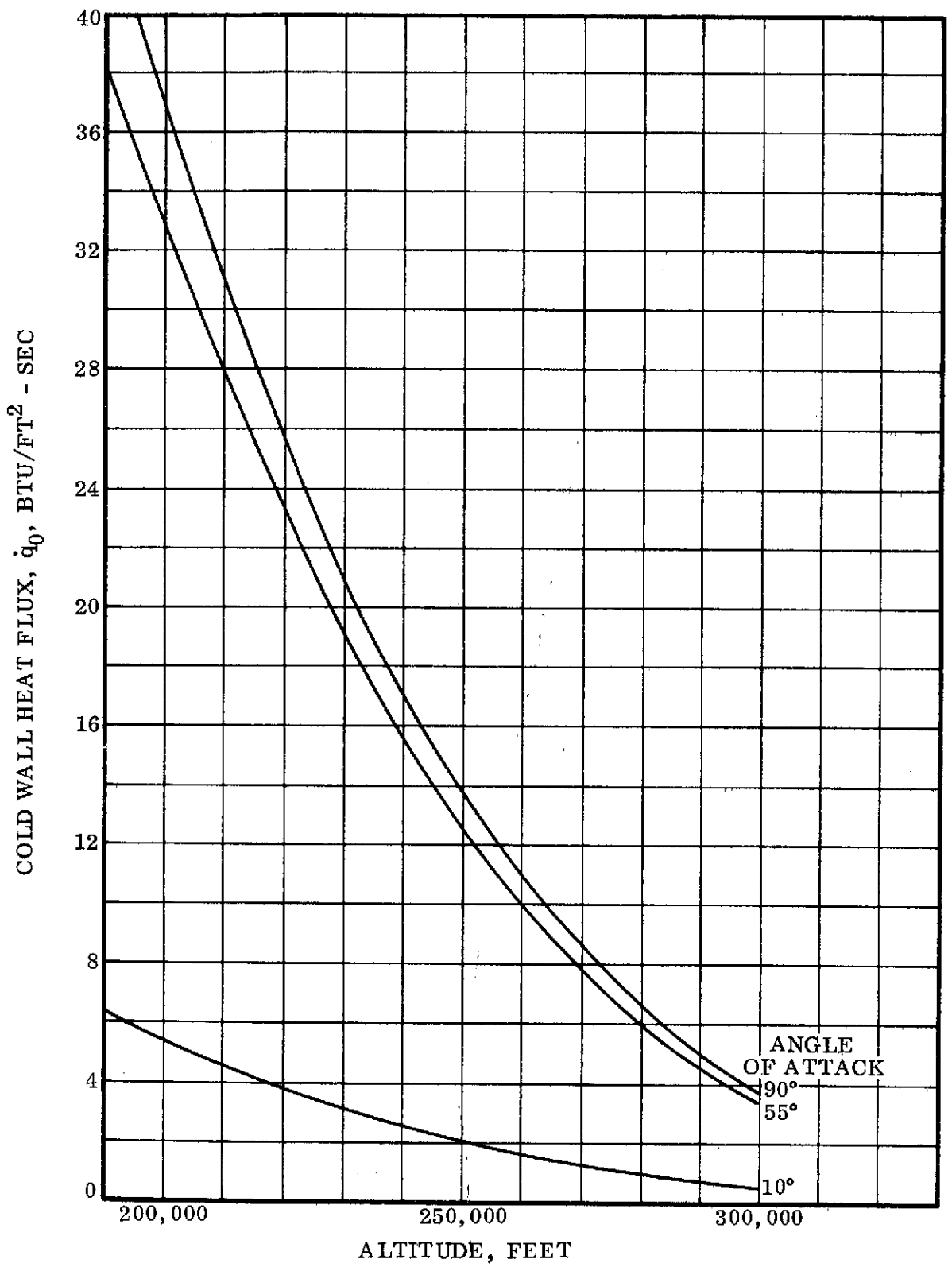


Figure 2-48. Atlas ABRES F/HIRS trajectory.

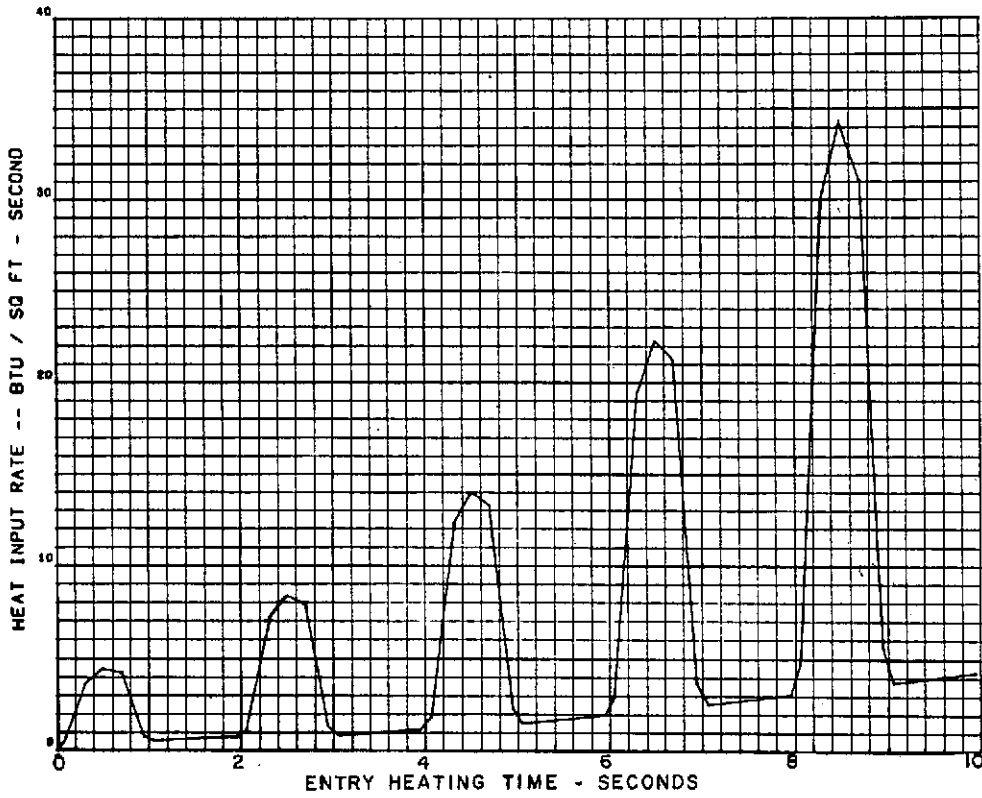


Figure 2-49. Atlas reentry heating for 180 deg/sec pitch rate computer program tabulation of cold wall heat flux.

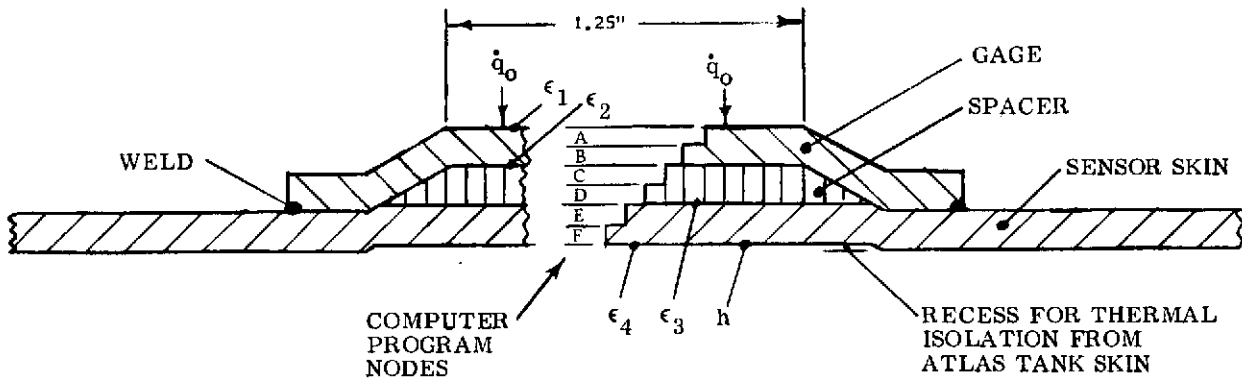


Figure 2-50. Schematic of generalized computer model for heating rate sensors.

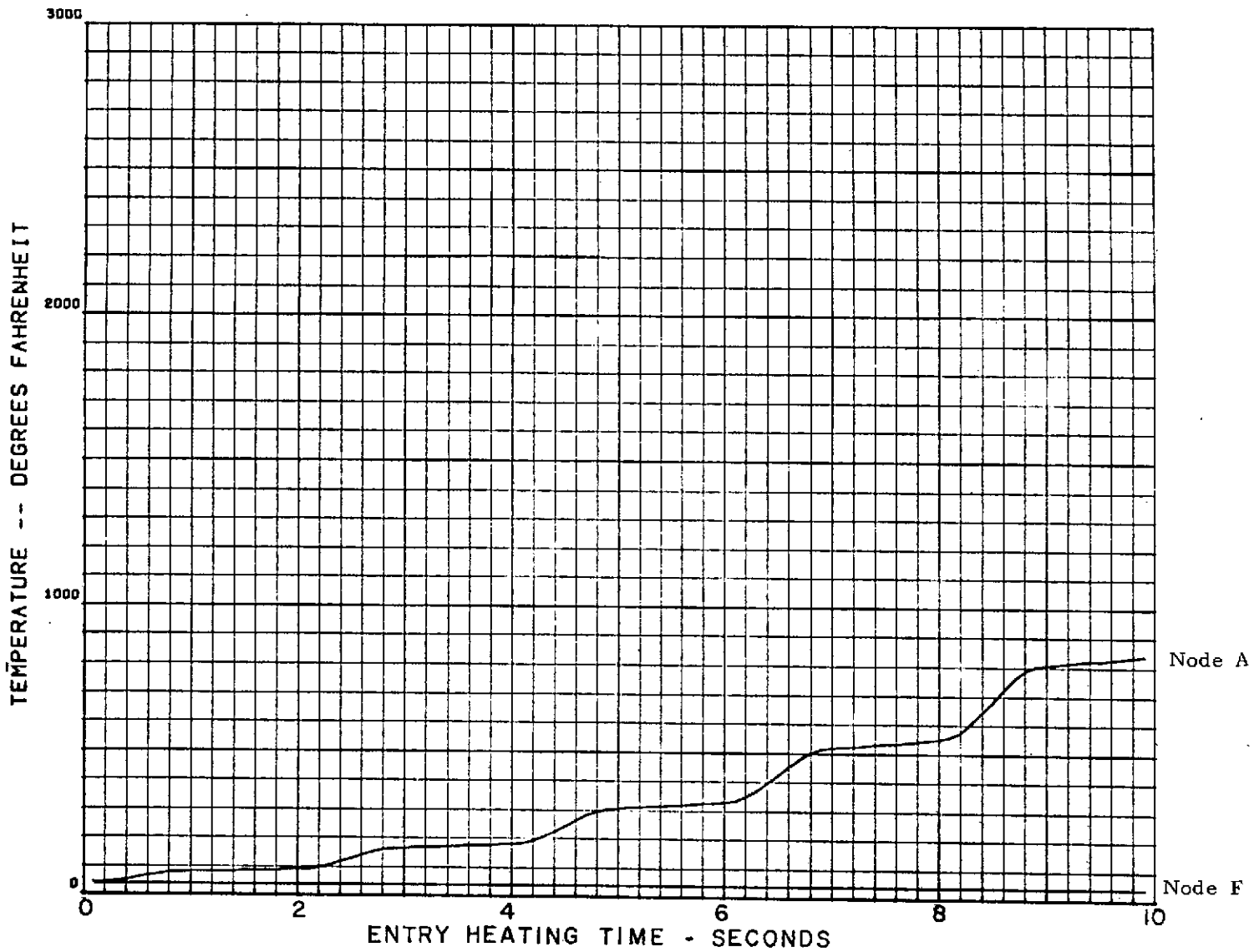


Figure 2-51. Atlas reentry heating for 180 deg/sec pitch rate model 01, 15 mil gage, 16 mil skin, no gap radiation.

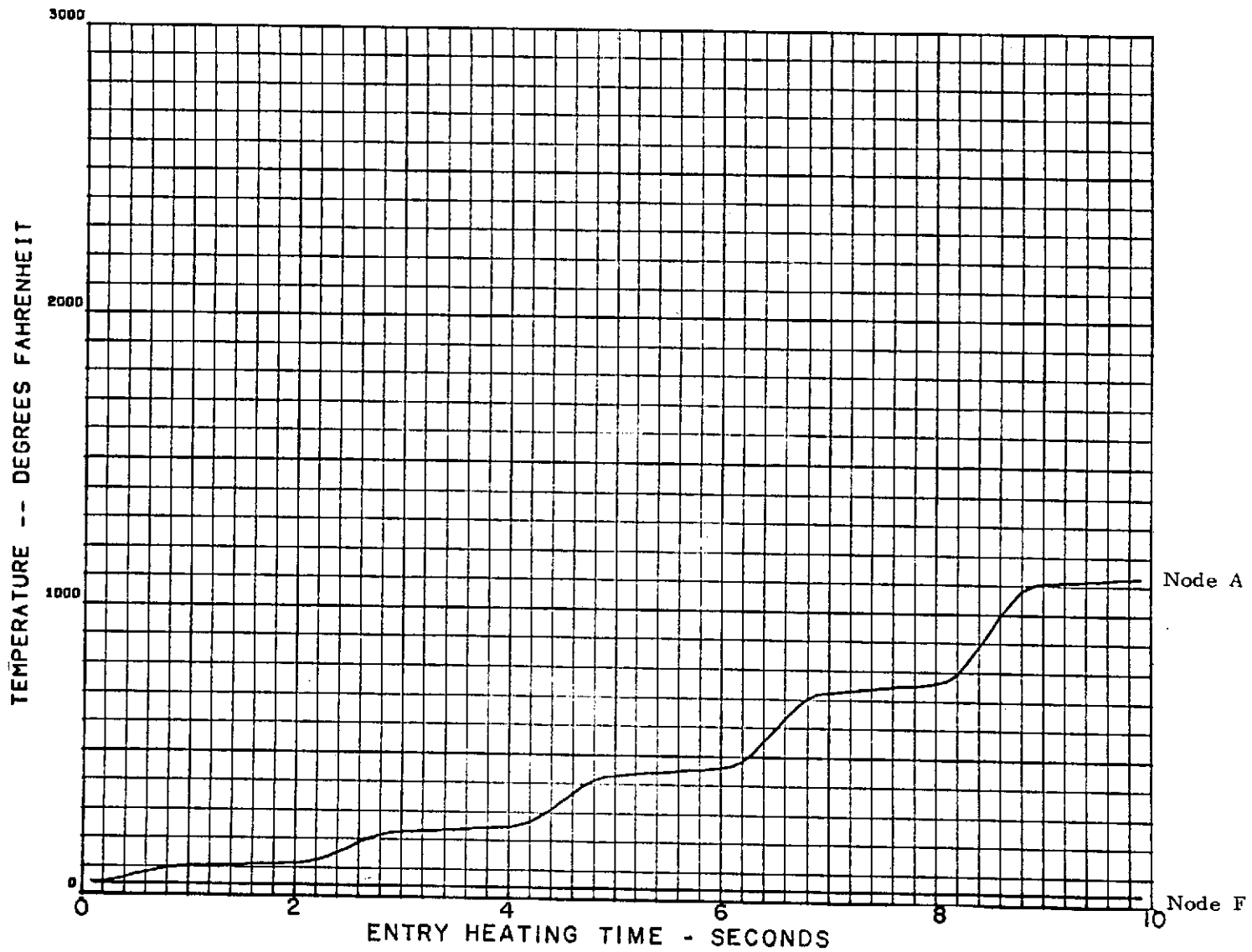


Figure 2-52. Atlas reentry heating for 180 deg/sec pitch rate model 02, 10 mil gage, 16 mil skin, no gap radiation.

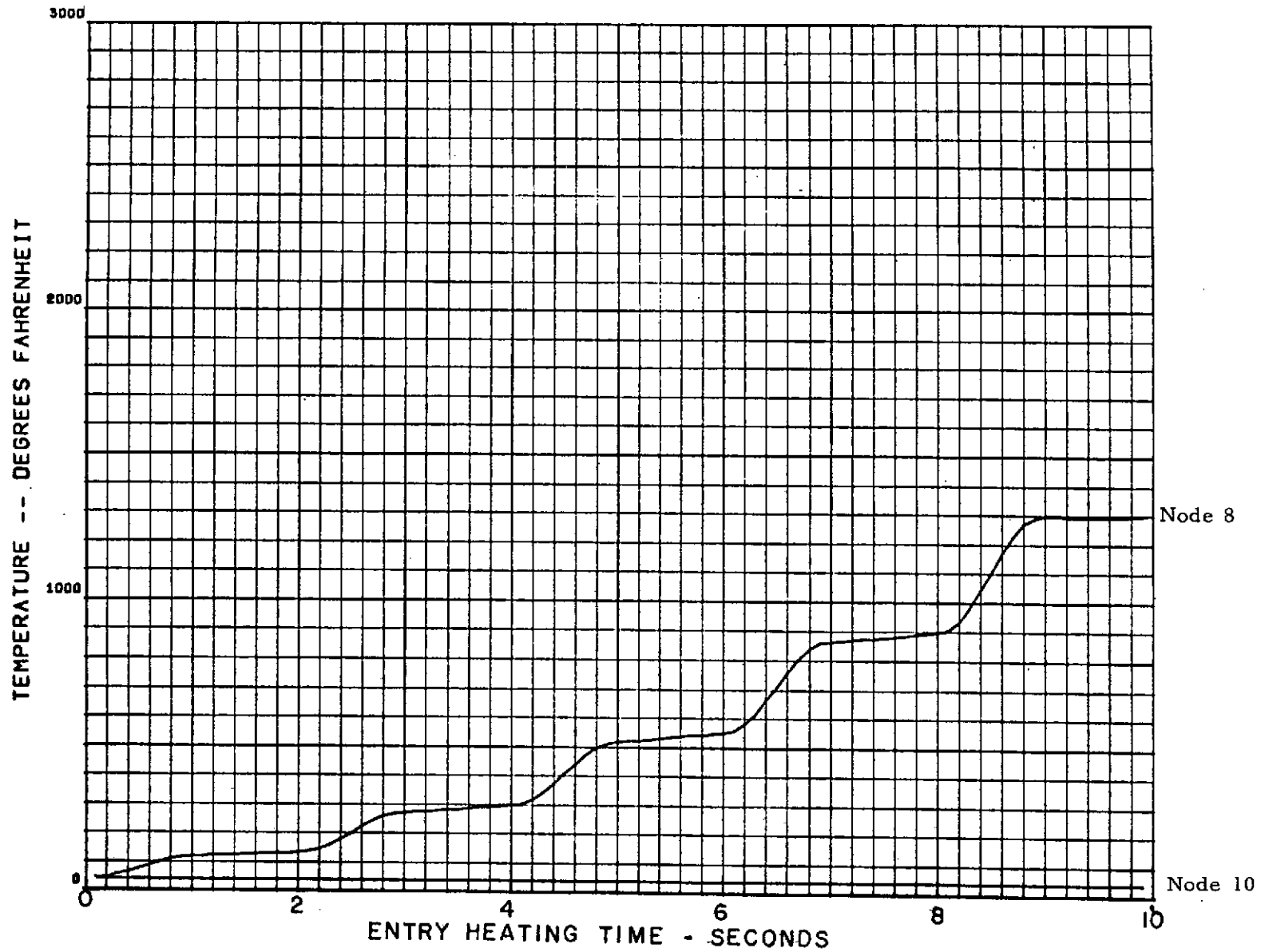


Figure 2-53. Atlas reentry heating for 180 deg/sec pitch rate model 03, 8 mil gage, 16 mil skin, no gap radiation.

C-2

2-81

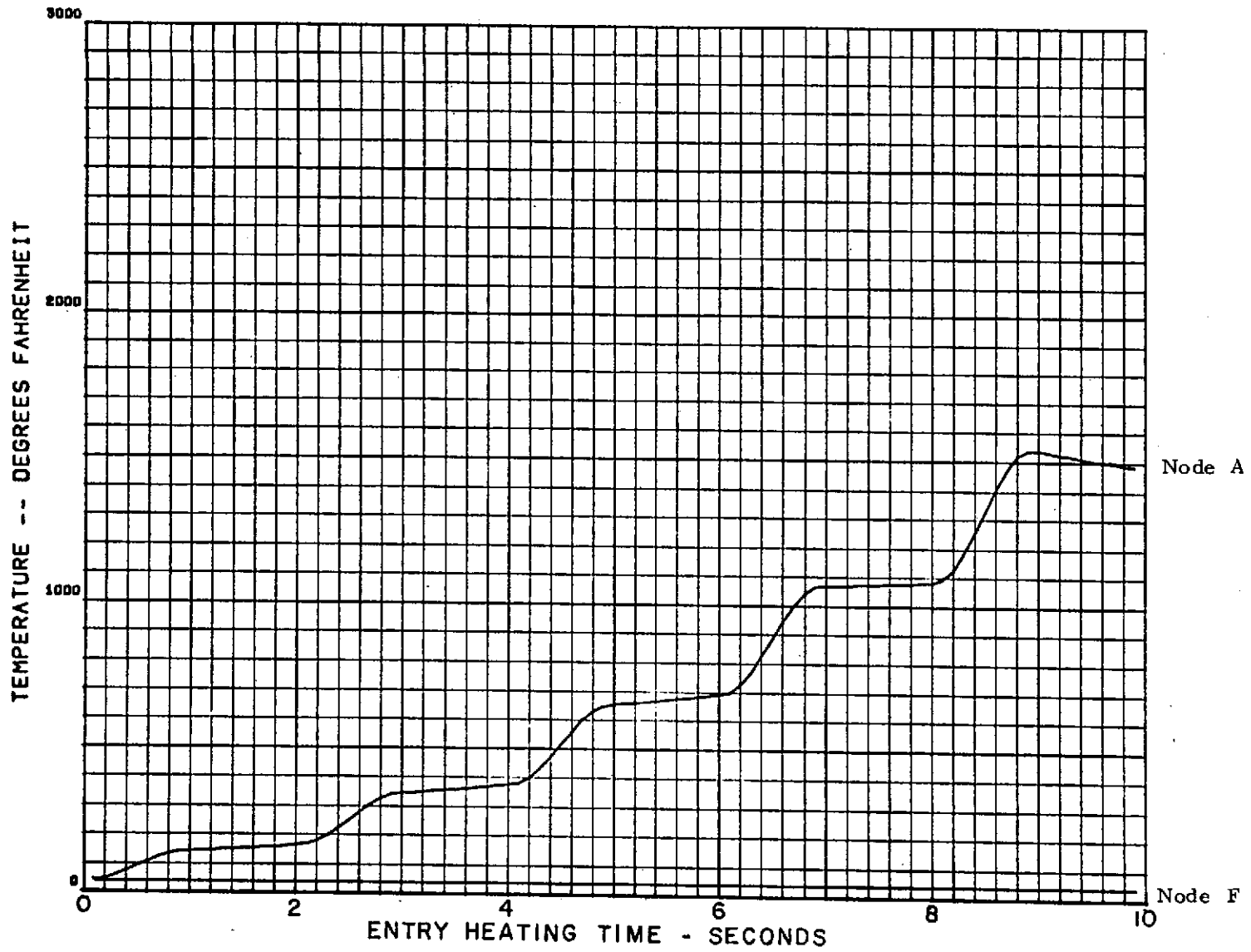


Figure 2-54. Atlas reentry heating for 180 deg/sec pitch rate model 04, 6 mil gage, 16 mil skin, low gap radiation.



Figure 2-55. Atlas reentry heating for 180 deg/sec pitch rate model 05, 5 mil gage, 16 mil skin, low gap radiation.

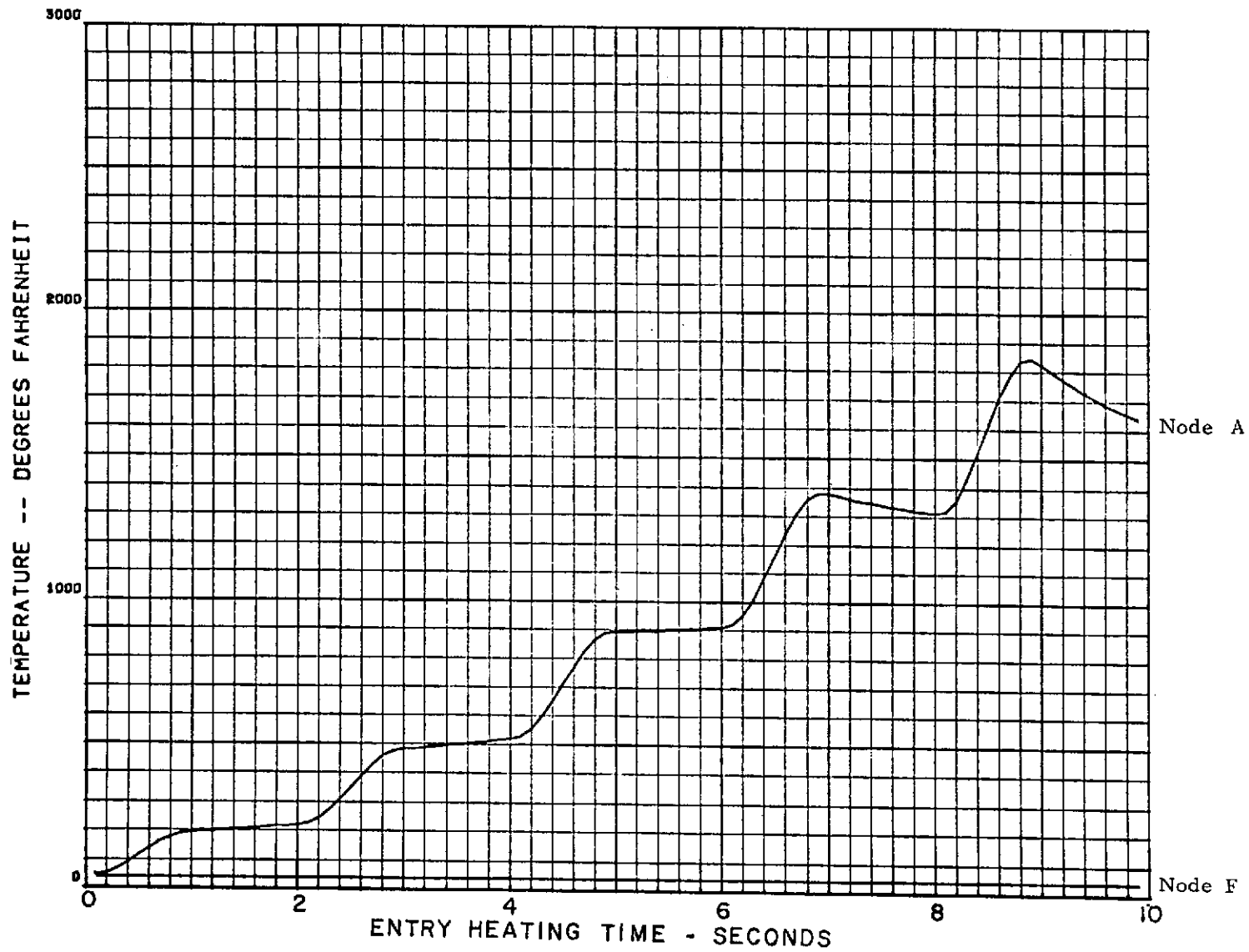


Figure 2-56. Atlas reentry heating for 180 deg/sec pitch rate model 06, 4 mil gage, 16 mil skin, low gap radiation.

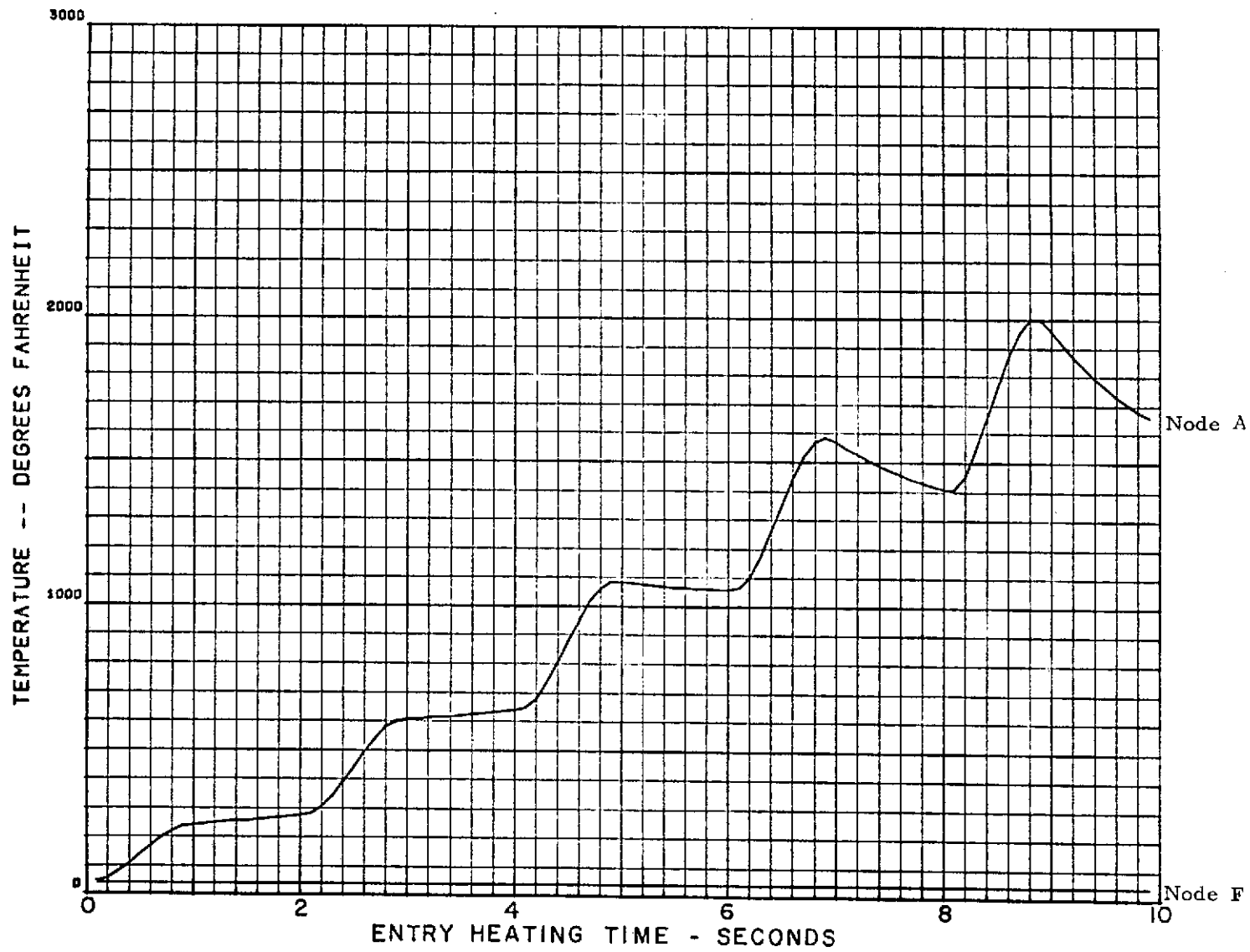


Figure 2-57. Atlas reentry heating for 180 deg/sec pitch rate model 07, 3 mil gage, 16 mil skin, low gap radiation.

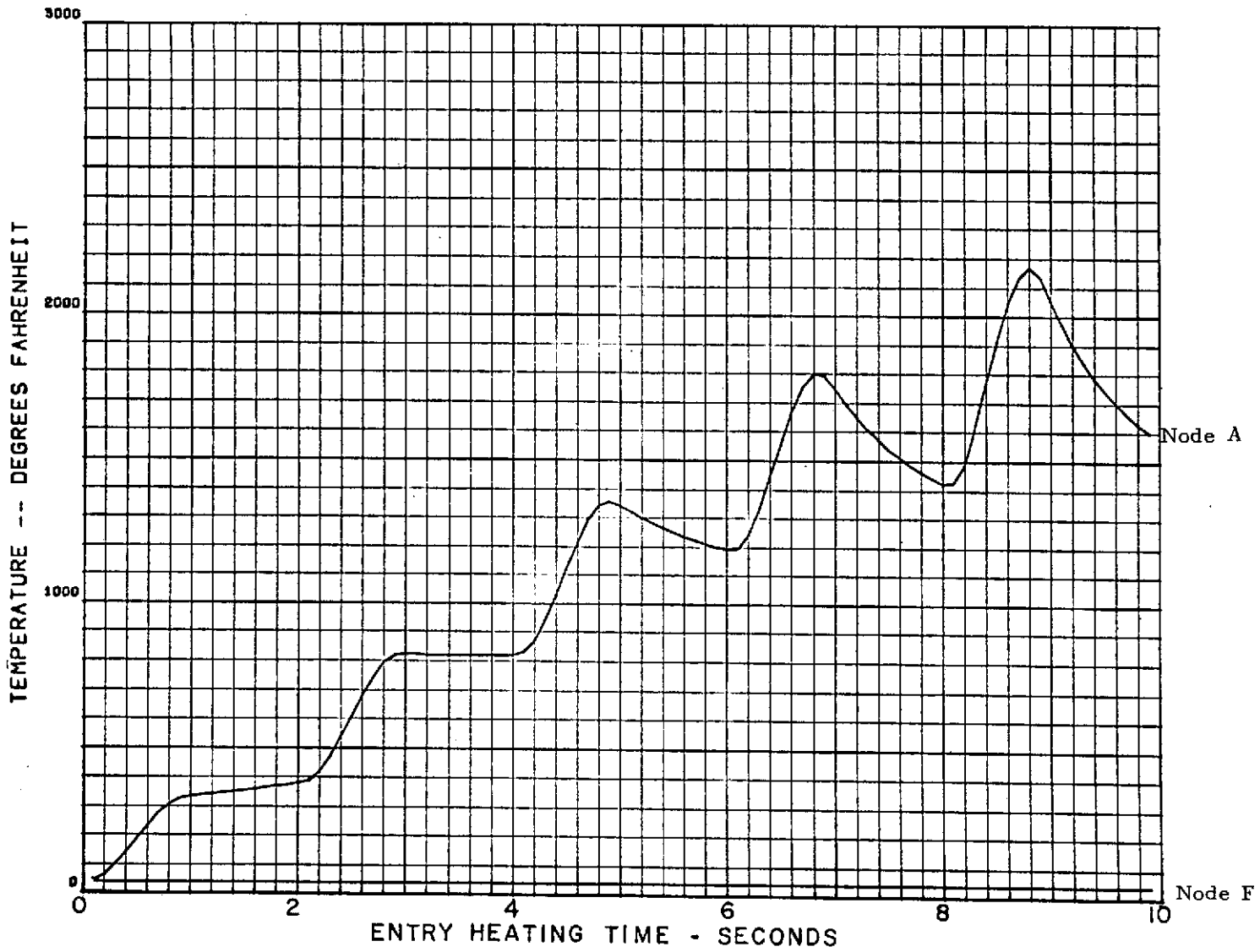


Figure 2-58. Atlas reentry heating for 180 deg/sec pitch rate model 08, 2 mil gage, 16 mil skin, low gap radiation.

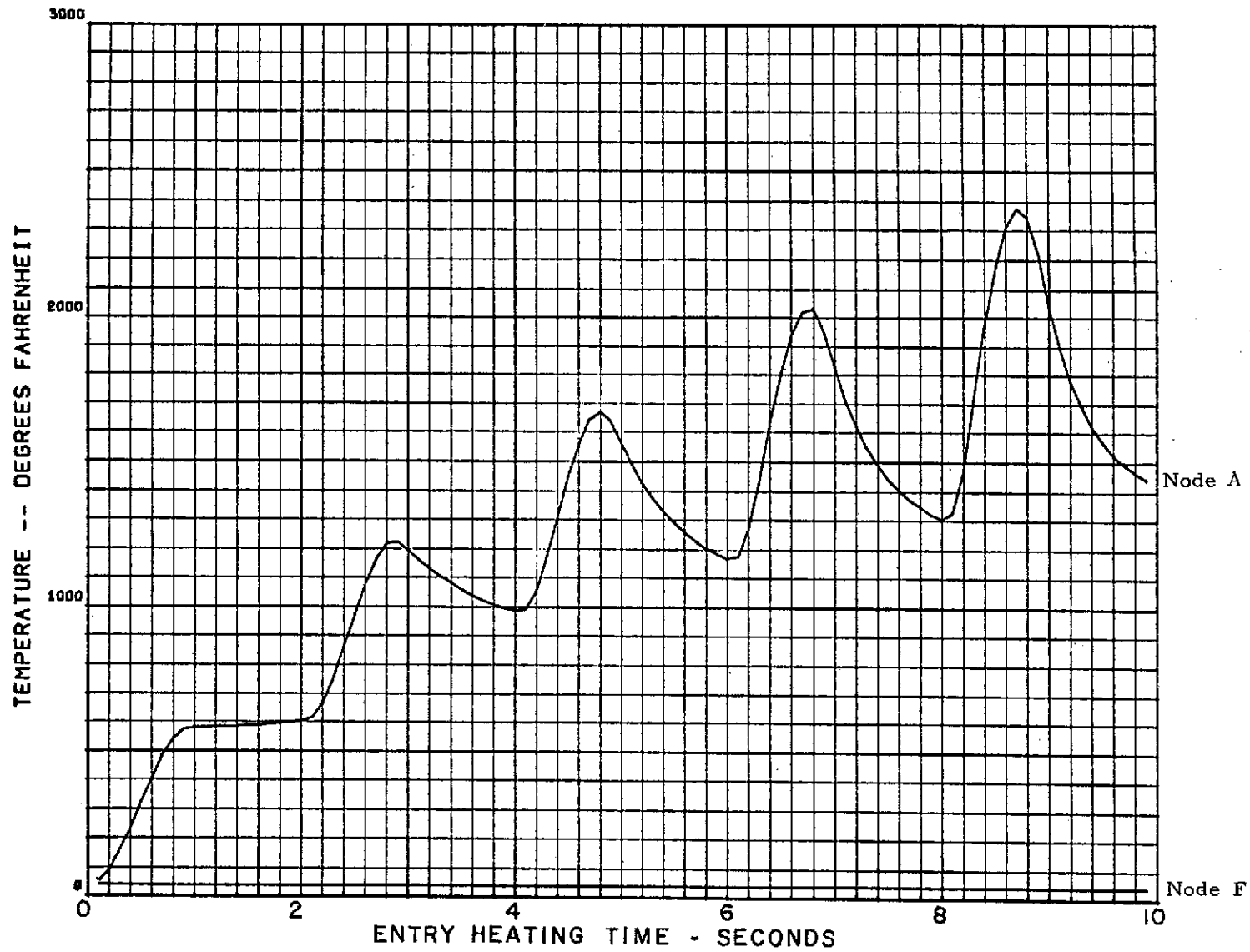


Figure 2-59. Atlas reentry heating for 180 deg/sec pitch rate model 09, 1 mil gage, 16 mil skin, low gap radiation.

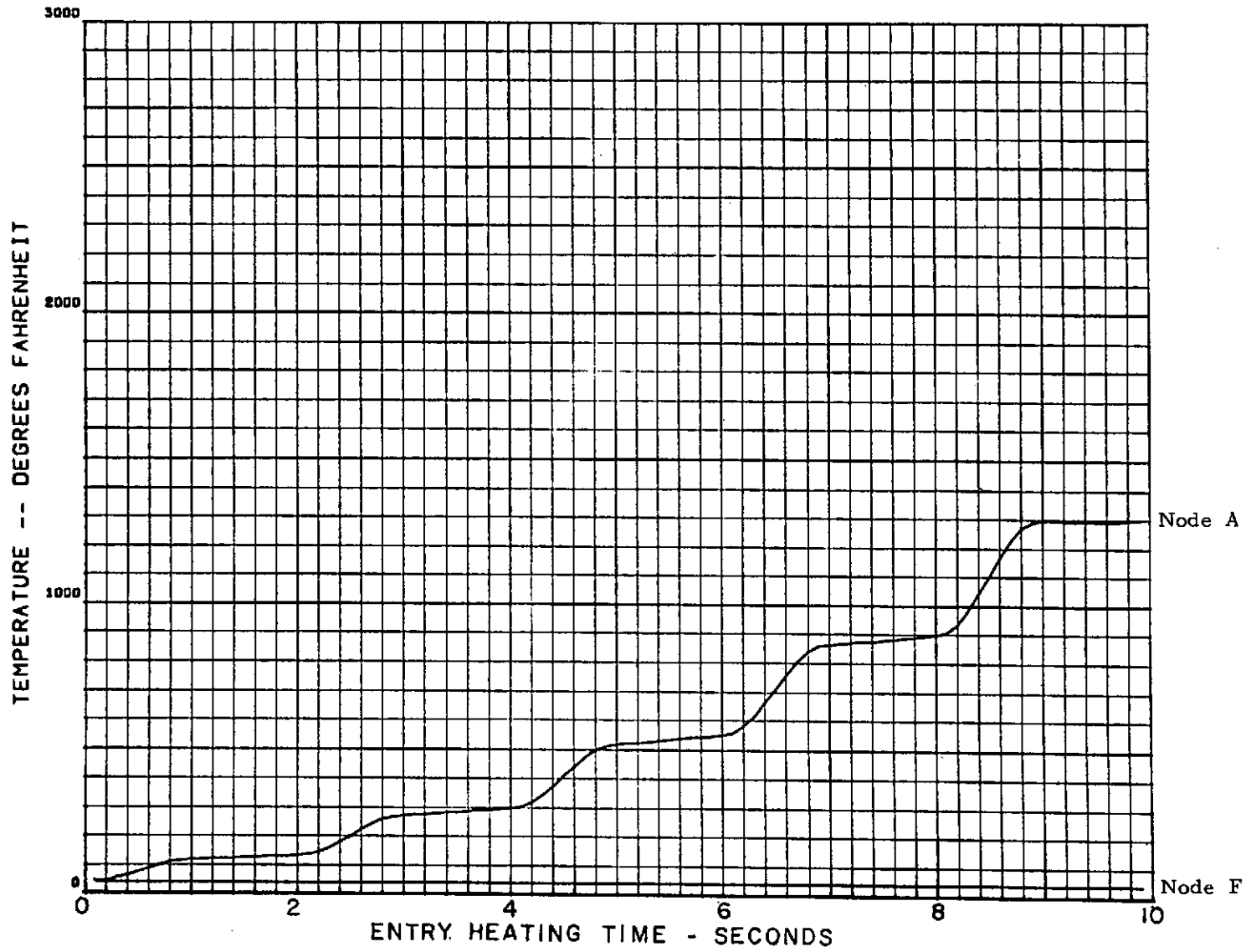


Figure 2-60. Atlas reentry heating for 180 deg/sec pitch rate model 10, 8 mil gage, 16 mil skin, max gap radiation.

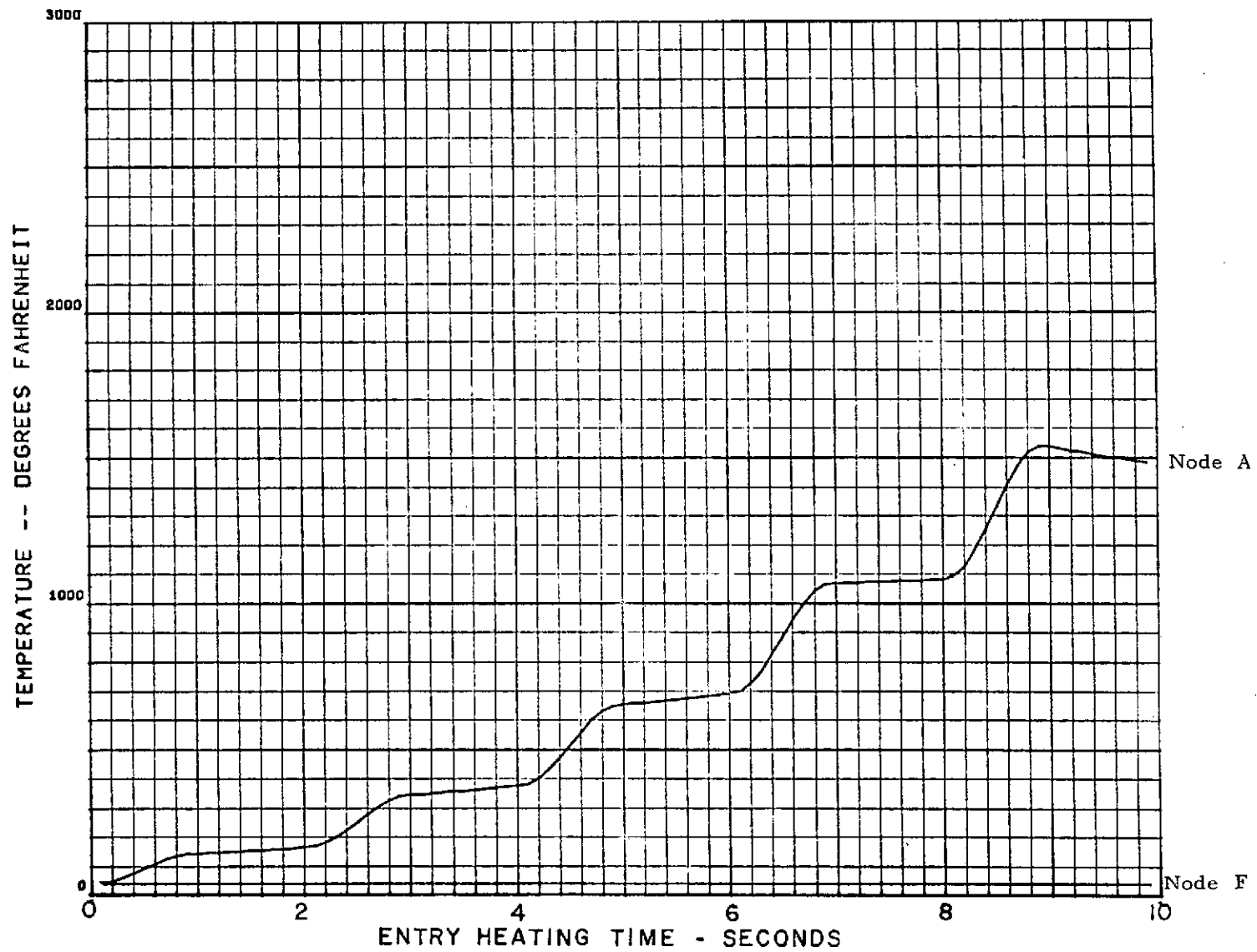


Figure 2-61. Atlas reentry heating for 180 deg/sec pitch rate model 11, 6 mil gage, 16 mil skin, max gap radiation.

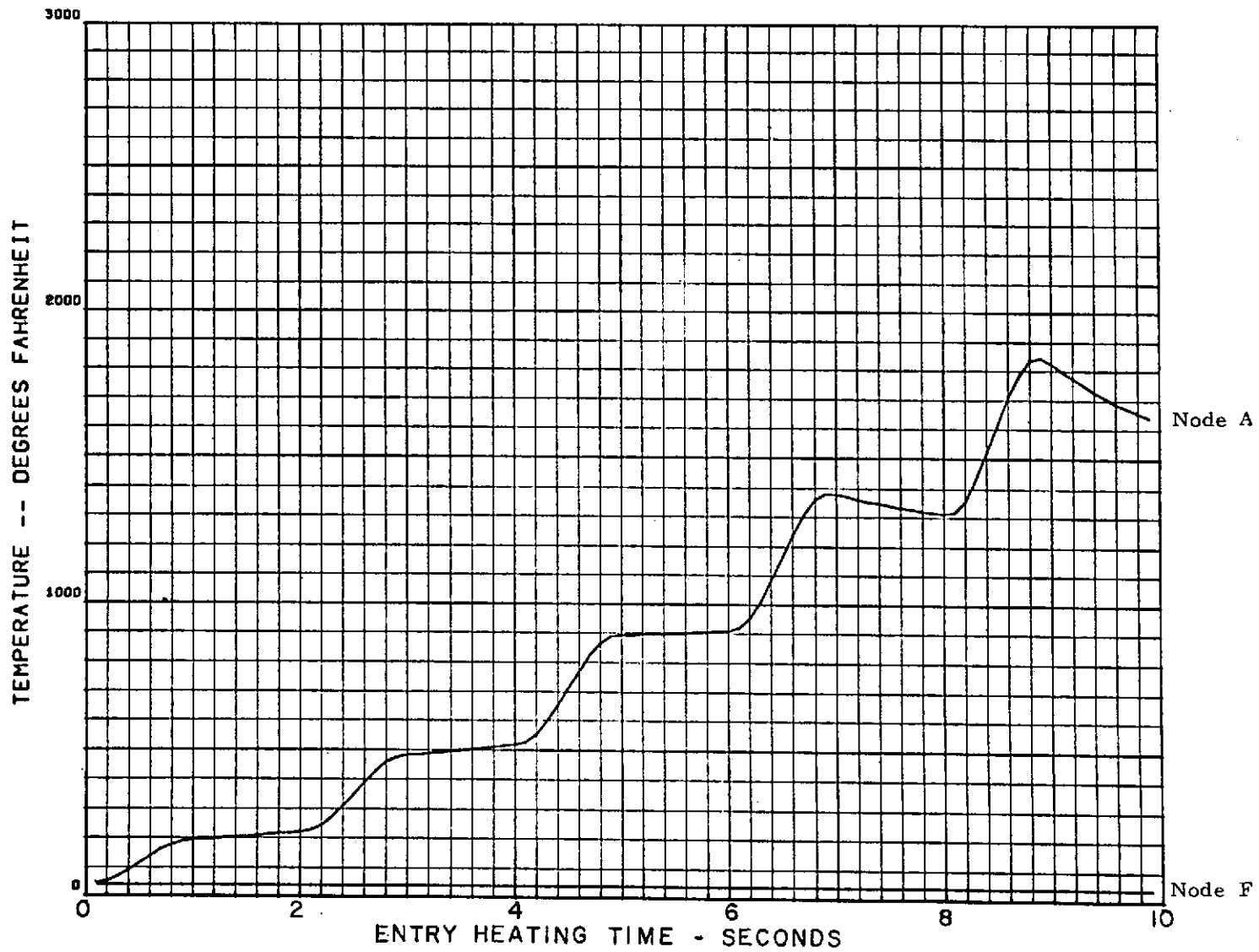


Figure 2-62. Atlas reentry heating for 180 deg/sec pitch rate model 12, 4 mil gage, 16 mil skin, max gap radiation.

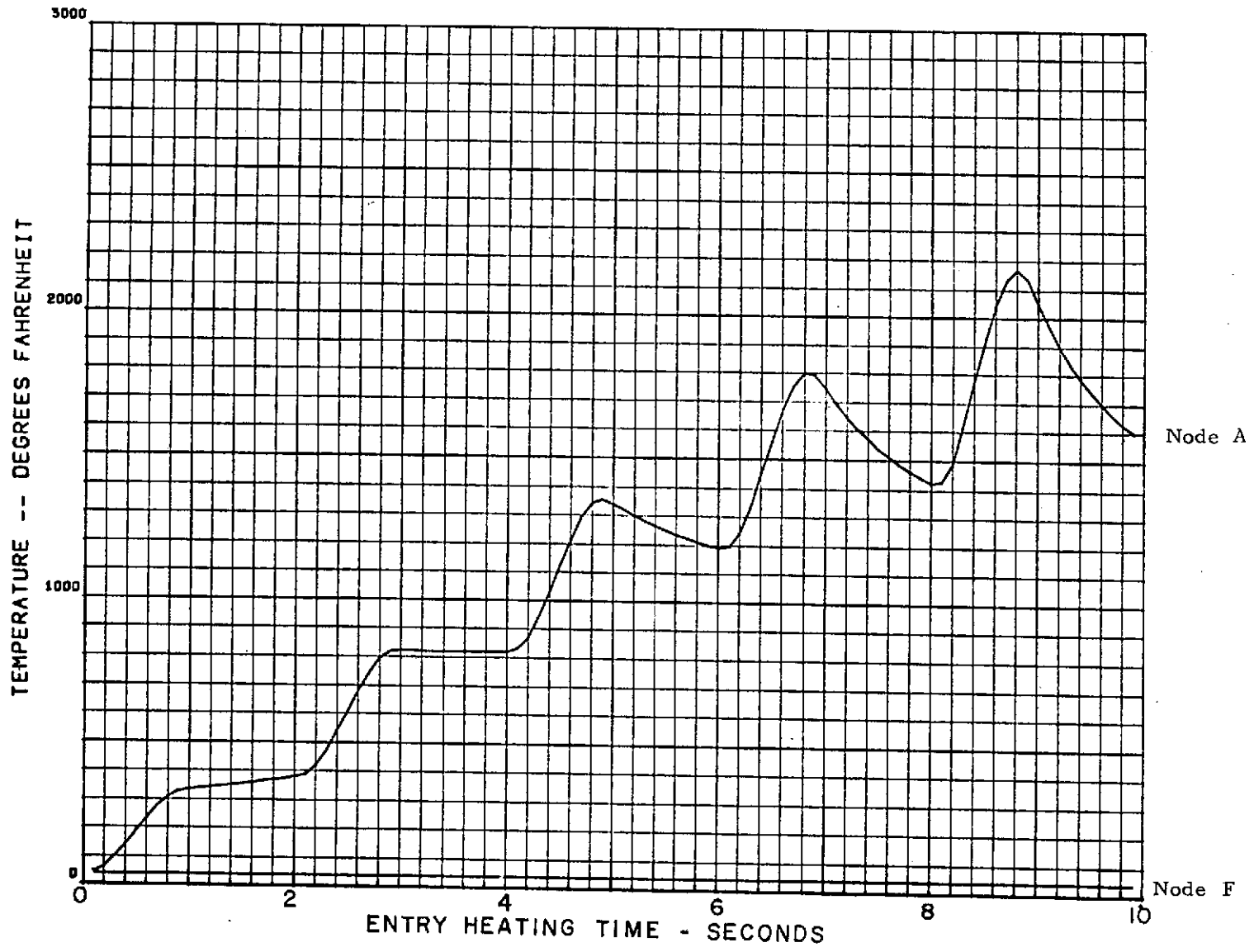


Figure 2-63. Atlas reentry heating for 180 deg/sec pitch rate model 13, 2 mil gage, 16 mil skin, max gap radiation.

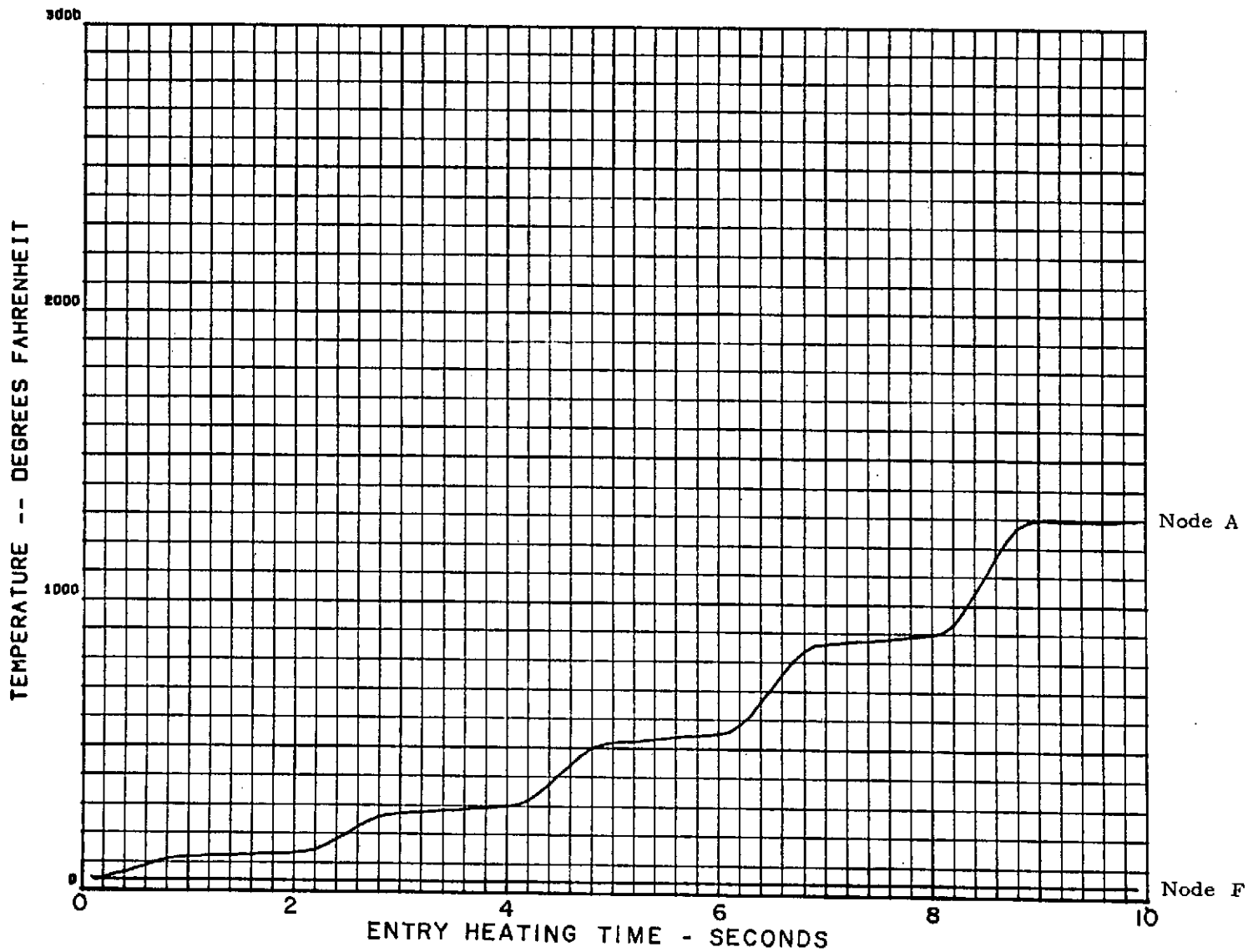


Figure 2-64. Atlas reentry heating for 180 deg/sec pitch rate model 14, 8 mil gage, 16 mil skin, gap radiates, $h_i=10$.

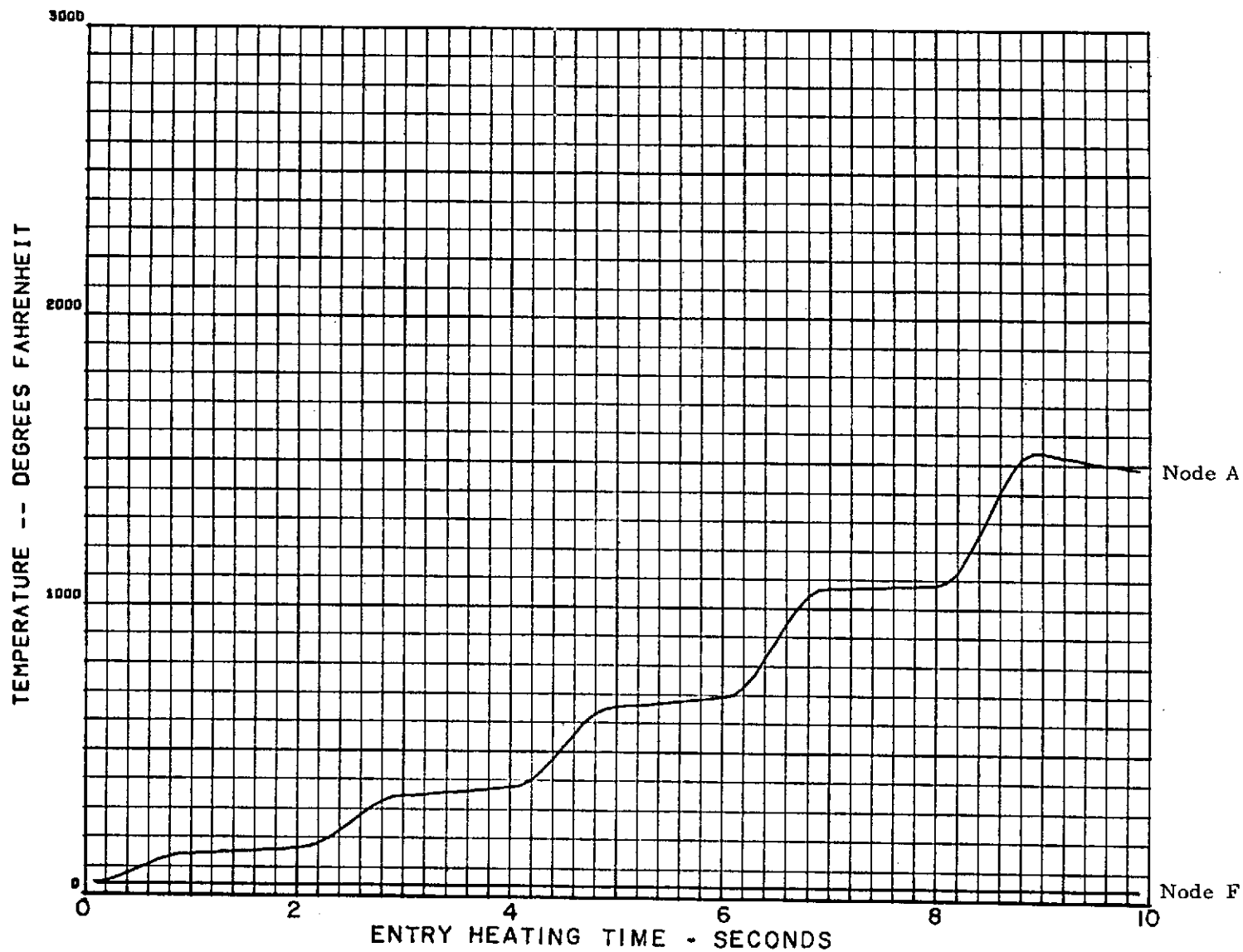


Figure 2-65. Atlas reentry heating for 180 deg/sec pitch rate model 15, 6 mil gage, 16 mil skin, gap radiates, $h_i=10$.

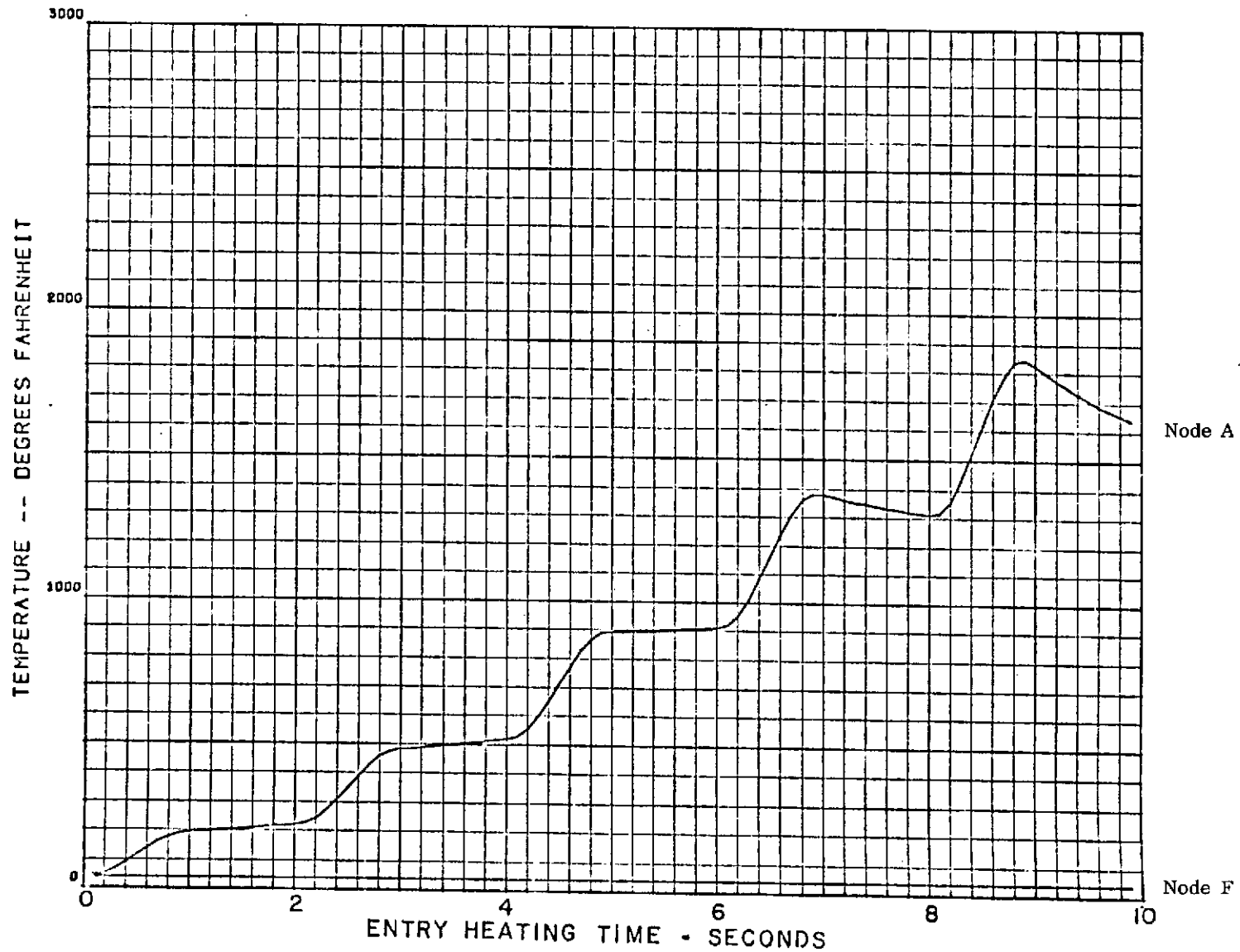


Figure 2-66. Atlas reentry heating for 180 deg/sec pitch rate model 16, 4 mil gage, 16 mil skin, gap radiates, $h_i=10$.

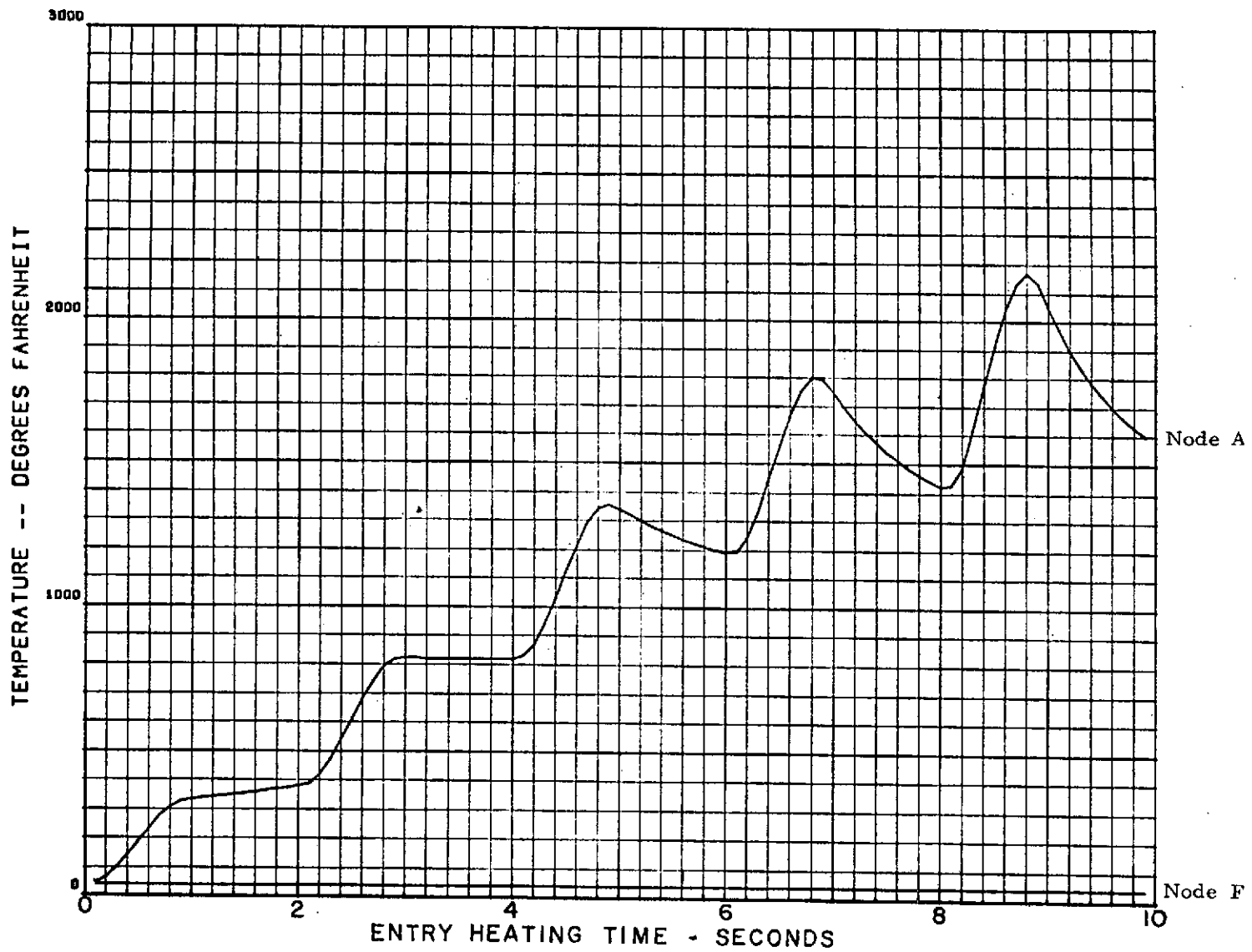


Figure 2-67. Atlas reentry heating for 180 deg/sec pitch rate model 17, 2 mil gage, 16 mil skin, gap radiates, $h_i=10$.

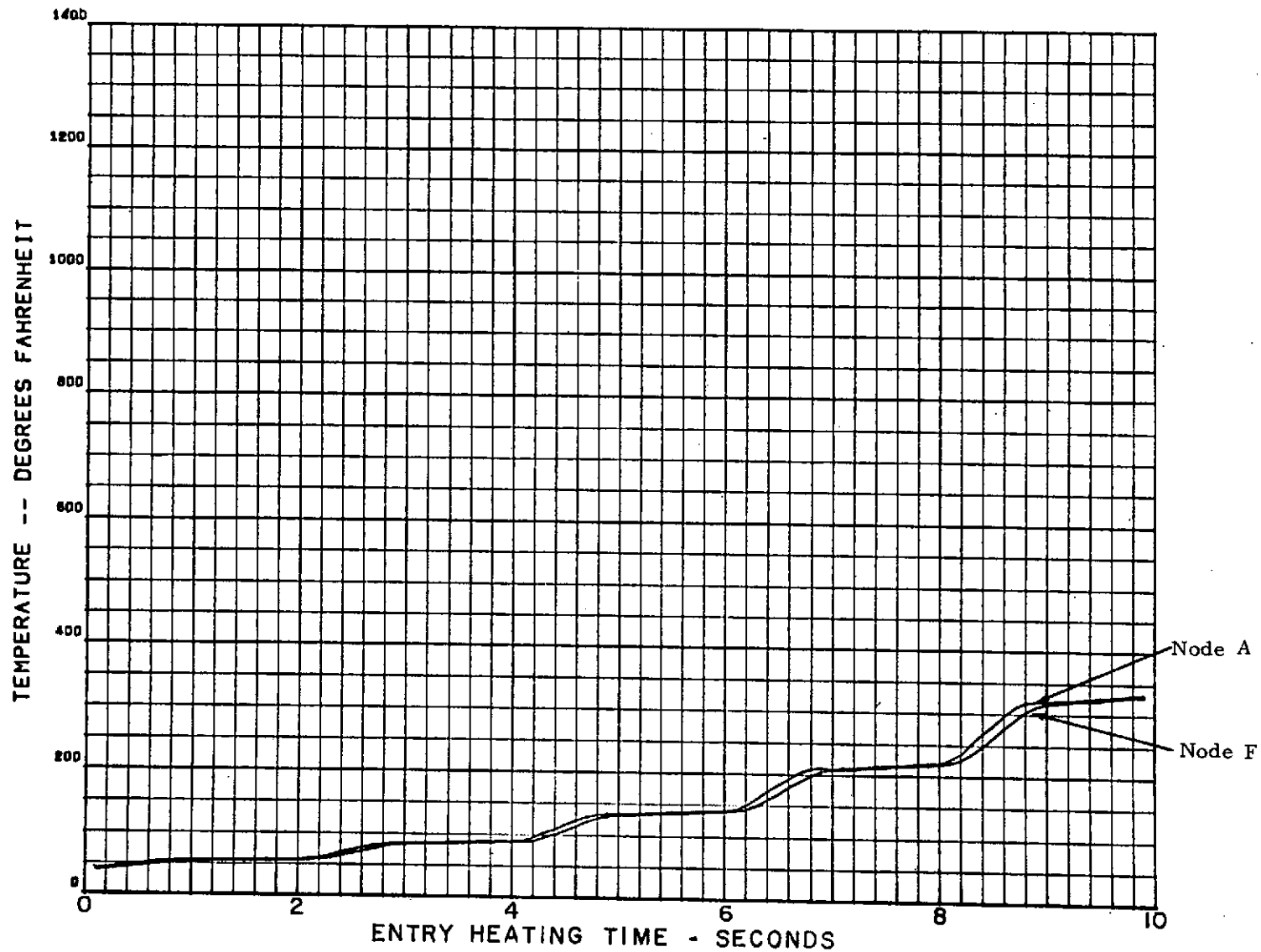


Figure 2-68. Atlas reentry heating for 180 deg/sec pitch rate model 18, 8 mil gage, 16 mil skin, heat leak, rho=485.

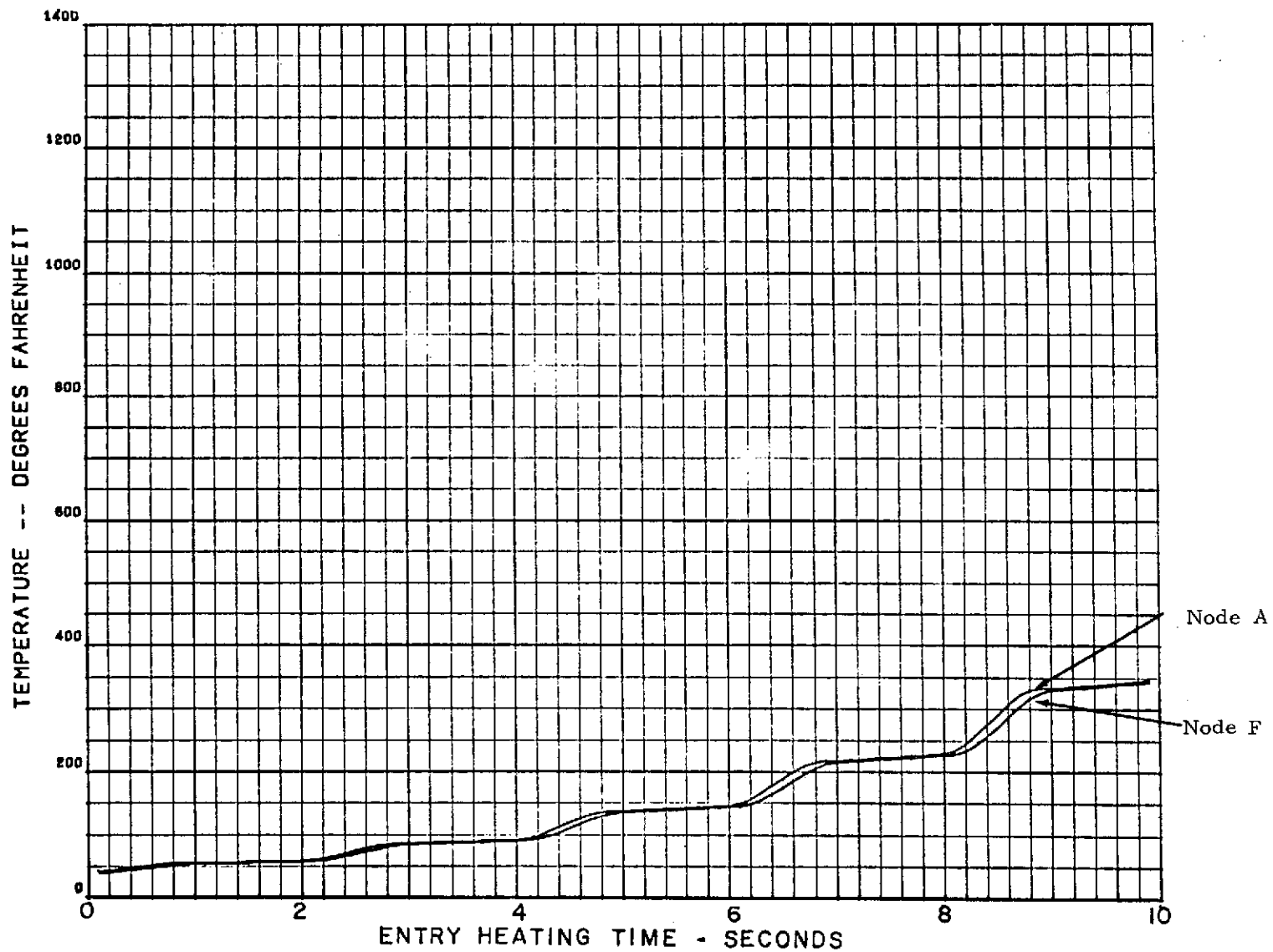


Figure 2-69. Atlas reentry heating for 180 deg/sec pitch rate model 19, 6 mil gage, 16 mil skin, heat leak, rho=485.

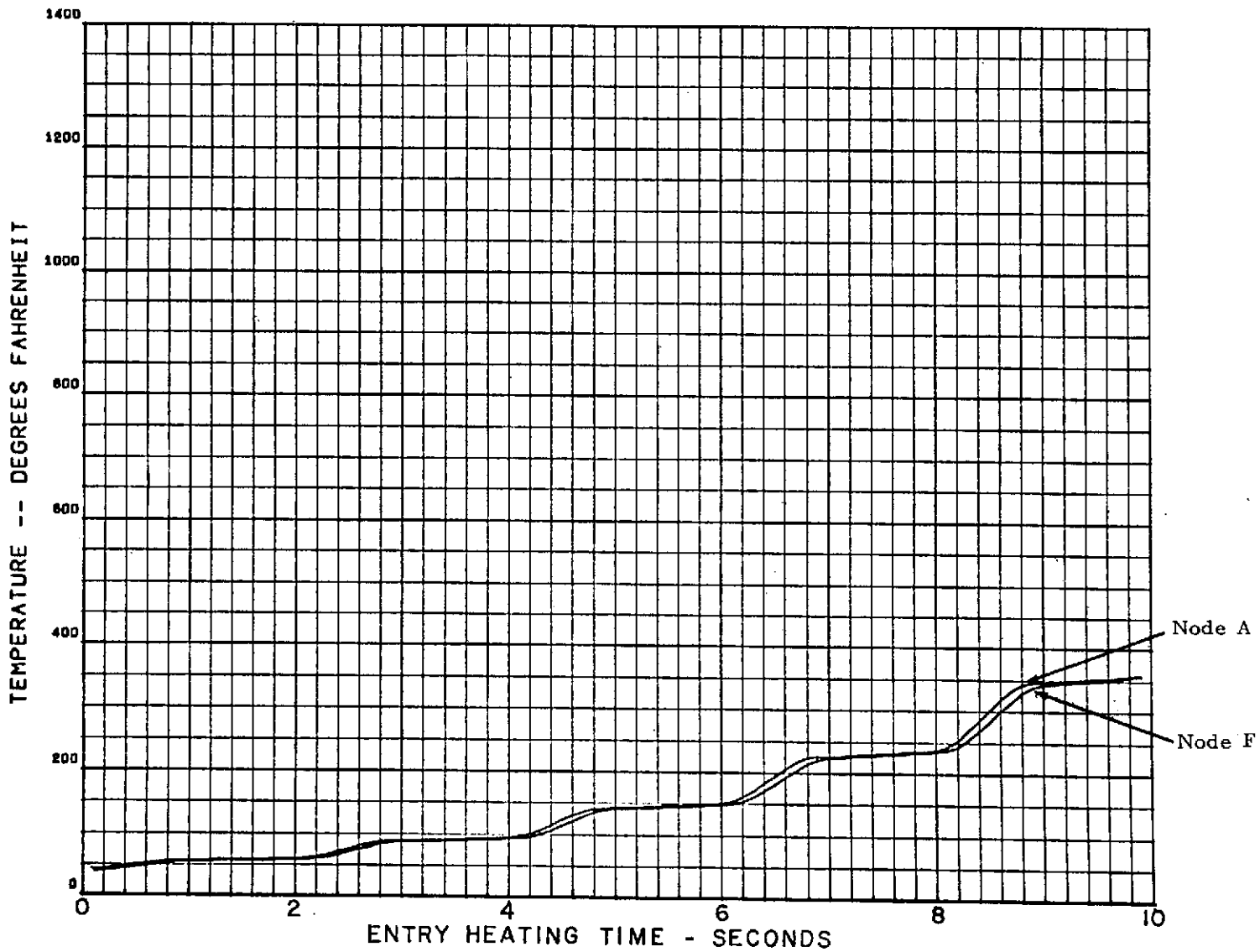


Figure 2-70. Atlas reentry heating for 180 deg/sec pitch rate model 20, 4 mil gage, 16 mil skin, heat leak, rho=485.

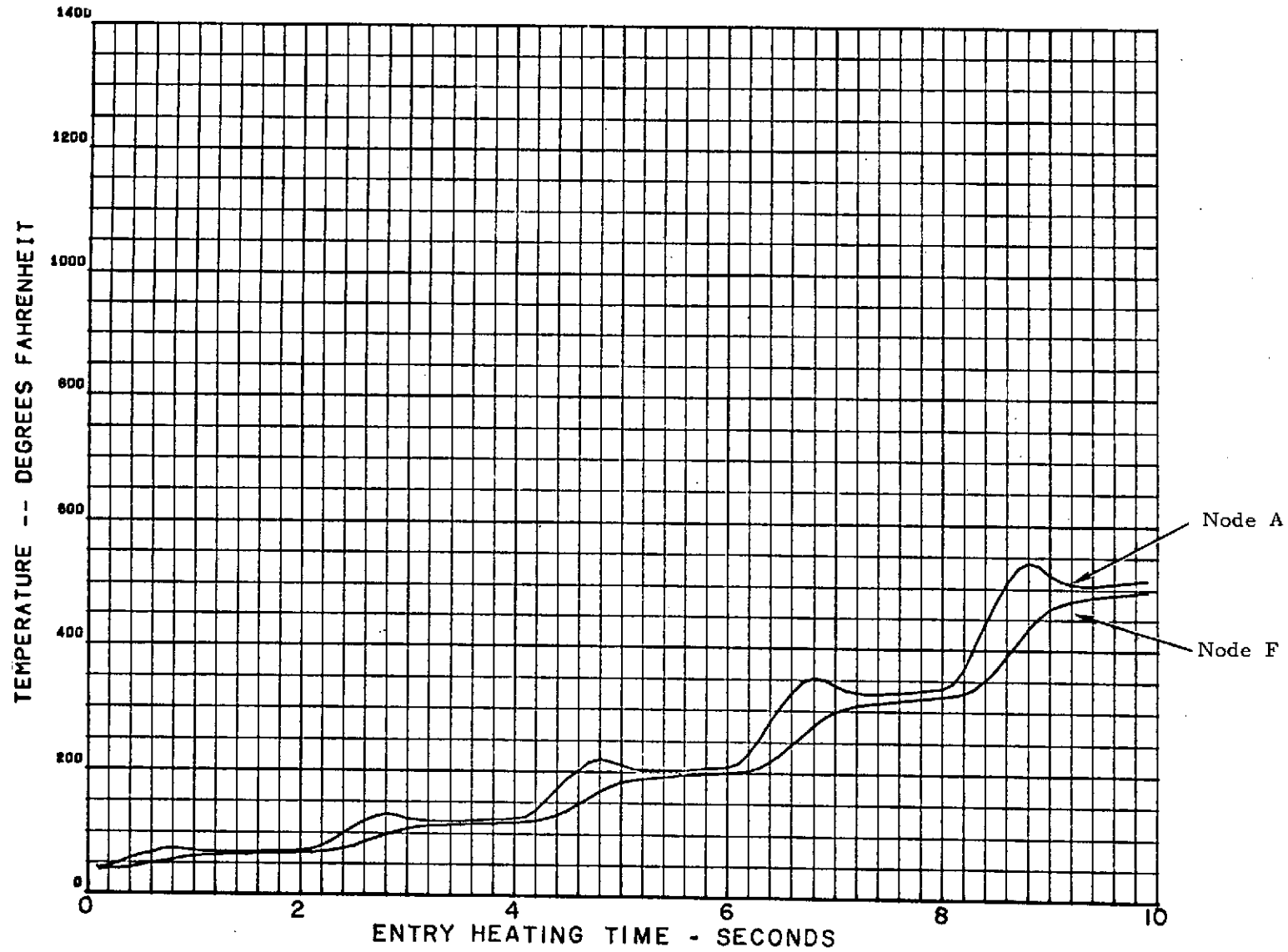


Figure 2-71. Atlas reentry heating for 180 deg/sec pitch rate model 21, 8 mil gage, 16 mil skin, heat leak, rho=48.5.

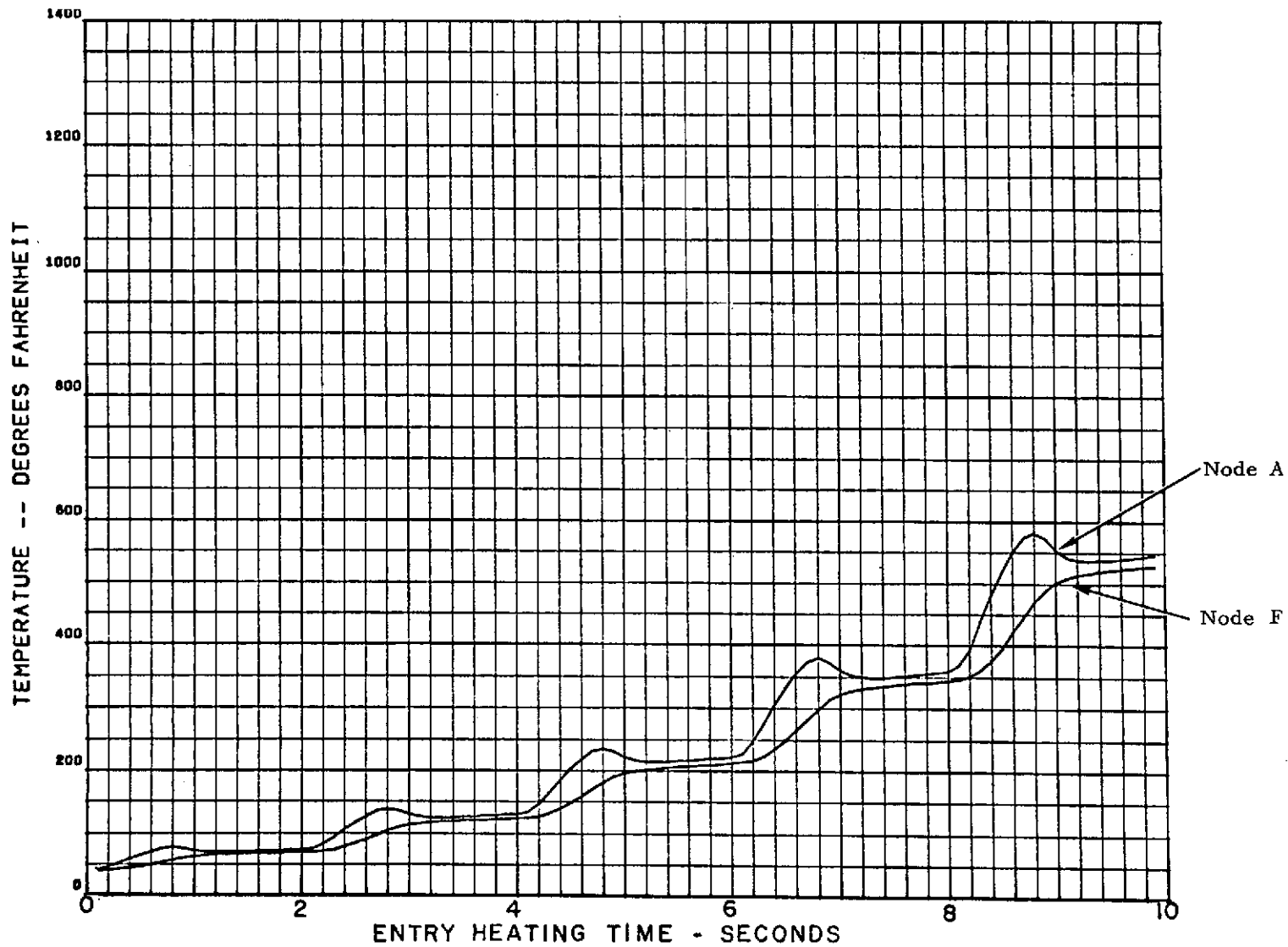


Figure 2-72. Atlas reentry heating for 180 deg/sec pitch rate model 22, 6 mil gage, 16 mil skin, heat leak, rho=48.5.

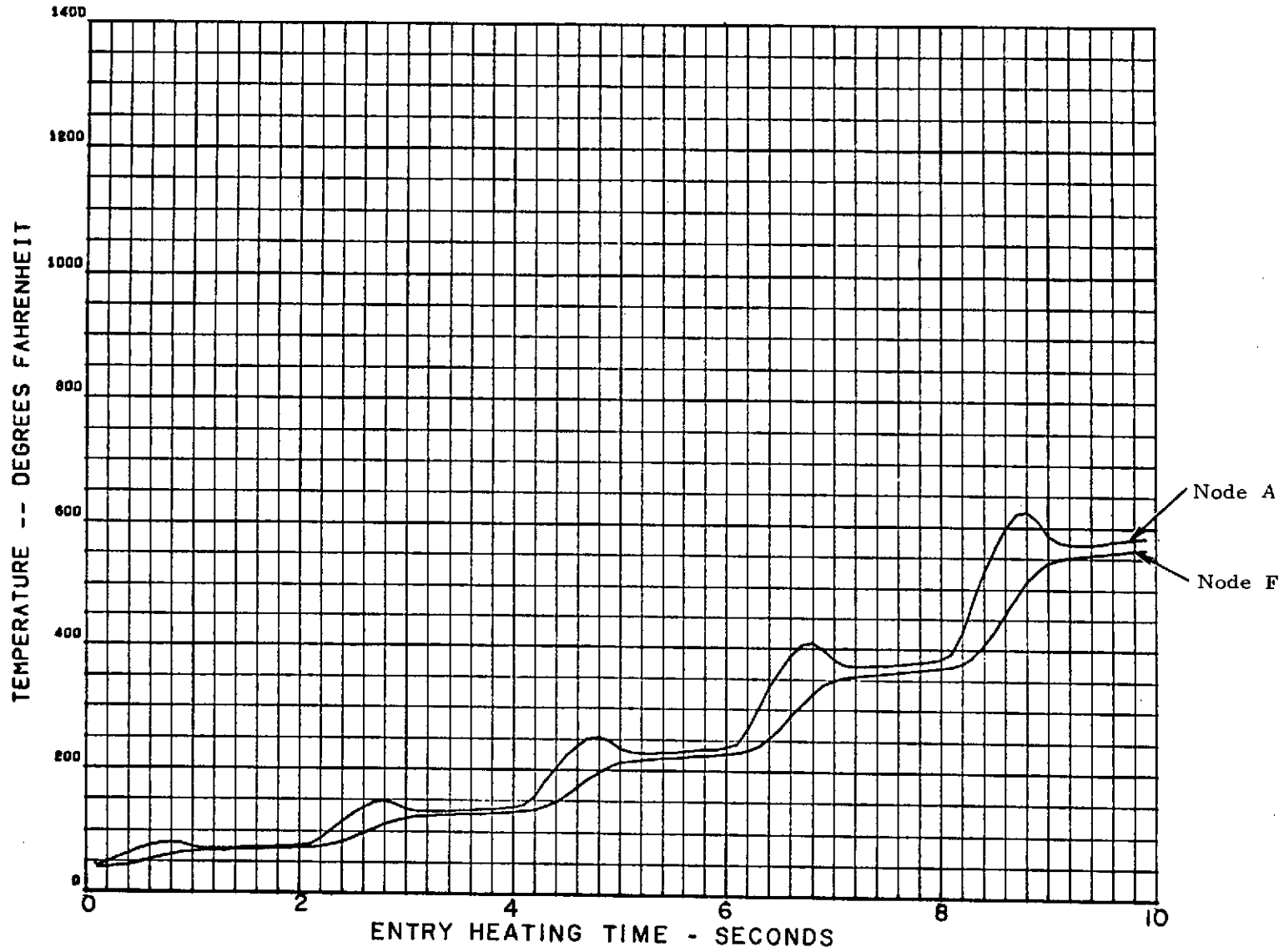


Figure 2-73. Atlas reentry heating for 180 deg/sec pitch rate model 23, 4 mil gage, 16 mil skin, heat leak, rho=48.5.

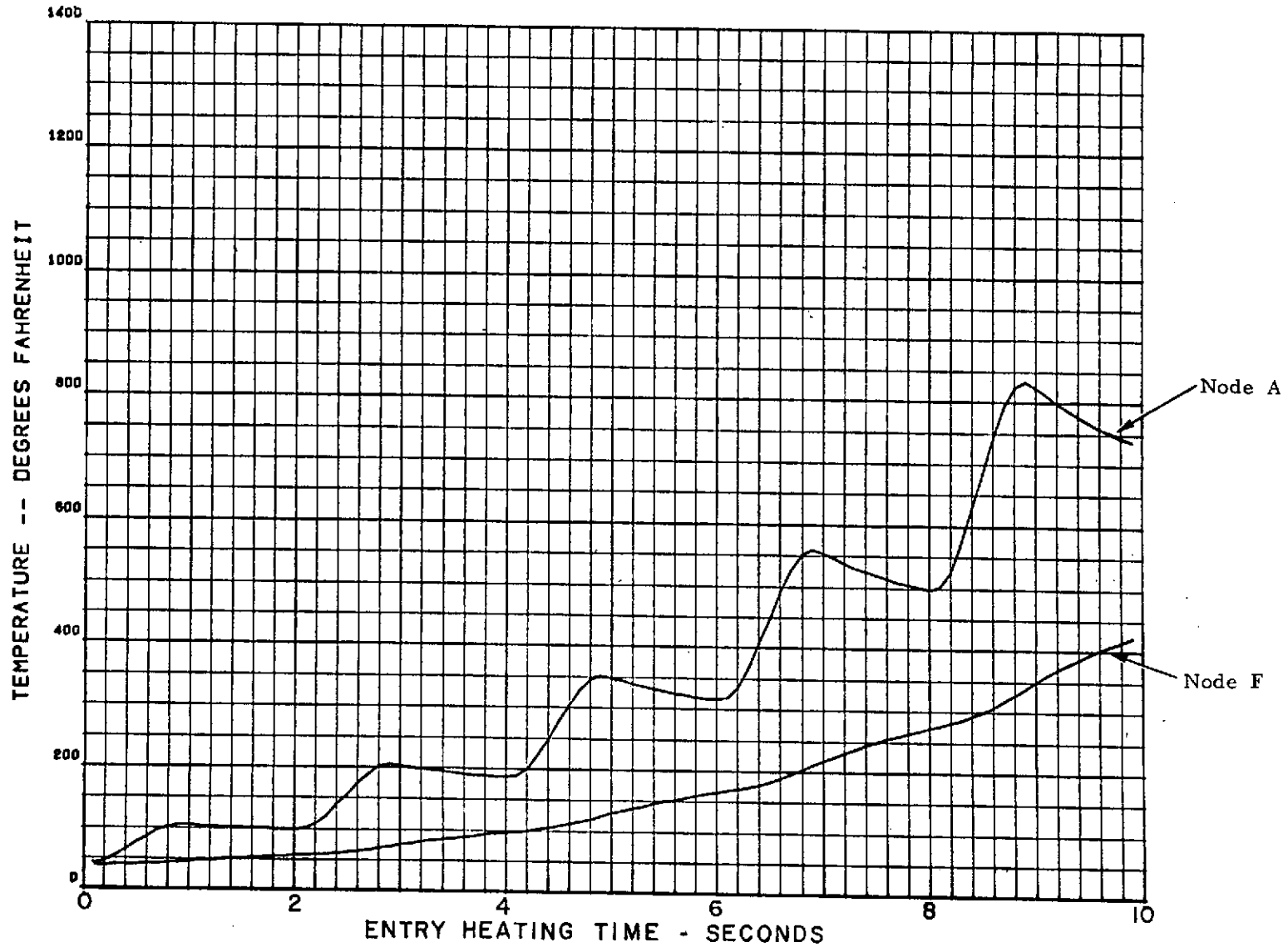


Figure 2-74. Atlas reentry heating for 180 deg/sec pitch rate model 24, 8 mil gage, 16 mil skin, heat leak, $\rho=4.85$.

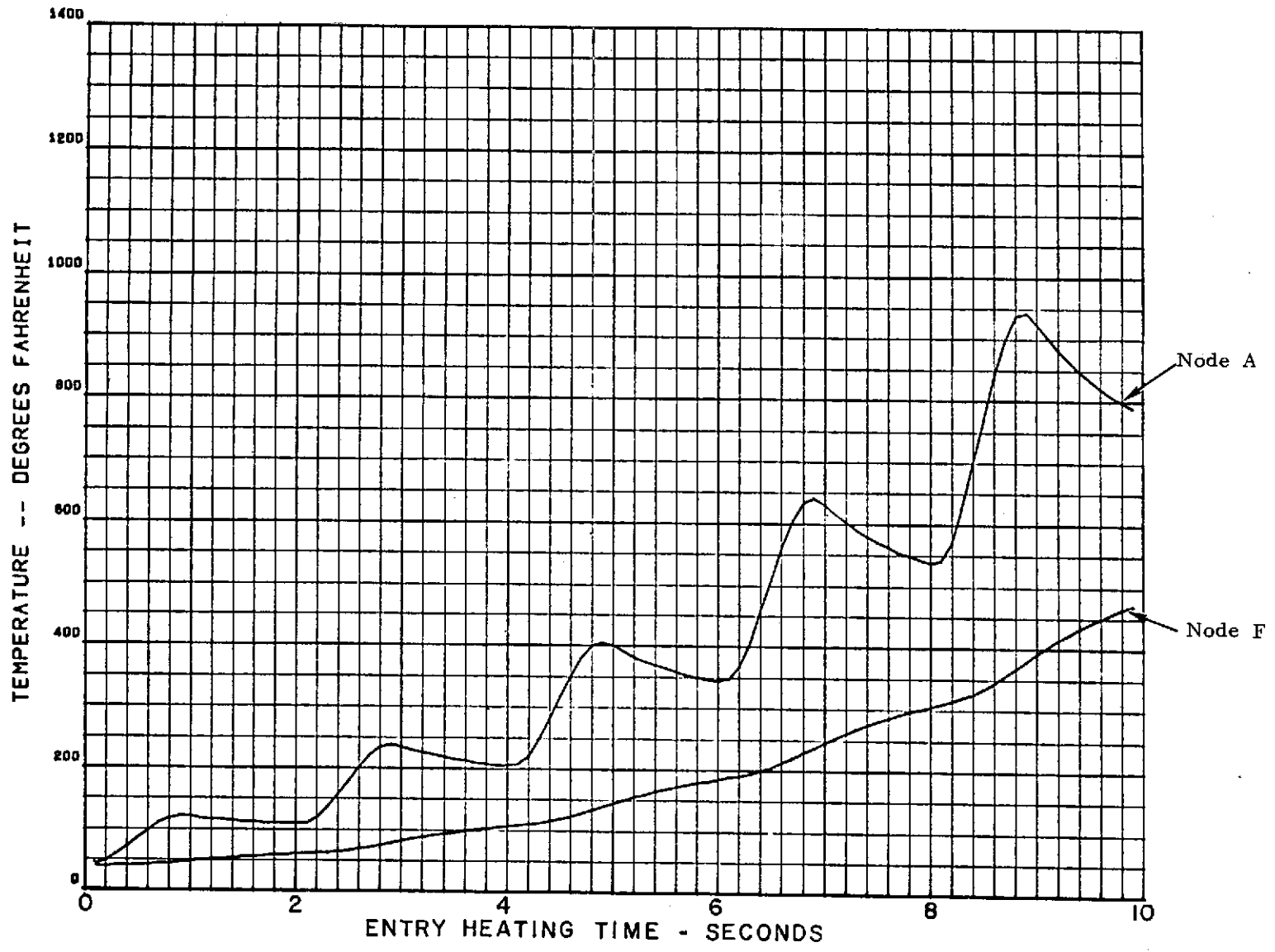


Figure 2-75. Atlas reentry heating for 180 deg/sec pitch rate model 25, 6 mil gage, 16 mil skin, heat leak, rho=4.85.

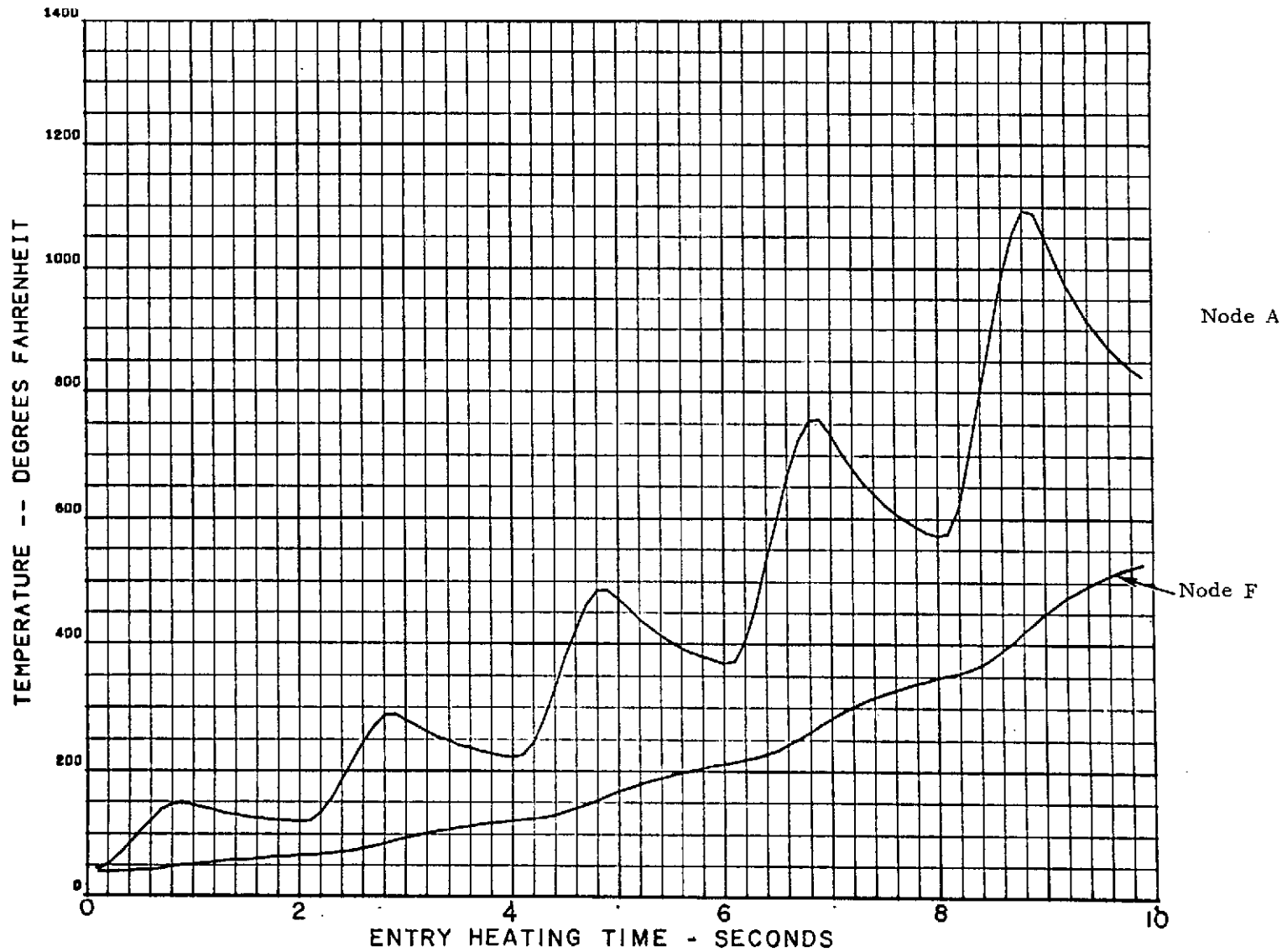


Figure 2-76. Atlas reentry heating for 180 deg/sec pitch rate model 26, 4 mil gage, 16 mil skin, heat leak, rho=4.85.

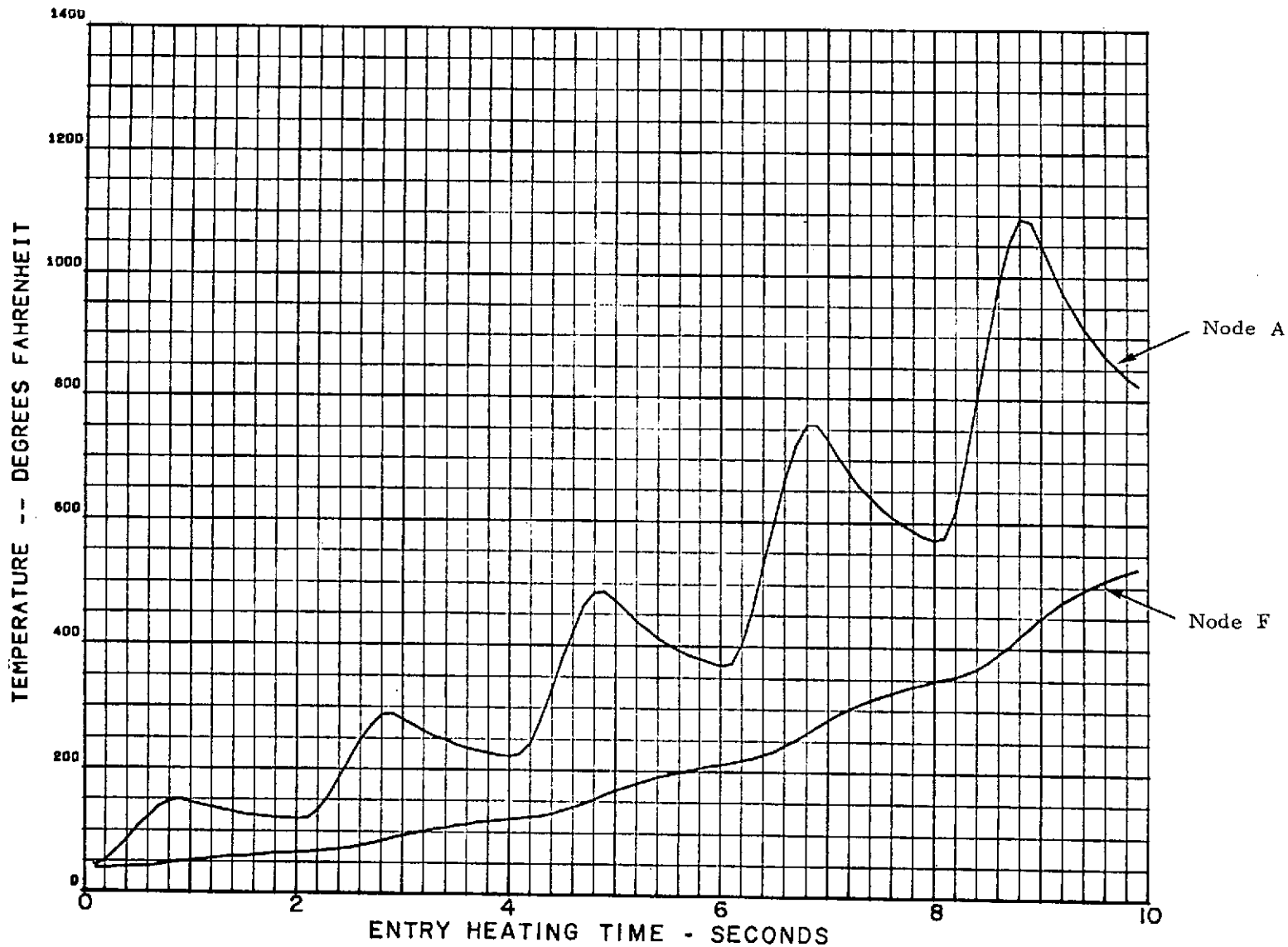


Figure 2-77. Atlas reentry heating for 180 deg/sec pitch rate model 27, 4 mil gage, 16 mil skin, heat leak, $\rho=4.85$.

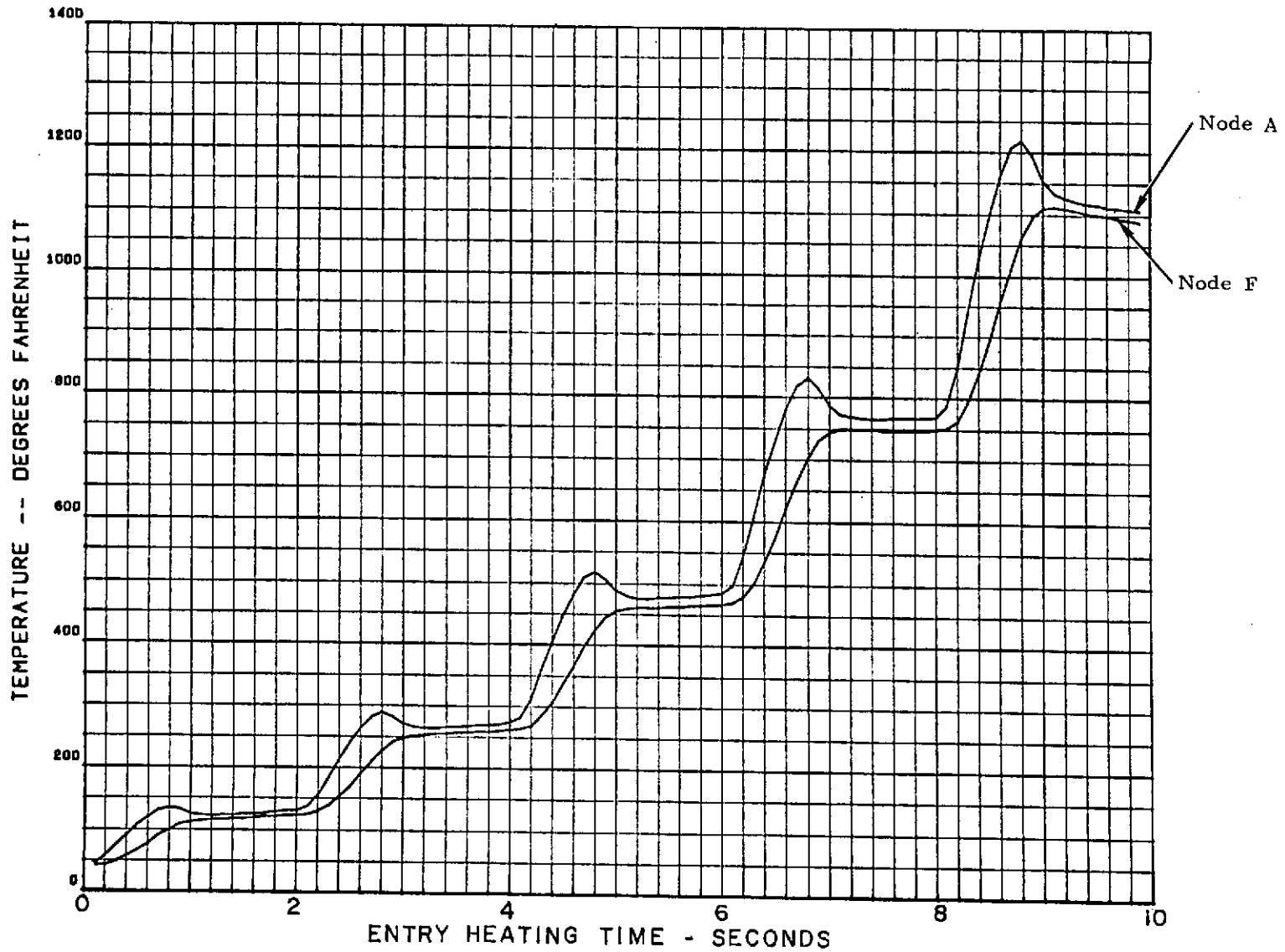


Figure 2-78. Atlas reentry heating for 180 deg/sec pitch rate model 28, 2 mil gage, 16 mil skin, heat leak, $\rho=4.85$.

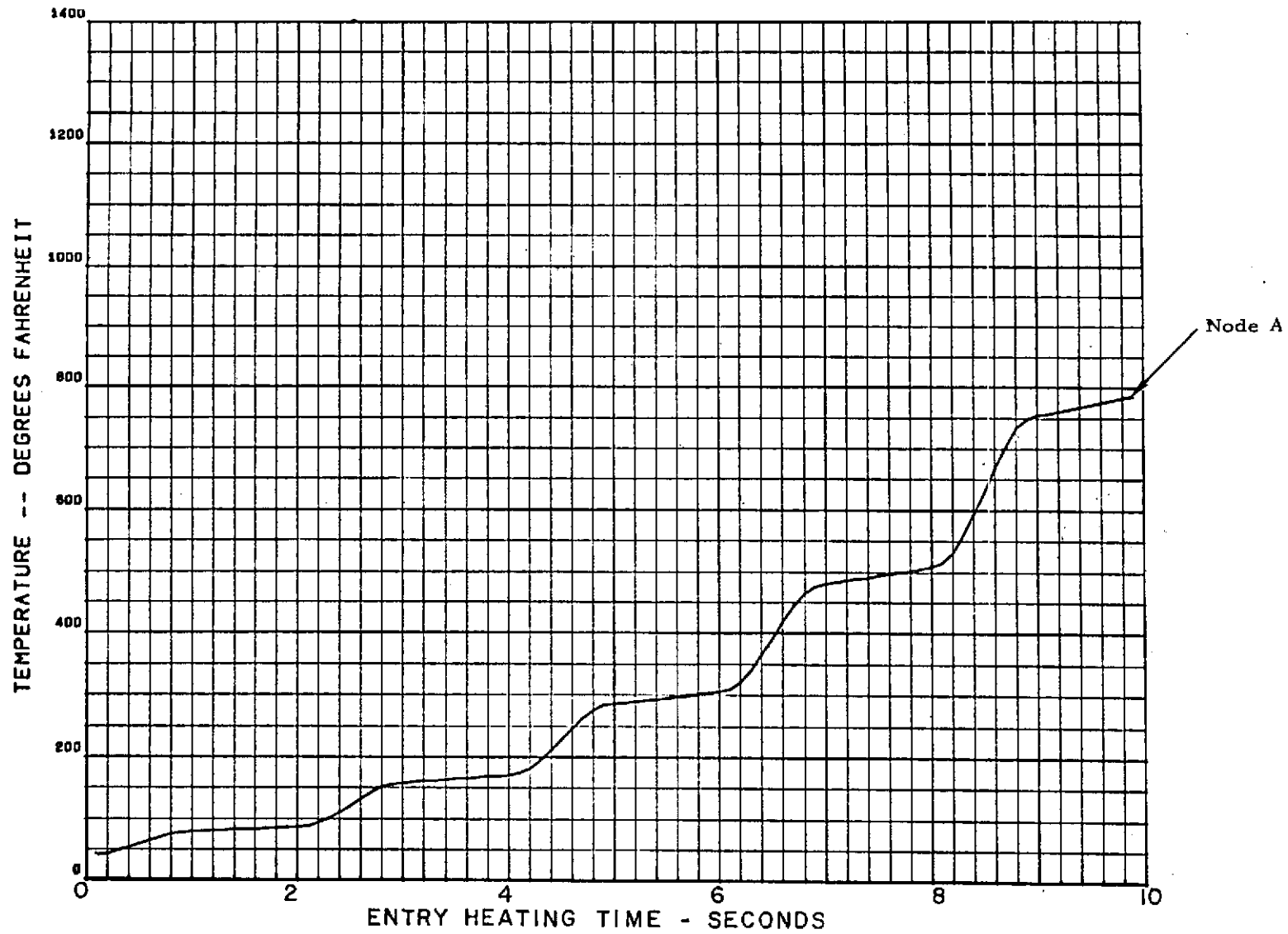


Figure 2-79. Atlas reentry heating for 180 deg/sec pitch rate model 29, 16 mil skin only, epsilon=.15 (in-out), hi=4.

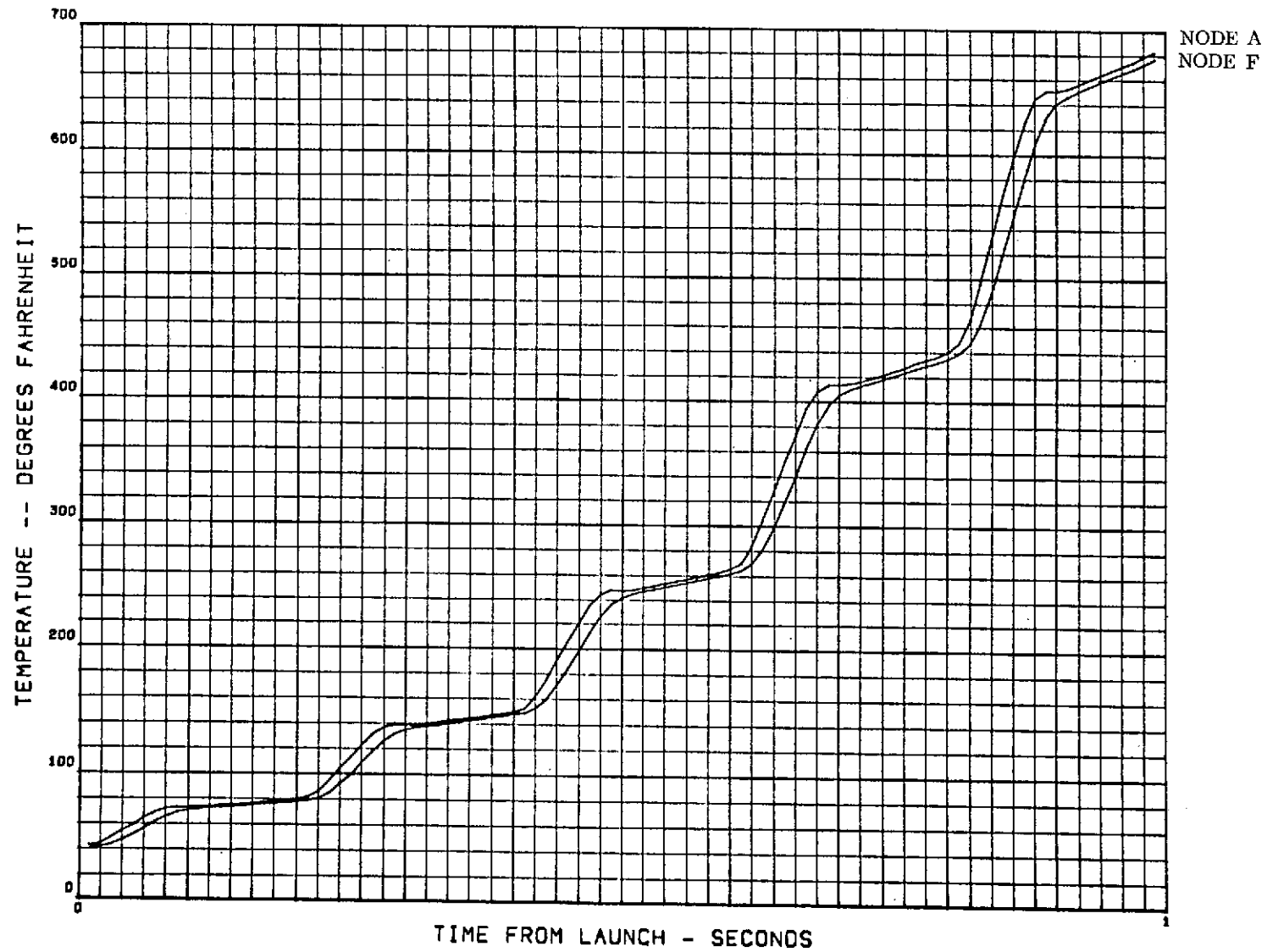


Figure 2-80. Atlas reentry heating for 180 deg/sec pitch rate model 30, 8 mil gage, 8 mil skin, gap radiates, $h_i=10$.

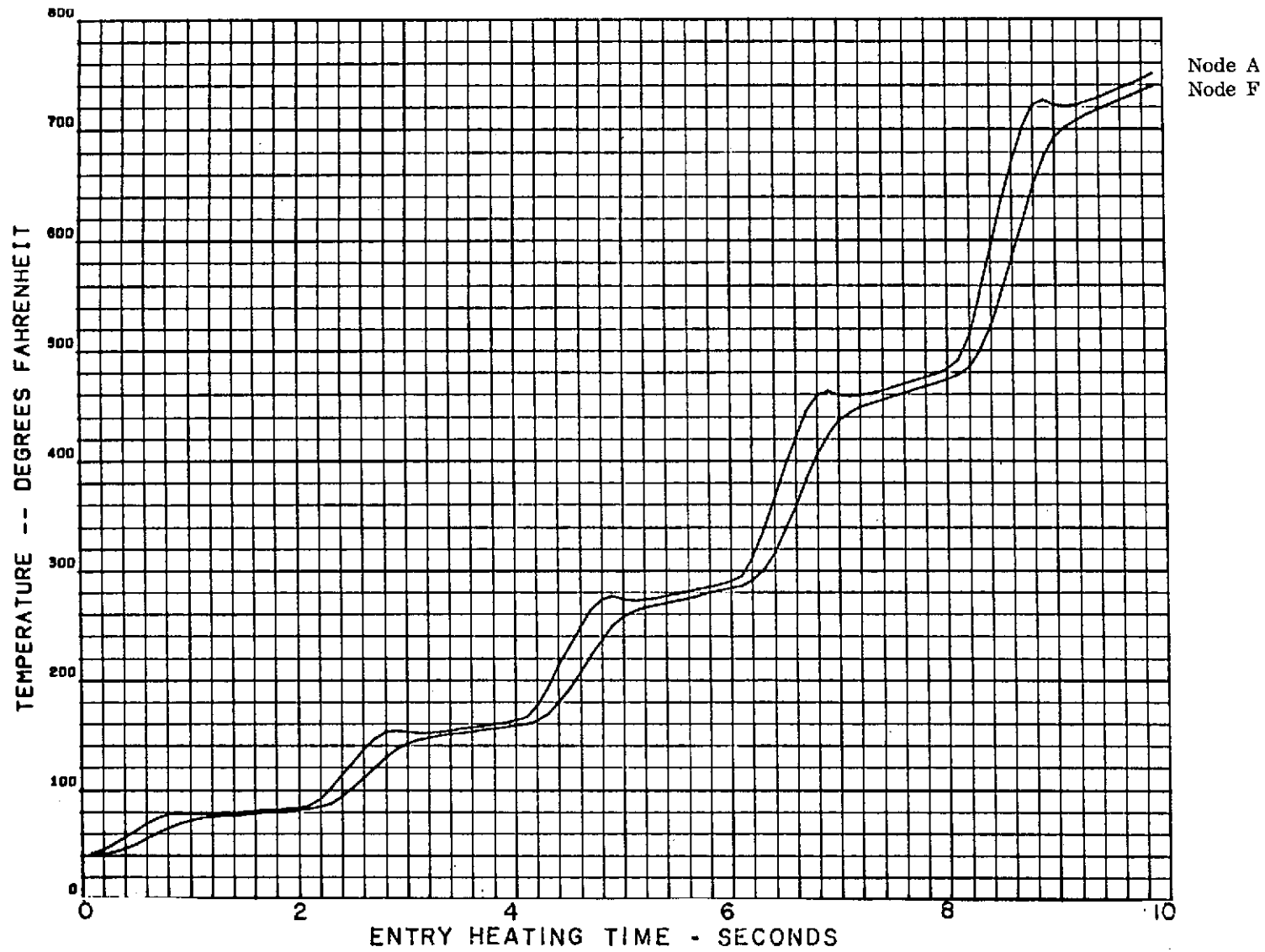


Figure 2-81. Atlas reentry heating for 180 deg/sec pitch rate model 31, 8 mil gage, 8 mil skin, 20 mil spacer/48.5.

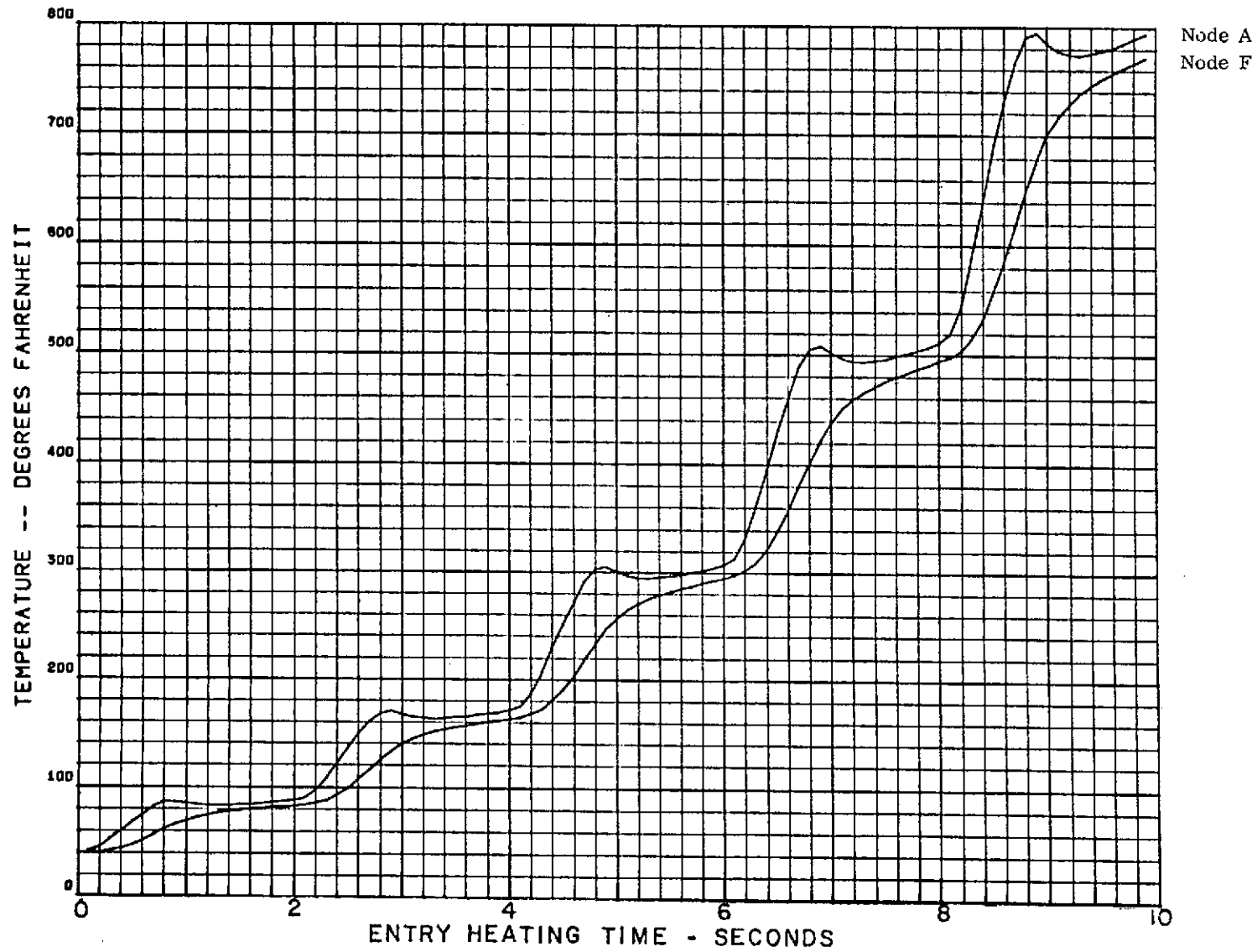


Figure 2-82. Atlas reentry heating for 180 deg/sec pitch rate model 32, 8 mil gage, 8 mil skin, 20 mil spacer/24.2.

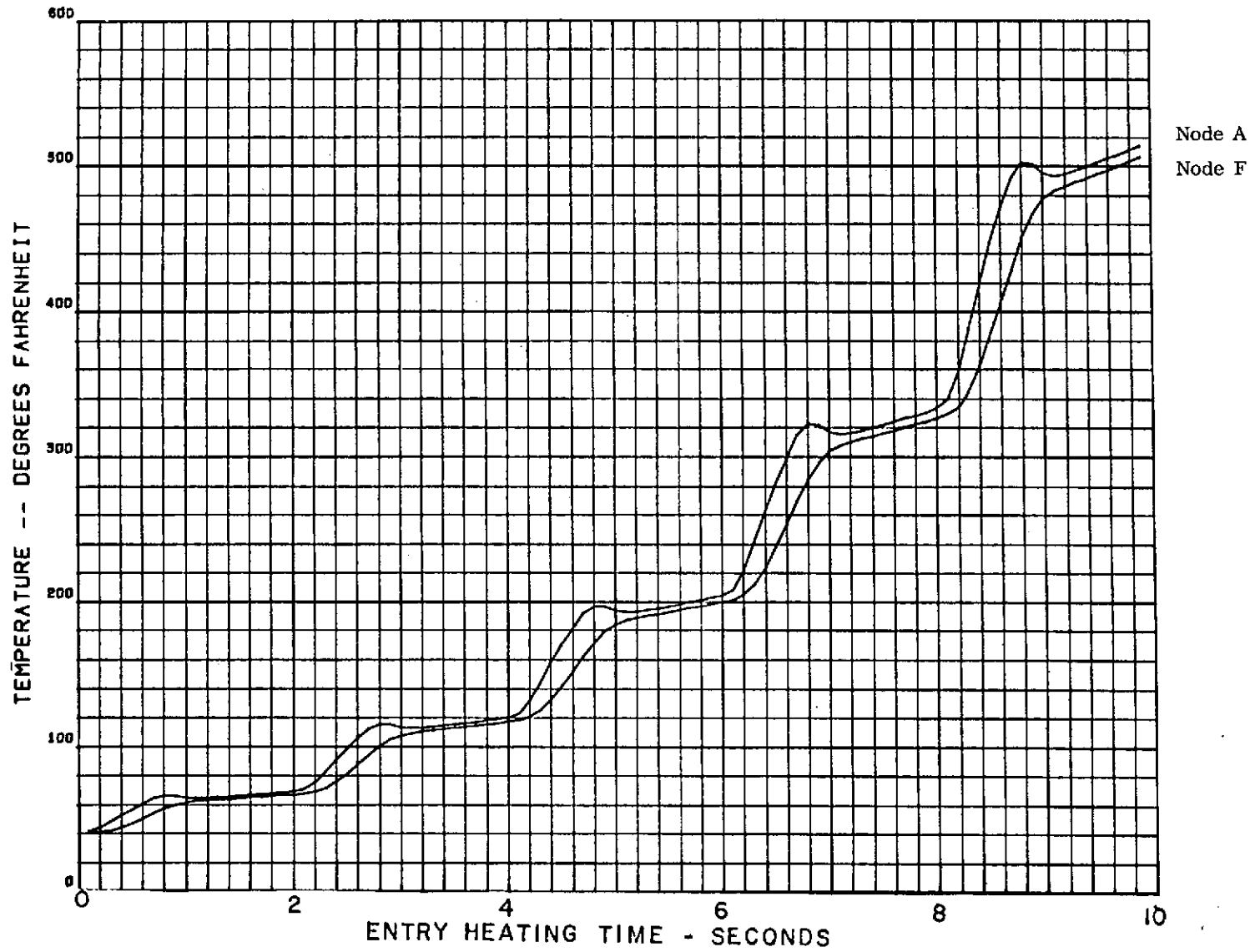


Figure 2-83. Atlas reentry heating for 180 deg/sec pitch rate model 33, 8 mil gage, 16 mil skin, 20 mil spacer/97.0.

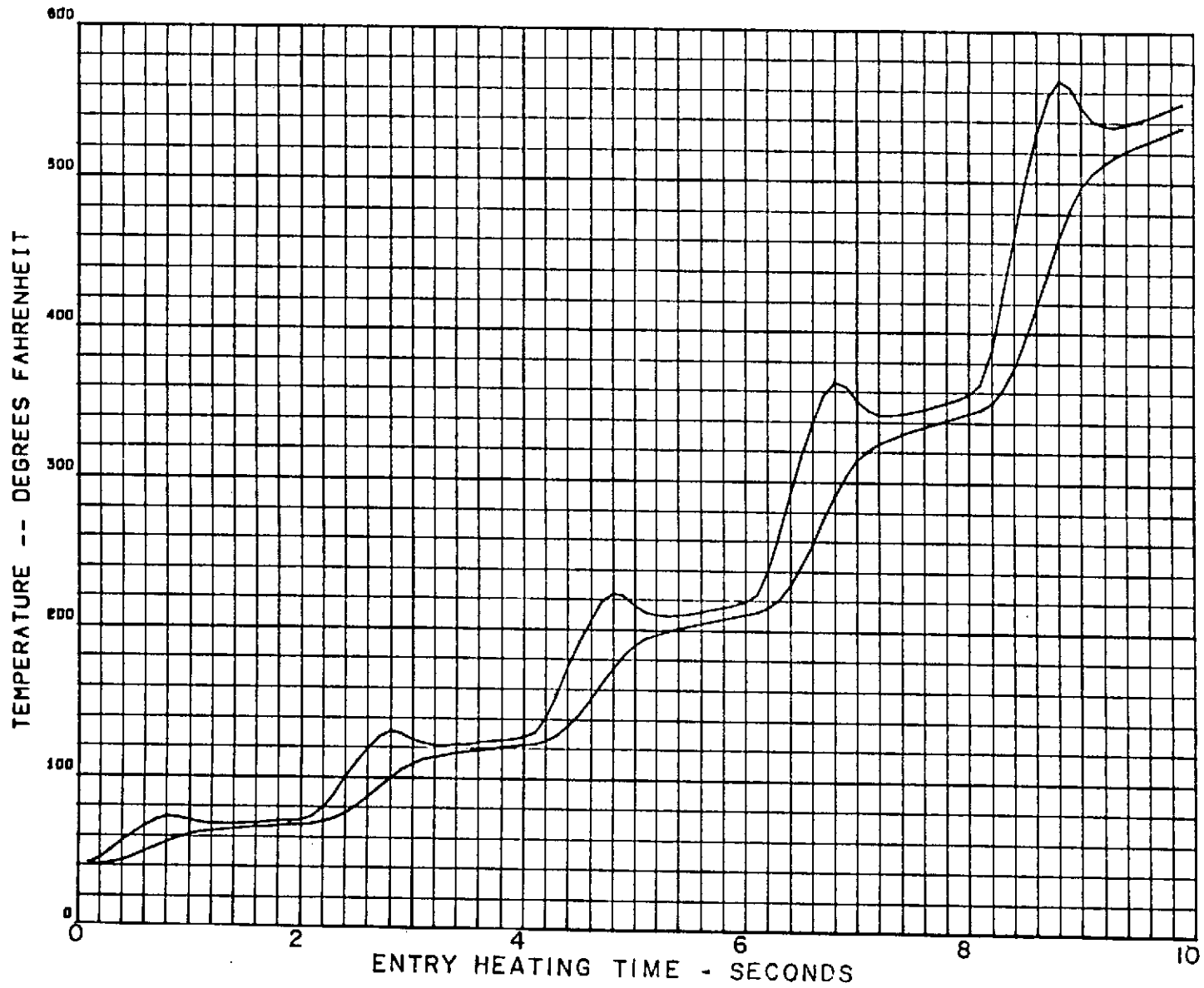


Figure 2-84. Atlas reentry heating for 180 deg/sec pitch rate model 34, 8 mil gage, 16 mil skin, 20 mil spacer/48.5.

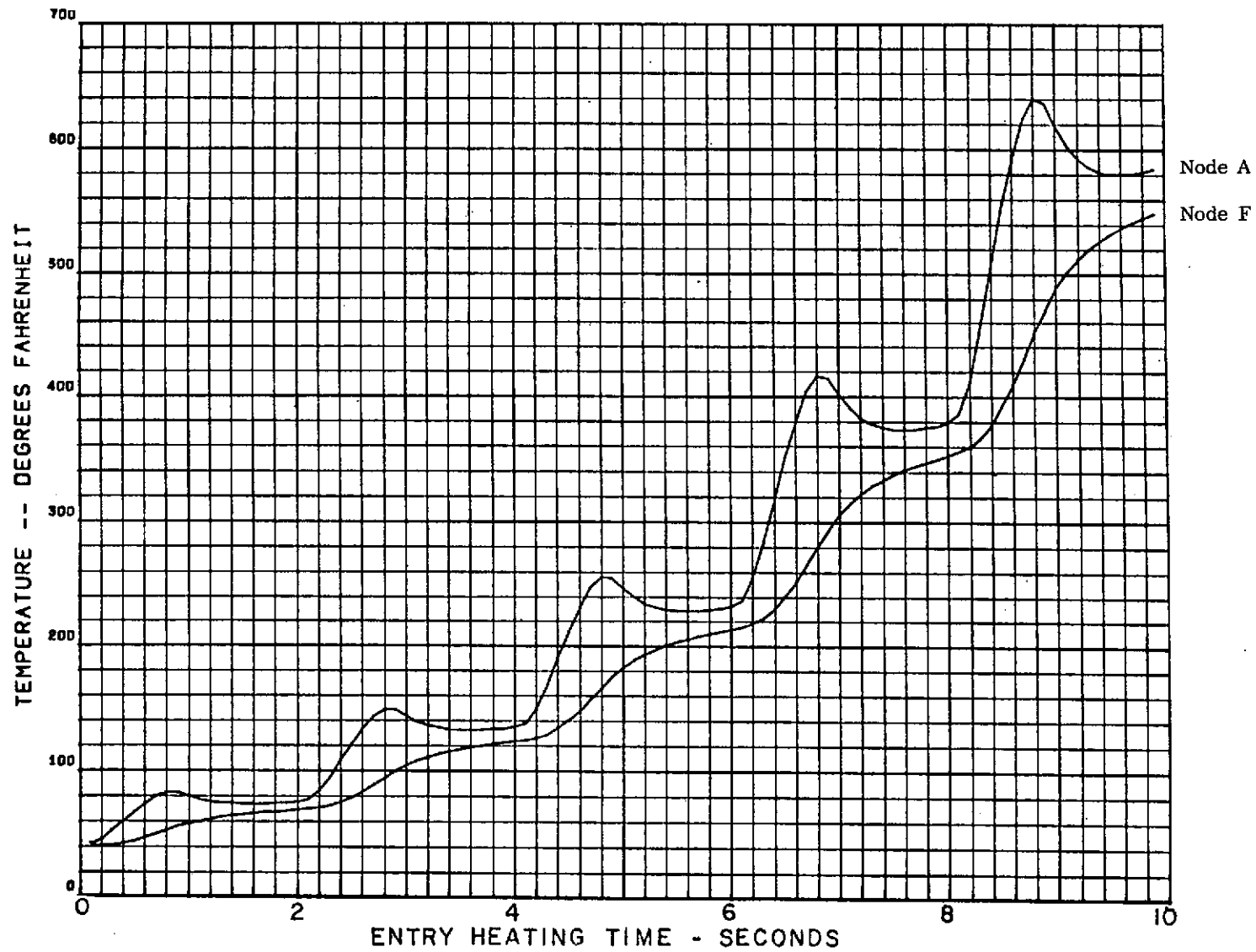


Figure 2-85. Atlas reentry heating for 180 deg/sec pitch rate model 35, 8 mil gage, 16 mil skin, 20 mil spacer/24.2.

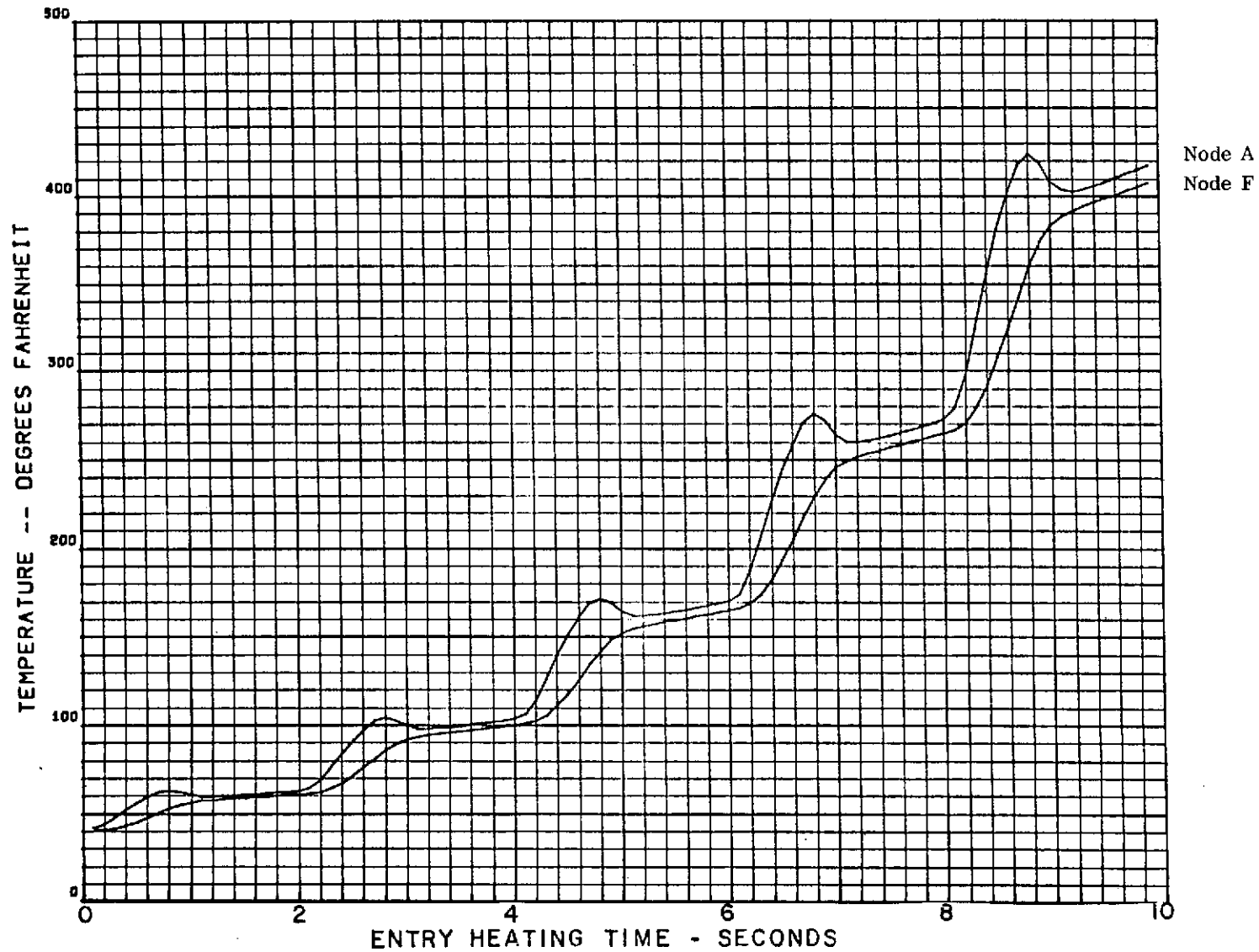


Figure 2-86. Atlas reentry heating for 180 deg/sec pitch rate model 36, 8 mil gage, 24 mil skin, 20 mil spacer/97.0.

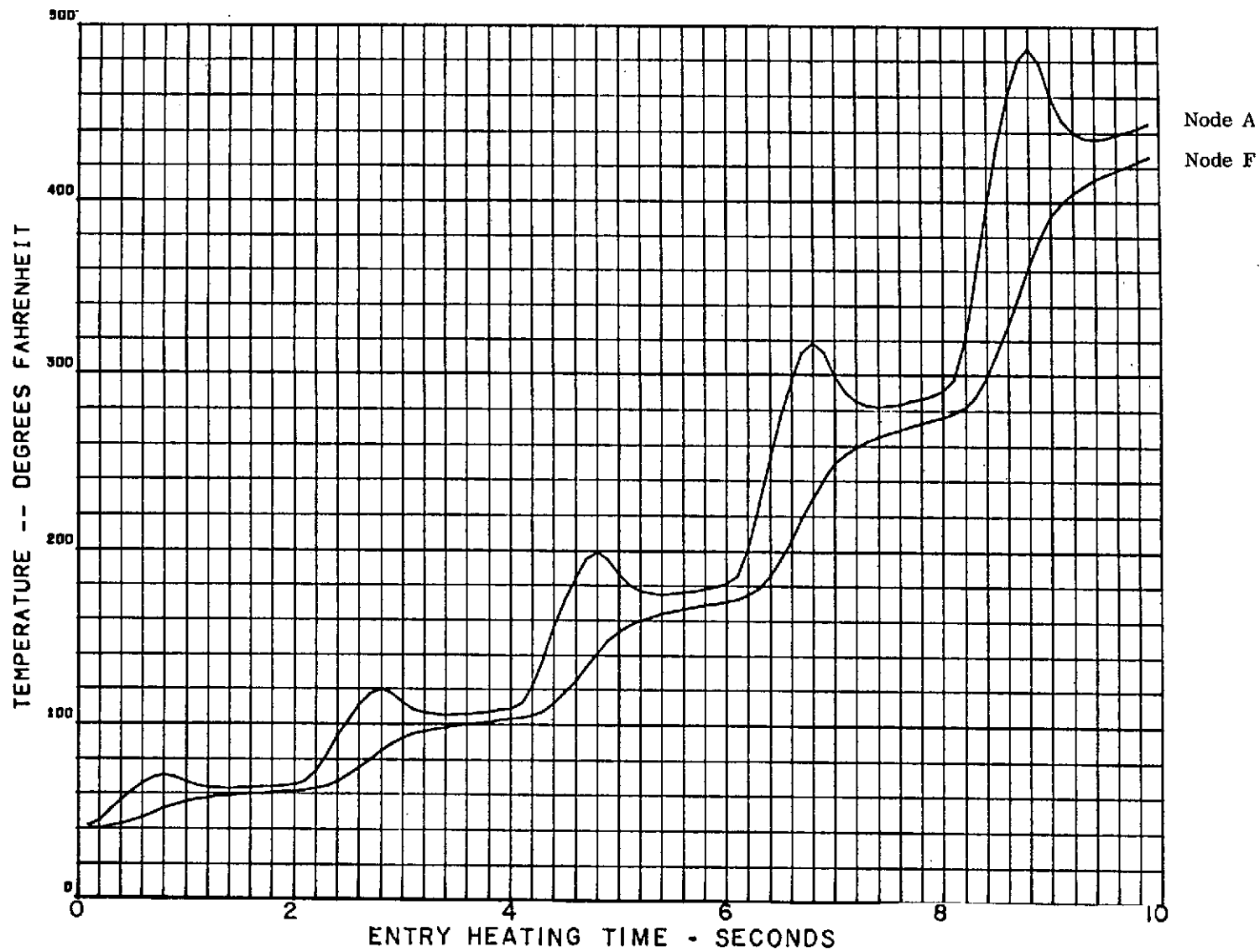


Figure 2-87. Atlas reentry heating for 180 deg/sec pitch rate model 37, 8 mil gage, 24 mil skin, 20 mil spacer/48.5.

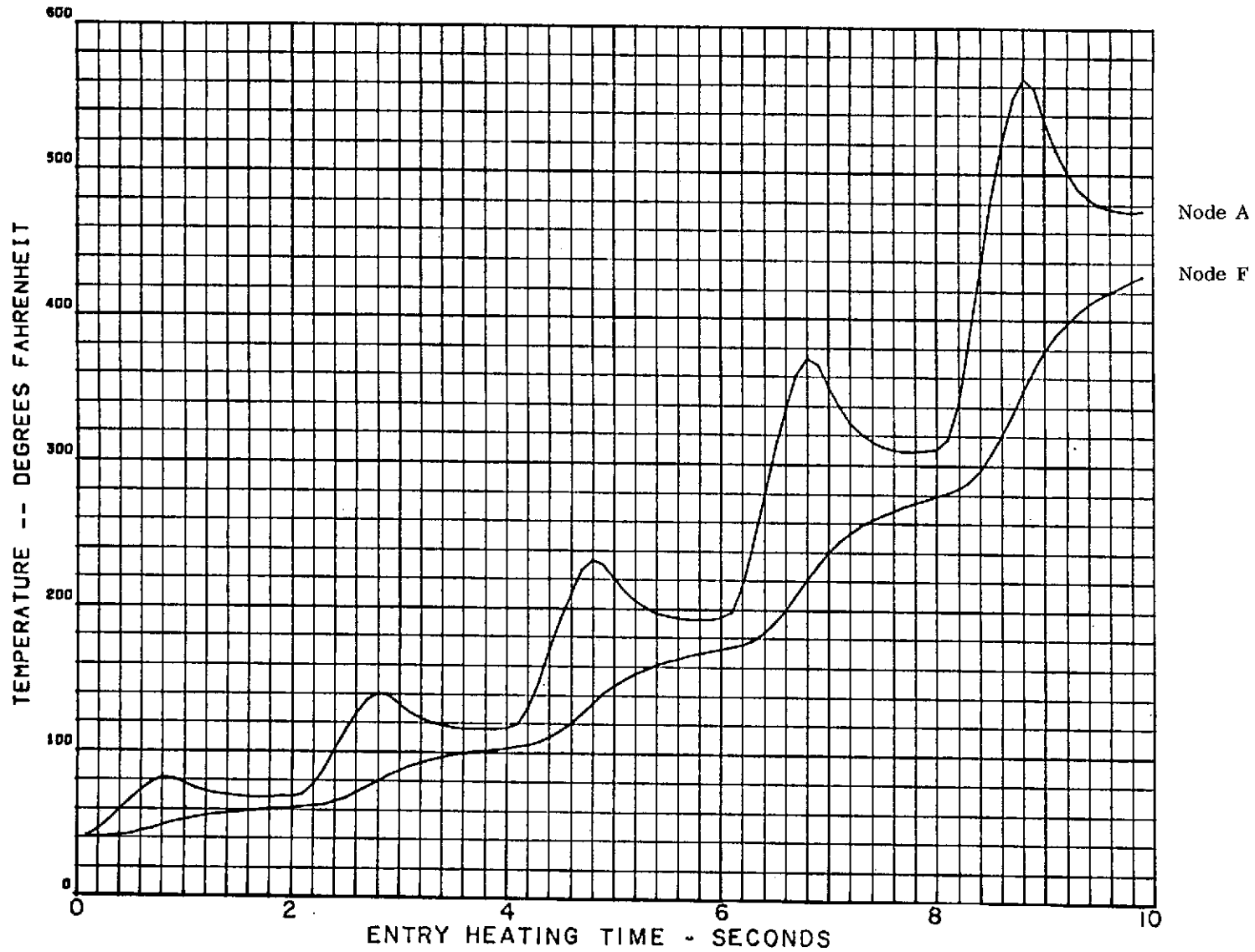


Figure 2-88. Atlas reentry heating for 180 deg/sec pitch rate model 38, 8 mil gage, 24 mil skin, 20 mil spacer/24.2.

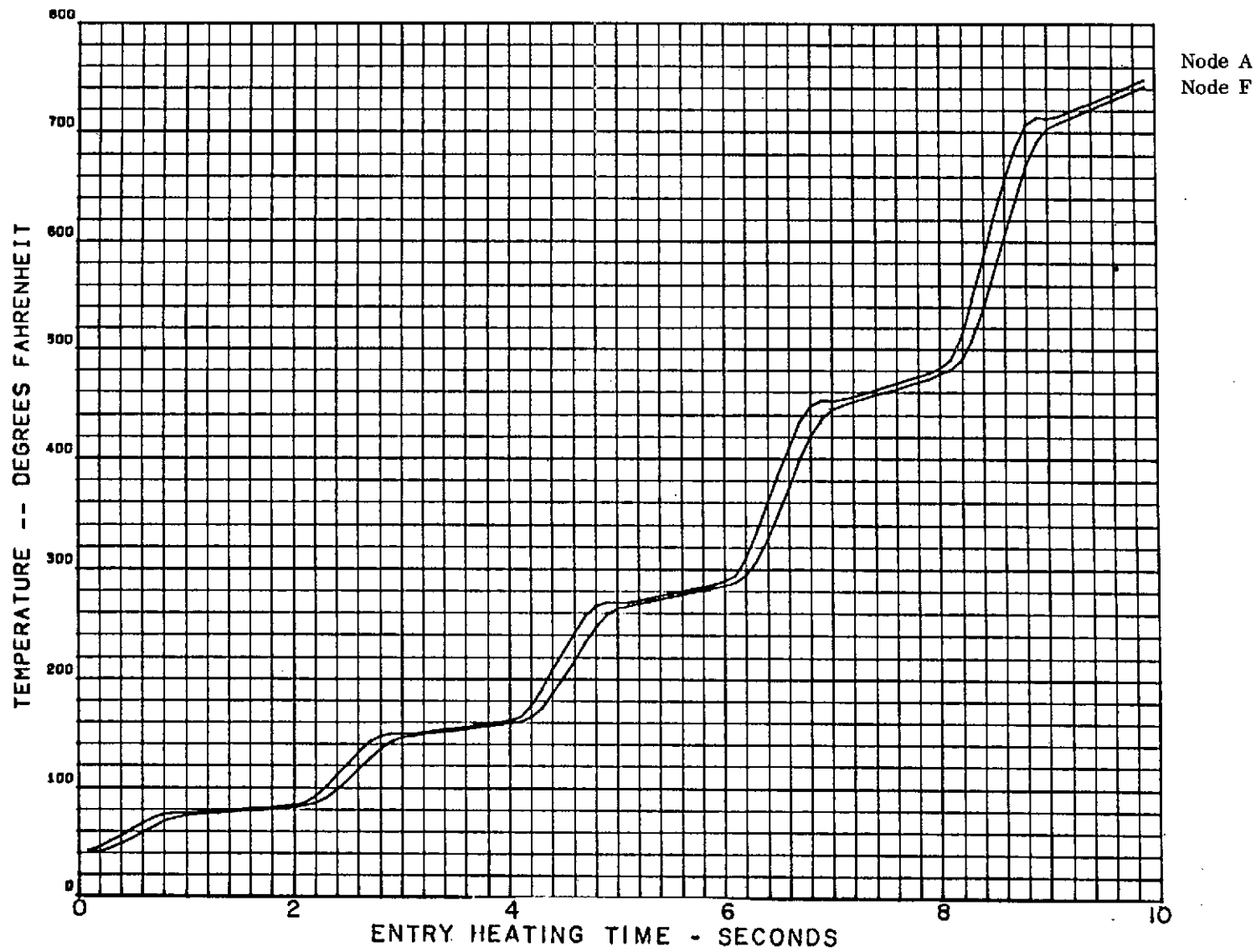


Figure 2-89. Atlas reentry heating for 180 deg/sec pitch rate model 39, 6 mil gage, 8 mil skin, 20 mil spacer/97.0.

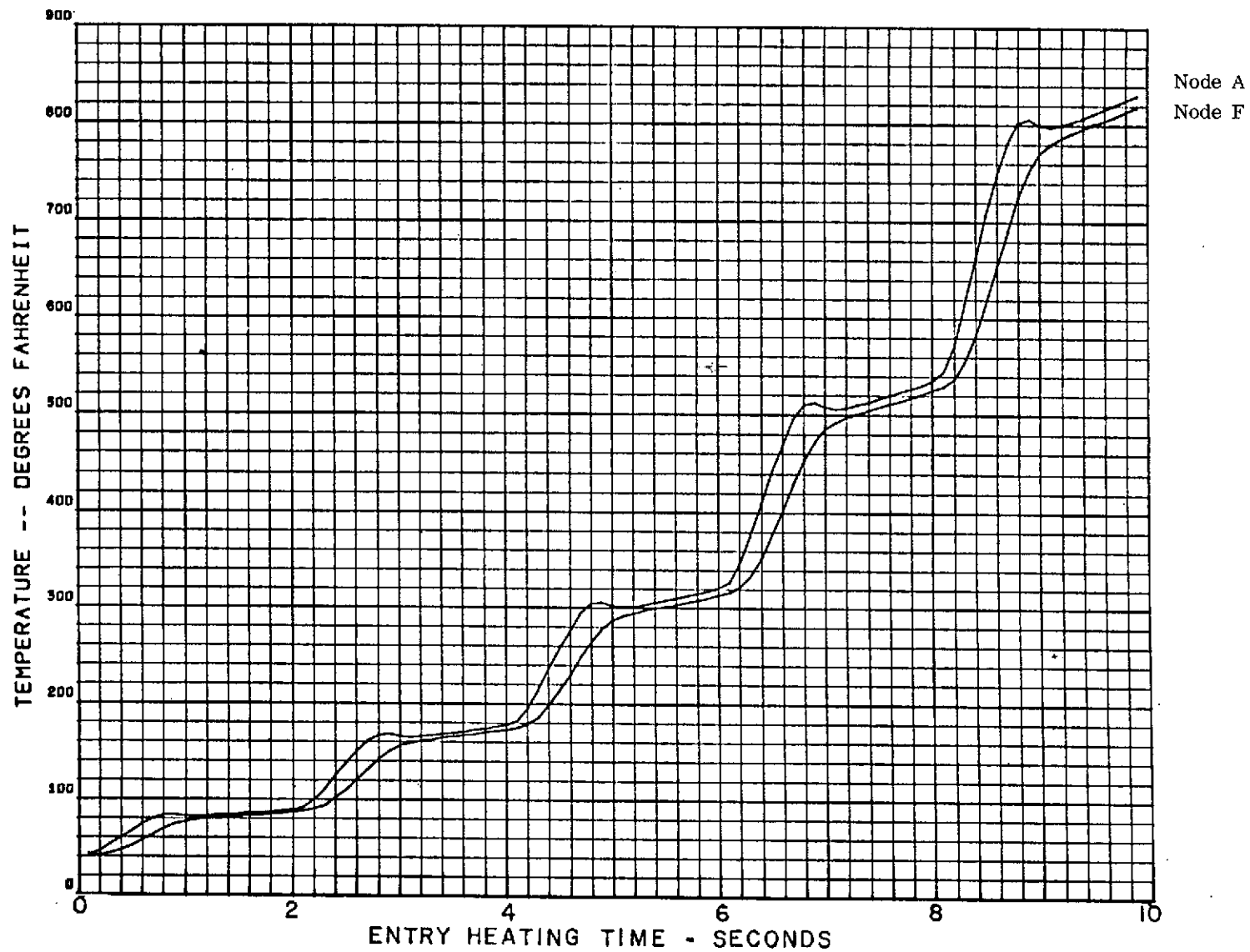


Figure 2-90. Atlas reentry heating for 180 deg/sec pitch rate model 40, 6 mil gage, 8 mil skin, 20 mil spacer/48.5.

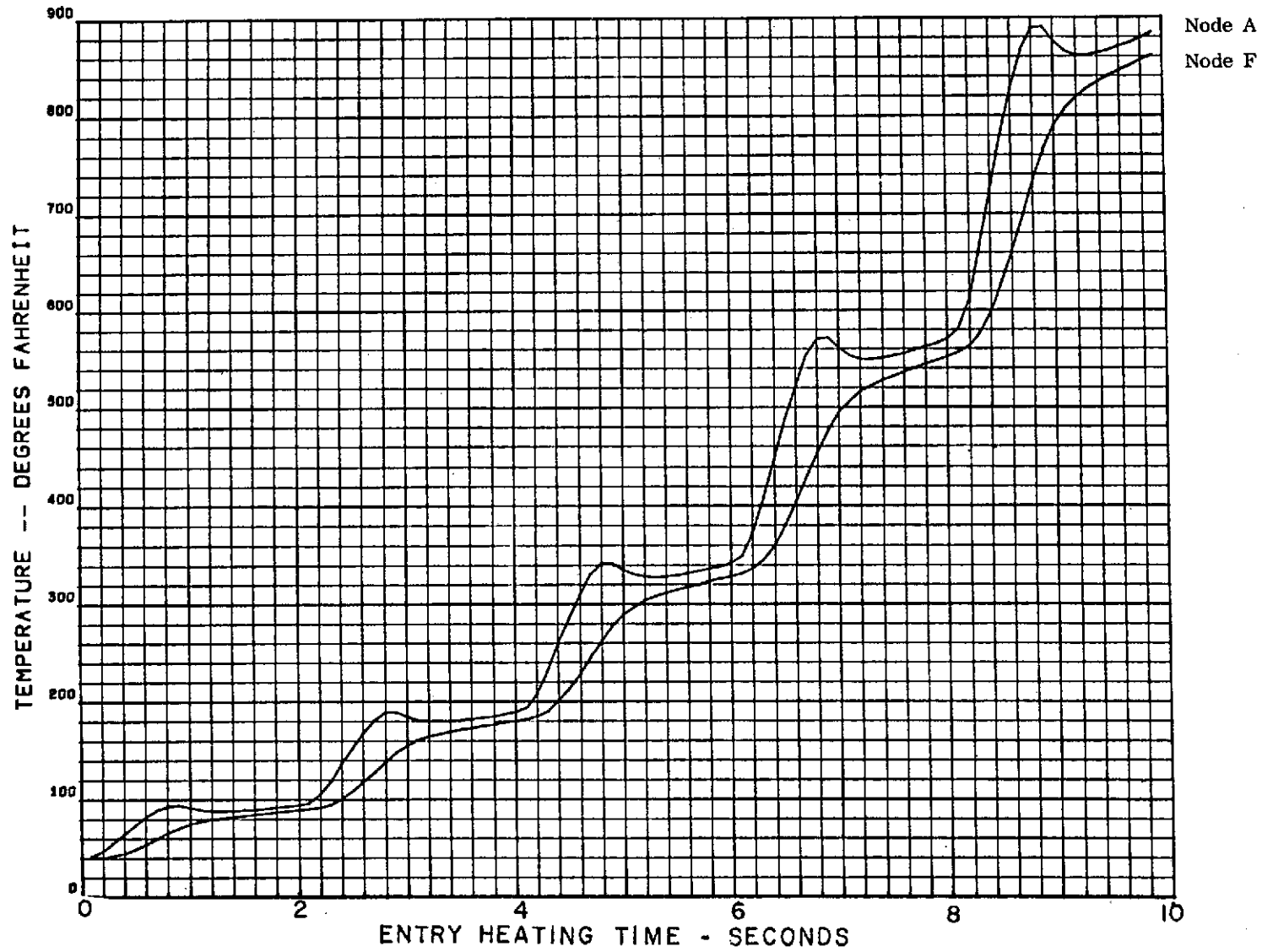


Figure 2-91. Atlas reentry heating for 180 deg/sec pitch rate model 41, 6 mil gage, 8 mil skin, 20 mil spacer/24.2.

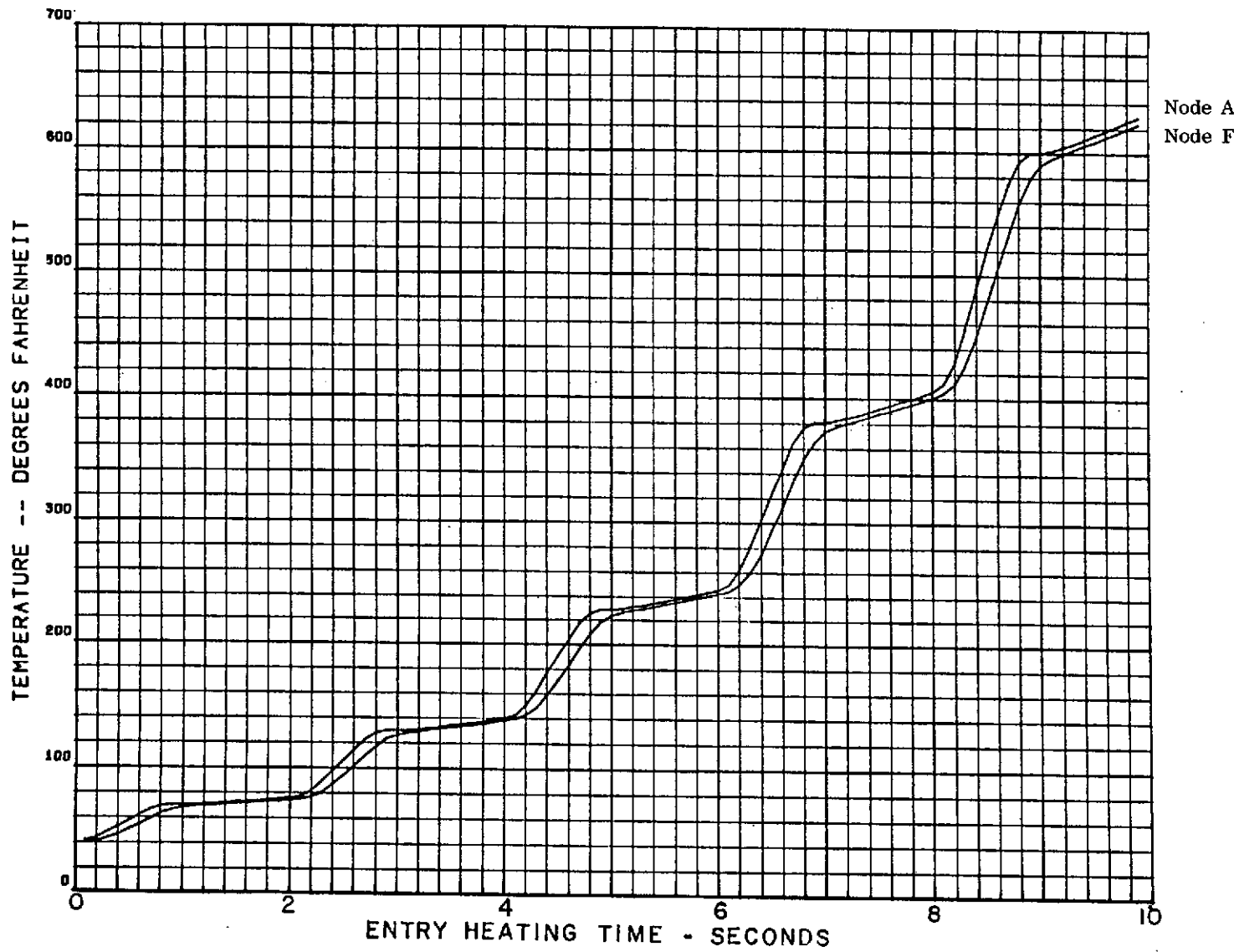


Figure 2-92. Atlas reentry heating for 180 deg/sec pitch rate model 42, 10 mil gage, 8 mil skin, 20 mil spacer/97.0.

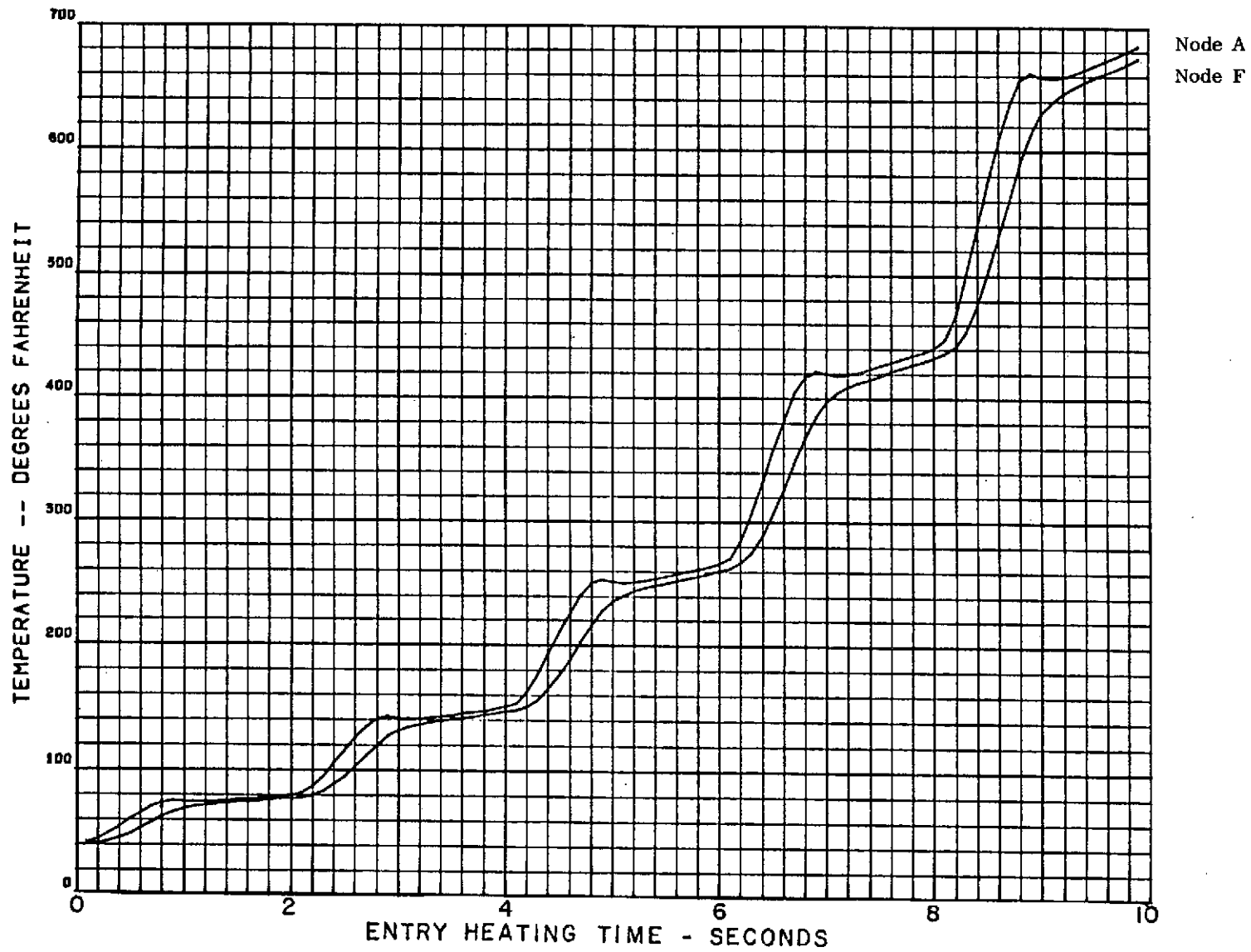


Figure 2-93. Atlas reentry heating for 180 deg/sec pitch rate model 43, 10 mil gage, 8 mil skin, 20 mil spacer/48.5.

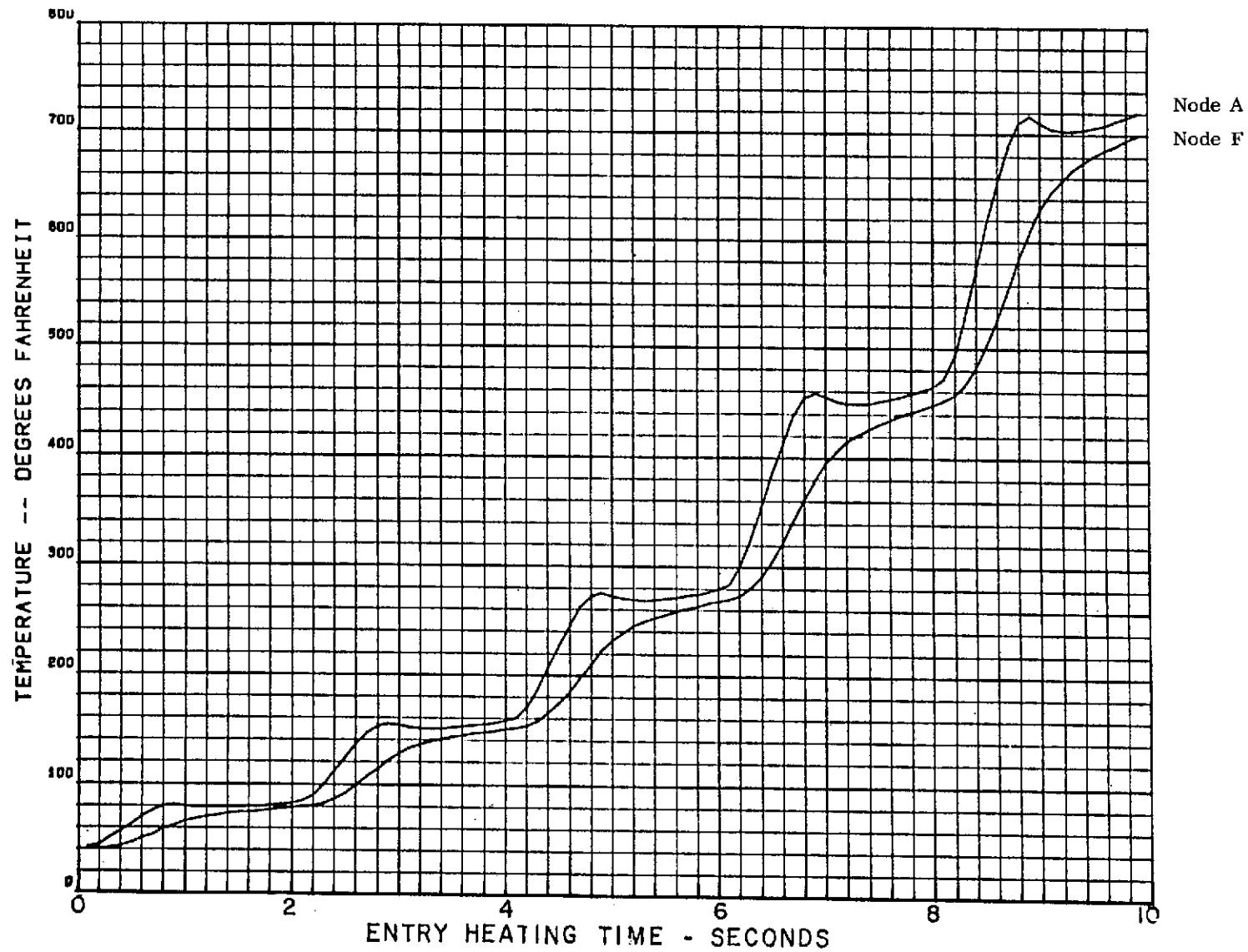


Figure 2-94. Atlas reentry heating for 180 deg/sec pitch rate model 44, 10 mil gage, 8 mil skin, 20 mil spacer/24.2.

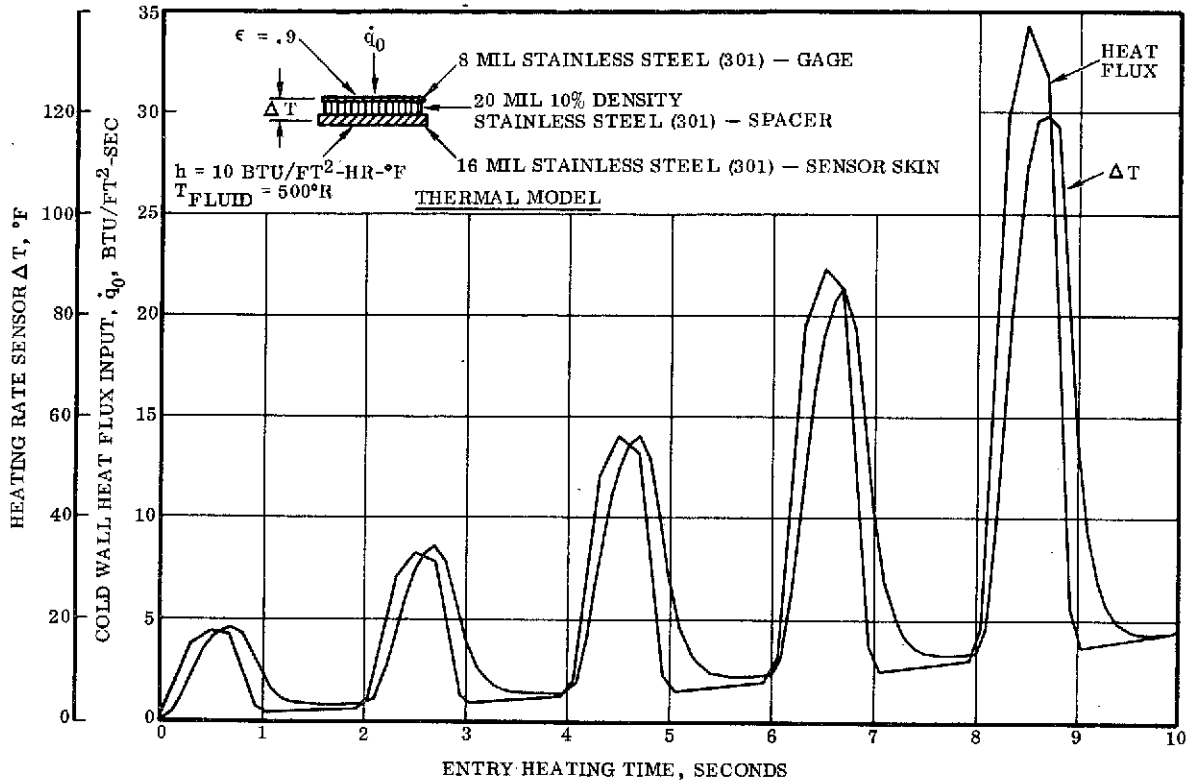


Figure 2-95. Model 21 heating rate sensor ΔT and cold wall heat flux input versus entry heating time.

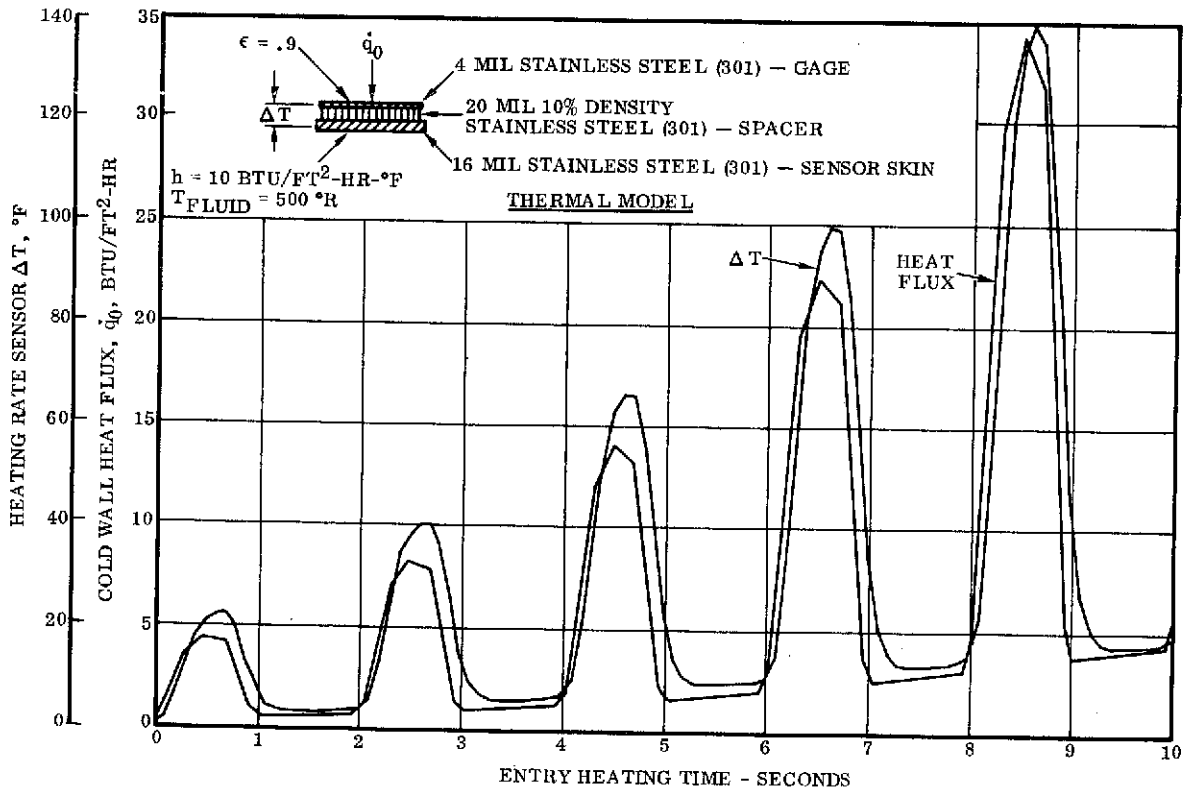


Figure 2-96. Model 23 heating rate sensor ΔT and cold wall heat flux input versus entry heating time.

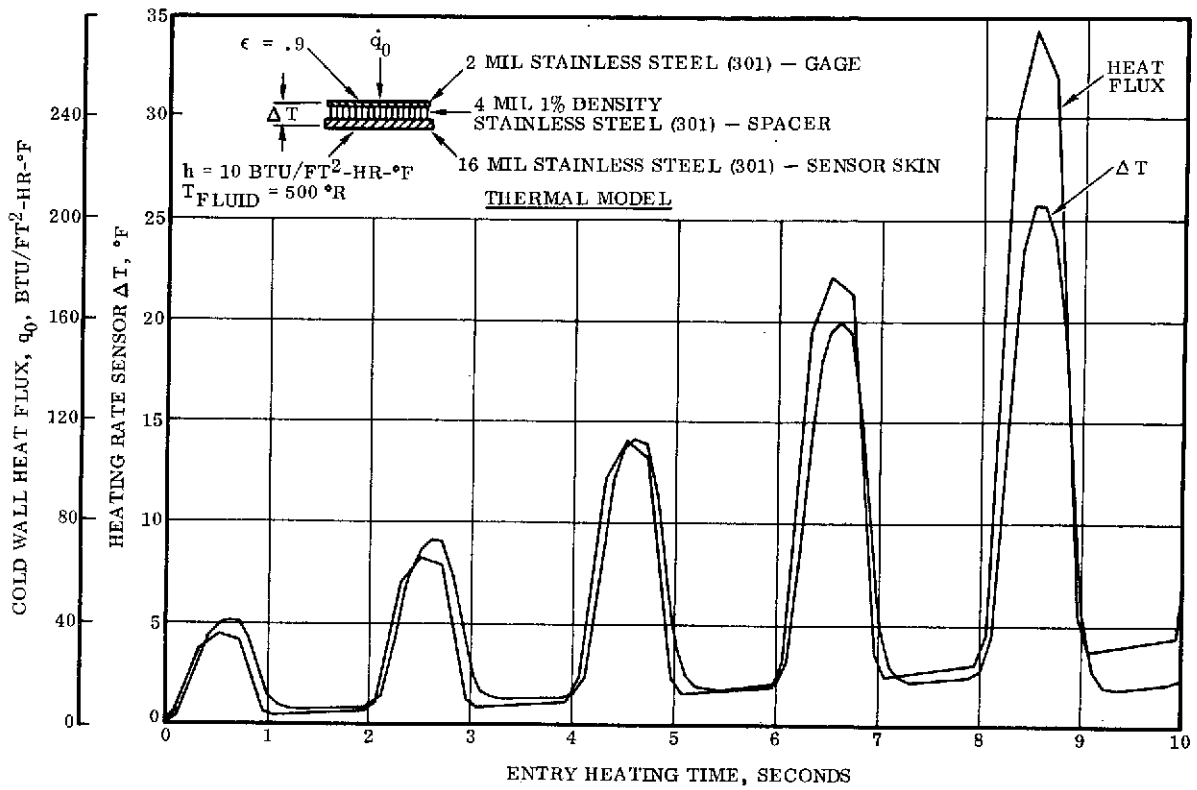


Figure 2-97. Model 28 heating rate sensor ΔT and cold wall heat flux input versus entry heating time.

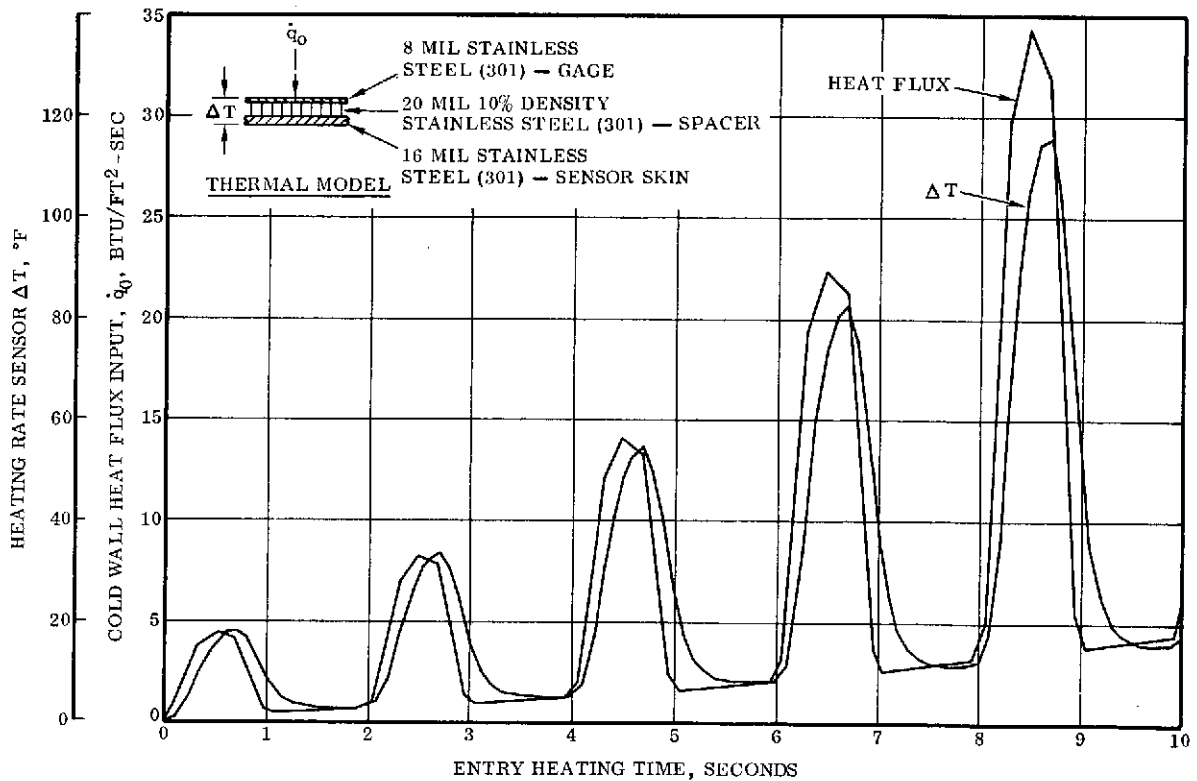


Figure 2-98. Model 34 heating rate sensor ΔT and cold wall heat flux input versus entry heating time.

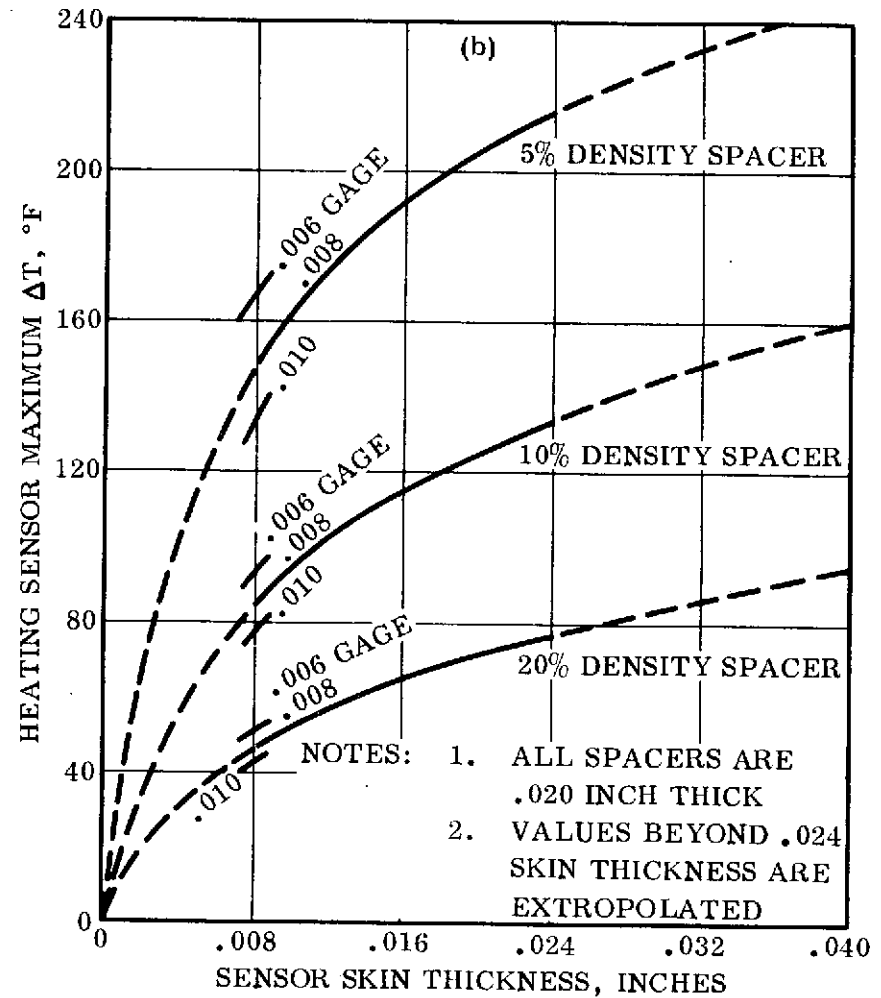
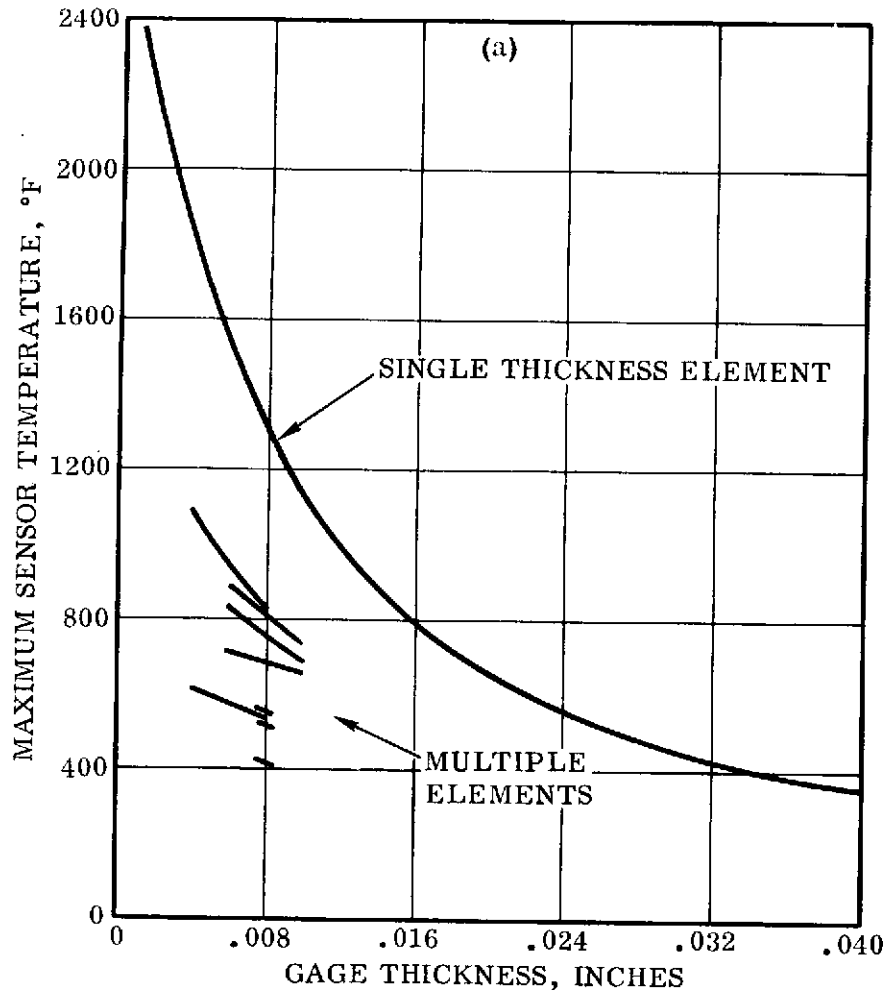


Figure 2-99. Computer output results: (a) maximum sensor temperature versus gage thickness; (b) heat sensor maximum ΔT versus skin thickness.

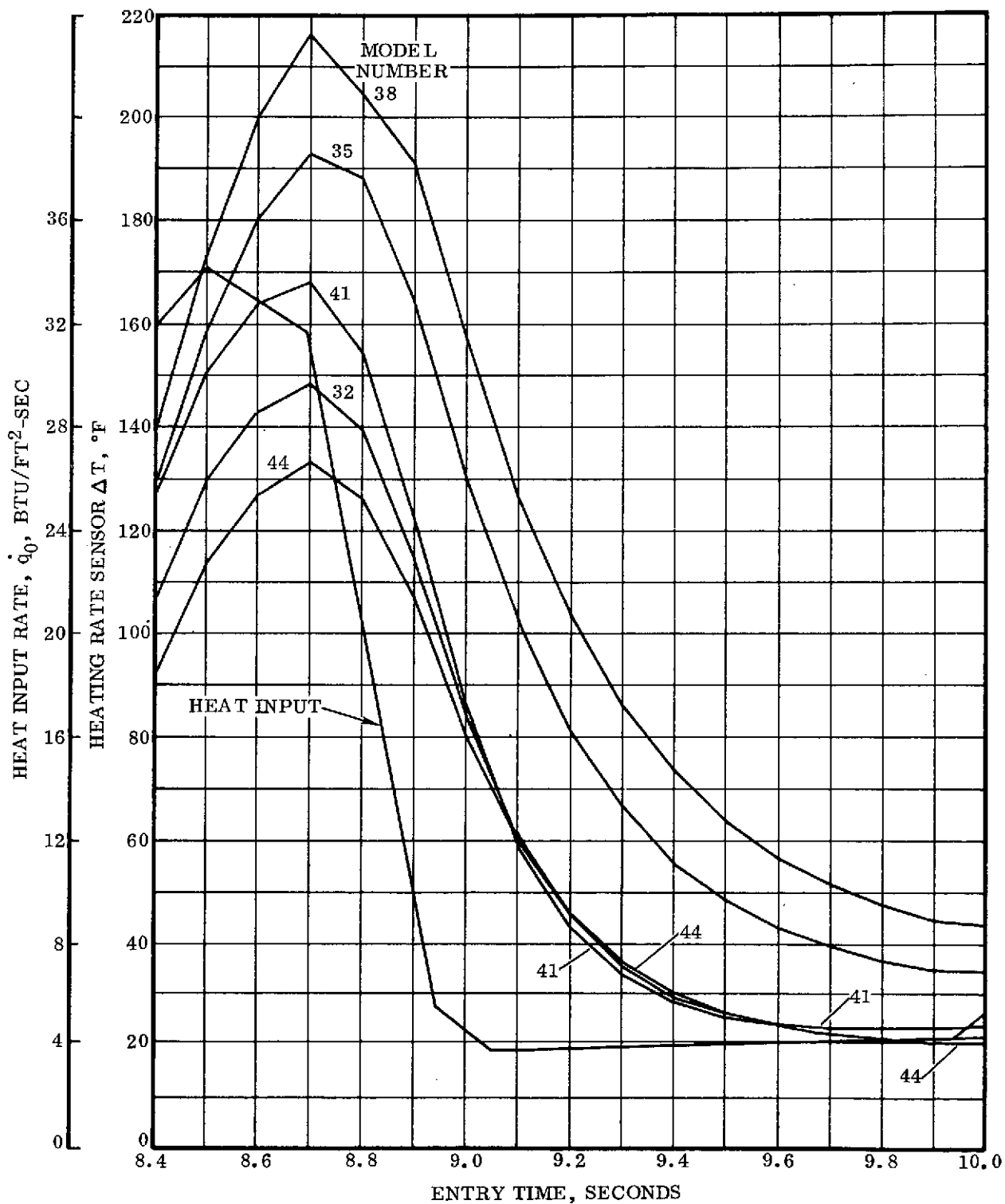


Figure 2-100. Response of 5% density spacer sensor models.

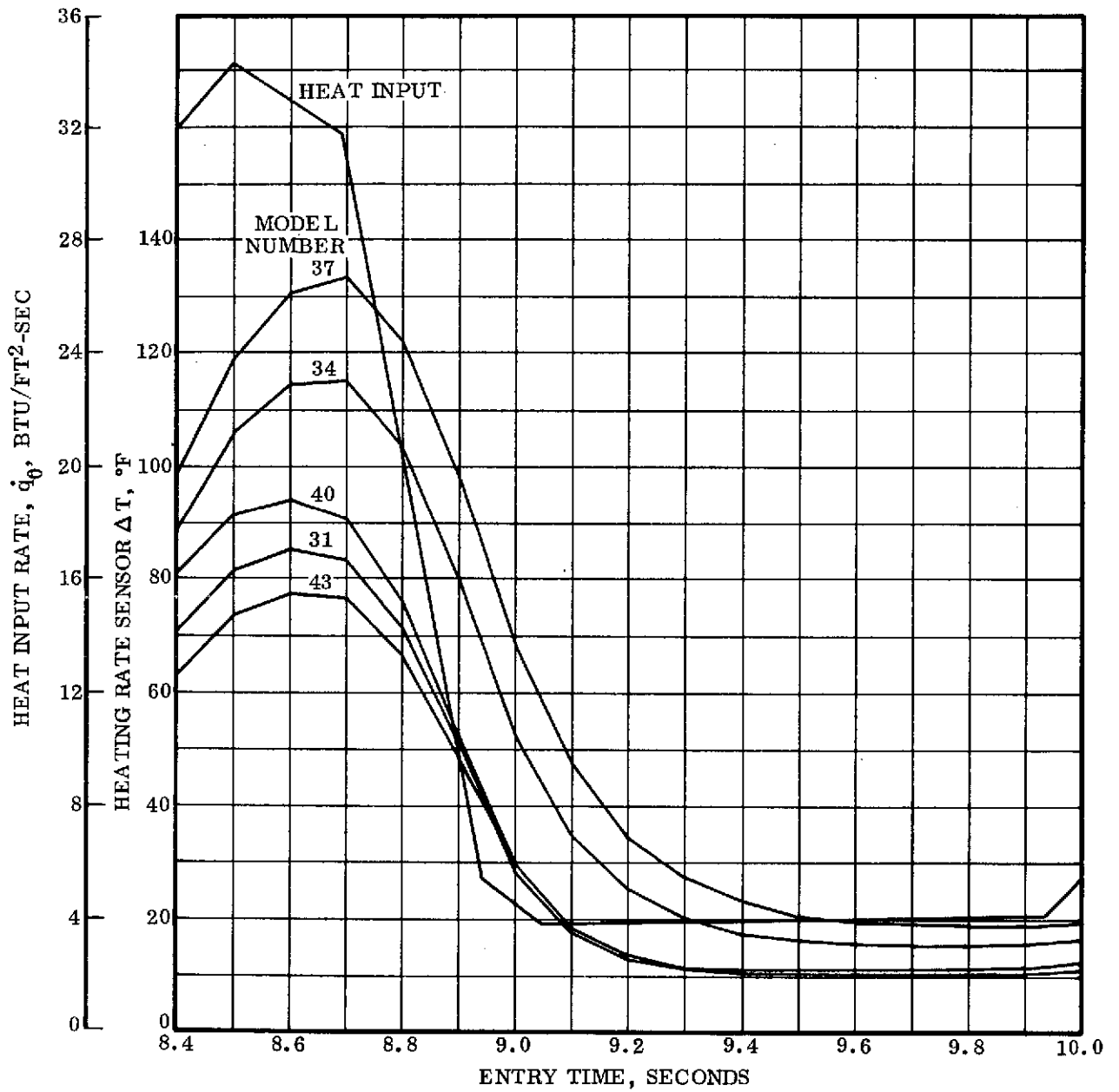


Figure 2-101. Response of 10% density spacer sensor models.

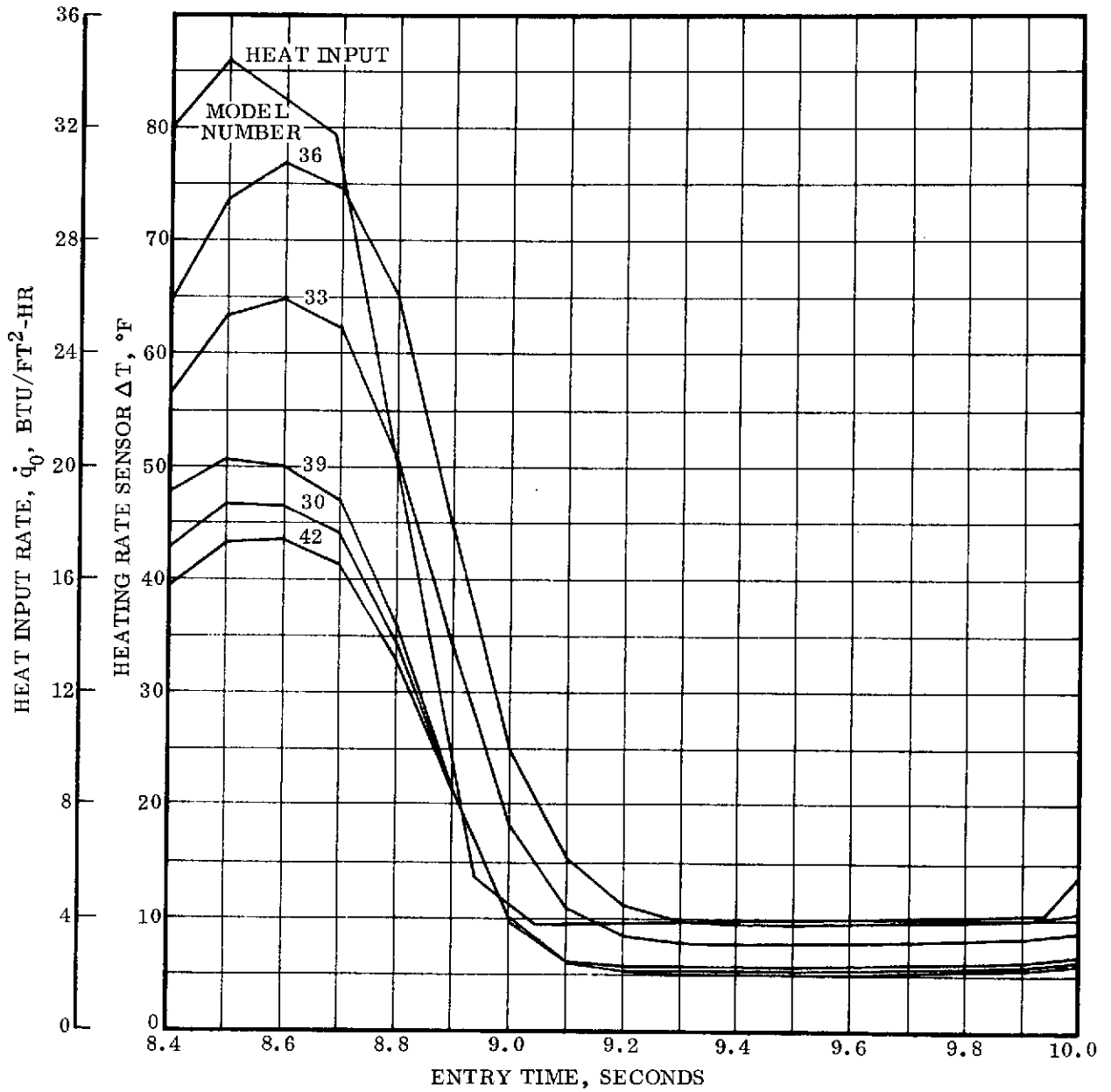


Figure 2-102. Response of 20% density spacer sensor models.

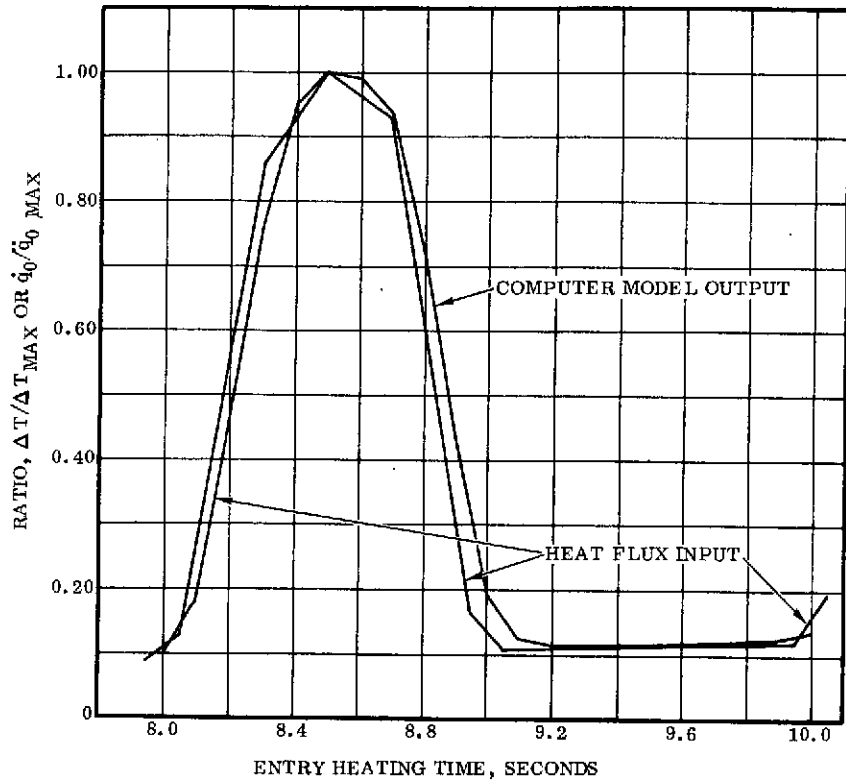


Figure 2-103. Model 39 sensor output performance comparison with heat flux input.

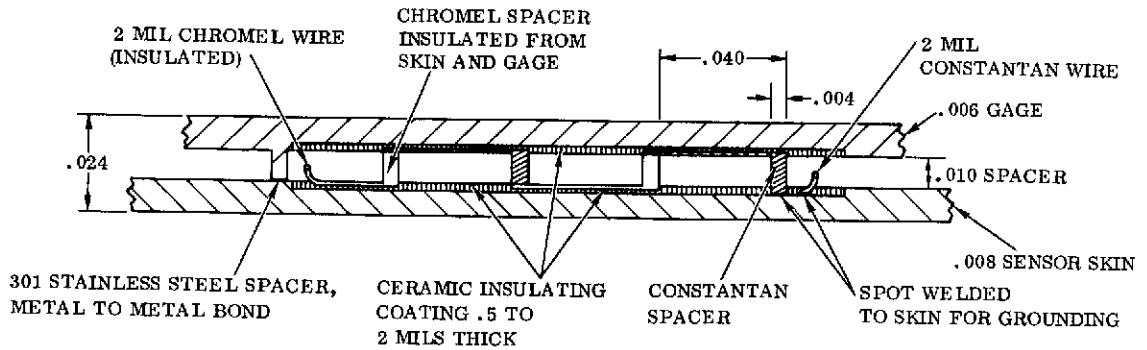


Figure 2-104. Cross-section through high performance heating rate sensor.

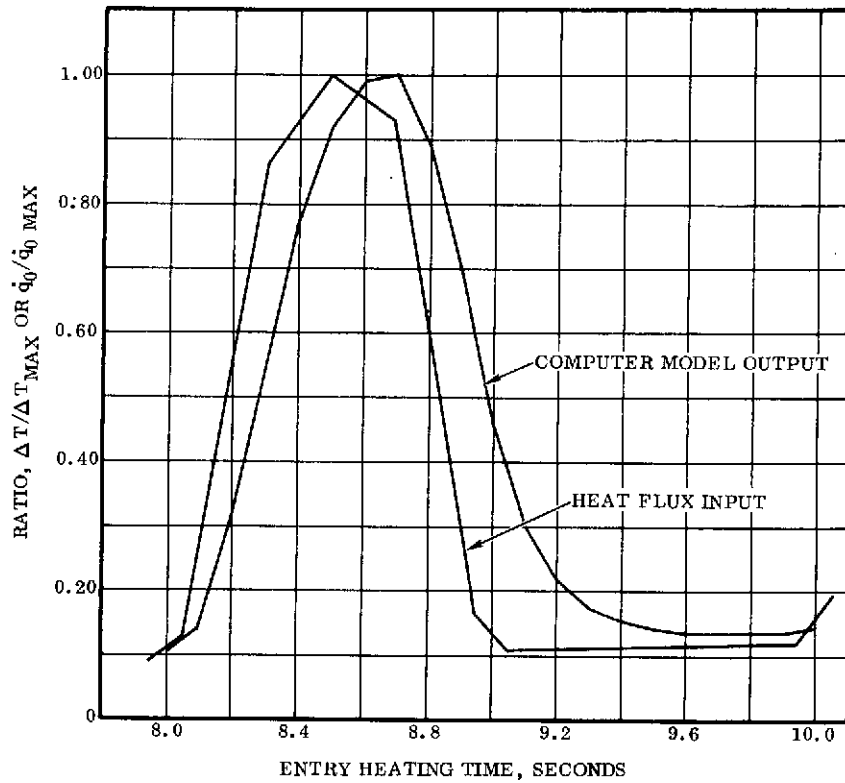


Figure 2-105. Model 34 sensor output performance comparison with heat input flux.

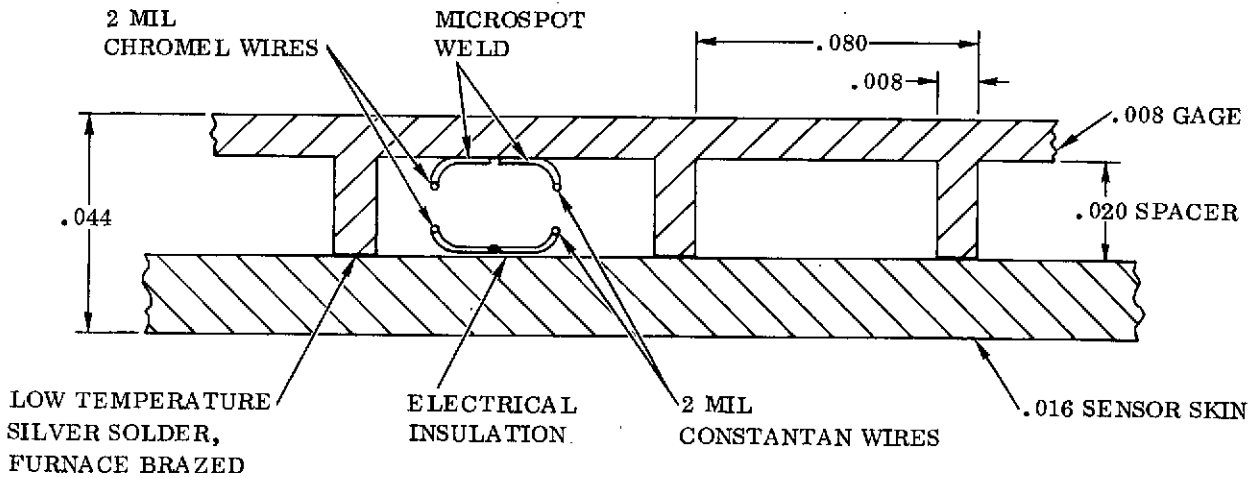


Figure 2-106. Cross-section through recommended heating rate sensor.

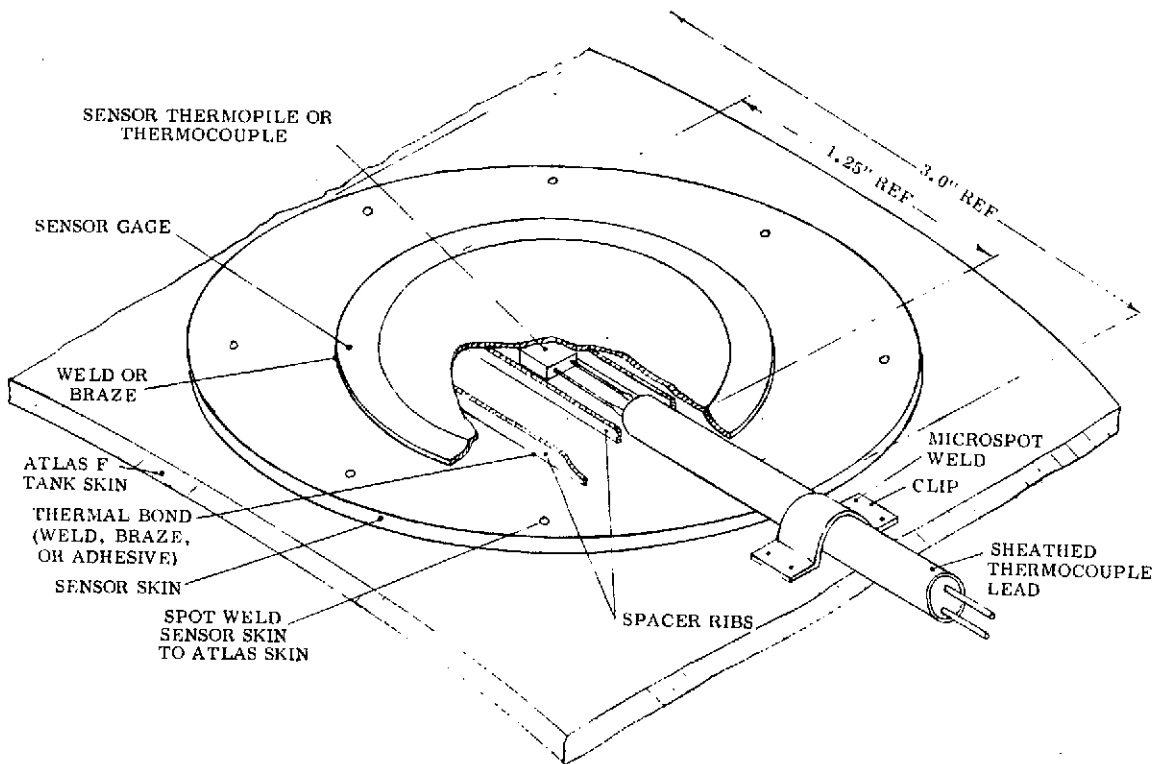


Figure 2-107. Sketch of heating rate sensor on Atlas tank skin with cut-away section of sensor gage.

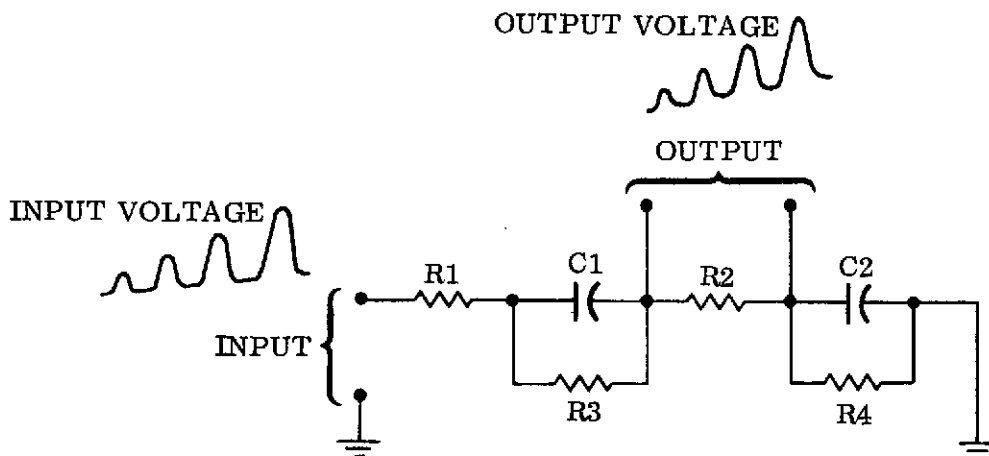


Figure 2-108. An electrical analog of heat rate sensor.

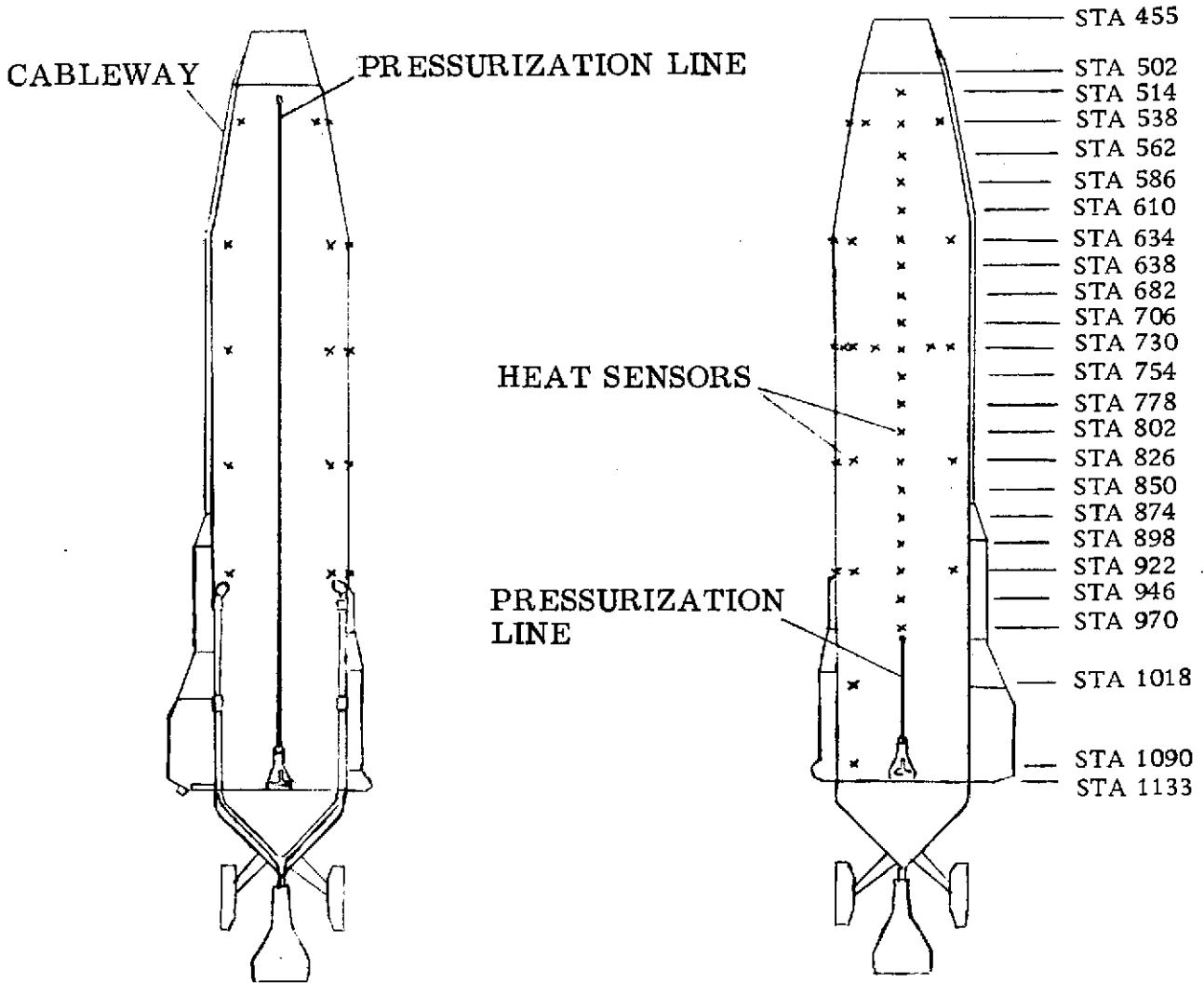
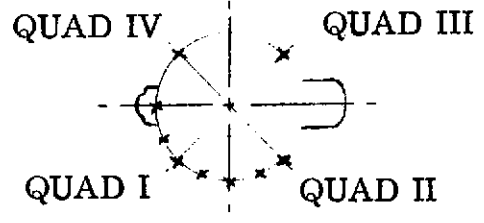
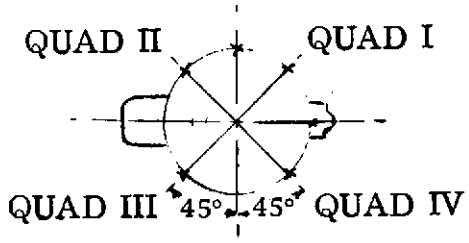


Figure 2-109. Recommended heat sensor locations on Atlas F.

2.5 VEHICLE ATTITUDE MEASUREMENT

To correlate the aerodynamic heating data with angle of attack, it is necessary to measure the vehicle attitude in three axes (pitch, yaw, and roll) with an accuracy of about 3 to 5 degrees. After only a cursory review of the inertial components provided on the baseline Atlas F vehicle, it was apparent they were incapable of performing the function. The position gyros have gimbal limits of ± 10 degrees (maximum) compared with a mission requirement of 360 degrees because of the tumbling mode of the vehicle. The rate gyros were looked at, with the concept in mind that their output could be integrated to yield position data. However, the existing gyros have a rate limit of ± 20 degrees per second (maximum) which precludes their further consideration. The consideration that any system containing only rate gyros (without another device to provide an absolute attitude reference near the entry site) would require continuous integration of their output from the launch site to the entry site ruled out this system for further investigation. This would require a net of tracking ships, and instrument and telemetry accuracies not currently available, to meet the desired 3 to 5 degree accuracy in position attitude during entry.

A survey was made of existing operational guidance sets, and all identified had serious deficiencies. These are discussed briefly below:

- a. Centaur (Honeywell) - requires about a 12 hour pre-launch alignment procedure, and extensive, costly GSE not available at WTR.
- b. Minuteman (North American) - has gimbal freedom constraint which would require extensive modification.
- c. SPRINT (Honeywell) - requires extensive repackaging and development of an on-board data processor/telemetry interface package.

A survey of vendors of aircraft type navigational and attitude reference systems was conducted. The vendors contacted include:

- a. Northrop Precision Instruments
- b. Teledyne/Ryan
- c. Bendix
- d. Cubic Corp/Lear-Siegler
- e. Kearfott

Of these, only Northrop indicated that they had an off-the-shelf operational system compatible with the Atlas F vibration level and the mission requirements. This is their NIS-200 family of inertial platforms, initially designed for the B-1 bomber. Subsequent adaption to other missile and aircraft applications has resulted in a "family" of off-the-shelf gyro and platform options, each with their own peculiar accuracy and

range characteristics. A system comprised of a three-axis four-gimbal platform with 3 GI-G6 gyros and a standard onboard data processor was selected as the most suitable member of the family. Preliminary calculations indicate that this system should have a measurement error of less than 3 degrees (3 sigma) for this mission.

The ground support equipment requirements and preflight alignment and checkout procedures were investigated briefly. It was concluded that, since this is aircraft-type equipment with accuracy requirements significantly less than for missile guidance systems, only a minimum of ground equipment and preflight procedures are required. Approximately six simple on/off switch functions are required for system power control and uncaging/caging the gyros and platform axes. The preflight procedure consists of turning on the system power about one hour before launch, uncaging the gyros, and monitoring the attitude output and drift rates (via the telemetry system) for the launch readiness assessment and postflight attitude data correction.

To provide a comparison with the Northrop Inertial System (in the absence of any other existing, viable, system), several alternate concepts were investigated briefly. These were based on the use of a 3-rate gyro package and a device to provide an absolute attitude reference just prior to entry, obviating the need for continuous integration of the output from the launch site. Two attitude reference devices were considered: a TV camera, and a set of 4 infra-red scanners (Barnes Engineering Model 13-133A Horizon Sensor). Accuracy, the first consideration, was immediately found to be in jeopardy. Assuming an end-to-end instrument to ground readout accuracy (an optimistic $\pm 2\%$), the cumulative position error after integrating the output for 10 seconds (about the minimum time between the scan before entering the sensible atmosphere with consequent plasma effects, and reaching 200,000 ft altitude) would be about $0.02 \times 10 \text{ sec} \times 180 \text{ degrees/sec}$, or 36 degrees. This error could be reduced to about 4 degrees, assuming: a rate gyro instrument-only accuracy of $1/2\%$ (also optimistic); and an onboard data processor (to be developed) which would digitize the output and reduce the telemetry system error to substantially zero. However, it was estimated that the cost of development of the data processor and the system alone, exclusive of the cost of the gyros and 4 Barnes scanners required (or TV system) would exceed the cost of the Northrop Inertial System. It became obvious that total system cost, including the Barnes sensors (or TV system) could not be competitive.

Similarly, for schedule considerations, it is not credible that the data processor system could be developed from a conceptual state in the time required to purchase an off-the-shelf inertial system.

It is concluded that the Northrop NIS-200 Inertial Platform is the most viable solution for a mission in the 1974 period.

NOTE: If the flight date for this mission should, for any reason, slip into the 1975 period, the North American/N57 Electrostatic Gyro and the North American/Ring Laser System should be considered.

Both of these are in the development process now, and the vendor hopefully estimates operational status by late 1973 or early 1974. However, making allowances for unforeseen development problems and the time required to develop a system to employ them for this mission, a 1975 date would be more realistic for this application.

2.6 DATA TRANSMISSION

This section contains the results of five subtasks:

1. Evaluation of RF transmission from the existing S-Band telemetry system during entry conditions.
2. Investigation of alternate concepts for data recovery.
3. Conceptual study of an alternate X-Band data transmission system.
4. Conceptual study of a special early test to acquire data during reentry from the existing S-Band system to establish a datum for signal strength and quality assessment by NASA/LRC.
5. Identification of modifications to the S-Band telemetry system, if the assessment of data from the above-mentioned test was favorable.

2.6.1 S-BAND RF TRANSMISSION. The plasma sheath is formed by ionized gases and free electrons surrounding the vehicle as it reenters. Kinetic energy is given to atmospheric molecules when struck by the reentry vehicle. The resulting gas temperature is high enough to cause dissociation of the molecules, excitation of atoms, and ionization of atoms and molecules. The plasma flows around the vehicle from the stagnation point in a manner that depends upon the vehicle shape, velocity, and altitude.

The plasma sheath impedes the transmission of RF energy by three mechanisms: attenuation, reflection, and antenna pattern distortion. Much theoretical and experimental work has been done over the past ten years in this field. Both ground testing and flight testing have been performed. NASA Langley, AFCL, Cornell Aeronautical Laboratories, and Sanford Research Institute are some of the agencies that have done extensive work in this area. Flight tests have included Scout and Trailblazer missiles. From this and other work, the following is known about the plasma sheath:

- a. **Frequency Dependence:** Measurements have been made from P to K-Band. The severity of signal degradation increases as the transmission frequency is lowered. A trajectory resulting in an S-Band blackout at 250,000 ft may not experience X-Band blackout until below 200,000 ft.
- b. **Power Dependence:** Higher transmitted powers somewhat raise the altitude at which blackout will begin.
- c. **Body Shape:** A streamlined, aerodynamic body will be accompanied by less plasma than a blunt, nonaerodynamically-styled body at a given velocity and altitude.
- d. **Alleviation Techniques:** RF blackout occurs when the plasma sheath electron density reaches a critical value. The electron density may be reduced by various alleviation techniques. Ablative products may be added to the

reentering body to accomplish this or various chemicals, including water, may be injected directly into the plasma from nozzles located on the surface of the body.

In the present case, upon reentry, after completion of its primary mission, the Atlas tank will reenter with the velocity and altitude profile shown on Figure 2-110. Velocity between 300,000 and 200,000 feet will remain nearly constant at 22,300 ft/sec. This altitude range will be traversed in 8.9 seconds. A blackout curve was obtained from Reference 9, which is felt to be a reasonably close approximation to the present case. This prediction by Cornell Aeronautical Laboratories was made for the Apollo missions and has been subject to some flight verification. The prediction is for an RF frequency of 2.287 GHz which is close to the 2.2435 and 2.2585 GHz S-band Atlas telemetry frequencies. The prediction is for free air (no ablation or fluid injection) as is the case for Atlas. The reentering body is Apollo entering blunt-end-first presenting an aerodynamic profile somewhat like an Atlas tank, at least to the extent that both bodies are not aerodynamically streamlined.

Figure 2-110 shows that RF blackout will probably begin at approximately 249,000 feet and RF communications will not be possible until the tank (if still intact) is below 110,000 feet. Only 4.4 seconds of RF transmission is probable between 300,000 and 249,000 feet altitude. This 4.4 seconds will be further reduced by RF dropouts due to antenna pattern nulls as the tank tumbles, although using multiple ground receiving stations will help somewhat.

2.6.2 ALTERNATE APPROACHES TO THE PROBLEM. If data is required down to 200,000 feet altitude, the present S-Band telemetry system will not suffice. Some alternate approaches possible are:

- a. Raising the link frequency to C or X-Band. (This is described further in Section 2.6.3).
- b. S-Band data recovery below 100,000 feet. If the Atlas tank can be kept intact, an on-board time delay data recorder could record the data between 250,000 and 200,000 feet and replay this data after cessation of blackout. This approach does not appear feasible, however, unless large modifications are made to the Atlas to prevent tank breakup.
- c. Recoverable ejectable capsule or pod. Data between 300,000 and 200,000 feet could be recorded in a capsule that would be ejected below 200,000 feet. The capsule would survive reentry and would be recoverable.
- d. Radiating ejectable capsule or pod. This idea is similar to item c except that recorded data would be retransmitted after the blackout region has been traversed.

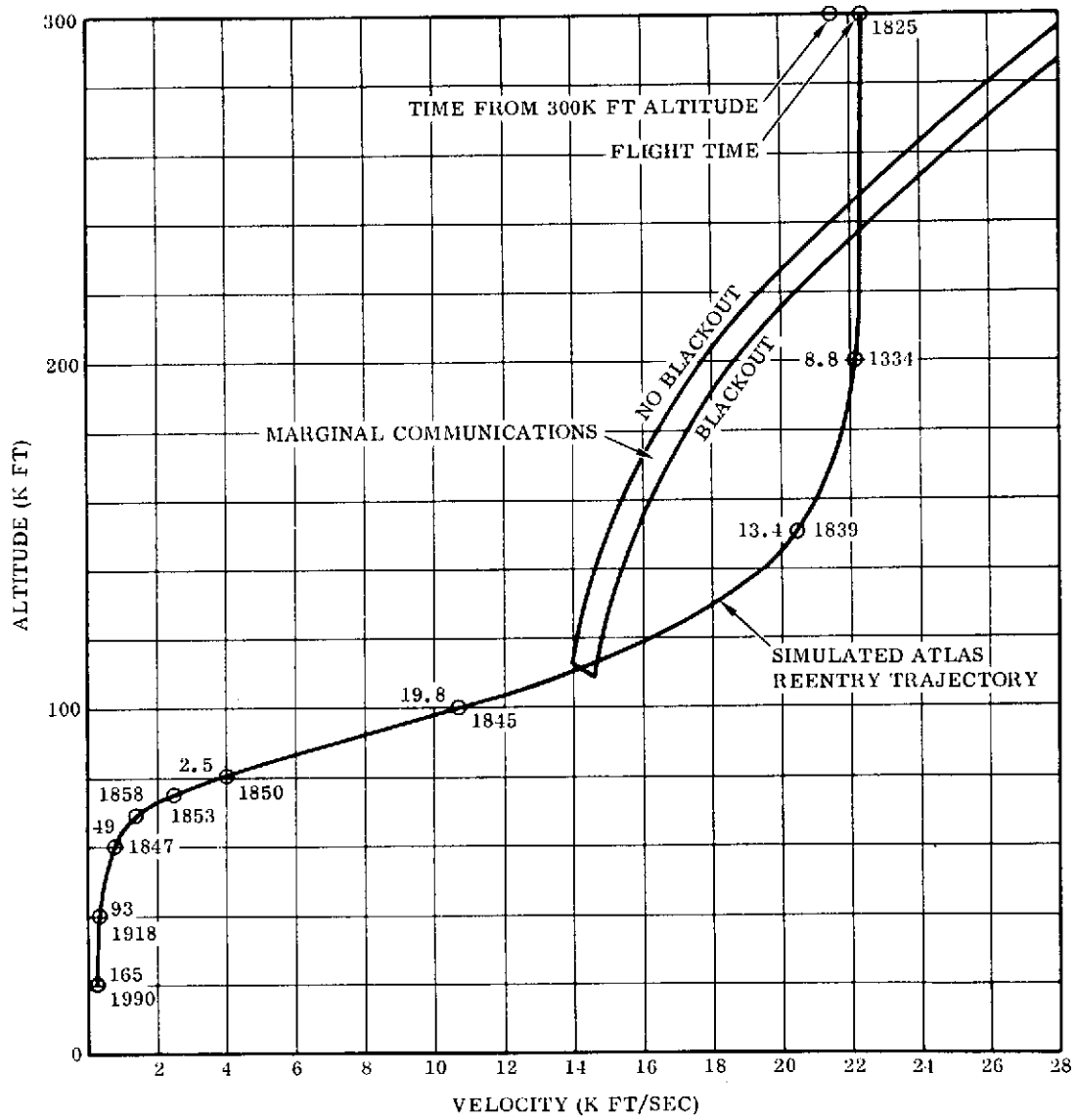


Figure 2-110. Blackout boundaries.

- e. Alleviation techniques. Further study would be required to determine if alleviants in the plasma sheath would allow S-band data reception all the way down to 200,000 feet. This method is not considered feasible because of the extensive missile modifications required.

Table 2-11 presents a rating of these alternate approaches in terms of cost, schedule and risk to the primary mission.

Table 2-11. Alternate data recovery systems.

Approach	Cost	Schedule	Risk
Raising Link Frequency	1 *	1	1
Recovery from Atlas below † 100,000 feet	4	4	4
Recoverable Ejectable Capsule †	3	3	3
Radiating Ejectable Capsule †	2	2	2
Alleviation Techniques	5	5	5

Notes: * A rating of 1 denotes least cost, shortest schedule, and least risk to the primary mission. A rating of 5 denotes most cost, longest schedule, and most risk to the primary mission.

† Based on axial and lateral loads values discussed in Subsection 2.2.3, the availability of off-the-shelf data recorders appears highly questionable.

2.6.3 ALTERNATE CONCEPT — X-BAND. Ideally, minimum modification to the existing Atlas telemetry system would be obtained if the present S-Band telemetry transmitter and antenna could be replaced with X-Band units. Commutators, sub-carrier oscillators, and signal conditioning from the present telepac would continue to be used. The composite video signal would be switched from the S-Band transmitter input to the X-Band transmitter input at the appropriate flight time. However, the approach is not considered feasible. The slant range to Kwajalein when the Atlas is at 300,000 ft altitude is 772,000 feet and, since we should acquire the vehicle before this, we would require a system operable at a minimum distance of 1 million feet. The present telepac uses IRIG channels up to number 18, requiring ground receiver bandwidths on the order of 500 KHz. To obtain positive link margins, the transmitter output power must be high and the X-Band ground receiving antenna must be large, neither

of which is true in the present case. Power levels available at X-Band for FM/FM telemeters are considerably less than one watt and even these would be a development item. Using a TWT or BWO is feasible but again, development would be required. Additionally, no X-Band capability exists at Kwajalein and, therefore, a relatively small, portable antenna system must be used. The result is that an FM/FM X-Band telemetry link has been ruled out for the present application.

Another possibility, which has been successfully used on the RAM program, is to put an X-Band transponder data system on the Atlas. These systems use a radar transponder to transmit telemetry information. When the airborne transponder is interrogated by a ground based radar, it replies with a series of pulses. The position in time of the pulses contains the encoded value of a measurement and the identification of the measurement channel. When the next interrogation pulse is received, the transponder will reply with information about the next measurement channel. When all measurement channels have been sampled, the sequence is repeated. These transponder data systems are available with up to 64 measurement channels. At an interrogation rate of 500 PPS, each channel is sampled roughly 8 times per second, a response that is considered marginal for the thermal data desired. (However, by reducing the number of measurements to about 30, the sampling rate could be doubled to 16 times per second. Alternatively, by employing 2 encoder/transponder units, the 16 samples per second could be attained while retaining the 64 measurement capability.) The transponder data system encoder is designed to accept an input signal of 0 to 5 vdc. On the ground, a companion decoder is mated with the X-Band radar to retrieve the airborne data. Units are available with peak output powers up to 1 kw.

- a. Proposed Vehicle Configuration. The proposed airborne configuration is shown in Figure 2-111. Each measurement channel originates as a low level dc voltage generated by a thermocouple. The voltage is then amplified to present a 5 vdc output at full scale by a dc to dc amplifier in a signal conditioning box. (The amplifiers are off-the-shelf, but a box or plate would have to be designed to house them.) The amplified signal is then fed into a transponder encoder along with the rest of the measurements. The encoder output then allows the X-Band transponder to pulse position modulate the reply to each interrogation pulse. Frequency of operation is in the 9100 to 9600 MHz band.

In addition to the transponder, X-Band antennas, a power divider, and RF cables or waveguide will be required. At least two, and possibly three or four, antennas will be fed by a power divider. Coaxial cable may be used to carry the X-Band signal, but, due to the distance between the B-1 and B-2 pods, waveguide may be required to keep RF attenuation losses to a reasonable value.

- b. Ground Requirements. On the ground near the reentry area, X-Band radar capability will be required. Since none presently exists in the Kwajalein Missile Range, a portable unit will have to be supplied. A decoder unit which is compatible with the airborne encoder will be required to separate the data from the basic signal. The decoder output must then be recorded. A portable unit is currently available at the Langley Research Center. Indications are that with minor changes (principally the incorporation of a newer version of the decoder) this unit could be made available and used for this experiment.

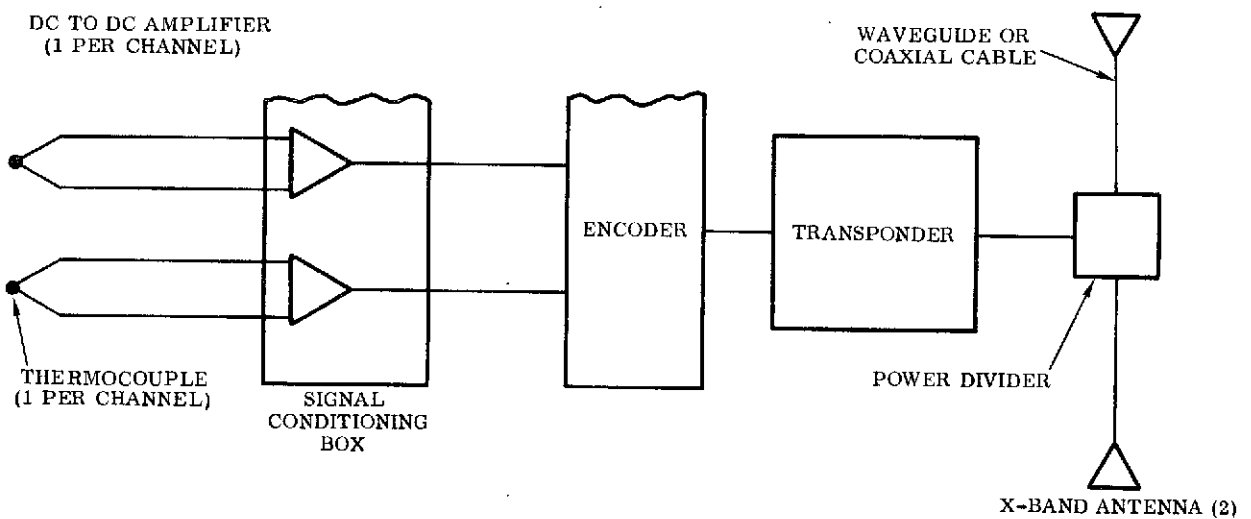


Figure 2-111. Proposed X-Band TLM configuration.

2.6.4 SPECIAL S-BAND RF TRANSMISSION TEST. The doubts raised by the results of the S-Band feasibility analysis led to a review of the RF transmission problem by Mr. Paul Huber, Assistant Head, Hypersonic Propulsion Branch, Hyd. NASA-LRC, a noted authority on the subject. The results of his review (Reference 10) indicated:

- a. A rigorous analysis would involve a very complex and time-consuming analysis of the flow field over the Atlas tank throughout the angle of attack and altitude range of variations during entry, followed by an equally complex evaluation of the RF attenuation caused by the variable flow field characteristics (plasma sheath) and the specific Atlas antennae patterns.
- b. In lieu of this, a more general review was made which confirmed the results of the study reported in Subsection 2.6.1, and stated that an X-Band or C-Band system appeared feasible, provided that a suitable antenna pattern was achieved.

During the review, it was suggested that a test be conducted to bypass the lengthy analysis with its attendant uncertainties for the S-Band system. In addition, the S-band data would serve as a reference point from which to apply the predicted improvement afforded by an X-Band system compared with an S-Band system (which is easier to predict than an absolute performance level). In response to this suggestion, a brief investigation was made of ways to acquire this S-Band data during an additional experiment to be conducted on an early Atlas flight.

A relatively full complement of measurements is available for constant monitoring to evaluate S-Band telemetry transmission capability throughout Atlas flight and re-entry. The sensor excitation is supplied by the telepac which is, in turn, battery-powered and not dependent upon the inverter.

The investigation uncovered two requirements (with alternates):

- a. Either verify that the electrical system inverter can be maintained within safe operating temperature limits by radiation cooling (under vacuum conditions) until main missile battery depletion, or shut down the inverter after primary mission completion.
- b. Either use a larger battery to replace the existing telemetry battery to insure operation during entry, or provide a second battery, switched to after primary mission completion.

Three design approaches were formulated which appear feasible, and could be candidates for an early flight. All approaches, with whatever variations are chosen, will employ an additional battery to assure adequate power to the telepac for the flight duration.

2.6.4.1 Design Approach No. 1

- a. Parallel a second telemetry battery directly with the remotely activated battery.
- b. Allow the main missile battery-inverter combination to run until main missile battery depletion.

Two tests are required to substantiate this approach:

- a. Activation of a remotely activated battery into an already manually activated battery to simulate the launch condition.
- b. Battery inverter test to battery depletion (under vacuum conditions).

Advantage: Minimum change

Disadvantage: Lab testing requirement

2.6.4.2 Design Approach No. 2

- a. Parallel a second telemetry battery through a relay. Connect the second battery in parallel with the remotely activated telemetry battery some time after normal Atlas flight.
- b. Shut down the Atlas inverter after normal Atlas flight by transferring the power changeover switch to external by programmer command via a discrete timer switch.

Advantage: Eliminates need for lab test

Disadvantage: Requires more changes to the vehicle

2.6.4.3 Design Approach No. 3

- a. Replace the existing telemetry battery with another battery of adequate capacity to support telemetry for the stated 2100 seconds. (The OV-1 battery or a partially discharged SLV-3 manually activated main missile battery are candidates for evaluation).
- b. Shut down the Atlas inverter after normal Atlas flight by transferring the power changeover switch to external by programmer command via a discrete timer switch.

Advantage: Simplest and therefore most desirable technical approach

Disadvantage: Requires the most changes on the vehicle.

2.6.4.4 Recommended Approach

Design Approach no. 2 is recommended because:

- a. It avoids the costly vacuum tests associated with Approach No. 1
- b. It permits greater isolation from the primary mission hardware, and therefore less risk to that mission than Approach No. 3 with essentially the same implementation schedule.

2.6.5 MODIFICATIONS TO THE S-BAND TELEMETER. Depending on the outcome of the tests described above, the existing S-Band RF may be used. If so, modifications of the measurement signal paths and an increase in the telemeter battery capacity are required. Conceptually, four alternative approaches were investigated. These were:

1. Use available spare channels for secondary mission measurements (heating sensors and attitude angles).
2. Add switch ahead of commutator to change from primary to secondary mission measurement (see Figure 2-112(a)).

3. Provide additional commutator and switch(es) to change subcarrier inputs from primary to secondary mission measurements (see Figure 2-112(b)).
4. Add second complete telemetry system for secondary mission measurements.

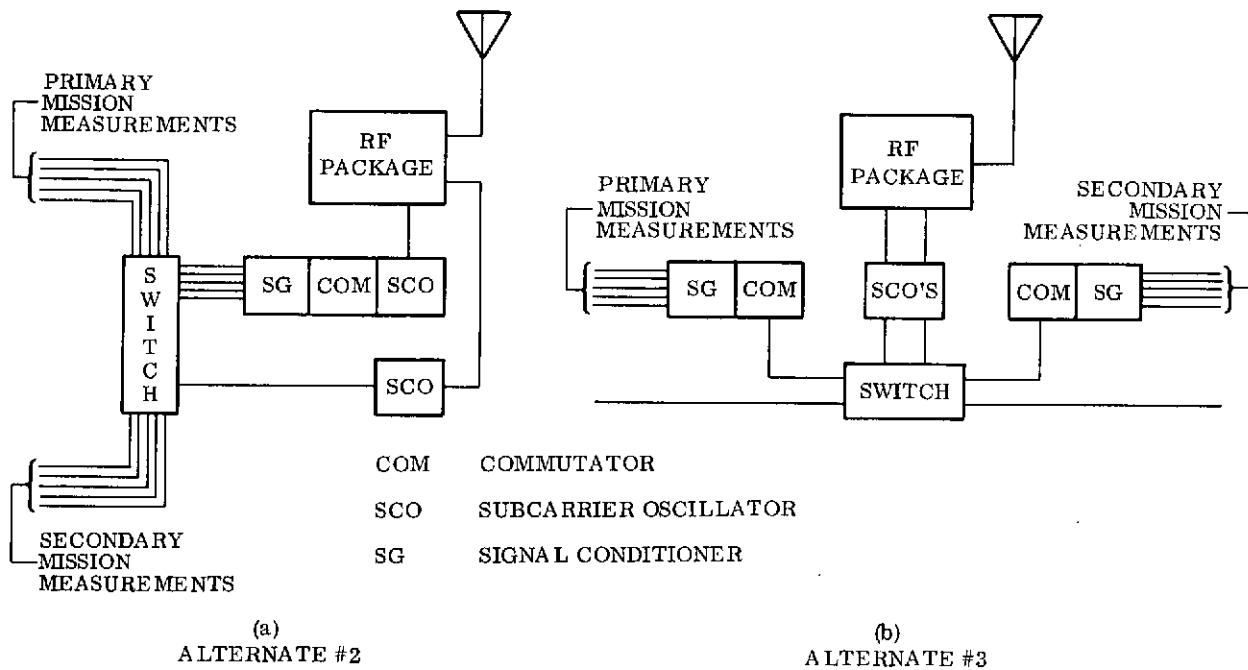


Figure 2-112. Alternate S-Band telemetry configurations.

Alternative No. 1 is the most attractive from a cost standpoint, but it doesn't meet the requirement: there are not enough assured spares available. Furthermore, it is subject to the risk that, near the launch date, additional mandatory instrumentation may be required for an urgent new primary mission measurement that will require "bumping" of secondary mission measurements.

Alternative No. 2 is generally unfavorable because it requires over 3,000 electrical terminations, considering commutator segments, signal conditioners, and harness changes.

Alternative No. 3 is recommended because the risk is only slightly higher than Alternative No. 4 (the lowest risk, viable system), and the cost is lowest of the viable systems. (See Table 2-12)

Alternative No. 4 has the least risk and schedule considerations, but the highest cost.

Table 2-12. S-Band telemetry system alternatives.

Alternatives	Cost	Schedule	Risk
1. Use space available on existing telemetry system	1	4	4
2. Switch inputs to commutator	3	3	3
3. Add commutator and SCO input switches	2	2	2
4. Install 2nd telemetry system	4	1	1

2.7 SUMMARY OF MODIFICATIONS AND SPECIAL EQUIPMENT REQUIRED

The following required modifications to the baseline Atlas F ABRES vehicle have been identified:

- a. HIRS Pitch Rocket (if used on launch vehicle for this mission) will require precise alignment to thrust through the predicted vehicle roll axis.
- b. HIRS Adapter Access Door cut-out and blow-off cover to accommodate pitch rotation rocket exhaust plume.
- c. LO₂ Suction Line for sustainer engine reworked to accept LO₂ tank venting system activated after retrorocket firing.
- d. Telemetry System (assuming retention of baseline S-Band System) will require addition of:
 - (1) Another battery with greater capacity.
 - (2) Relay switch to switch-in above battery after retrorocket firing.
 - (3) Extra commutator and signal conditioners for heat sensor measurements.
 - (4) Two subcarrier oscillator (SCO) input switches.
- e. Discrete Timer will provide additional functions occurring after retrorocket firing (using currently available unused switches) as follows:
 - (1) Switch-in second telemetry battery.
 - (2) Switch-in mission peculiar inputs to subcarrier oscillators.
 - (3) Fire pitch rotation rocket.
 - (4) Shut down missile electrical system inverter.
 - (5) Vent LO₂ tank.
- f. Mounting Provisions for miscellaneous hardware items for above items; i. e., telemetry system commutator, switches, battery, harnesses, etc.

The following special mission peculiar equipment will be required:

- a. Fifty Heating Rate Sensors, together with their associated measurement line harnesses and cableway fairing provisions.
- b. Vehicle Attitude Sensor, consisting of a Northrop NIS-200 inertial platform and data processor.
- c. Pitch Rotation Rocket Motor, consisting of a unit identical to one of the existing HIRS retrorockets, and its new mounting bracket/frame.
- d. LO₂ Tank Venting System, consisting of an ordnance operated (off to on) valve, a poppet-type relief valve, and associated dual overboard dump lines (non-propulsive).

3

PROGRAM CONSIDERATIONS

A conceptual level work statement was generated, and a rough order of magnitude (ROM) estimate for the span times and costs of the various elements was prepared.

3.1 SCHEDULE CONSIDERATIONS

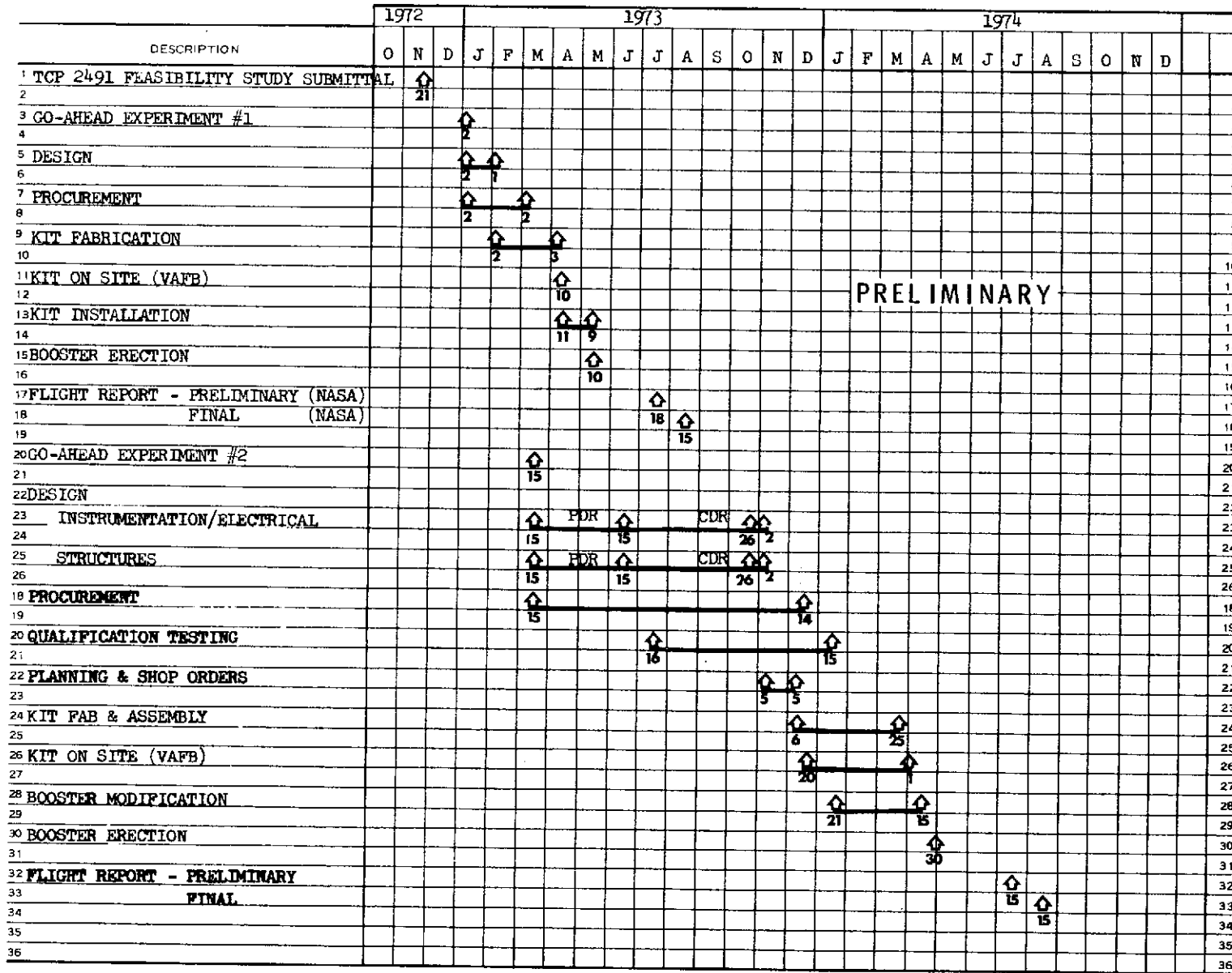
The preliminary schedule is shown in Figure 3-1. It is assumed that the program will proceed in two phases. The first phase will contain the additional structural analysis of tank-mounted components required for structural integrity assurance, and the early S-Band telemetry signal strength and quality test required for definition of the RF blackout problem, defined as Experiment No. 1. The second contains the development activities required to provide the vehicle modifications and special equipment, identified as Experiment No. 2. The time required is 18 months from go-ahead on Experiment No. 1 to flight date of Experiment No. 2. An additional time of about 1-1/2 months is required to reduce the data, prepare a report, and deliver the heating data to LRC for Experiment No. 2. (Note: The flight report shown in Experiment No. 1 is assumed to be supplied to Convair Aerospace Division by NASA-LRC, and consists of the S-Band telemetry data and the NASA-LRC assessment of S-Band telemeter acceptability).

3.2 COST CONSIDERATIONS

A detailed cost estimate was prepared and will be submitted under separate cover. Considerable difficulty was experienced because of the conceptual nature of the work statement, and lack of the detailed definition usually associated with this type of exercise. The overall cost was estimated, excluding consideration of any additional required modifications to tank-mounted equipment and additional modifications or replacement of the S-Band telemetry which might arise from the results of the Experiment No. 1.

3.3 RANGE DATA AVAILABILITY/ARRANGEMENT

The Kwajalein Test Range (KTR) representative at the Western Test Range (WTR) was contacted to determine the capability and required arrangements for obtaining atmospheric density sounding rocket data to 300,000 ft altitude, and radar tracking of the entry vehicle to provide altitude vs time data. The current KTR capability provides sounding rocket data only up to about 200,000 ft. However, an improved rocket is scheduled to be available by mid-1973 which will extend the altitude capability to about 225,000 ft. While not meeting the desired altitude objectives, this will probably provide enough data and the basis for extrapolation to the higher altitudes to be satisfactory.



5481-1 (10-66)

LEGEND

- ↑ SCHEDULED ACTION
- ▲ COMPLETED ACTION
- ◊.....◊ FORECASTED CHANGE
- ▬ TIME SPAN WITH PROGRESS
- ▬ COMPLETED AHEAD OF SCHEDULE
- ▬ CONTINUOUS ACTION

Figure 3-1. NASA aerothermic experiments implementation plan.

Obtaining radar attitude-time data is more straightforward. The equipment for this is currently available and can readily be arranged. The KTR representative indicated that the sounding rocket and radar arrangements can be handled expeditiously if accomplished through the Special Projects Office (SPO) of the ABRES Program at SAMSO. This would require only relatively informal paperwork with about six months advance notice of intent.

4

CONCLUSIONS AND RECOMMENDATIONS

4.1 MISSION AND TRAJECTORY

The most favorable launch vehicle for this mission is one of the general ABRES family which does not employ a HIRS pitch (tumble) rocket.

The time available for gathering data (time interval between 300,000 and 200,000 feet altitude) would be about 8.9 seconds.

The velocity in this interval would be essentially constant at $22,200 \pm 200$ feet per second.

4.2 ENTRY ATTITUDE PREDICTABILITY

The minimum (marginal) pitch rotation rate required to prevent the vehicle from a quasi-stable tail-first entry mode before reaching 200,000 feet altitude is 150 degrees per second.

An initial pitch rotation rate of approximately 180 degrees per second is recommended to provide some margin, and also to increase the yield of heat transfer data.

The High Impulse Retrorocket System (HIRS) pitch rocket should be aligned to thrust through the roll axis as nearly as possible (to minimize roll before the firing of the large pitch rocket) to minimize a yaw component of rotation. (Note: This is not required if a launch vehicle is utilized, which does not employ a HIRS pitch rocket. In this case, the roll rate during data gathering will be less than about 30 degrees per second which is desirable.)

4.3 VEHICLE STRUCTURAL INTEGRITY

Venting of the LO₂ tank to maintain about 21 psi will be required (commencing shortly after retrorocket firing) to prevent overpressurization during coast to the entry area, and to provide the bending moment capability to react entry loads.

One rocket, of the type used for the HIRS retrorocket, mounted normal to the roll axis at the forward end of the HIRS adapter (approximately at Station 415) will provide the desired pitch rate, without exceeding allowable structural loading limits.

The "dirty" aerodynamic configuration at the front end (i.e., open HIRS retro-rocket doors, deployed payload adapter, blunt front end, etc.) does not appear amenable to "cleanup" for an acceptable cost.

The vehicle propellant tanks themselves are capable of sustaining the entry axial, lateral, and bending loads down to 200,000 ft during entry.

Some tank-mounted components and attachment provisions will be loaded in excess of baseline vehicle design criteria (pertinent for launch ascent powered flight) during the 240,000 to 200,000 ft altitude range. The critical components identified were subjected to an "engineering judgment" type review, considering their different condition (pressure level, propellant load, etc.) during entry compared to powered ascent, and it was concluded that they probably would not fail in a manner to cause loss of structural integrity of the tanks.

A preliminary design analysis (as contrasted with conceptual or "engineering judgment," as accomplished thus far) should be conducted on the tank-mounted components and their attachments to the tanks.

4.4 HEATING RATE SENSORS

Simple propellant tank skin-mounted thermocouples do not have adequate response or sensitivity to provide heating rate data of the desired accuracy over the interval of altitude from 300,000 to 200,000 feet.

A straightforward heating rate sensor has been conceptually defined. This sensor should possess the required sensitivity at the lower rates, withstand temperatures associated with the high rates, and provide differential temperature data which is much more readily reduced to heating rates than is data from skin-mounted thermocouples.

4.5 VEHICLE ATTITUDE SENSOR

Existing vehicle equipment is not capable of measuring the vehicle attitude during the entry regime, nor is it capable of being modified to do so.

Only one viable concept based on off-the-shelf developed equipment (available in the 1973 time period) was found to satisfy the mission peculiar requirements after an extensive vendor survey. This concept is based on the Northrop Precision Products/NIS-200 aircraft-type navigation system.

4.6 DATA TRANSMISSION

The existing baseline S-Band telemetry system will probably be subjected to RF black-out at altitudes of 250,000 to 110,000 feet during entry.

An X-Band data transmission system, patterned after that used on the NASA-LRC conducted RAM program is the most viable candidate concept.

A simple S-Band telemetry test, in which additional battery capacity is provided to assure telemetry system operation during the entry of a near-term Atlas F ABRES flight, is recommended. This would provide data to assess the actual signal strength and quality during at least a portion of the suspect altitude range during entry, and provide a datum to forecast the performance of an X-Band system should the S-Band blackout be confirmed.

4.7 PROGRAM CONSIDERATIONS

It is feasible to instrument an expended Atlas F vehicle launched from WTR and obtain heating data as a secondary experiment during the entry altitude interval of from 300,000 to 200,000 feet.

A time span of approximately 18 months from program go-ahead to flight will be required to accomplish the required vehicle modifications and installation of special mission peculiar equipment. The data report would be furnished approximately 1-1/2 months later.

The sounding rockets required to provide the density-altitude data to 225,000 feet, and the radar trackers to provide altitude-time data can be made available through arrangement with the Kwajalein Test Range.

5

REFERENCES

1. Hypersonic Aerodynamic Parameter Program, GDC-ERR-AN-794, December 31, 1965.
2. TOR-669 (S6801-02)-45 Reissue A, Rev. 1, Atlas Series E/F Baseline Missile Performance and Trajectory Parameters, June 1967 (Secret).
3. GD/CA-ABM-70-026 Atmospheric Dispersion Models From the Surface to 700 KM for Space Launch Vehicle Design Analysis, September 8, 1970.
4. Conway, R. J., "Post VECO Atlas Propellant Tank Pressure Study," 966-3-AR-18, 20 October 1967.
5. Conway, R. J., "Atlas Heating Version 5, Part I," GDC-BBA65-002, 15 October 1965.
6. Beckwith, I. E., and Gallaher, J. J., "Local Heat Transfer and Recovery Temperatures on a Yawed Cylinder at a Mach Number of 4.15 and High Reynolds Numbers," NASA-TR-R-104, 1961.
7. Shih, K. T., "Aerodynamic/Structural Heating Computer Program P5613," General Dynamics/Convair Aerospace Report GDCA-ERR-1707, June 1972.
8. O'Neil, R. F., Worscheck, G. A., and Kramer, J. L., "Variable Boundary II Heat Conduction Program," General Dynamics Convair Report GDC-BTD 67-004A Revision A, dated 5 September 1968.
9. Dunn, M. G., "Comparison Between Predicted and Measured Blackout Boundaries for Earth Entry of Apollo," Vol. 1 NASA SP-252, 1971.
10. Huber, P., "Telemetry Attenuation on a Proposed Tumbling Atlas Booster Reentry," Memo to J. Dunavant, NASA-Langley Research Center, October 3, 1962.